CHARACTERISATION OF FLOW
IN
SUSPENSION POLYMERISATION REACTORS

by

MARIA LUISA PEREIRA LEÃO

A thesis submitted to the University of London for the
Degree of Doctor of Philosophy

Department of Chemical Engineering and Chemical Technology,
Imperial College of Science, Technology and Medicine,
Prince Consort Rd.,
London, SW7 2BY, U.K..

July 1989

Aos Meus Pais

Ao Serge

e à Anne–Sophie

ACKNOWLEDGEMENTS

I would like to express my sincere gratitude to my supervisor Dr. G. C. Maitland, for his continued help, guidance and patient supervision throughout this project. The collaboration of Dr. S. M. Richardson and Dr. M. A. Tehrani during the course of this work was of invaluable help.

The technical staff of the Department of Chemical Engineering is thanked for their helpful contribution.

I would like to thank I.C.I. plc for the provision of equipment and technical support, and Dr. A. F. Faraday and Dr. P. V. Smallwood for many constructive discussions and suggestions.

The Comissão Permanente INVOTAN (Lisboa) is thanked for its financial support during the course of this work and the Universidade Nova de Lisboa (Faculdade de Ciências e Tecnologia) for a leave of absence.

The typing effort of Mrs Miranda Lubbock, Miss Sarah Everall and Mrs Josephine Lines to bring the manuscript into this final form are gratefully acknowledged.

Special thanks are owed to my husband and my parents for their devoted support and encouragement during the last stage of this work.

ABSTRACT

The aim of the work described in this thesis was to provide a clearer understanding of how the agitation conditions inside stirred batch suspension polymerisation reactors affect product properties. In the present work suspension polymerisation experiments were carried out in model one–litre batch reactors, under the same conditions for which the fluid in the reactors had been characterised in detail.

Three flow characterisation techniques were used: streak photography; dynamic video monitoring; and laser doppler anemometry. The flow was studied as a function of agitator geometry/speed and baffle characteristics. The flow data have been interpreted in terms of the circulation time distribution (CTD) of particles around the reactor.

Suspension polymerisations of styrene were then carried out under conditions where particle aggregation occurred during the course of the process. The evolution of the polymer particle size distribution with time and monomer conversion was monitored using light scattering techniques and the final product analysed in terms of both its particle size and molecular weight distributions.

The results showed that stirrer speed, the introduction of baffles and by–passing of the liquid surface influenced the circulation times of droplets. The resulting particle size distributions were affected by the onset of aggregation, stirrer speed or presence of baffles. Smaller but significant changes in the molecular weight distribution were observed.

Models were developed to quantify the observed behaviour. The physical parameters required are measures of circulation time distribution, the probability of droplet/particle break–up by the agitator and the critical conversion for the onset of particle aggregation (shown to be related to the evolving glass transition temperature of the reacting systems). This approach is shown to rationalise the behaviour of a range of reactor configurations and agitator variables in terms of universal correlations linking the above parameters to the polymer mean particle size at various stages of the polymerisation.

The present approach is compared with previous, usually more restricted, correlations which attempt to link agitation variables to product properties directly.

TABLE OF CONTENTS

PAGE

ABSTRACT 2

ACKNOWLEDGEMENTS 3

LIST OF TABLES 10

LIST OF FIGURES 13

GLOSSARY OF ABBREVIATIONS 26

CHAPTER ONE – INTRODUCTION 27

References 35

CHAPTER TWO – SUSPENSION POLYMERISATION PROCESSES 36

2.1 Single–Phase Flow 36

2.2 Two–Phase Flow 40

2.3 Polymerising Two–Phase Flow 46

References 50

CHAPTER THREE – FLOW CHARACTERISATION TECHNIQUES 54

3.1 Static Streak Photography 55

3.1.1 Experimental Arrangement 56

(a) Illuminating System 56

(b) Photographic Equipment 62

(c) Choice of Tracer Particles 62

(d) Film Developing Technique 63

3.1.2 Experimental Procedure 64

PAGE

3.2 Dynamic Video Monitoring System 67

3.2.1 Experimental Set–up 67

3.2.2 Data Analysis 70

(a) Software Manipulations 73

3.2.3 Experimental Procedure 74

3.3 Laser Doppler Anemometry 75

3.3.1 Malvern Instrument 76

3.3.2 Signal Processing 77

3.3.3 Definition of Direction of Measurement 87

3.3.4 Commissioning of the Laser Doppler Anemometer 92

3.3.5 Reproducibility of Results 100

3.3.6 Velocity Profile Measurements 101

3.3.7 Reproducibility of Results in 1–litre Autoclave 105

3.3.8 Choice of Traversing System 108

3.3.9 Initial Alignment Procedure for LDA 109

References 115

CHAPTER FOUR – SUSPENSION POLYMERISATION EQUIPMENT 116

4.1 Reactor Geometry 120

4.2 Experimental Procedure 125

PAGE

CHAPTER FIVE – POLYMER CHARACTERISATION TECHNIQUES 129

5.1 Measurement of Particle Size Distribution 130

5.1.1 Measuring Principle of Malvern Particle Size Analyser 131

5.1.2 Experimental Procedure 135

5.1.3 Comparison of Results between Malvern Instrument and Coulter Counter 137

5.2 Measurement of Molecular Weight Distribution 137

5.2.1 Experimental Procedure 141

References 145

CHAPTER SIX – EXPERIMENTAL RESULTS 146

6.1 Preliminary Comparison of Results with Existing Correlations 146

6.2 2–Bladed Paddle ("Simple") Geometry 154

6.2.1 Flow Characterisation Experiments 154

(a) Static Streak Photography 154

(b) Dynamic Video Monitoring System 156

(c) Laser Doppler Anemometry 162

6.2.2 Suspension Polymerisation Experiments 181

(a) Choice of Polymerisation Recipe 181

(b) Variation of Stirrer Speed 188

6.2.3 Polymer Characterisation 190

(a) Particle Size Distribution 190

(b) Molecular Weight Distribution 196

PAGE

6.3 4–Bladed Paddle ("Complex") Geometry 199

6.3.1 Flow Characterisation Experiments 199

(a) Static Streak Photography 199

(b) Dynamic Video Monitoring 205

(c) Laser Doppler Anemometry 211

(d) Comparison between "Mixflow" 231

Solution and LDA Data 234

6.3.2 Suspension Polymerisation experiments 234

(a) Choice of Polymerisation Recipe 234

(b) Variation of Agitation Conditions:

Stirrer Speed and Baffling 239

6.3.3 Polymer and Process Characterisation 241

(a) Particle Size Distribution 241

(b) Suspension Process Characterisation 257

(c) Molecular Weight Distribution 266

References 269

CHAPTER SEVEN – DISCUSSION AND CONCLUSION 271

7.1 Introduction 271

7.2 Qualitative Model of Suspension Polymerisation 271

7.3 Quantitative Models 275

7.3.1 Product Particle Size Distribution 281

(a) Equilibrium Size Distribution 281

(b) Final Aggregate Product 285

(c) Final Product after Treatment

with Ultra–Sound 289

PAGE

7.3.2 Product Molecular Weight Distribution 291

7.4 Concluding Remarks 293

References 297

APPENDIX I Definition of virtual position of cross–over for a square–sectioned glass channel 298

APPENDIX II Derivation of cross–over and photomultiplier positions for horizontal and vertical anemometer laser beams in the case of the glass reactor 302

Part I Determination of cross–over position with laser beams in horizontal plane 302

(i) Left beam 304

(ii) Right beam 306

Part II Determination of cross–over position with laser beams in vertical plane 309

(i) Incidence at outer glass surface (Finding γ_1) 309

(ii) Lowering of beam (z–direction) inside glass wall (c) 312

(iii) Calculation of γ_3, the angle of incidence on the glass–water interface 314

(iv) The beam in water 316

(v) Coordinates of cross–over 319

		PAGE
Part III	Determination of photomultiplier position in order to see light scattered from the cross–over	321
Nomenclature		324
APPENDIX III	Derivation of an expression for monomer conversion as a function of time and calculation of monomer conversion at various temperatures for onset of aggregation	325
APPENDIX IV	Computer Programs for LDA	330
	1 Bacscat 321	330
	2 Bacscat 341	338

LIST OF TABLES

		PAGE
Table 3.1	Table of Results for 15 Repeat Runs for Vertical Velocity in Perspex Flow Cell	101
Table 3.2	Experimental Results for Tangential Velocity in Ten Repeat Runs	106
Table 6.1	Sauter Mean Diameter from Calderbank Equation and from Experiments in this Work	148
Table 6.2	Circulation Time Distribution for Simple Geometry	171
Table 6.3	Experimental Conditions for Polymers 1–12, using the 2–Bladed Paddle	182
Table 6.4	Variation of Stirrer Speed for 2–Bladed Paddle Polymerisations	188
Table 6.5	Table of Results for Molecular Weight Distribution of Polymers 1–16	196
Table 6.6	Table of Results for Experimental and Theoretical Values for Molecular Weight Distribution of Polymers 1, 3–16	197
Table 6.7	Circulation Time Distribution for 4–Bladed Paddle	227
Table 6.8	Average Shear Rate for 4–Bladed Paddle, for the Various Agitation Conditions	228

		PAGE
Table 6.9	Variation of Suspending Agent Concentration for 4–Bladed Paddle Polymerisations	235
Table 6.10	Agitation Conditions for Suspension Polymerisations of Styrene in Complex Geometry	240
Table 6.11	Polymerisation Temperatures, t_{agg} and x_{agg} for Suspension Polymerisations of Styrene in Complex Geometry	261
Table 6.12	Molecular Weight Distribution for Polystyrene Obtained with 4–Bladed Paddle Geometry	266
Table 6.13	Table of Results for Theoretical Molecular Weight Distribution at 80° C and Experimental Values of Simple and Complex Geometry	267
Table 6.14	Table of Results for Experimental and Theoretical Values of Molecular Weight Distribution for Various Polymerisation Temperatures	268
Table 7.1	Quantification of Model Between Agitation Variables and Circulation Time Characteristics	279
Table 7.2	Exponent of power law dependence of circulation time with stirrer speed for the various reactor geometries	280
Table 7.3	Mean Diameter and Width of Primary (d_1) and Secondary (d_2) Peaks for PSD of Complex Geometry at t = 2.5h	281

PAGE

Table 7.4	50% mean and Sauter Mean Diameter for final Aggregated Polymers in Complex Geometry	285
Table 7.5	Table of Results for PSD of Final Product After Ultra–Sound Treatment, for 2–Bladed and 4–Bladed Paddle	289
Table III.1	Table of Results for Time and Conversion at Onset of Aggregation, as a Function of Temperature	328
Table III.2	Table of Results for Variation of Experimental Conversion at Onset of Aggregation as a Function of Temperature, when Errors are Introduced	329

LIST OF FIGURES

		PAGE
Figure 3.1	Illumination system with slide projector	59
Figure 3.2	Streak photography using a narrow illuminating plane of light (narrower than 2.5 min)	59
Figure 3.3	Streak photography using a medium wide illuminating plane of light (2.5–4.5 min)	60
Figure 3.4	Streak photography using a wide illuminating plane of light (wider than 4.5 min)	61
Figure 3.5	Photograph with experimental arrangement of reactor for streak photography	65
Figure 3.6	Schematic diagram with arrangement for streak photography	66
Figure 3.7	Variation of percentage time in zone for floats denser and lighter than water	69
Figure 3.8	Variation of percentage time in zone for float with density match	71
Figure 3.9	Definition of scanning area in relation to screen, in dynamic video monitoring system	72
Figure 3.10	Block diagram of Laser doppler anemometer	78
Figure 3.11	Measuring volume showing fringes	79
Figure 3.12	Detection of photons at photomultiplier	80
Figure 3.13	Block diagram of clipping system	82
Figure 3.14	Autocorrelation function	85
Figure 3.15	Schematic diagram of possible scattering arrangements	88

		PAGE
Figure 3.16	Phase shift due to applied sawtooth voltage	91
Figure 3.17	Perspex cell for flow measurement	94
Figure 3.18	Effect of the variation of sample time on velocity and turbulence intensity, for a mean velocity, from flow rate measurements, of 0.85cm s^{-1}	96
Figure 3.19	Probability distribution functions for velocity	97
Figure 3.20	Effect of the variation of sample time on velocity and turbulence intensity for a mean velocity, from flow rate measurements, of 0.58cm s^{-1}	99
Figure 3.21	Glass cell used for determination of velocity profile	103
Figure 3.22	Velocity profile in a rectangular channel	104
Figure 3.23	Schematic view of LDA arrangement	111
Figure 3.24	Schematic diagram of deck–plate and adjustable nuts	111
Figure 3.25	Positioning of laser along x–axis	112
Figure 4.1	Photographs of reactor and motor assembly	117
Figure 4.2	Schematic diagram of reactor assembly	118
Figure 4.3	Photograph of deck–plate attachments	119
Figure 4.4	Heating/cooling system for glass reactor	121

		PAGE
Figure 4.5	2–bladed paddle used in "simple geometry"	122
Figure 4.6	4–bladed paddle used in "complex geometry"	122
Figure 4.7	Baffle used in complex geometry	123
Figure 4.8	Baffle disc	124
Figure 5.1	Block diagram of Malvern Particle Size Analyser	133
Figure 5.2	Schematic diagram of detector of Malvern Particle Size Analyser	134
Figure 5.3	Cumulative and differential undersize volume curves for a test polymer sample	138
Figure 5.4	Number and weight molecular weight distribution curves	139
Figure 5.5	Typical gel permeation chromatogram for polystyrene samples	143
Figure 5.6	Calibration curve for gel permeation chromatography	144
Figure 6.1	Comparison of experimental results and predictive models of mean particle size as a function of stirrer speed	150
Figure 6.2	Streak photography of vertical flow patterns in simple geometry at 150 and 300 rpm	155
Figure 6.3	Variation of scanning time for 2–bladed paddle at 150 rpm	157
Figure 6.4	Variation of percentage time spent in zone with stirrer speed for 2–bladed paddle	158

		PAGE
Figure 6.5	Probability of direction change at zone, for 2–bladed paddle, at 150 rpm, for 25 minutes	160
Figure 6.6	Variation of probability of direction change at zone with stirrer speed for 2–bladed paddle for 10 minutes	161
Figure 6.7	Measuring positions for LDA for the 2–bladed paddle at the bottom of the reactor	163
Figure 6.8	Tangential velocity profiles for 2–bladed paddle at the bottom of the reactor, at 300 rpm	164
Figure 6.9	Tangential velocity profiles for 2–bladed paddle at the bottom of the reactor, at 400 rpm	165
Figure 6.10	Vertical velocity profiles for 2–bladed paddle at the bottom of the reactor, at 300 rpm	166
Figure 6.11	Vertical velocity profiles for 2–bladed paddle at the bottom of the reactor, at 400 rpm	167
Figure 6.12	LDA measuring positions with shaft encoder	172
Figure 6.13	Tangential velocity measurements with and without shaft encoder, at the radial position of R = 3.2 cm and 400 rpm, for the 2–bladed paddle geometry	174

		PAGE
Figure 6.14	LDA measuring positions for 2–bladed paddle in the middle of the reactor	175
Figure 6.15	Tangential velocity profiles for 2–bladed paddle in the middle of reactor, at 200 rpm	176
Figure 6.16	Tangential velocity profiles for 2–bladed paddle in the middle of the reactor, at 200 rpm, for various radial positions	177
Figure 6.17	Vertical velocity for 2–bladed paddle in the middle of the reactor at 200 rpm	178
Figure 6.18	Vertical velocity profiles for 2–bladed paddle in the middle of the reactor, at 200 rpm, for various radial positions	179
Figure 6.19	Effect of the variation of suspending agent concentration on the particle size distribution of polystyrene, at 400 rpm, for the 2–bladed paddle	184
Figure 6.20	Effect of the variation of suspending agent concentration on 50% mean diameter for the 2–bladed paddle at 400 rpm	185
Figure 6.21	Particle size distribution of Polymers 2 and 3, in 2–bladed paddle geometry	186
Figure 6.22	Photograph of Polymer 3 showing the aggregated particles	189

		PAGE
Figure 6.23	Temperature and pressure profiles during a typical polymerisation reaction	191
Figure 6.24	Effect of the variation of stirrer speed on the particle size distribution for 2–bladed paddle	193
Figure 6.25	High resolution particle size distribution of polymers obtained in simple geometry at various stirrer speeds	194
Figure 6.26	Variation of mean diameter, $d_{50\%}$ with stirrer speed, for 2–bladed paddle at a PVA concentration of 2.5 $g.l^{-1}$	195
Figure 6.27	Streak photography of vertical flow patterns for the 4–bladed paddle at 150 and 300 rpm, without baffles	200
Figure 6.28	Streak photography of vertical flow patterns for the 4–bladed paddle with and without baffles, at 150 rpm	201
Figure 6.29	Streak photography of vertical flow patterns for the 4–bladed paddle with 86 and 112 mm baffles, at 150 rpm	203
Figure 6.30	Streak photography of vertical flow patterns for the 4–bladed paddle with 112 mm baffles at 90 ° and 10 ° to the light plane, at 150 rpm	204
Figure 6.31	Variation of percentage time in zone versus stirrer speed for the 4–bladed paddle without baffles	206

		PAGE
Figure 6.32	Variation of percentage time in zone with stirrer speed for the 4–bladed paddle with 112 mm baffles	208
Figure 6.33	Probability of direction change at zone for the 4–bladed paddle, with and without baffles, at 150 rpm, for 25 minutes	210
Figure 6.34	Variation of probability of direction change at zone with stirrer speed, for the 4–bladed paddle, with and without baffles, for 10 minutes	212
Figure 6.35	Measuring positions in LDA for the 4–bladed paddle	214
Figure 6.36	Tangential velocity profiles for the 4–bladed paddle, at 150 rpm, without baffles	215
Figure 6.37	Tangential velocity profiles for the 4–bladed paddle at 400 rpm, without baffles	216
Figure 6.38	Tangential velocity profiles for the 4–bladed paddle at 150 rpm, with baffles	217
Figure 6.39	Tangential velocity profiles for the 4–bladed paddle, at 400 rpm, with baffles	218

		PAGE
Figure 6.40	Vertical velocity profiles for the 4–bladed paddle, at 150 rpm, without baffles	219
Figure 6.41	Vertical velocity profiles for the 4–bladed paddle, at 400 rpm, without baffles	220
Figure 6.42	Vertical velocity profiles for the 4–bladed paddle, at 150 rpm, with baffles	221
Figure 6.43	Vertical velocity profiles for the 4–bladed paddle, at 400 rpm, with baffles	222
Figure 6.44	Shear rate profiles based on tangential velocity for the 4–bladed paddle at 150 and 400 rpm	229
Figure 6.45	Shear rate profiles based on vertical velocity for the 4–bladed paddle at 150 and 400 rpm	230
Figure 6.46	"Mixflow" simulation profiles for tangential velocity at various heights in the reactor	232
Figure 6.47	"Mixflow" simulation profiles for vertical velocity at various heights in the reactor	233
Figure 6.48	Effect of suspending agent concentration on the particle size distribution of polystyrne obtained with 4–bladed paddle, at 400 rpm	236

		PAGE
Figure 6.49	Effect of suspending agent concentration on the particle size distribution of polystyrene obtained with 4–bladed paddle, at 400 rpm, after 1 minute ultra–sound treatment	238
Figure 6.50	Evolution of the particle size distribution with time for the suspension polymerisation of styrene at 200 rpm, without baffles, with the 4–bladed paddle	242
Figure 6.51	Evolution of the particle size distribution with time for the suspension polymerisation of styrene at 200 pm, with baffles, with the 4–bladed paddle	243
Figure 6.52	High resolution particle size distribution, at t = 2.5 h, for the complex geometry, at 200 rpm with and without baffles	244
Figure 6.53	High resolution particle size distribution for the final product, for the complex geometry, at 200 rpm, with and without baffles	245
Figure 6.54	High resolution particle size distribution for the final product, after ultra–sound treatment, for the complex geometry, at 200 rpm, with and without baffles	246

		PAGE
Figure 6.55	Evolution of the particle size distribution with time for styrene suspension polymerisation with the 4–bladed paddle, at 400 rpm, without baffles	247
Figure 6.56	Evolution of the particle size distribution with time for styrene suspension polymerisation with the 4–bladed paddle, at 400 rpm, with baffles	248
Figure 6.57	High resolution particle size distribution, at t = 2.5 h for the computer geometry at 400 rpm with and without baffles	249
Figure 6.58	High resolution particle size distribution for the final product, for the complex geometry, at 400 rpm, with and without baffles	250
Figure 6.59	High resolution particle size distrbution for the final product, after ultra–sound treatment, for the complex geometry, at 400 rpm, with and without baffles	251
Figure 6.60	Evolution of the particle size distribution with time for styrene suspension polymerisation, with 4–bladed paddle, without baffles, at 75.5 °C	256

		PAGE
Figure 6.61	Glass transition temperature of droplet (monomer and polymer) versus conversion	260
Figure 6.62	Temperature profiles for polymerisations performed at different temperatures	262
Figure 6.63	Variation of time of aggregation as a function of polymerisation temperature	264
Figure 6.64	Variation of temperature of polymerisation versus conversion at onset of net aggregation	265
Figure 7.1	Schematic structure of quantitative models between agitation variables, reactor flow and polymer properties	276
Figure 7.2	Correlations between PSD with effective circulation time for equilbrium size distribution, t = 2.5 h, for 4–bladed paddle	282
Figure 7.3	Correlation between the normalised spread of sizes within each peak with spread of circulation time distribution for the equilibrium size distribution, for the 4–bladed paddle	284
Figure 7.4	Correlation between the 50% mean and Sauter mean diameter of the final aggregated product with the effective circulation time, in the complex geometry case	286

		PAGE
Figure 7.5	Correlations between breadth of distribution distribution of final aggregated product with spread and effective circulation time, in the complex geometry	288
Figure 7.6	Correlation between the PSD of final product after ultra–sound treatment with the ratio of the effective circulation time over number of blades, for 2–bladed and 4–bladed paddle	290
Figure 7.7	Correlation between the normalised spread of sizes within each peak with spread of circulation time distribution for the final product after ultra–sound treatment in 2–bladed and 4–bladed paddle	292
Figure 7.8	Correlation between weight average molecular weight and the polydispersity with the effective incubation time, for the 2–bladed and 4–bladed paddle	294
Figure I.1	Determination of virtual position of cross–over in a square–sectioned glass channel	299
Figure II.1	Multiple refraction of laser beams, when in horizontal plane, and going through air, glass and water	303
Figure II.2	Multiple refractions for left laser beam, horizontal plane, showing relevant points and angles	305

		PAGE
Figure II.3	Multiple refractions for right beam, horizontal plane, showing relevant points and angles	307
Figure II.4	Incidence of upper laser beam, vertical plane, on outer glass wall	310
Figure II.5	Lowering of beam inside glass wall, in z–direction	313
Figure II.6	Slab of reactor used for determination of angle of incidence of beam on glass/water interface	315
Figure II.7	Slab of reactor used for determination of cross–over point, in water	317
Figure II.8	Diagram of system showing movement of laser beam in the XY plane	320
Figure II.9	Diagram of the path of a ray of light coming from the cross–over and reaching the photomultiplier	322

GLOSSARY OF ABBREVIATIONS

CTD Circulation Time Distribution

LDA Laser Doppler Anemometry

MWD Molecular Weight Distribution

PDF Probability Distribution function

PSD Particle Size Distribution

PVA Polyvinyl alcohol

PVC Polyvinyl chloride

CHAPTER ONE

INTRODUCTION

The importance of the polymer manufacturing industry has grown steadily since the early days in 1907, when Leo Baekeland synthetised the first commercial polymer: the phenol–formaldehyde resin (Bakelite). The West European market of polystyrene and polyvinyl chloride alone accounted for a production of 8 million tonnes in 1988[1] which gives an idea of the significance of this industry.

The role of the polymer reaction engineer is to produce polymers that are suitable for undergoing particular processing transformations and have the required product specifications, for example, mechanical strength, electrical properties, corrosion resistance, for their final applications.

The physical properties of the polymers are determined essentially by two characteristics over which the reactor engineer has some control: molecular weight distribution (MWD) e.g. degree of branching, copolymerisation, and product morphology e.g. crystallinity, physical state (powder or melt), porosity and particle size. The viscoelastic properties of the melt (or solution) that determine the processability of the polymer are strongly affected by the high molecular weight tail of the distribution, while the stability and chemical reactivity might often depend on the low molecular weight tail. The particle size and porosity can determine the level of plasticizer uptake in polyvinyl chloride, for example, which determines the mechanical strength of the final product.

These two characteristics are in turn influenced by various factors due to the

process conditions: the temperature and pressure determine the chemical kinetics of a particular system; the polymerisation method chosen (which can take place in the liquid (bulk, solution, suspension and emulsion), gas or solid phase, and involve either homogeneous or heterogeneous phase conditions) largely controls the heat transfer characteristics and hence indirectly the temperature history; and the type of reactor in which the polymerisation is being carried out (batch, continuous or semi–batch) which determines the residence time distribution inside the reactor, hence the reactant concentrations and the kind of molecular weight distribution possible for a certain polymerisation mechanism.

A common feature to all polymerisation methods and reactors, with the exception of ideal plug flow reactors and quiescent polymerisations in moulds, is the need for thorough material mixing which constitutes the critical transport process for polymerisation reactor performance and greatly affects the polymer products.

Agitation affects the macromixing, i.e. the circulation of material in the reactor; the heat transfer between the polymerising system and the reactor wall; the level of micromixing, i.e. the initial droplet size distribution in heterogeneous systems (suspension); and the physical nature of the polymer product (e.g. porosity). The combination of poor heat conductivity of the polymer melt and its high viscosity can greatly reduce the amount of heat transfer in the system, creating temperature and concentration gradients, which can cause a departure from steady–state kinetics with the onset of the gel effect [2] and considerably affecting the resulting molecular weight distribution. By providing a suitable level of agitation it may be possible to reduce this problem or, at least, to delay its occurrence. It is evident that by controlling the agitation both the molecular weight distribution and the morphology can be affected, which is of paramount importance either for homogeneous or heterogeneous processes.

The present study has focused on one particular polymerisation process where the consequences of agitation performance are particularly important in controlling product properties. This is the suspension polymerisation process [2] which is a heterogeneous method which avoids the major heat transfer problems found in the bulk processes by suspending droplets of a water–insoluble monomer in an aqueous phase. The continuous medium is usually water and a stable dispersion is maintained by the use of agitation and the addition of a water–soluble protective colloid (polyvinyl alcohol, for example). The relatively low viscosity of the water suspension combined with the fact that this will change very little during polymerisation reduces considerably the risks of having a run–away reaction and heat can be effectively transferred through the walls of the reactor. The initiator is soluble in the monomer (dispersed) phase, and within each droplet there is a mini–bulk polymerisation taking place. The kinetics of the suspension process are therefore well–known, and identical to the bulk process in the same kind of reactor, which for a given monomer will yield a molecular weight distribution determined by the polymerisation temperature and pressure.

The resulting particle size distribution is critically dependent on the agitation conditions in the reactor and the level of protective colloid used to prevent excessive agglomeration of the dispersed phase. The usual particle diameter in a suspension polymerisation ranges from 10–1000 μm. The resulting polymer particles can have a range of morphologies, from pearl–like spherical beads, for well protected monomer–soluble polymers formed entirely below their glass–transition temperature, to highly irregular porous agglomerates where the surface protection was less than perfect or phase separation occurred. Another advantage of this process is that the polymer particles can be easily separated from the continuous medium and after washing and drying they are ready for processing.

The level of agitation is crucial and affects various aspects during the course of a suspension polymerisation:

(i) the initial monomer droplet formation;

(ii) any subsequent coalescence–aggregation/break–up process of the polymerising droplet (containing monomer plus growing polymer);

(iii) the convective contribution to the overall heat transfer between the exothermally polymerising droplets and the reactor walls, which will mainly influence the molecular weight distribution of the polymers, as already described.

The balance between the droplet break–up process caused by appropriate fluid flow conditions (e.g. high shear, extensional/turbulent eddies) in certain regions of the reactor and any recombination, coalescence or aggregation processes (where the particle collisions and their surface characteristics permit, usually in the reactor regions involving less extreme flow conditions) is affected by both the agitation conditions in the reactor and the evolving material characteristics of the polymerising particles such as surface tension, viscosity, adhesion and elasticity, influenced in turn by the nature and amount of any protective colloid used. Hence, if enough protective colloid is added for a specific agitation condition, then it is possible to run suspension polymerisations in a non–coalescing mode, where the final particle size distribution is mainly the initial one and the product is essentially non–porous. On the other hand, there are systems where coalescence cannot be suppressed totally, like in the case of polyvinyl chloride, and the balance between coalescence and break–up will determine the final particle size as well as the porosity.

The nature of the agitation in a suspension polymerisation can be changed by either modifications to the autoclave geometry or in the agitation conditions, i.e. agitator type, its size or speed and the presence or absence of baffles. A change in any of these characteristics will produce modifications in product properties.

The present level of understanding between agitation variables and product properties is limited to empirical correlations for restricted ranges of conditions, without a full understanding of their physical basis. The work done has usually tried to link the final product properties to material properties and agitation parameters (such as stirrer speed), mostly through the use of dimensionless numbers (e.g. Reynolds or Weber). The validity of these correlations is very limited, with the parameter involved varying from system to system and even changing within one system from higher to lower speed ranges. This approach is often inadequate to suitably describe the complex phenomena that occur is suspension polymerisation processes. In addition to their lack of universal applicability, a number of other deficiencies can be pointed out: namely the shape of the particle size distribution and its dynamics are not considered; these correlations are mostly restricted to non–agglomerating systems, because the physics of the coalescence process is not included.

The agitation variables relevant to a particular stirred reactor are only linked to the final product properties through the characteristics of the flow they induce i.e. the flow pattern and the fluid velocities. These features determine the flow history of polymerising fluid elements in the reactor, which in turn dictate the evolution of the polymer properties. The shortcomings of the previous attempts to correlate suspension polymer properties with "agitation" has arisen by not giving

sufficient attention to the detail of this vital middle link, the "flow". It is the purpose of this work to fill in some of these gaps, by characterising the flow in stirred polymerisation autoclaves in some detail. This constitutes a novel way of looking at this problem by utilising techniques that have been fairly widely used for non–reactive systems, but hardly at all for those involving polymerisation.

During a suspension polymerisation a droplet will be subjected to a variety of flow conditions, from the more turbulent regions near the agitator to the more quiescent ones near the surface, i.e. from highly extensional flow regions to more simple shear zones. The details of the circulation mode of the polymerising droplets between these different regimes are of crucial importance to determine the final product properties, and the original approach adopted here aims to investigate these factors in some detail.

The objectives set at the beginning of this work were:

1. To characterise the flow in stirred autoclaves as a function of reactor/agitator geometry and speed, using three flow characterisation techniques, designed to examine the reactor flow at different length scales: streak photography, dynamic video monitoring and laser doppler anemomometry.

2. To carry out suspension polymerisations under these well characterised flow conditions, to monitor the evolution of the particle size distribution with time, and to analyse both the particle size and molecular weight distributions of the resulting final polymers.

3. To understand the nature of the link between the flow characteristics and the polymer properties in terms of the flow history of the polymerising droplets/particles and their frequency of return to the agitator.

4. To devise a more general model than those previously available i.e. to be able to state the required agitation conditions that would define certain flow characteristics necessary to produce a particular set of polymer characteristics.

The monomer chosen to work with was styrene which is often described as a non–coalescing system, where the polymer is soluble in the monomer and which did not require the use of any special safety measures beyond conventional laboratory practice. However, by working at low levels of protective colloid, styrene can also be deliberately run in coalescing mode. It can therefore act as a simple model system for more complex coalescing situations, like the commercially important polyvinyl chloride where the monomer is carcinogenic and hence leads to prohibitively restrictive laboratory safety procedures. (For polyvinyl chloride, where in contrast to polystyrene the polymer is insoluble in its own monomer, the porosity within the original droplets is in addition to the porosity between droplets in the polymerised aggregates. Only the latter source of porosity is present in styrene studies).

The next chapter will review the current state of knowledge regarding suspension polymerisation processes. This is followed by two chapters (three and four) where the flow characterisation and the suspension polymerisation techniques used are explained in detail and chapter five describes the polymer characterisation techniques. In chapter six a detailed description of the experimental results for both

flow and polymer characterisation is given. This chapter also analyses their inter–relation in terms of the droplet flow history during the process. Finally chapter seven discusses further the results and contains a more detailed analysis, presenting quantitative correlations between flow parameters and product properties.

References to Chapter One

[1] UBS Philips and Drew stockbrokers (1989)

[2] "Principles of Polymer Systems" F. Rodriguez, McGraw–Hill (New York), 2nd Edition, 1968

CHAPTER TWO

SUSPENSION POLYMERISATION PROCESSES

This chapter will critically review important past work concerned with the agitation effects on suspension polymerisation processes and most particularly to the polystyrene case. Owing to the nature of the suspension process: liquid droplets dispersed by agitation in a continuous medium, it is useful to cover also some associated important aspects relating to non–polymerising single– and two– phase liquid systems, before drawing our attention to polymerising two–phase systems.

2.1 Single–Phase Flow

The fluid flow inside agitated autoclaves under turbulent conditions is a highly complex phenomenon and its complete quantitative prediction has not yet been possible. There are a number of computational methods aimed at simulating as much detail of the turbulent motion as possible or, more usually, its overall effect on the mean flow behaviour. Turbulence is a three–dimensional, time–dependent, non–linear phenomenon [1] and can be described by the Navier–Stokes momentum equations, which express the conservation of momentum for a continuum fluid with viscous stress directly proportional to the rate of strain. Turbulence is dissipated and momentum exchanged by small scale fluctuations: eddies. There is no existing or foreseen computer system with large enough memory or speed to allow the resolution of the small scale effects. Therefore, in quantitative work it is necessary to use turbulence models based on averaged Navier–Stokes equations. Next, we shall review past attempts on this subject which are concerned with flow in stirred reactors.

Cutter (1966) [2] derived some equations to describe the fluid flow in a stirred tank. The starting point were the Navier–Stokes equations and the energy equation and he made several assumptions: all velocities outside the impeller stream were negligible compared with those in the impeller stream; vertical mean velocities were negligible compared with radial and tangential components; there was circular symmetry in all velocity components and there was symmetry between top and bottom halves of the impeller stream. Under these conditions he arrived at equations that were used, together with results obtained by streak photography, to estimate angular momentum at different radial sections of the tank and to calculate the flow of energy through these sections. He concluded that turbulence was higher near the impeller and less intense in other regions.

Harvey and Greaves (1982) [3, 4] used the turbulence intensity, k/ϵ, dissipation model developed by Launder and Spalding [5] for the flow in agitated, baffled vessels. Nevertheless, it could not describe the flow near baffles or the agitator; it gave only gross circulation patterns, although the qualitative agreement with experiments was good.

More recently Placek et al [6] applied the turbulent intensity/dissipation (k–ϵ) model to a baffled vessel with a turbine impeller and included the turbulent energy vortices and the inertial range eddies to construct an algorithm for the computation of profiles of mean velocity, kinetic energy of turbulence and dissipation rate of turbulence. The results showed good agreement with reported circulation time correlations for this kind of stirrer.

The incomplete level of theoretical single–flow quantification reinforces the

need for accurate experimental velocity measurements inside agitated reactors, to provide some reliable data so that computer predictions can be checked and also as basis for giving reliable flow characterisation for understanding processes dependent on the details of that flow.

The experimental work done on characterisation of fluid flow inside agitated vessels that developed alongside with the theoretical predictions will be reviewed.

Sachs and Rushton (1954) [7] used streak photography to obtain the three components of velocity inside an agitated vessel. A shutter–tripping device was used to set the position of the impeller in relation to the illuminated plane of light. A carbon–arc light and two slits were used to produce sheets of light of approximately 4.8 mm which did not diverge appreciably.

The same experimental arrangement was used by Metzner and Taylor (1960) [8] who used streak photography to obtain shear rates and power consumption for Newtonian and non–Newtonian fluids at low Reynolds numbers (mainly laminar and transition regions).

Cutter (1966) [8] used licopodium tracer particles to obtain streak photography results. The light source was provided by a flash tube firing through a rotating slotting disc and very short exposure times were used (1/600 s). This photographic method was confirmed by measurements using a Kiel impact tube.

Kuboi et al (1972) [10] used a high–speed cine–photography camera to continuously record the motion of particles in an illuminated vertical slice (1 cm wide) of the tank. A film motion analyzer was used to measure particle

displacement with an accuracy of 5×10^{-3} cm. Their results point out that particle motion is essentially determined by turbulent eddies, whose characteristic length is comparable with particle diameters.

Work done by Van't Riet and Smith (1975) [11] on the discharge stream of a disc turbine, using photographic (still camera rotating synchronously with the agitator) velocity measurements, revealed the existence of trailing vortices behind each blade. This trailing pair originates behind the top and bottom edges of the moving blade as rolling vortices with horizontal axes. Their identity was maintained for 2 to 3 blade lengths.

Van der Molen and Van Maanen (1978) [12] used laser doppler anemometry to measure the various fluid velocity components in the impeller discharge stream. A frequency shift device was used to eliminate directional ambiguity. Their accurate velocity measurements confirmed the previous findings of Van't Riet and Smith [11] that close to the impeller the flow is dominated by the periodically fluctuating flow of the trailing vortices behind the impeller blades, the mean velocity in the trailing vortices was found to be dependent on impeller geometry.

Callender (1983) [13] obtained good streak photography results using a 1 KW spotlight and a vertical slit to illuminate an agitated tank. Detailed photographic parameters are given. He also reported that a low power laser modified by a cylindrical lens gave rise to a useful lighting system, although a single experiment was performed.

More recently Yianneskis et al (1987) [14] conducted flow visualisation and laser doppler anemometry experiments in stirred reactors. Flow visualisation was

used to obtain qualitative information on flow patterns using a 500 mW Argon–Ion laser and a cylindrical lens to view planes of liquid seeded with polystyrene beads (diameter = 500 μm). The laser doppler anemometer results revealed a flow structure controlled mainly by convection and pressure forces with turbulent mixing important in the impeller region. The trailing vortices behind each blade had velocities that were of the order of 0.25 of the blade tip velocity.

This summary of past work on the experimental side of the fluid flow characterisation shows that if accurate and reliable velocity measurements are needed, then laser doppler anemometry is the most used technique. Streak photography can be used to yield useful information on flow patterns and either a white or laser light sources have been successfully used. The possibility of using high–speed cine cameras is also reported.

2.2 Two–phase flow

The addition of a second phase in the theoretical treatment of fluid flow inside agitated reactors increases the complexity of the system by several fold and the theoretical quantification is much more limited that for single–phase flow. The approaches that have been generally followed to tackle liquid–liquid dispersions involve assuming either that only break–up or coalescence occur.

This work will be reviewed in chronological order, with particular attention focused on the mechanism of droplet deformation, droplet break–up, coalescence and the various factors that are relevant in the droplet break–up/coalescence process.

Taylor (1934) [15] did pioneering work on the mechanism of drop deformation in laminar flows and proposed an equation involving the speed of flow, interfacial tension, viscosity and the radius of drop as variables, to account for small deformations from the spherical form at slow speeds.

Torza, Cox and Mason (1972) [16] conducted experiments of deformation and droplet bursting in laminar flow and were led to the conclusion that the mode of break–up depended upon the rate at which the shear rate was applied. The bursting mode was classified according to Rumscheidt and Mason (1961) [17]. It was reported that big and viscous drops were more easily pulled out into liquid threads than small and inviscid drops, which then eventually became varicose and broke into smaller drops along with the formation of even smaller satellite droplets.

The subject of droplet break–up in well–defined flow fields has been recently investigated by Tehrani (1987) [18], under extensional and rotational flow conditions. The system studied was 1,1,1–trichloethane and n–hexane in glycerol, using polyvinyl alcohol as protective agent (interfacial tension = 1 mNm^{-1}). In the latter case there was little evidence of droplet break–up, whereas in extensional flows there was evidence of droplet break–up and a mean size of $\sim$ 50 μm was obtained for the final equilibrium size distribution, at an extensional rate of 40 sec^{-1}.

A related process that causes droplet break–up takes place in turbulent flow fields, particularly important for the kind of work that was carried out in this study. Hinze (1955) [19] proposed that the total local shear stress imposed by the continuous phase acted to deform a drop and to break it if the droplet's surface tension and viscosity were overcome; and that only the energy associated with eddies smaller than the droplet diameter would cause break–up (larger eddies

merely transport the droplet). As a result there was a critical Weber Number for break–up which depended upon the viscosities of the dispersed and continuous phase and their density difference.

The importance of trailing vortices was reported by [11, 12, 14] for 2–phase agitated flows was demonstrated by Stephenson (1974) [20], who studied droplet break–up in baffled and unbaffled agitated vessels, using a high–speed cine camera to continuously view paddle tip flow (dyed dispersed phase). His findings show that a liquid droplet caught in the paddle tip vortex is stretched at a high rate into a filament around the axis of the vortex; the subsequent break–up results in short strands of liquid, some of which reform into droplets of varying size.

The same experimental technique was used by Konno et al (1983) [21] to view droplet break–up in agitated tanks which was then used to model the break–up process. Non–coalescing conditions were assumed and the transient drop size distribution was given by a population balance equation for break–up. The dominant factor for drop break–up was considered to be inertial rather than viscous when drop size is considerably large in comparison with the scale of the energy dissipation eddy. Some agreement was found with experimental observations.

This past work has investigated the different droplet break–up modes that are possible in agitated reactors and revealed the trailing vortices at blade tip as the most probable locus of droplet break–up.

We now turn our attention to the various attempts at deriving predictive expressions for mean droplet diameter in liquid–liquid dispersions.

Calderbank (1958) [22] listed the forces that influenced the dispersion of

liquid–liquid and liquid–gas systems. For mild agitation, dispersion was controlled by dynamic and surface tension forces, while for severe agitation, dynamic and viscous forces may control the process. His experimental results were correlated by an equation for the Sauter mean diameter, d_{32}, in terms of fluid properties and agitator/vessel parameters, using dimensional analysis.

$$\frac{d_{32}}{D} = 0.224\ We^{-0.6} \left[\frac{V}{D^3}\right]^{0.4} P_o^{-0.4} \left[\frac{H}{1-H}\right]^{0.5} \left[\frac{\mu_d}{\mu_c}\right]^{0.25} \qquad (2.1)$$

where $d_{32} = \dfrac{\sum_i N_i\ d_i^{\,3}}{\sum_i N_i\ d_i^{\,2}}$

D is the agitator diameter

We is the Weber number $= \dfrac{N_s^{\,2} D^3 \rho}{\sigma}$ N_s is the stirrer speed

ρ is the density

V is the volume of liquid in vessel,

P_o is the power number $= \dfrac{P}{N_s^{\,3} D^4 \rho}$ σ is the interfacial tension

P is the power

H is the phase hold–up,

μ is the viscosity,

c refers to the continuous phase, and

d to the dispersed phase.

The mean diameter obtained was attained in the first minutes and stayed constant with time.

Shinnar and Church (1961) [23] predicted the existence of a triangular region of stability, based on an equation for a minimum diameter, d_{min}, below which coalescence could occur, a maximum diameter, d_{max}, above which break–up would happen and a d'_{max} above which suspension was not possible. Their hypothesis was tested using a molten microcrystalline wax in water with various stabilizers, and using a dye mixing technique. Their equations were only valid if the viscosity of the dispersed phase was not much larger than that of the continuous phase.

$$\frac{d_{max}}{D} = C\ We^{-0.6} \qquad (2.2)$$

where C is a constant.

We is the Weber number.

Coulaloglou and Tavlarides (1976) [24] measured the drop size distribution in continuous systems, without protective colloid and for a phase hold–up of 0.025–0.15. Their results gave the following correlation:

$$\frac{d_{32}}{D} = C_1\ (1 + C_2\ H)\ We^{-0.6} \qquad (2.3)$$

where C_1 and C_2 are constants.

Another correlation based on the volume swept by the agitator was developed by McManamy (1979) [25]:

$$d_{32} = C_3 \left[\frac{\sigma}{\rho}\right]^{0.6} N_s^{-1.2}\ D^{-0.8} \qquad (2.4)$$

where C_3 is a constant

This equation was valid for low concentration dispersions (H = 0.05), correlating his own and other sets of data.

Lee and Tasakorn (1979) [26] studied liquid dispersions stabilised by polyvinyl alcohol, at phase hold–up values of H = 0.05 and H = 0.3, for baffled and unbaffled vessels. They assumed that coalescence was completely suppressed by the presence of the protective colloid (the agitation was stopped and the settling velocity with time was observed). The Sauter mean diameter could be correlated by a similar equation to Calderbank [22] and Coulalogou and Tavlarides [24]

$$\frac{d_{32}}{D} = C_4\,(1 + C_5\,H)\,We^{-0.6} \qquad (2.5)$$

where C_4 and C_5 are constants.

More recent work by Konno et al (1982) [27] and Lagisetty et al (1986) [28] has taken into account the effect of the non–Newtonian rheology of the dispersed phase, and a Voigt element was used to represent drop deformation.

$$\frac{d_{32}}{D} = C_6\,(1 + C_4\,H)^{1.2}\,We^{0.6} \qquad (2.6)$$

The model could account for the variation of the dispersed phase viscosity

and applied to non–Newtonian fluids, which is of course highly relevant to polymerising systems.

These correlations constitute a representative sample of past work on prediction of mean droplet diameter. All the correlations are based on dimensionless groups rather than fluid flow characteristics, and they do not seem to have improved substantially from the early predictions of Calderbank, in that the constant involved generally apply to a relatively small range of agitation conditions.

2.3 Polymerising two–phase systems

In this section the polymerising two–phase systems will be reviewed looking at the way the process conditions, particularly agitation can affect the resulting polymer properties.

One of the first and more complete attempts to explain the effects of various experimental conditions on non–aggregating suspension polymerisations was done by Hopff et al (1964) [29, 30, 31] for several monomeric systems. They found that the size of the polymer beads was determined at the beginning of the polymerisation, before a noticeable conversion has taken place. Therefore, variations in the dispersed phase properties (viscosity, density and interfacial tension) during polymerisation will not affect the final particle size for this class of reactions. Using dimensional analysis to obtain empirical correlations between mean particle size and process variables, allowed them to conclude that monomer dispersion into small droplets was due to viscosity and inertia forces of the continuous phase, which act against interfacial tension.

These findings are in disagreement with the evidence presented by other researchers: Hohenstein and Mark (1946) [32], Langner et al (1979) [33], Schröder

and Piotrowski (1982) [34] in which the ultimate particle size was the result of a dynamic equilibrium between coalescence and break–up of the polymerising droplets. There are critical values of droplet viscosity above which coalescence or break–up can no longer take place, and the coalescence process is present up to high monomer conversion [33]. If such a dynamic equilibrium exists, then these authors predict an influence of the varying physical properties of the polymerising droplet on the dependence of particle size on stirring speed.

The equilibrium size distribution was found to take up to 2 hours to be achieved, at 80 °C, the case of styrene [33], leading to coarse polymer particles, as compared with the initial monomer droplets. This effect increased in intensity with rising polymerisation rate. Also, the attainment of the equilibrium size distribution could not be accelerated by more turbulent mixing systems (baffled 6–bladed impeller against blade–type stirrer), but no explanation was given.

The shape of the size distribution was also used [34] to obtain information about the coalescence and break–up phenomena. If there was only droplet break–up, then the resulting particle size distribution would exhibit a normal distribution due to the random break–up process. When coalescence is also important, its effect will be superimposed on the other distribution, yielding bimodal distributions. Their own experimental results for certain types of stirrers show such type of behaviour. The absence of bimodal distributions when using an Intermig stirrer was explained by the short circulation path, with few opportunities for droplet coalescence, but without the support of any other type of evidence.

Bimodal distributions have also been observed by Konno et al (1982) [27] during suspension polymerisations of styrene. Here the lower droplet size peak remained constant, but the higher size range was shifted to higher values during the course of the reaction. Such behaviour was explained by assuming that the

protective colloid did not prevent the coalescence of droplets whose size was bigger than d_{max} (largest diameter that droplets may attain before break–up), due to droplet deformation. These researchers have also found that the droplet size distribution did not depend on suspending agent concentration during the early stages of the polymerisation, but that this parameter became important after the middle stages of the reaction.

The effect of increasing stirrer speed causes a decrease in the mean particle size and all work done in this area has reached this conclusion. The mean particle size has been widely correlated [29, 30, 31, 33, 34, 35] by the general equation:

$$d = a\, N_s^{\,b} \qquad (2.7)$$

where d is the mean particle size

a and b are constants

The absolute values of a and b depend on the particular polymerising system under examination in addition to the suspending agent concentration and the reactor/agitator geometry. In a number of cases [33, 35] the polymerisation of styrene exhibited a variation in the slope of mean particle size versus stirrer speed, which was interpreted as an apparent change in dispersion mechanism. Leng and Quarderer (1982) [35] attributed this change in the dispersion mechanism for baffled vessels, where the larger droplets ($\bar{d} > 250\ \mu m$) were created by a shear mechanism, and the smaller droplets ($\bar{d} < 200\ \mu m$) by a turbulent mechanism. These researchers developed four models for droplet break–up: two based on shear stresses and two based on turbulence forces, each on the micro and macro scales. Their

results as well as those obtained by Hopff et al [28, 30, 31] show that macro–models are inappropriate and that local turbulence must be taken into account.

The agitation effects on the suspension polymerisation of polyvinyl chloride have been described by Johnson (1980) [36] and Lewis and Johnson (1981) [37], who found that the mean particle size correlated with the Weber number. Approximately parabolic curves were obtained, showing the existence of an optimum stirrer speed value, beyond which extensive agglomeration occurred. This pattern remained unchanged from bench, to pilot and commercial plant scale [37].

These results have shown that the understanding of the influence of agitation conditions on polymerisation product properties is largely limited to empirical correlations based on gross flow properties which are far from universal in their applicability. In general they fail to incorporate a detailed understanding of the link between agitation variables and the fluid flow characteristics that actually influence the product properties in suspension polymerisation processes.

References to Chapter Two

[1] N.C. Markatos, "The mathematical modelling of turbulent flow", Appl. Math. Modelling, 10, 190–220 (1986)

[2] L.A. Cutter, "Flow and Turbulence in a Stirred Tank", A.I.Ch.E.J., 12 (1), 35–45 (1966)

[3] P.S. Harvey, M. Greaves, "Turbulent Flow in an Agitated Vessel. Part I: A Predictive Model", Trans. Inst. Chem. Eng., 60, 196–200 (1982)

[4] P.S. Harvey, M. Greaves, "Turbulent Flow in an Agitated Vessel. Part II: Numerical Solution and Model Predictions", Trans. Inst. Chem. Eng., 60, 201–210 (1982).

[5] B.E. Launder, D.B. Spalding, "The Numerical Computation of Turbulent Flow", Comp. Meth. Appl. Mech. Eng., 3, 269–289 (1974).

[6] J. Placek, L.L. Tavlarides, G.W. Smith, I. Fort, "Turbulent Flow in Stirred Tanks. Part II: A Two–Scale Model of Turbulence", A.I.Ch.E.J., 32 (11), 1771–1786 (1986).

[7] J.P. Sachs, J.H. Rushton, "Discharge Flow from Turbine–Type Mixing Impeller", Chem. Eng. Prog., 50 (12), 597–603 (1954).

[8] A.B. Metzner, J.S. Taylor, "Flow Patterns in Agitated Vessels", A.I.Ch.E.J., 6 (1), 109–114 (1960).

[9] L.A. Cutter, "Flow and Turbulence in a Stirred Tank", A.I.Ch.E.J., 12 (1), 35–45 (1966).

[10] R. Kuboi, I. Komasawa, T. Otake, "Behaviour of Dispersed Particles in Turbulent Liquid Flow", J. Chem. Eng. Japan, 5 (4), 349–355 (1972).

[11] K. Van't Riet, J.M. Smith, "The Trailing Vortex System produced by Rushton Turbine Agitator", Chem. Eng. Sci., 30, 1093–1105 (1975).

[12] K. Van Der Molen, H.R.E. Van Maanen, "Laser–Doppler Measurements of the Turbulent Flow in Stirred Vessels to Establish Scaling Rules", Chem. Eng. Sci., 33, 1161–1168 (1978).

[13] R.H. Callender, "Photographic Techniques of Flow Visualization", British J. Phot., 30, (6395), 195 (1983).

[14] M. Yianneskis, Z. Popiolek, J.H. Whitelaw, "An Experimental Study of the Steady and Unsteady Flow Characteristics of Stirred Reactors", J. Fluid Mech., 175, 537–555 (1987).

[15] G.I. Taylor, "The Formation of Emulsions in Definable Fields of Flow", Proc. Royal Soc., A146, 501–523 (1934).

[16] S. Torza, R.G. Cox, S.G. Mason, "Particle Motions in Sheared Suspensions. XXVII. Transient and Steady Deformation and Burst of Liquid Drops", J. Coll. Int. Sci., 38 (2), 395–411 (1972).

[17] F.D. Rumscheidt, S.G. Mason, "Particle Motion in Sheared Suspensions. 12. Deformation and Burst of Fluid Drops in Shear and Hyperbolic Flows", J. Colloid Int. Sci., 16, 238–261 (1961).

[18] M.A. Tehrani, "The Role of Agitation in Suspension Polymerisation Processes", Report to the Department of Chemical Engineering and Chemical Technology, Imperial College, London (1987).

[19] J.O. Hinze, "Fundamentals of the Hydrodynamic Mechanism of Splitting in Dispersion Processes", A.I.Ch.E.J., 1 (3), 289–295 (1955).

[20] R. Stephenson, "The Effect of Agitation on Stirred Suspension Drop Size: A Model Study", Inst. Chem. Eng. Symp. Series, 38, C4, 1–22 (1974).

[21] M. Konno, M. Aoki, S. Saito, "Scale Effect on Breakup Process in Liquid–Liquid Agitated Tanks", J. Chem. Eng. Japan, 16 (4), 312–319 (1983).

[22] P.H. Calderbank, "Physical Rate processes in Industrial Fermentation. Part I. The Interfacial Area in Gas–Liquid Contacting with Mechanical Agitation", Trans. Inst. Chem. Eng., 36, 443–463 (1958).

[23] R. Shinnar, J.M. Church, "Stabilizing Liquid–Liquid Dispersions by Agitation", Ind. Eng. Chem., 53 (6), 479–484 (1961).

[24] C.A. Coulaloglou, L.L. Tavlarides, "Drop Size Distributions and Coalescence Frequencies of Liquid–Liquid Dispersions in Flow Vessels", A.I.Ch.E.J., 22 (2), 289–297 (1976).

[25] W.J. McManamey, "Sauter Mean and Maximum Drop Diameter of Liquid–Liquid Dispersions in Turbulent Agitated Vessels at Low Dispersed Phase Hold–Up", Chem. Eng., Sci. 34, 432–434 (1979).

[26] J.C. Lee, P. Tasakorn, "Characteristics of Agitated Tanks in Relation to Suspension Polymerisation, Proc. 3rd Eur. Conf. Mixing, Vol. 1, 157–170 (1979).

[27] M. Konno, K. Arai, S. Saito, "The Effect of Stabilizer on Coalescence of Dispersed Drops in Suspension Polymerisation of Styrene", J. Chem. Eng. Japan, 15(2), 131–135 (1982).

[28] J.S. Lagisetty, P.K. Das, R. Kumar, K.S. Gandhi, "Breakage of Viscous and Non–Newtonian Drops in Stirred Dispersions", Chem. Eng. Sci., 41 (1), 65–72 (1986).

[29] H. Hopff, H. Lüssi, P. Gerspacher, "Zur Kenntnis Der Perlpolymerisation. 1. Mitteilung. Grundlagen", Makromol. Chemie, 78, 24 37 (1964).

[30] H. Hopff, H. Lüssi, P. Gerspacher, "Zur Kenntnis Der Perlpolymerisation. 2. Mitteilung. Praktishe Anwendung der Dimensionsanalyse auf das system MMA–Mowiol 70/88 (1964).

[31] H. Hopff, H. Lüssi, P. Gerspacher, E. Hammer, "Zur Kenntnis der Perlpolymerisation", Chemie–Ing.–Techn., 11, 1085–1089 (1964).

[32] W.P. Hohenstein, W.P. Mark, "Polymerisation of Olefins and Diolefins in Suspension and Emulsion. Part I", J. Polym. Sci, 1 (2), 127–145 (1946).

[33] F. Langner, H., U. Moritz, K.H. Reichert, "On Particle Size of Suspension Polymers. II. Polymerising Two–Phase System", Ger. Chem. Eng., 2, 329–336 (1979).

[34] R. Schröder, B. Piotrowski, "On Particle Formation During Suspension Polymerisation of Styrene", Ger. Chem. Eng., 5, 139–146 (1982).

[35] D.E. Leng, G.J. Quarderer, "Drop Dispersion in Suspension Polymerisation", Chem. Eng. Commum., 14 (3–6), 177–201 (1982).

[36] G.R. Johnson, "Effects of Agitation during VCM Suspension Polymerisation", J. Vinyl Techn., 2 (3), 138–140 (1980).

[37] M.H. Lewis, G.R. Johnson, "Agitation Scale–up Effects during VCM Suspension Polymerisation", J. Vinyl Tech., 3 (2), 102–106 (1981).

CHAPTER THREE

FLOW CHARACTERISATION TECHNIQUES

Three different flow characterisation techniques were used during the course of this work, each with a particular scope. They were:

(i) Static streak photography;
(ii) Dynamic video monitoring;
(iii) Laser Doppler anemometry.

Streak photography is the technique used for a qualitative overall view of fluid flow inside an autoclave, as using a large number of tracer particles, it can give quick and easy information of flow patterns and how they change with stirrer speed/agitator geometry, baffles, and any other agitation variables. The visual information is basically a static view of the system taken by a photograph over a short time interval.

For further detail, there is the video system which monitors changes in the position of a single tracer particle with time. It can thus give information on residence time distribution of the representative particle in different areas inside the reactor and trace out typical flow histories experienced by the reactor contents. In contrast with streak photography, this method gives a dynamic view of the system in the form of spatial information as a function of time.

The results obtained with both these techniques give information on a

length scale (typically several mm) which is larger than the size of a polymerising droplet (d $\simeq$ 100 μm). In order to have some insight into fluid movement on this length scale, laser doppler anemometry (LDA) is the most appropriate technique, since the diameter of the control volume over which measurements are made is of the order of 100 μm.

Hence, three different and complementary flow characterisation techniques were used, each giving a partial view towards a more complete picture of the complex flow inside an agitated reactor. Each of these will now be described in some detail.

3.1 Static Streak Photography

This flow visualisation method is one of the oldest methods used to look at the flow inside stirred vessels. It usually involves projecting a narrow planar sheet of light into the autoclave. If the fluid is seeded with appropriate white particles and photographs are taken against a black background, then a flow pattern representative of the illuminated cross–section can be obtained; particle movement will register as white streaks against a black background.

The exposure time of the photographs, together with the streak length, can enable the calculation of fluid velocities in the plane of light. However, this possibility was not used in this work, since a more accurate method of determining fluid velocities was available: laser doppler anemometry. Besides, the estimation of velocity that could be obtained in that way would be based on a length scale of several mm, which is much bigger than the size of a

droplet (d $\simeq$ 100 μm). So streak photography will therefore give gross information on flow patterns and how they change with different agitation conditions. It cannot probe local fluctuations or differences which are at a particle level.

3.1.1 Experimental arrangement

(a) Illuminating System

The illumination system used had to meet two requirements:

(i) constant intensity over the whole of the autoclave, and
(ii) sheets of light with different widths should be easily obtainable for quick adjustments in a variety of flow situations.

A previous first attempt of doing streak photography in this laboratory [1] had used a 5 mW helium–neon laser modified by a 1/8" glass rod (acting as a cylindrical lens), which produced a narrow fan of light ($\sim$ 2 mm thick). This arrangement did not prove entirely satisfactory for two reasons. Firstly, because the plane of light was not wide enough to allow particles to produce streaks; only dots were obtained and hence a clear vertical flow pattern could not be distinguished. Secondly, the light intensity was not high enough to allow short exposure times to be used for clarity of picture. Even at 1 second exposure time the illumination was still insufficient for good photographs to be taken.

A second attempt [2] used a white light source: a 500 kW projector lamp was used in combination with a $\frac{1}{2}$" slit to illuminate a plane of the

autoclave. This set–up gave rise to photographs which contained long streaks, but these were showing too much of the rotational motion of the particles (i.e. a width too high) and a clear flow pattern in a narrow vertical plane of the autoclave was not evident. Although this arrangement was a step forward, it still did not meet all the necessary requirements that were stated at the beginning of this section (the plane of light did not have a constant width). However, this previous work showed that using a white light source gave superior illumination to a red laser light. In this work, various ways of producing a variable width uniform intensity white light sheet were evaluated.

1. A first experimental arrangement used a white light source and a combination of converging and cylindrical lens; however, a plane of light was not successfully obtained.

2. After this fruitless attempt a completely different approach was used and a new system was suggested in which a 5 mW helium–neon laser was shone onto a vibrating mirror, which then reflected it onto a rotating hexagonal prism, yielding a sheet of light. By varying the angle of incidence of the laser beam on the mirror and the mirror vibration amplitude, it was possible to change the width of the sheet of light.

This system gave rise to a stroboscopic effect when using a camera and taking photographs, so instead of getting streaks, only dots would appear on the photographs. Due to this stroboscopic effect, it was decided to move into a continuous illumination system.

3. The final arrangement that was tried used a slide projector (Rank

Aldis Tutor 1000, U.K., maximum lamp 1000 W) as the light source, with a variable width slit in place of the slide. This produced a plane of light with good intensity, whose width could be very easily modified using the slit and without much divergence over the path in the reactor (the typical width divergence over the reactor length was 0.5 mm). In Figure 3.1 the illumination system using the slide projector is presented.

A variable slit width was used which allowed continuous variation of width from 0 to about 10 mm, and very fine increments were possible using a calibrated screw adjustment. For a fixed agitation condition photographs were taken at a series of slit widths, from about 1.5 mm to a quite wide sheet of 10 mm (beam width values for the projected planes of light on agitator shaft).

Upon examination of these photographs it was verified that the very narrow sheets of light, that is, smaller than 2.5 mm, produced very small streaks due to the small transit time in the narrow illuminated plane, and it was difficult to distinguish a clear flow pattern, as is evident in the photograph shown in Figure 3.2.

Sheets of light with widths ranging from 2.5 to 4.5 mm produced clear flow patterns with vertical motion showing quite distinctly, and a typical photograph can be seen in Figure 3.3.

For widths bigger than 4.5 mm, there was too much swirling motion showing and results were not good for mapping vertical movement. They did, however, give information about the local spiralling motion of fluid elements in different parts of the reactor and added to the qualitative view of the overall flow pattern. This situation is presented in the photograph shown in Figure 3.4.

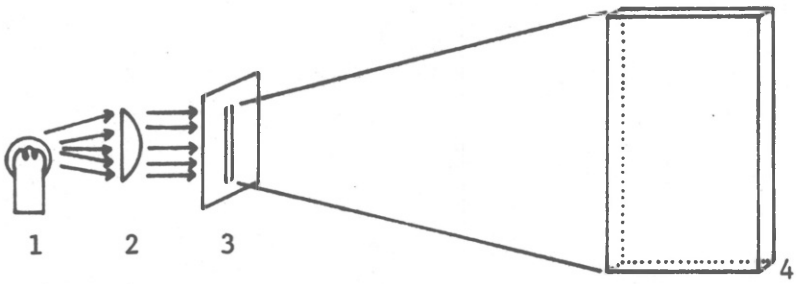


Figure 3.1 Illumination system with slide projector

1. Projector lamp
2. Converging lens
3. Slit
4. Plane of light

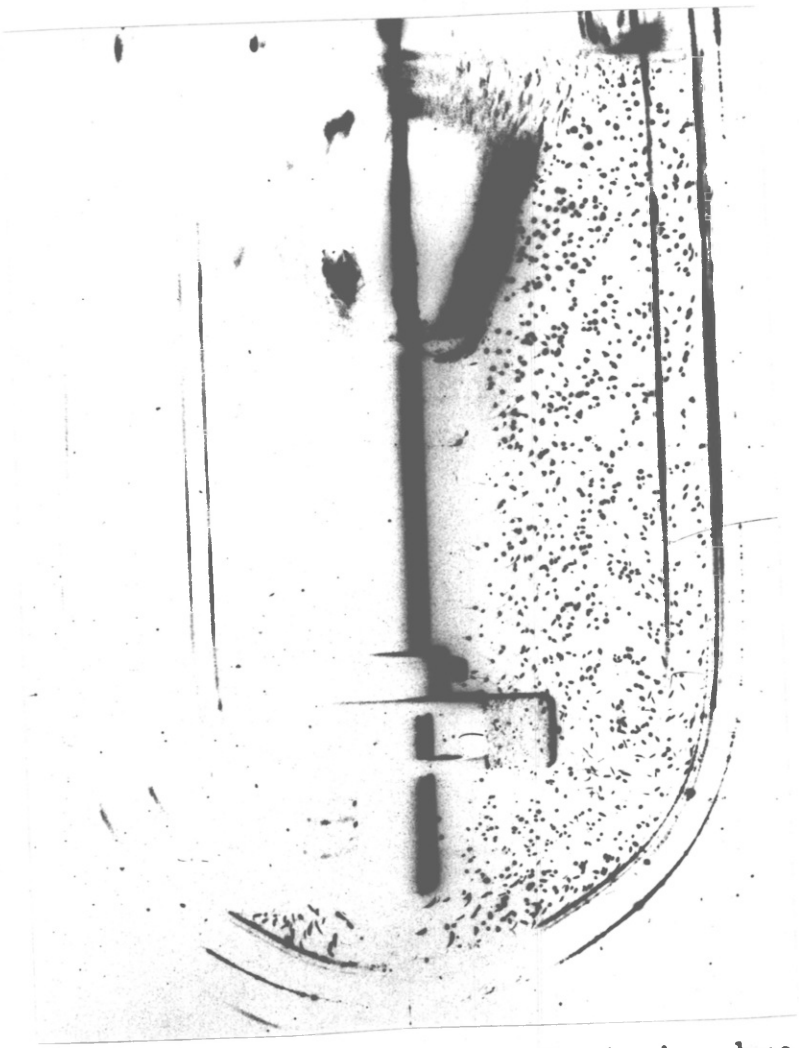


Figure 3.2 Streak photography using a narrow illumination plane of light (narrower than 2.5 mm)



Figure 3.3 Streak photography using a medium wide illuminating plane of light (2.5–4.5 mm)



Figure 3.4 Streak photography using a wide illuminating plane of light (wider than 4.5 mm)

The most useful slit widths were in the range 2.5–4.5 mm. Three fixed slits were cut that could produce planes of light that were 2.5, 3.5 and 4.5 mm wide, in the reactor, and were used throughout this work.

(b) Photographic Equipment

The camera used was a Nikon F3 HP (Japan) equipped with a data back Nikon MF–14. The camera could be used either in the automatic mode or the exposure time could be manually set from 1/2000 sec to 8 sec. A Micro–Nikkor 55 mm 1:2.8 (Japan) lens was used. The camera was mounted on a tripod (Manfrotto, Model 75, Italy) with vertical adjustment to provide a stable base. The photographic films used were 400 ASA black and white (Kodak Tri–X or Ilford HP5).

(c) Choice of Tracer Particles

The ideal tracer particle should have the same density as the fluid (in this case water) and a size small enough to follow the flow streamlines. The suitability of these particles depends on their settling velocity which is both a function of the density difference and the size:

$$U = \frac{2}{9} r^2 g \frac{(\rho_p - \rho)}{\mu} \qquad (3.1)$$

where U is the settling velocity; r is the radius of the particle, g is the acceleration of gravity, μ is the fluid viscosity, ρ_p and ρ are the densities of

the particle and fluid, respectively. U is zero when ρ_p and ρ are identical.

Since finding particles with a density exactly matching that of water is an almost impossible task, the procedure adopted was to get as close as possible and maintain the particle size below that at which significant settling would occur.

Convenient white tracer particles to use are suspension polyvinyl chloride with an average mean particle size of 100 μm. These have a settling velocity in water of 2.2 mm.s^{-1}.

A typical minimum vertical velocity in the stirred reactors of interest was of the order 0.01 m.s^{-1}. Since this was significantly larger than the settling velocity of the tracer particles, they were suitable for following the macroscopic flow patterns.

The optimum amount of tracer particles to be used was found to be a function of stirrer speed. The amount used ranged from 20 mg.ℓ^{-1} at 400 rpm to 33 mg.ℓ^{-1} at 150 rpm.

(d) Film Developing Technique

In the initial stages of this project the exposed film was developed by the Departmental Photographer. Most of the development, however, was carried out in the laboratory using a daylight film processing kit (Jobbo 2400 Daylight Tank). The developing solution employed was Ilford Microphen which facilitated an increase in film speed combined with a fine grain picture.

3.1.2 Experimental procedure

In this section the steps followed in a typical experiment of streak photography are described in sequence.

The desired agitator was fixed onto the shaft and both painted matt black to avoid reflection of light when taking photographs. The reactor was mounted and filled with the desired volume of distilled water, together with a few drops of a surface wetting agent to help disperse the tracer particles uniformly in the liquid suspension. The required amount of tracer particles was then added under agitation ($\sim$ 150 rpm) to ensure good dispersion.

The reactor was then surrounded by a cubic perspex tank filled with water, and positioned at right–angles to the incoming sheet of light. This was to minimise the optical distortion of the light beam due to the curvature of the reactor. The perspex tank was surrounded with black paper except on the side facing the camera, which was left completely open, and a slit on the orthogonal face to let in the incident plane of light. In Figure 3.5 a photograph showing this arrangement can be seen. The slide projector was positioned with the slit about 70–80 cm away from the agitator shaft, its position adjusted so that the plane of light was at right–angles with the tank face and collinear with the agitator shaft. The focusing was also adjusted in order that the plane of light was sharply focused on the agitator shaft. The camera was levelled on the tripod and positioned such that it viewed the entire illuminated half–section of the reactor, including the liquid surface. Figure 3.6 presents a schematic diagram of this experimental arrangement. The focusing was done using the vertical lines defining the edges of the light plane. A black cloth was used to cover the whole of the assembly – slide

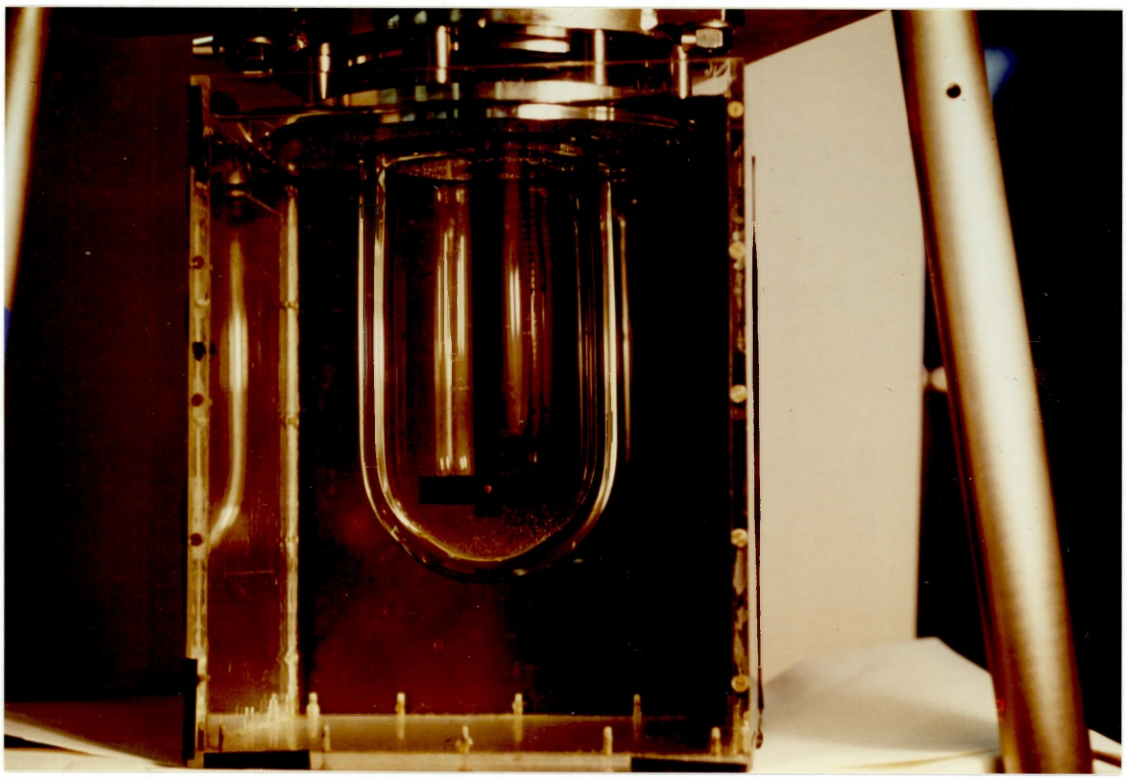


Figure 3.5 Photograph with experimental arrangement of reactor for streak photography

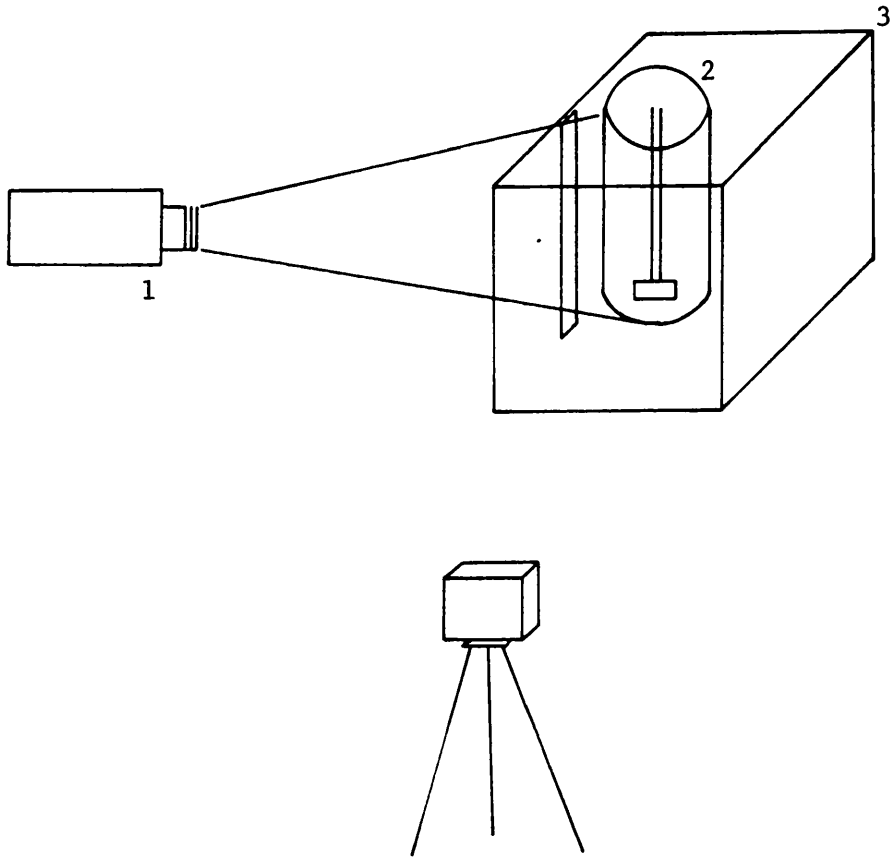


Figure 3.6 Schematic diagram with arrangement for streak photography

1. Slide projector
2. Reactor
3. Square–sectioned tank

projector, reactor and camera – to avoid any intrusion of foreign light. The stirrer speed was then adjusted to its desired value and the required photographic parameters were entered into the camera. The aperture setting best suited for this work was found to be f 2.8, together with an optimum exposure time of 1/8 sec.

3.2 Dynamic Video Monitoring System

The video monitoring technique uses a single tracer particle whose trajectory inside the reactor is monitored using a video camera. The video image is fed into a microcomputer and the data is analysed by software which has been developed at ICI plc. The computer program was slightly changed in this work to make it more suitable for these particular applications.

3.2.1 Experimental set–up

The video camera used was an Hitachi CCTV camera, Model HV–730K (Japan) using a 25 mm lens 1:1.9 from Cosmicar Television. The camera was mounted on a stand for easy adjustment.

The computer used was a Commodore, modified at ICI (Plastics and Paints Division, Dr. A. Faraday), with a Vuex interface, and the printer was a Commodore, 3040 series (dual drive).

The illumination was provided by a 0.5 kW projector lamp that gave good uniform lighting of the reactor. A white card was used as background to ensure maximum reflection of light and to avoid shadows.

The ideal flow follower should have the same characteristics as described in Section 3.1.1(c), for the tracer particles in streak photography. However, the size of the flow follower has to be bigger than that of the tracer particles in streak photography, in order to be seen by the video camera and thus enabling unambiguous detection by the software. Ideally, the size should be kept to a minimum value to make sure it is still following the flow, but the minimum size of particle that could easily be seen was 2 mm diameter. So to ensure that the flow follower followed the flow as closely as possible, one adopted the opposite tactic of reducing the settling velocity close to zero by making ρ_p approach ρ as closely as possible. Some floats were initially available, d $\simeq$ 5–6 mm, ρ_1 = 0.9998 g.cm^{-3} and ρ_2 = 1.005 g.cm^{-3}, both in dark blue colour, supplied by Daventest Ltd. (England), which were used at the start of the experimental work. Later some smaller floats became available, d = 3 mm, ρ = 1.0011g.cm^{-3}, dark blue in colour (Daventest Ltd. England) which were used, and the results obtained compared well with the previous ones using the bigger floats. The two floats initially available (d = 5–6 mm) would slowly float or sink in static water, which prompted us to test them in dynamic experiments before starting any measurements. Figure 3.7 shows the percentage of time spent in each of the five zones of the reactor for an experiment using a 4–bladed paddle at 150 rpm.

As is evident from the above figure, even though the densities of the two floats were very close to that of water, there was a clear bias in the results, with the float less dense than water spending most of its time at the top of the reactor, and the denser–than–water float having the opposite behaviour: most of its time was spent near the agitator.

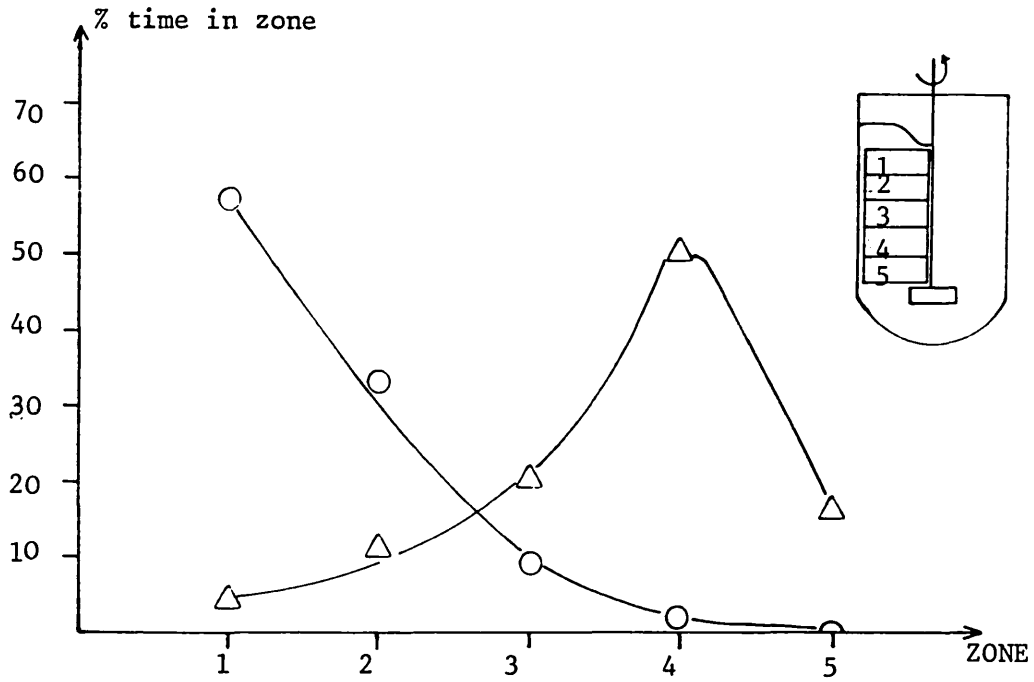


Figure 3.7 Variation of % time in zone for floats denser and lighter than water.

○ float less dense than water
△ float denser than water

Clearly, neither of these two floats was entirely suitable for our purpose. Therefore, an attempt was made to use the denser float and to match the liquid phase density to it exactly using a salt solution. Sodium chloride was added to water until the float was seen to remain buoyant in the middle of the liquid. The results obtained using this flow follower, for the same conditions as the previous experiment, are shown in Figure 3.8.

It is evident that no visible bias towards the top or the bottom of the vessel can be detected, the float spending almost equal amounts of time in each zone. A float denser than water in a salt solution with matching density was used in all subsequent experiments.

3.2.2 Data analysis

The data collection in this flow characterisation technique involved filming the path of a single particle, the flow follower, inside the autoclave, using a video camera. The reactor was well illuminated and the flow follower (d_1 = 5–6 mm or d_2 = 3 mm, both dark blue) being of a dark colour appeared as a black spot against a white screen. The video monitor screen was divided into 200 lines, each with 40 horizontal positions. The desired scanning area could be defined by entering the starting line and position and the number of lines and positions required, as can be seen in Figure 3.9.

The scanning area could be changed to fit the reactor's image on the screen. The program required a length calibration in order to convert from screen to actual reactor dimensions. The software scanned the video image bounded by the scanning area that was specified on the screen and searched

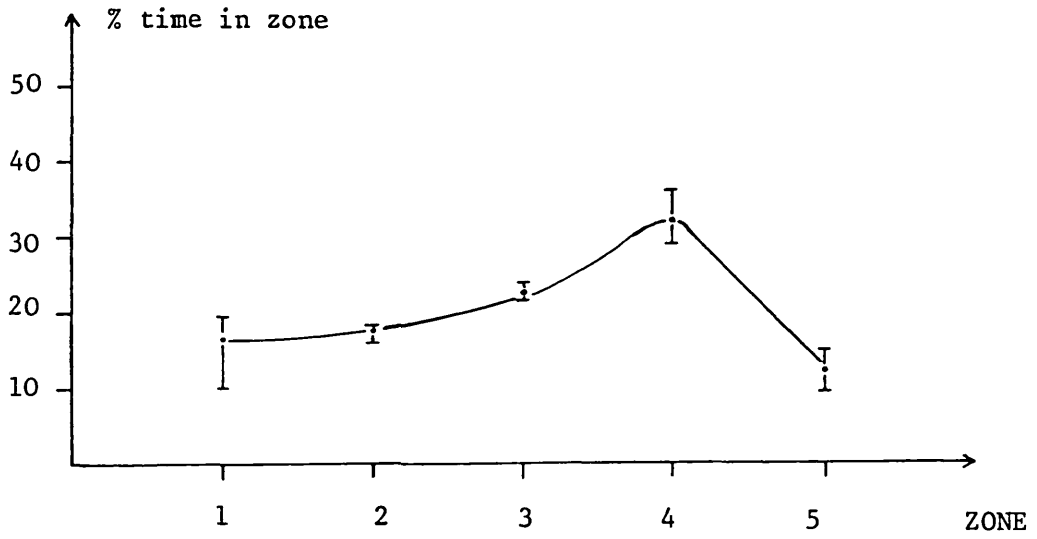


Figure 3.8 Variation of % time in zone for float with density match

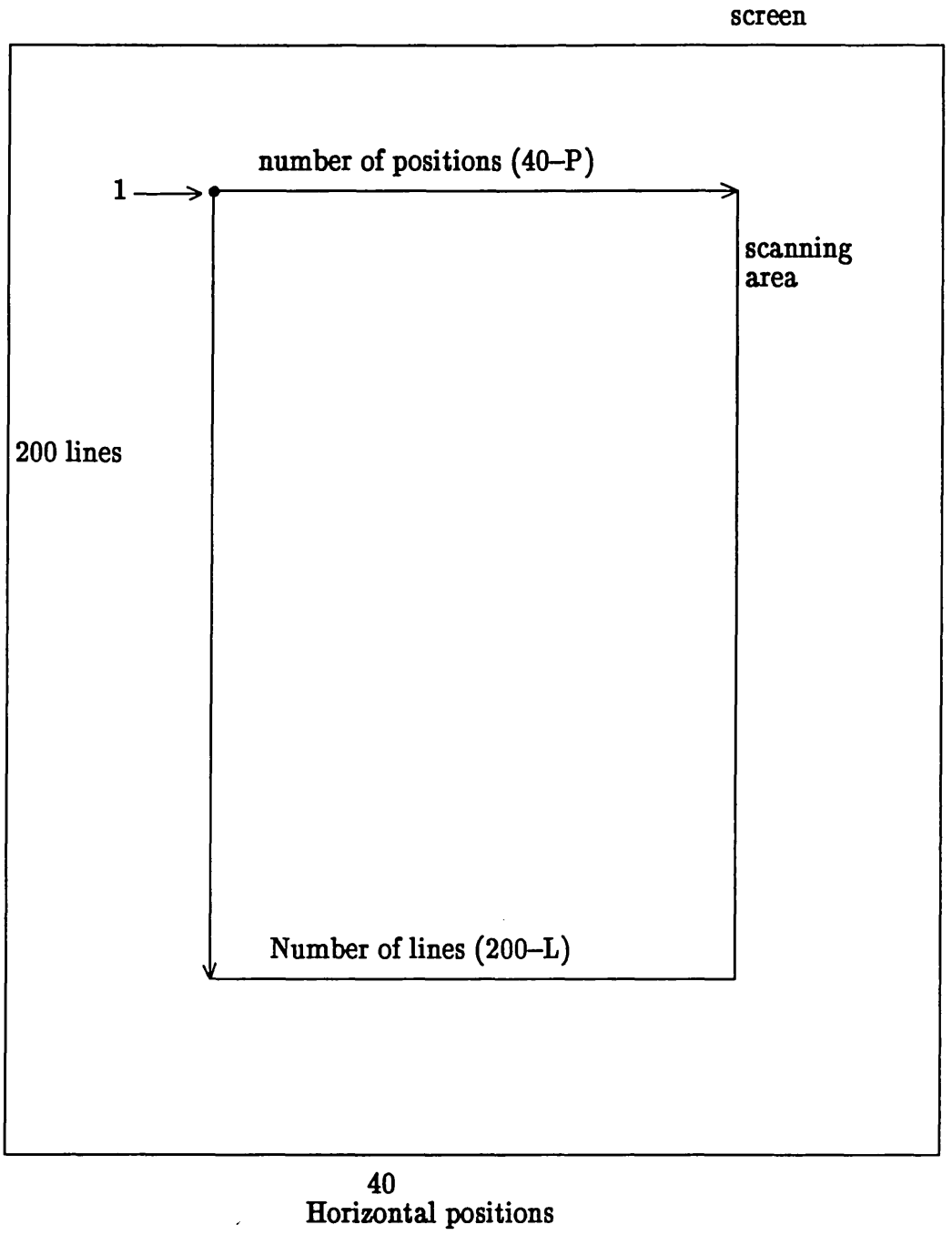


Figure 3.9 Definition of scanning area
in relation to screen, in dynamic video monitoring system
1 – starting line (L) and starting position (P)

for any dark pixels on the otherwise bright background. If one dark pixel was found then its coordinate was recorded as the flow follower position. The scan (sweep) of the entire picture was done line by line and the software allowed sweeps where all the lines were scanned to situations where not all the lines were checked, to a maximum of 8 lines per sweep. This made the detection of a big object quicker. The whole of this work was done at 2 lines per sweep. The scanning area should be of uniform brightness, with no shadows, so that only the flow follower will act as a trigger for detection. The time of each scan depends on the area of the picture and the lines per sweep and for most of this work it was between 8 and 10 jiffies per scan (1 jiffy = 1/60 second), that is, 0.133–0.167 sec, and the scanning continued until the desired time for a scanning had elapsed. The data collected was stored in data pairs recording flow follower position (number of line where seen/time of sighting). The position recorded was only the vertical position, the existing software being unable to discriminate any horizontal coordinate. From this raw data other information about the flow history could be extracted.

(a) Software Manipulations

The movement of the probe particle could be characterised by introducing the mean free path (MFP) concept, defined here as the distance travelled by the flow follower between two consecutive changes in vertical direction, i.e. reversal of sign of vertical velocity, v_z. At the beginning of the scanning the first contribution to the mean free path to be recorded was only after the occurrence of a change in direction, to avoid spurious recordings. If, at any position, the flow follower was seen there for more than 25 consecutive scans, it was assumed that it had gone out of sight and the following reappearance started another chain of mean free path calculations (the software

kept in its memory the position at which the flow follower was last sighted and only updated it when a new sighting had occurred). Also, the path leading to its disappearance was not included in the mean free path estimation.

Another variable of interest was the percentage of time the flow follower spent in different regions of the agitated vessel. The scanning area could be divided up into to a maximum of twenty zones; a value of five was used in the present case, due to the small size of our vessel and hence the small ratio between volume of zone and volume of reactor.

A third output of the program of potential interest to us was the probability of direction change, that is, the probability that the flow follower will change its direction in any given zone.

3.2.3 Experimental procedure

The reactor was mounted, having the appropriate agitator fixed on the shaft, and it was filled with the desired amount of salted water, whose density had been checked, after which the float was added. The light was carefully adjusted such that the area to be scanned had a uniform intensity, with no shadows. The distance of the video camera from the reactor was adjusted such that the reactor image just filled the video screen, showing the top part of the agitator at the bottom and the bottom part of the vortex at the top. Since the agitator was top entry the scanning area to be defined could only be in one half of the reactor, otherwise the shaft would act as a trigger for detection. Care was taken that nothing else but the flow follower (e.g.

shadow) was triggering detection and that the float was constantly seen by the camera in the half hemisphere of detection.

Data analysis variables were then entered into the computer: lines per sweep (usually set at 2); starting position; line length; starting line; number of lines; number of jiffies per scan (usually 6); time for scanning; height of screen; agitator speed; agitator diameter, and liquid height.

The experiment was initiated by starting the scanning sequence.

3.3 Laser Doppler Anemometry

Laser doppler anemometry (LDA) is an optical scattering technique by means of which fluid velocities can be determined by the rate at which tracer particles cross through a series of interference fringes. This technique has some unique features which make it of outstanding value in the field of fluid mechanics. Unlike many established methods of measuring fluid velocities (like the hot–wire anemometer or pitot tubes, which require the insertion of a probe into the flow, causing flow disturbance) LDA performs these measurements without any intrusive probe, and hence without any flow disturbance. The technique also offers a very high accuracy, without the need for calibration, besides a very rapid response to velocity changes. For successful operation LDA needs an optically transparent medium and fluid, and the presence of small (few μm) particles to scatter light. These conditions do not usually cause any problems for most applications.

A laser doppler anemometer consists of:

(a) a laser light source;

(b) a first optical arrangement to split the beam into two, and then make the two beams converge to produce interference fringes on a small volume zone where measurements are going to be made;

(c) a second optical arrangement to collect light scattered from the measuring volume;

(d) a photodetector to convert the scattered optical signal into an electronic signal; and

(e) a signal–processing system to convert the time–dependent scattered signal to a fluid velocity.

Any LDA system will have these five main constituents, but a range of alternative optical arrangements and signal–processing systems are available.

3.3.1 Malvern Instrument

The particular instrument used in this work was a Malvern Instruments RF313/K7027/50 ns Laser Photon Correlation Anemometer. The optical arrangement is a dual beam or fringe system, where the two intersecting laser beams are of equal intensity and, as the name indicates, the signal–processing system is of the photon correlation type. The choice of an LDA working in the time domain was based on its high sensitivity which allowed the use of a low power laser and no artificial seeding was usually necessary (the instrument can operate at the low scattering levels associated with natural dust or entrainment bubbles). As disadvantages, one can point out that only low doppler frequencies are available, which is of no consequence

in this study time–averaged information only is possible, and evaluation of the signal requires extensive computation. The block diagram of this LDA system is shown in Figure 3.10.

The laser beam which emerges from the laser tube (1) (Hughes Aircraft Company, USA, Laser model 3227 H–PC, 15 mW) goes into a beam splitter (2), where it is split into two parallel beams of equal intensity. At the front end of the beam splitter, a converging lens (3) is placed which makes the two parallel beams converge 50 cm away. At the intersection of the two overlapping beams, the measuring volume (or "cross–over") is defined (diameter = 300 μm) and interference fringes are formed in a particular plane of the measuring volume. When a tracer (or dust) particle crosses the measuring volume, light is scattered in different amounts depending whether it is going through a bright (higher intensity of scattered light) or dark fringe (lower intensity of scattered light), as shown in Figure 3.11.

The scattered photons are detected by the photomultiplier as a series of single pulses which arrive at the photodetector at different times. The photomultiplier is equipped with a Helius (Japan) 85–210 mm automatic zoom lens with macrofocusing and the voltage supply comes from a Thorn EMI Electron Tube (England), type PM 28B. As the particle crosses the measuring volume, more pulses are likely to arrive when it is crossing a bright fringe than a dark fringe, hence producing sinusoidal variations in the rate of photon arrival (Figure 3.12).

3.3.2 Signal processing

The pulse train seen in Figure 3.12 is fed to the correlator, which

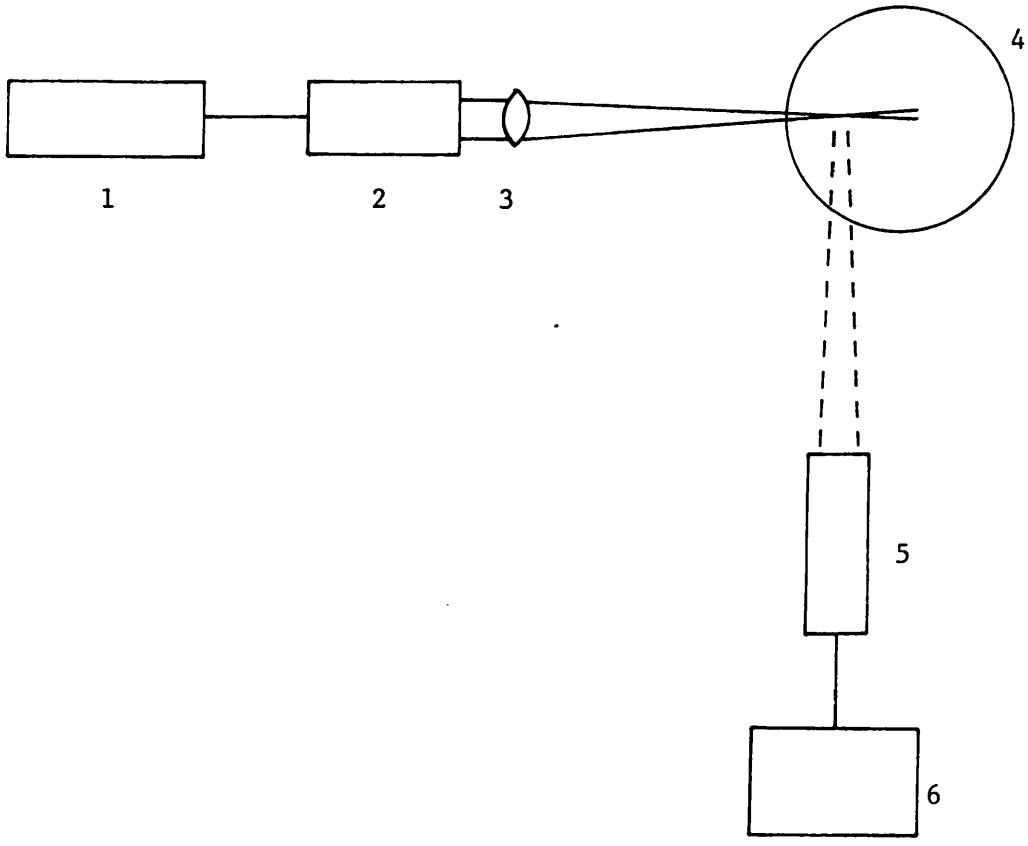


Figure 3.10 Block diagram of Laser Doppler Anemometer

1. Laser
2. Beam splitter
3. Converging lens
4. Reactor
5. Photomultiplier
6. Correlator

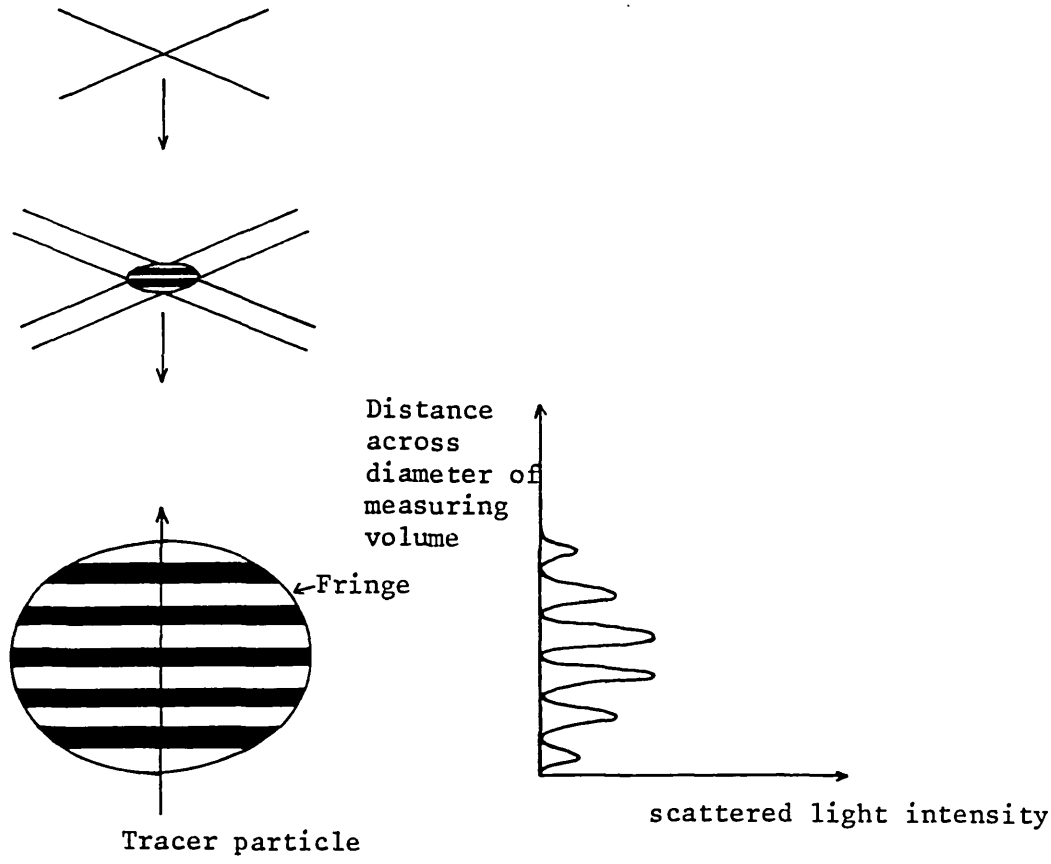


Figure 3.11 Measuring volume showing fringes

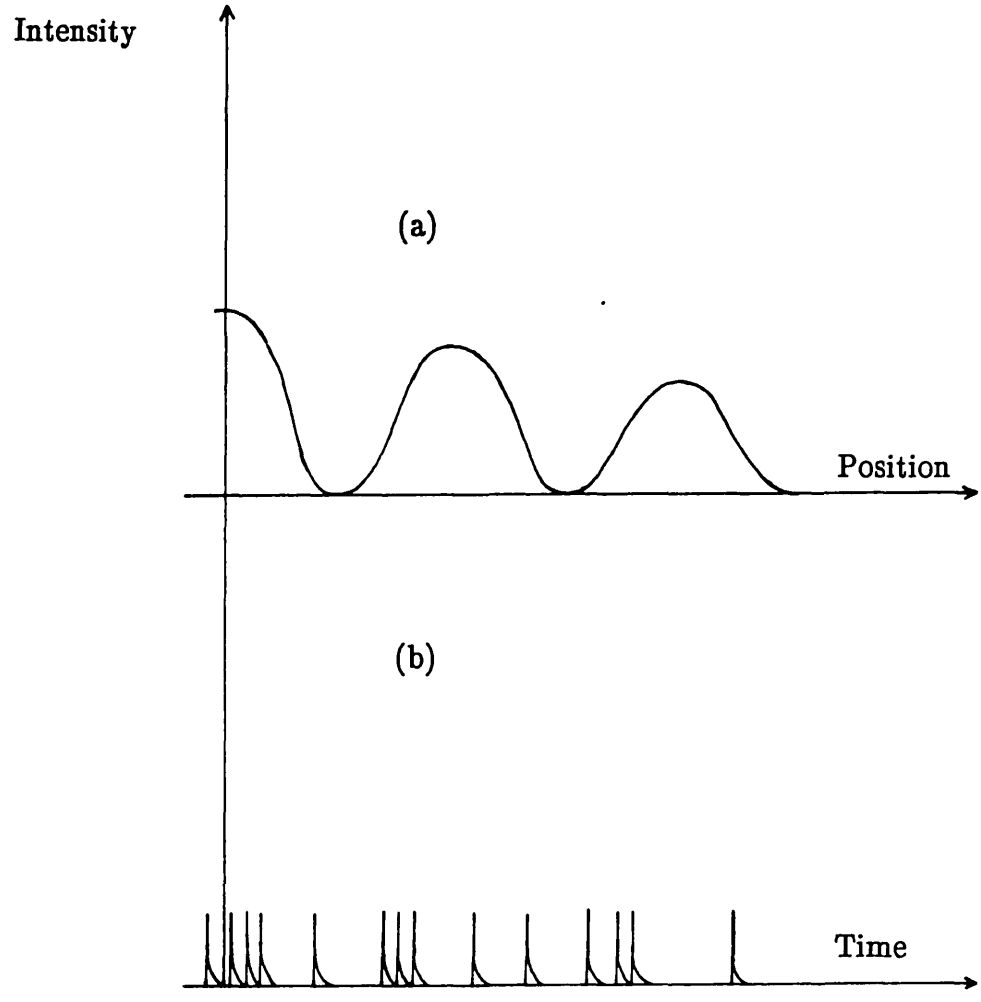


Figure 3.12 Detection of Photons at Photomultiplier

(a) Light intensity in measuring volume
(b) Photons detected by photomultiplier

then evaluates the autocorrelation function G(sT) [3], [4], [5].

$$G(sT) = \sum_{s=0}^{M} N(t)N(t-sT) \qquad s = 0, 1, 2,...,M \tag{3.2}$$

where N(t) is the number of photons detected in some small time interval T, starting at time t, and M is the number of sample times of duration T included in the experiment.

However, the commercial instrument used in this work employs a clipping technique, enabling much faster operation, as well as measurements at low dopppler frequencies (1 MHz or less). When the clipping technique is used the signal collected by the photomultiplier, N(t), is transformed into "ones" and "zeros", before autocorrelation takes place: a discrimination level, k, is set and a "zero" is recorded if the signal is below that preset level, i.e. $N(t) < k \rightarrow N_k(t) = 0$ and a "one" if it is above, i.e. $N(t) \geq k \rightarrow N_k(t) = 1$. The clipped autocorrelation function is now defined by:

$$G(sT) = \sum_{s=0}^{M} N(t)N_k(t-sT) = N \langle N(t)N_k(t-sT) \rangle \tag{3.3}$$

where N is the total number of photons counted and N_k is zero or one according to whether N(t) is less or greater than the clipping level k.

The actual operation of the correlator can be better understood if a block diagram of a clipping system is shown in Figure 3.13 [6–8].

At the beginning all the stores are clear and all the stages of the shift

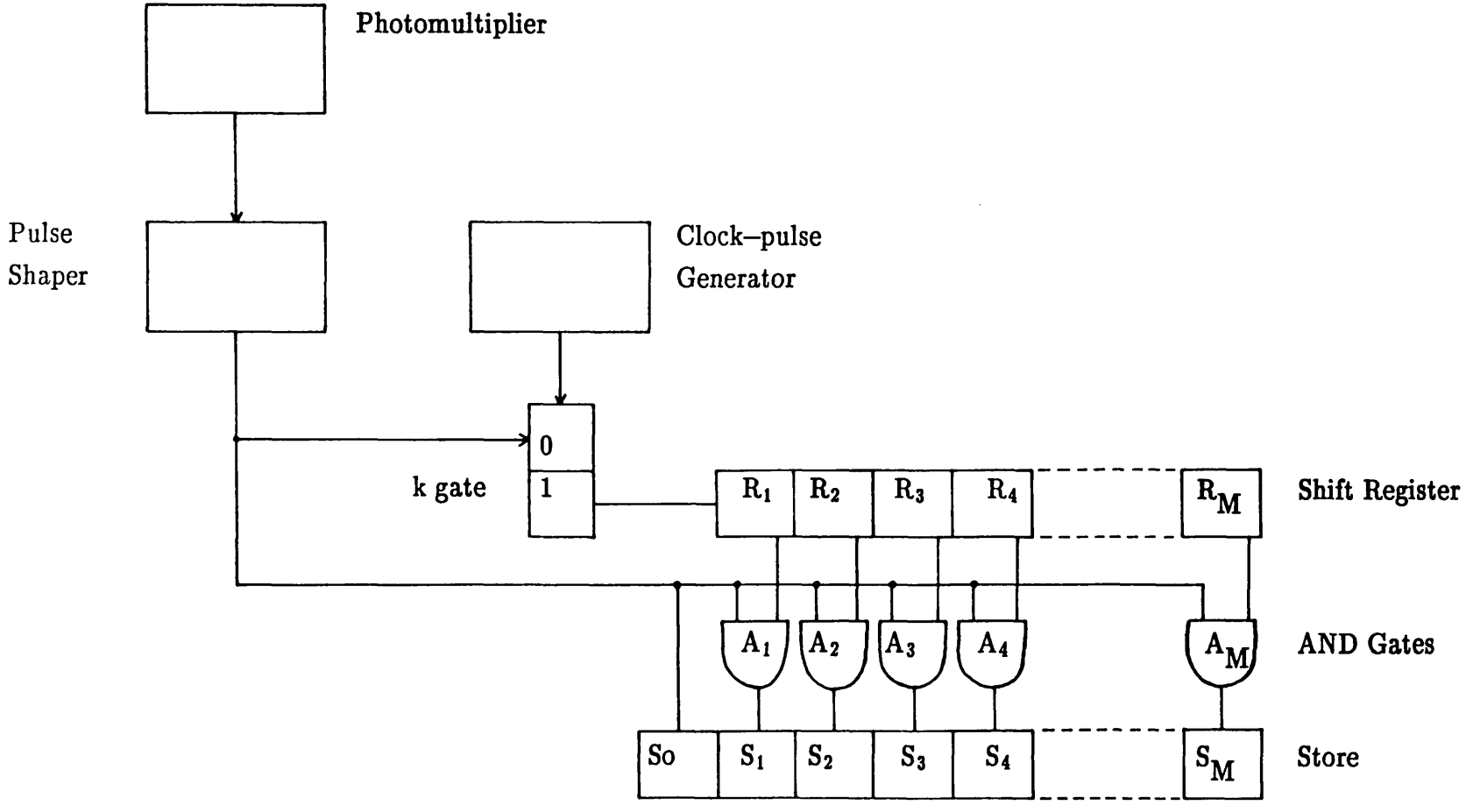


Figure 3.13 Block diagram of clipping system

register are set to zero. A sample time interval T is selected, usually about one fifth of the mean signal period (typically of the order 1–10 μs), and the clipping level, k, is set to a value near the mean count rate per sample time. The mean count rate per sample time can be determined by trial and error, by observing the rate of growth of channels 1 and 3 on the video display. Channel 1 records the number of times the clip level was exceeded and channel 3 records the number of samples. In ideal operation, the count at channel 1 should be half the number of count in channel 3, meaning that the probability of exceeding the clip level, in any particular sample, is equal to 0.5. The first pulse from the clock–pulse generator puts the k gate into the "zero" state. During the first time interval T all pulses received from the pulse shaper will go into store S_0 (the AND gates A_1, A_2, ... are shut due to the empty shift registers R_1, R_2,...). Pulses above the clip level that are received during this time interval will put the k gate into the state "one". At the end of the time interval T, the clock–pulse generator produces another clock–pulse that causes the shift register to be stepped, entering the state of the gate k into R_1. The clock–pulse resets the k gate to "zero", and a second time interval is started. At the end of each time interval the clock–pulse generator causes the state of the gate k (zero or one) to be entered into the shift register, R_1 and at the same time the contents of all the shift registers are shifted one place to the right. Thus, the shift register, R, is maintaining a record of the clipped counting sequence, i.e. $N_k(t–sT)$. To form the autocorrelation function this clipped information has to be multiplied by the unclipped input, N(t). So during each sample time interval, and in parallel with the above series of operations for the shift register, the unclipped information is accumulated in the store, $S_1,...,S_M$ via the AND gates which are controlled by the stored values of the clipped sequence. Hence, the store

builds up $N(t)N_k(t-sT)$ such that the array $S_0,...S_M$ contains the autocorrelation values, $G(sT)$, for $t = 0$ to $t = sT$.

With the type of correlator used (minimum sample time of 50 ns) the autocorrelation function is made up from contributions of a series of particles to yield information on mean velocity in the sample volume and its fluctuations. In this circumstance, the autocorrelation function has a sinusoidal form with a rapidly decaying amplitude superimposed on a decaying mean value as can be seen in Figure 3.14.

The period of the fluctuations, τ, is directly related to the mean particle velocity in the plane of the fringes, $\bar{U}$:

$$\bar{U} = \frac{\lambda}{2\tau \sin\phi} \tag{3.4}$$

where λ is the laser wavelength and ϕ is the half–angle of intersection of the two laser beams.

The damping of the autocorrelation function provides a measure of the spread of velocities, which is here expressed in terms of a function called the relative turbulence intensity, $I_R = u/\bar{U}$, defined as:

$$I_R = \frac{u}{\bar{U}} = \frac{1}{\pi}\sqrt{\frac{1}{2}\frac{(G_2-G_1)}{(G_2-G_3)} - 1 + \frac{1}{N_F^2}} \tag{3.5}$$

where N_F is the number of fringes in the beam waist diameter, u is the root mean square velocity fluctuation, and G_i are values of the autocorrelation function (see Figure 3.14).

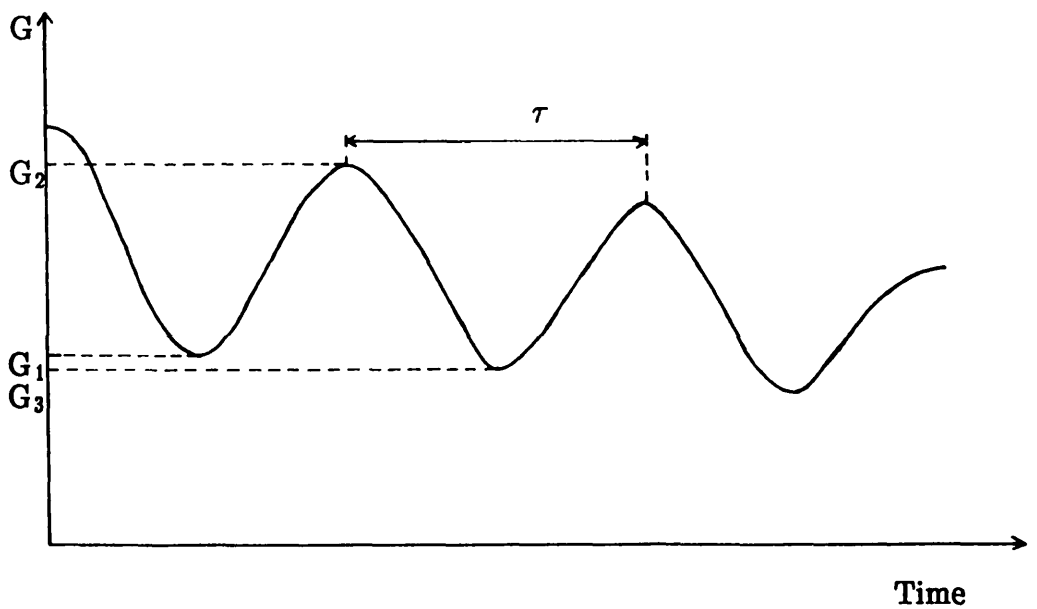


Figure 3.14 Autocorrelation Function

The autocorrelation function sits on a base line due to the detection of photons associated with wall flare, stray light, etc., which are not correlated with those from the scattering particles. It is necessary to minimise this kind of background so that it does not swamp the fluctuating component containing the useful information, which is done by adopting a sideways or backward scattering geometry.

Once the autocorrelation function has been built up the mean velocity, $\overline{U}$, and the turbulence intensity, I_R, can be determined according to the above expressions (3.4) and (3.5). However, in cases of turbulent flows the period of the fluctuations, τ, cannot be determined reliably, due to the damping caused by the increase in turbulence intensity. In this case, the mean velocity and turbulence intensity have to be determined by another method, which will be only briefly discussed here.

In a turbulent flow there is going to be a fluid velocity probability density function, PDF or $p_f(\overline{U})$, and the autocorrelation function, for turbulent flow $G(\tau)_T$ can be described by the integral over velocity of the laminar autocorrelation, $G(\tau)$, weighted by $\overline{U}\ p_f(\overline{U})$, which characterises the turbulence field [3]:

$$G(\tau)_T = \int_{-\infty}^{+\infty} \overline{U}[p_f(\overline{U})]G(\tau)d\overline{U} \qquad (3.6)$$

By careful simplification of $G(\tau)$ the following form of $G(\tau)_T$ can thus be obtained:

$$G(\tau)_T \alpha \int_{-\infty}^{+\infty} p_f(\bar{U}) \cos \frac{2\pi \bar{U}\tau}{\lambda} d\bar{U} \qquad (3.7)$$

This form of the autocorrelation function is a Fourier cosine transform of the velocity probability distribution function, which on inversion gives the desired velocity probability distribution function. This distribution function is then scanned to find the most probable peak velocity, the mean and variance of which are calculated to yield the mean velocity, $\bar{U}$, and the turbulence intensity, I_R.

3.3.3 Definition of direction of measurement

Laser doppler anemometry determines the fluid velocity in a single plane, so it enables the independent measurement of all three components of velocity, if required. The beam splitter is a moving optics part that can be rotated making the interference fringe plane lie either on the vertical or horizontal spatial plane, hence allowing the measurement of the vertical and the two horizontal components of velocity.

Before proceeding any further it is worth saying a few words about the choice of an optimum scattering geometry to be used throughout this work. Of the several arrangements possible three were considered, as shown in a schematic way in Figure 3.15.

In the case of full forward scatter, the main problem would arise from flare at the glass surface, which would be very difficult to reduce or even

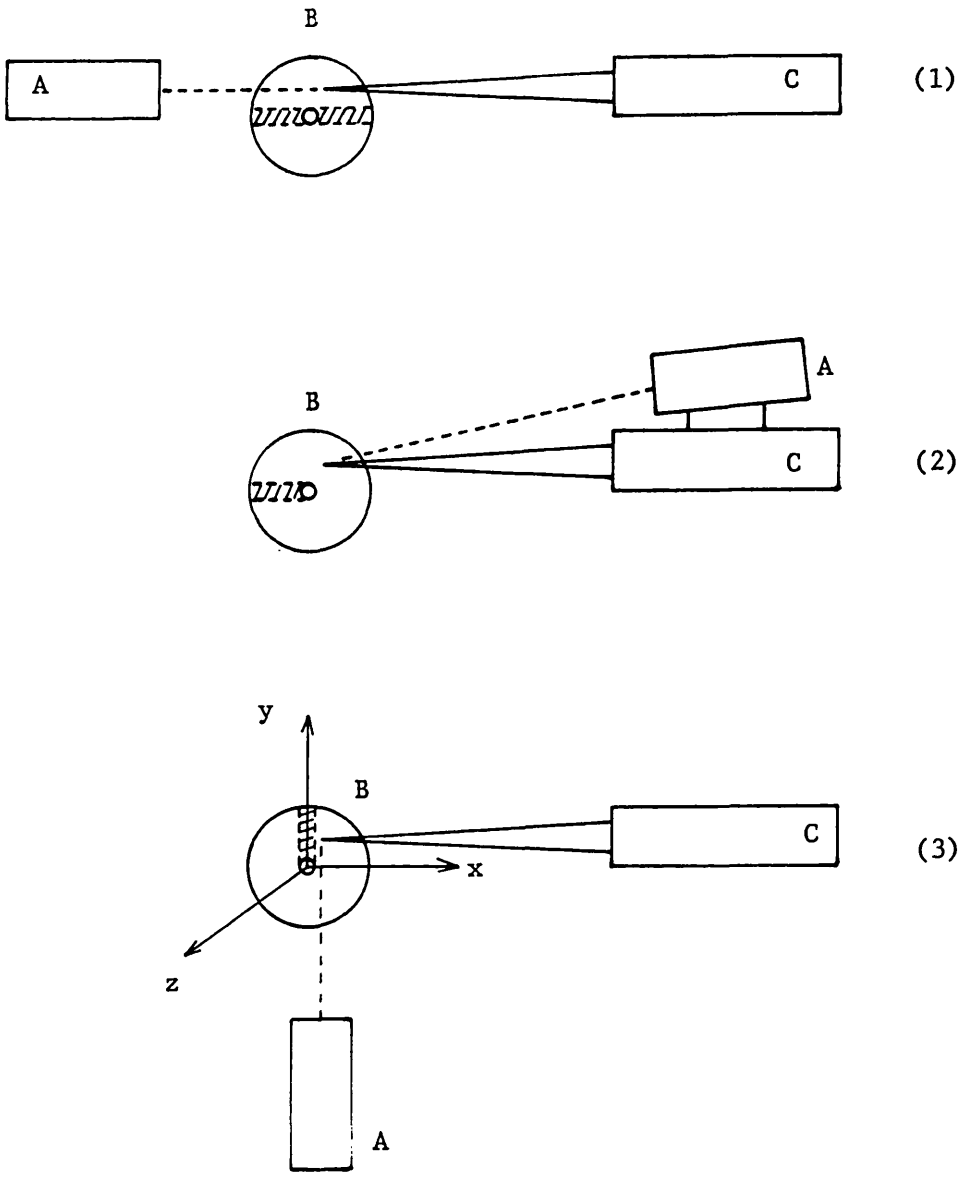


Figure 3.15 Schematic diagram of possible scattering arrangements

(1) Full forward scatter
(2) Full back scatter
(3) 90° sideways scatter
A – Photomultiplier
B – Reactor
C – Laser

Shaded area excluded for measurements.

eliminate, due to the small beam separation (the beam separation is 2 cm at source, narrowing down to a few millimetres at the outer glass surface. Multiple reflections would be very difficult to mask without being in the way of the incoming beams). Also the shaded area would never be available for measurements (Figure 3.15(1)).

The second possibility is full back scatter in which the photomultiplier is mounted over the laser and looks at the cross–over at an angle, effectively reducing the amount of flare reaching the photomultiplier, but also producing the lowest level of signal of the three geometries. However, this is not a problem with the type of instrument available, since it can cope with low levels of photons reaching the photomultiplier and still give a good signal (if necessary, the count time can be increased to increase signal to noise). The excluded area is halved with respect to full forward scatter.

The last arrangement, 90° sideways scatter, would give rise to the least flare, with a level of signal between the two other geometries. The invisible area is the same as in the previous case.

From the arguments presented, the best choice for our particular case was the 90° sideways scatter, balancing the requirements of a good signal and avoiding flare from surfaces. With this scattering geometry the y–component of velocity can be measured when the LDA components are as in Figure 3.15(3) (with the two laser beams in the horizontal plane), while the x–component of velocity can be measured by moving both the laser and photomultiplier by 90° to each other, but maintaining the two laser beams in the horizontal plane. The vertical component of velocity is measured by

rotating the beam splitter by 90°, making the two laser beams lie in the vertical spatial plane.

As described so far, the laser doppler anemometer allows the measurement of fluid velocities in the plane of the fringes, but no sense of direction within the plane can be derived. However, if a phase shifting device is incorporated into the system such directional ambiguity can be removed and the direction of velocity can be obtained. Such a facility is of particular importance in oscillatory flow with a near–zero mean velocity, highly turbulent flows, etc. In the case of the present instrument the phase shifting is obtained by introducing an electro–optic phase modulating crystal into the basic anemometer system (K9023 Phase Modulator – Malvern Instruments). The phase of a plane linearly polarized light wave represents the particular stage in a periodic sequence of movement, i.e. in a complete vibration the phase will have changed by 2π. Hence, when two laser beams overlap to form the interference fringes, their pattern remains stationary in space as long as the phase difference is constant. If the phase of any of the two light beams is changed relative to the other, the fringes will move in space by an amount proportional to the phase difference of the two beams. When a suitable saw–tooth voltage is applied to an electro–optic crystal, the phase of a light beam passing through the crystals may be advanced or retarded, and it is possible to advance the phase of one beam from the beam splitter, whilst retarding the phase of the other one (Figure 3.16).

If the relative phase of the two outgoing beams is changed by 2π, then the fringes would have moved in space by one fringe spacing. Application of such a saw–tooth voltage to the phase modulator will cause the

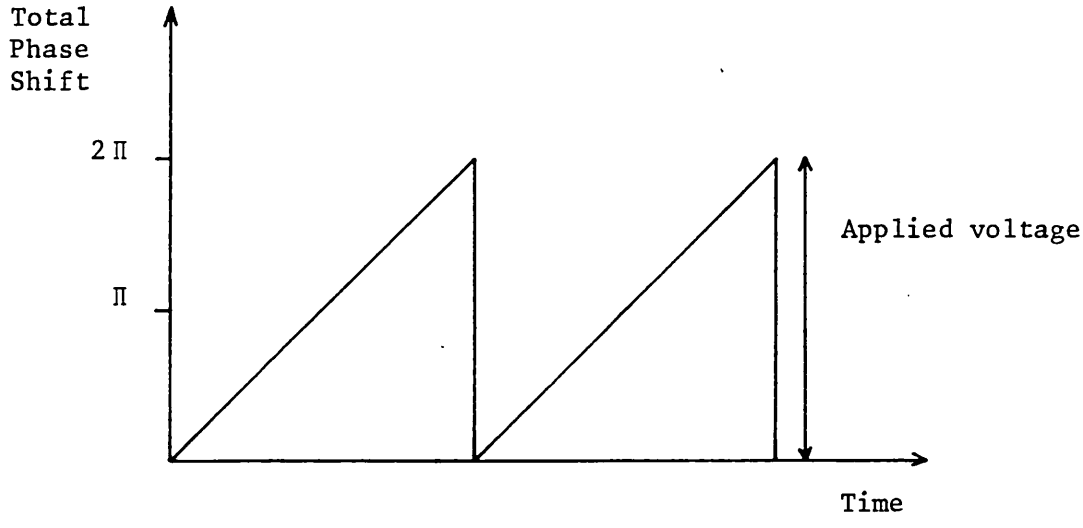


Figure 3.16 Phase shift due to applied sawtooth voltage

uniform movement of the fringes in space. The moving fringes can be going against or with the flow, causing an increase or decrease of the period of the cosine autocorrelation function detected by the signal–processing system, and establishing the directional sense of the flow.

3.3.4 Commissioning of the laser doppler anemometer

The commissioning of the laser doppler anemometer involved a substantial amount of work, since there was no previous experience with such an instrument in the laboratory. The first months were spent establishing a reliable operating procedure for this equipment. This started with the problems of focusing the detector on light scattered from the small cross–over of the split converging laser beam, and reducing flare from solid surfaces. The system was then evaluated on simple, well–characterised flow situations (laminar flow). Finally, it was applied to increasingly more complex cases: closed flow in a rectangular channel, until the stage was reached where the technique could be confidently applied to the real system: the 1–litre glass autoclave.

The first steps were associated with the optics side of the instrument. It was necessary to locate exactly the true cross–over. This was done by positioning a converging lens at its location to magnify the measuring volume. This enabled the interference fringes to be clearly seen on a target. If a phase shift was applied, then the fringes would disappear, when the lens was located exactly at the cross–over.

Next came the practice of focusing the photomultiplier on the

cross–over, by means of a target, making sure the focused cross–over would fall well inside the photomultiplier pinhole. This was done in two parts: first we had to make sure the target was exactly placed at the cross–over by blanking one of the beams at a time and viewing the resulting effect through the photomultiplier's eyepiece or with the help of a blue filter. If the target was at the centre of the cross–over, then the image remained unmoved in space, only a lower light intensity was noticed when either of the beams was blanked. Secondly, viewing the cross–over through the photomultiplier's eyepiece, the image was accurately focused and the photomultiplier's position was adjusted such that the focused cross–over image would fall inside the pinhole, without touching its edges.

Having ensured that the photomultiplier was focused on the scattering volume, a simple model flow was used to optimise the sample time, T, and duration of experiment suitable for measuring particular velocities.

A flow cell of rectangular section was used, in an attempt to produce a simple laminar flow. A perspex cell was constructed, as seen in Figure 3.17. The cell was connected to a pump and water was circulated, in a closed circuit, from a tank to the cell. In order to improve the near laminar conditions of flow, the bottom of the cell was filled with ceramic rings to allow an even distribution of the inlet jet of water. The photomultiplier was focused at a point in the middle of the rectangular section, midway between top and bottom of the cell, to ensure a fully–developed flow (the entry length was about 10 cm) and a series of measurements of fluid velocity were carried out.

The aim of these experiments was to know how to recognise a good

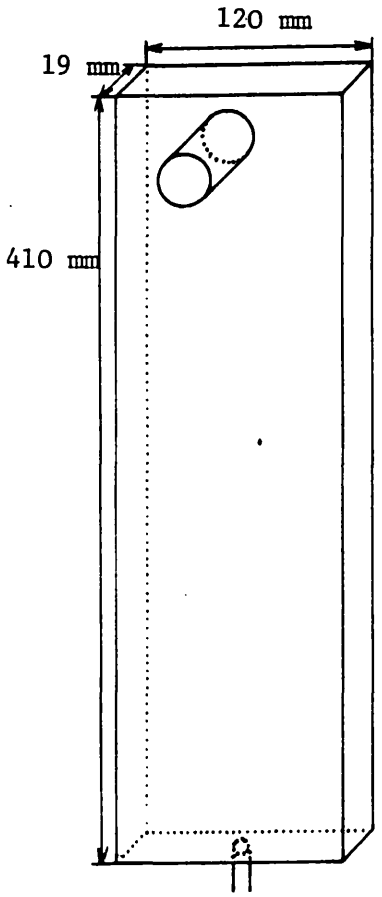


Figure 3.17 Perspex cell for flow measurement

signal giving a meaningful value for velocity and turbulence intensity. For a given volumetric flow rate velocity measurements were made and sample time was varied over a considerable range. The quality of the live correlogram display and probability distribution function (PDF) of velocity were noted, as well as the number of cycles of the correlation function present for each sample time. The probability distribution function of velocity was presented as a histogram showing the range of velocities present in the measuring volume.

Particular attention was paid to these observations, since sample time is a function of fluid velocity and cannot therefore be used as a universal criterion for knowing when a reliable value for velocity and turbulence intensity has been achieved. In Figure 3.18 are shown the results for fluid velocity and percentage turbulence intensity, as a function of sample time and number of cycles present in the correlogram.

The kind of results expected in a laminar flow should exhibit small variations in velocity and the turbulence intensity should be very small, close to zero. The experimental values of fluid velocity and turbulence intensity showed big fluctuations at a low number of cycles and the associated probability distribution curves showed thick tails, as can be seen in Figure 3.19(a). These fluctuations settled down and stable values were obtained at 4–5 cycles with better looking PDF curves (Figure 3.19(b)). Increasing further the sample time or number of cycles did not seem to increase the precision significantly.

The values of the measured velocity, $v_{meas} = 0.81 \pm 0.01$ cm.s^{-1}

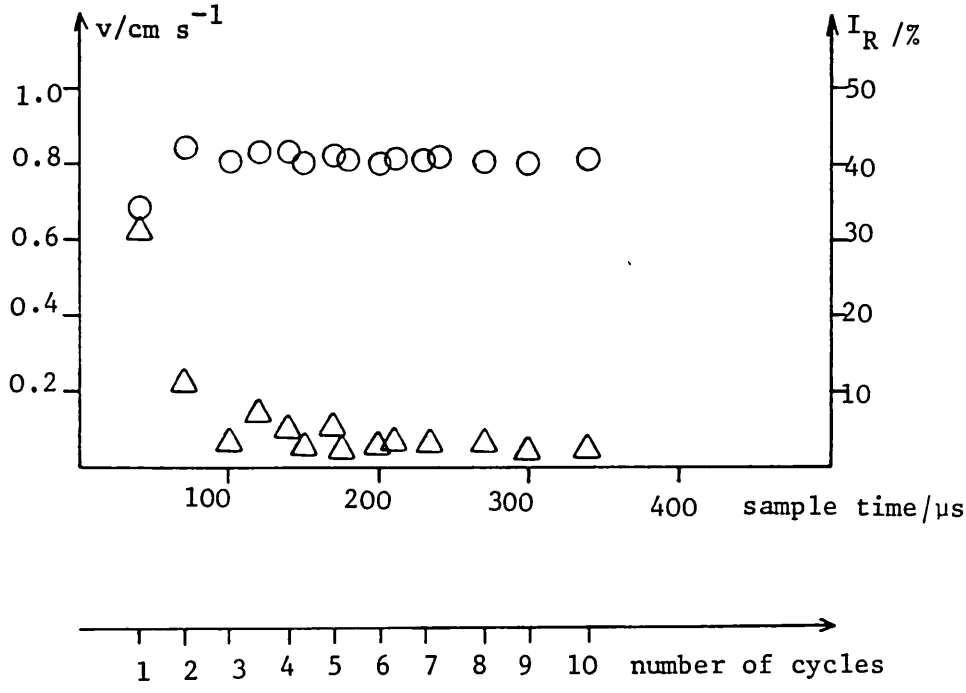


Figure 3.18 Effect of the variation of sample time on velocity and turbulence intensity.
$\bar{v}$ from flow rate measurement = 0.85 cm s^{-1}.

○ velocity
△ turbulence intensity

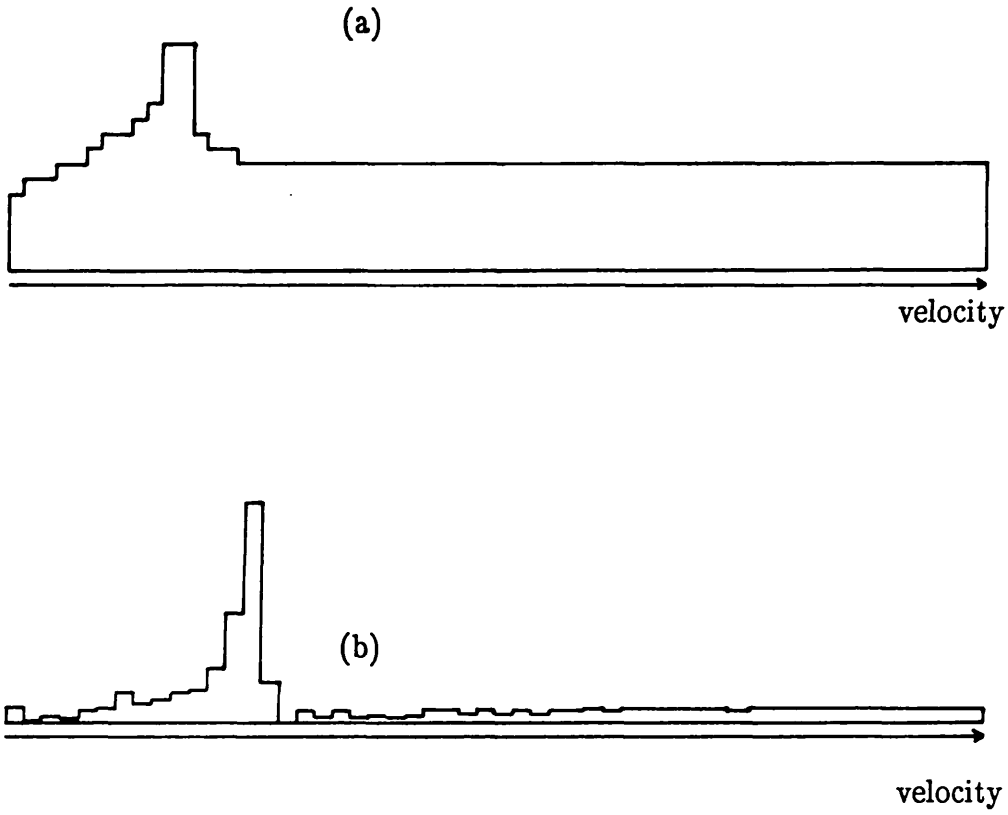


Figure 3.19 Probability Distribution Functions for Velocity

(a) Bad PDF curves
(b) Good PDF curves

compared with $v_{cal} = 0.85 \pm 0.08$ cm.s^{-1} obtained from flowrate calculations and the 5% difference between the two results was within experimental error for laser doppler anemometry and flowrate measurements. The value of 3% for turbulence intensity gave a clear indication of near laminar flow, with small velocity fluctuations, as anticipated.

Another smaller flowrate was established, corresponding to $v_{cal} = 0.58$ cm.s^{-1} and the above measurements were repeated for this new condition and the results are presented in Figure 3.20.

Again, the same comments are applicable as for Figure 3.18, with both fluid velocities and percentage turbulence intensity steadying at about 5 cycles, together with PDF curves showing a main sharp peak with no tail as in Figure 3.19(b).

The measured value of velocity, $v_{meas} = 0.59 \pm 0.01$ cm.s^{-1} is in very close agreement with the value obtained from flowrate measurements, $v_{cal} = 0.58 \pm 0.03$ cm.s^{-1}, and again the low value of $I_R = 4\%$ indicated the good stability of the flow regime.

These experiments indicated that a sample time yielding a signal with approximately 5 cycles should give a reliable value, within 5% accuracy, for fluid velocity and turbulence intensity. The value of the average velocity obtained at that number of cycles also compared well with an approximate calculation using the live display of the correlator. If sample time and clip level were chosen such as to produce just over one cycle and the channel at which the peak arised was read, then velocity could be estimated according to [9]:

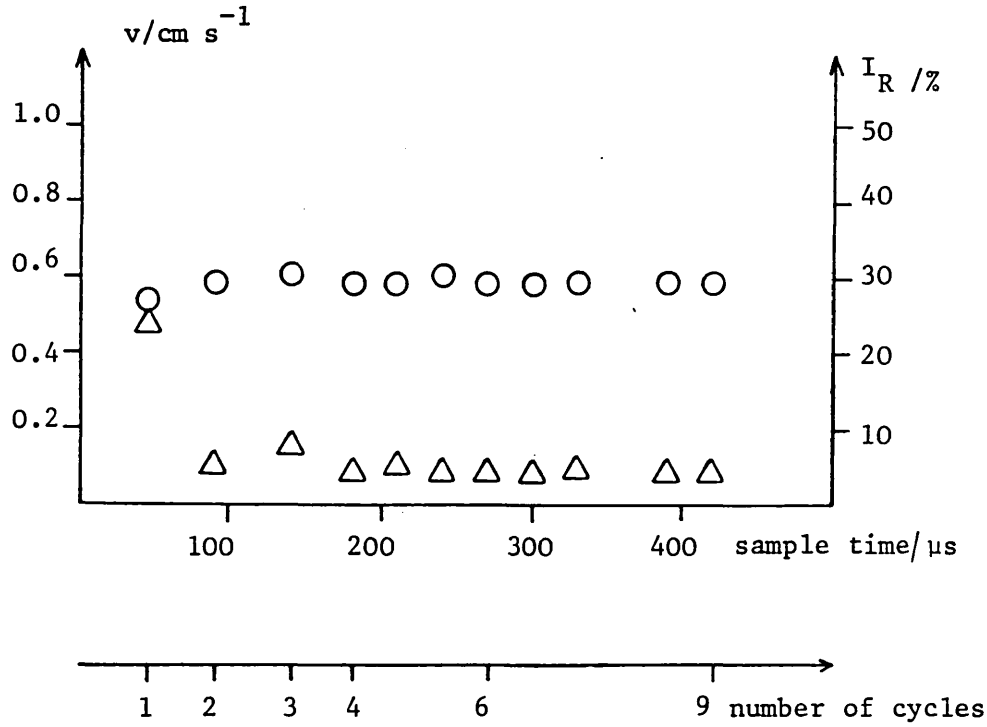


Figure 3.20 Effect of the variation of sample time on velocity and turbulence intensity.
$\bar{v}$ from flowrate measurements = 0.58 cm.s^{-1}

○ velocity
△ turbulence intensity

$$\text{velocity} = \frac{\text{fringe spacing}}{(\text{channel peak}-3) \times \text{sample time}} \qquad (3.7)$$

If this procedure was applied to the above series of measurements, the values obtained for velocity were 0.85 and 0.58 $cm.s^{-1}$, which agree very closely with the average values of 0.81 and 0.59 $cm.s^{-1}$ obtained from Figures 3.18 and 3.20, respectively. This method, which gave a reasonable estimate for velocity at only one cycle, was not suitable for obtaining information of turbulence intensity.

From this data at a range of flowrates just presented, it seems that for 4–5 cycles present in the live correlogram, the results obtained for both fluid velocity and turbulence intensity are independent of sample time.

3.3.5 Reproducibility of results

Once this criterion for recognising a good signal had been established, the reproducibility of the results was checked. A flowrate was established and experimental parameters were chosen to give five cycles in the live display and fifteen consecutive repeat runs were performed and are presented in Table 3.1 (sample time = 350 μs, clip level = 50, signal–to–noise ratio = 1:1, experimental duration = 60 s). The width is equivalent to % I_R, but expressed in velocity units, and limits are the channel numbers used to calculate velocity and % I_R, from the PDF.

The uncertainties in mean velocity and mean I_R are 4% and 8.9% respectively (based on two standard deviations), indicating a good reproducibility in the results. Nominal precisions of ± 5% and ± 10% can be

associated with $\bar{v}$ and I_R respectively.

Table 3.1. Table of results for 15 repeat runs for vertical velocity in perspex flow cell.

Run	Velocity/cm.s^{-1}	Width/cm.s^{-1}	% I_R	Limits
1	4.5	0.31	6.94	10, 16
2	4.6	0.32	7.01	10, 17
3	4.6	0.31	6.66	10, 16
4	4.8	0.34	7.14	10, 17
5	4.7	0.31	6.55	10, 17
6	4.8	0.30	6.32	10, 17
7	4.7	0.31	6.61	10, 17
8	4.8	0.31	6.57	10, 17
9	4.7	0.31	6.65	10, 17
10	4.8	0.30	6.31	11, 17
11	4.8	0.31	6.40	10, 17
12	4.8	0.32	6.71	10, 17
13	4.8	0.32	6.43	10, 17
14	4.8	0.34	7.23	10, 17
15	4.7	0.33	6.94	10, 17

3.3.6 Velocity profile measurements

The next target was trying to establish a velocity profile. The perspex cell used in the previous measurements proved unsuitable for this purpose, due to its small thickness (very few points available for measurement across the channel) and also because of optical imperfections in the wall,

making it impossible to construct an accurate velocity profile. A glass cell of rectangular section (3.25 x 2.50 cm) was available and it was suitable for these measurements (Figure 3.21).

The chosen scattering geometry was 90° sideways scatter, the cell was mounted on a small graduate traverse, and the photomultiplier was supported on a graduated optical bench (Ealing, U.K.), whose smallest division was 1 mm. The initial cross–over was located about 2/3 from the bottom of the channel, in the middle of the rectangular section. This first point was accurately focused onto the photomultiplier, PM, by placing a target inside the channel. Since it was impossible to physically focus the PM at all positions inside the cell that were needed to define a velocity profile, the cell was moved by a known distance (x) and the PM was moved accordingly (by a distance x(n–1)/x, where n is the water–air refractive index) to the new cross–over, without refocusing. The details of this geometrical optics derivation are given in Appendix I. Distilled water was circulated in a closed circuit as in the case of the perspex cell. Care was taken to have the cell outlet tube not immersed in the tank liquid, in order to avoid any syphoning effect. The mean linear velocity determined from the volumetric flowrate was 0.091 $cm.s^{-1}$, low enough to have a laminar flow (Re $\simeq$ 30). Laser doppler anemometry measurements were carried out for several positions along the width of the channel (2.5 cm). The results can be seen in Figure 3.22, together with the curve representing the theoretical velocity profile for laminar flow in a rectangular duct, normalized for the same average velocity [10]. These velocity measurements are quoted with a $\pm$ 5% error and if the position could be read within $\pm$ 0.5 mm, due to the difficulty of making precise movements in the present system, then the experimental results agree very

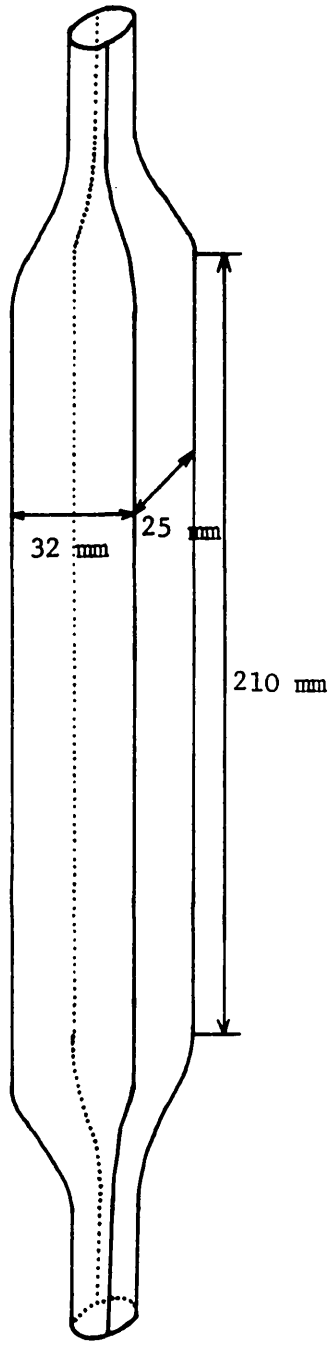


Figure 3.21 Glass cell used for determination of velocity profile

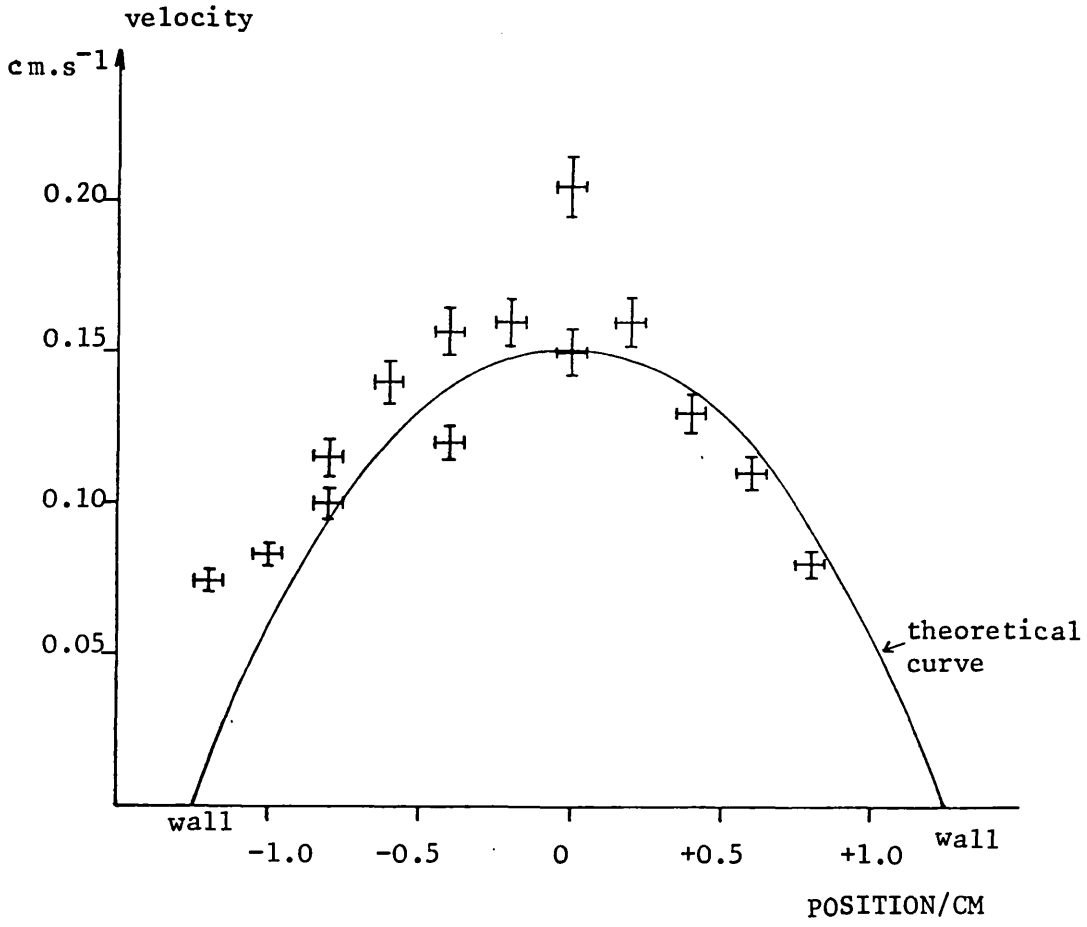


Figure 3.22 Velocity profile in a rectangular channel

closely with the theory.

The establishment of this velocity profile proved that the LDA instrument was giving reliable results and gave the necessary confidence in the system in order to move into the 1–litre glass reactor.

At this stage all the procedures had been developed and optimised to enable measurements of all three components of velocity in the complex autoclave flow.

3.3.7 Reproducibility of results in 1–litre autoclave

A few reproducibility tests were carried out for this geometry. As already mentioned in Section 3.3.3, the scattering geometry was of 90^0 sideways scatter. The measuring volume was located at a point near the agitator shaft and it was focused onto the detector pinhole with the help of a focusing target placed at 45° to both the photomultiplier and the laser axes. This was done with the reactor filled with water. After focusing, the target was removed and a background reading taken. The experimental variables (sample time, signal–to–noise ratio, clip level, frequency shift) were adjusted to give the best signal, with approximately five cycles in the correlogram. The reproduciblity of results was tested for a fixed position in space by measuring the tangential component of velocity. Ten repeat runs were performed at the same experimental conditions and the results are shown in Table 3.2.

These results show that a very good reproducibility was achieved with uncertainties based on two standard deviations (for 95% confidence limits) of 1.4% and 7.3% for velocity and turbulence intensity, respectively. These

results are consistent with the earlier measurements in simpler geometries. Further checks of reproducibility led to similar conclusions.

Table 3.2. Experimental results for tangential velocity in ten repeat runs.

Velocity/m.s^{-1}	Width m.s^{-1}	% I_R	Limits
0.334	0.046	14.0	7, 14
0.336	0.046	13.2	8, 14
0.329	0.042	12.8	7, 13
0.330	0.045	13.8	7, 14
0.334	0.045	13.6	8, 14
0.334	0.045	13.7	7, 14
0.330	0.044	13.3	7, 14
0.333	0.045	13.6	7, 14
0.334	0.041	12.4	8, 13
0.332	0.045	13.6	8, 14

$\bar{v}$ = 0.333 m.s^{-1} % I_R = 13.4

Experimental conditions: sample time = 2 μs; signal–to–noise ratio = 3; clip level = 2; frequency shift = 20 KHz; experimental duration = 100 s; stirrer speed = 200 rpm.

The effect of reducing experimental duration on the reproducibility of results was investigated, since a run time of 100 s corresponds to 5.0 x 10^7 sample times of 2 μs, which is probably in excess of what is necessary to achieve a meaningful average. Halving the experimental duration to 50 s

produced no significant change in the average values and respective errors for both velocity and turbulence intensity: $\bar{v} = 0.326 \pm 0.003$ m.s^{-1} and $I_R = 13.9 \pm 1.3$. An experimental duration of 50 s was considered long enough to yield statistically meaningful results and was used in all subsequent work. Before applying the procedure developed to characterising flow in the reactor, it was necessary to devise a way to measure all three components of velocity at any point.

3.3.8 Choice of traversing system

Before a decision could be made about the traversing system to be used, a question of prime importance had to be tackled regarding the relation between laser position, cross–over position in the reactor and detector position for correct focusing. As it is impractical, if not impossible, to re–focus at all points inside the reactor where a velocity measurement is needed, a procedure similar to that adopted for the simpler rectangular duct geometry was used. This involved focusing the photomultiplier at one single position initially and then obtaining all the other focusing positions by moving the laser or reactor and the photomultiplier by known amounts. Finding the exact distances the LDA components had to be moved to obtain a new measuring position inside the reactor was a non–trivial problem and arised from the curvature of the reactor, the finite thickness of the glass wall, the presence of three different media (air, glass and water), and hence of three different refractive indices. The solution involved using geometrical optics in order to determine:

(i) the cross–over coordinates for a given position of laser, for both horizontal and vertical laser beams, and

(ii) the photomultiplier's displacement to enable it to focus on light scattered from the cross–over zone.

The relevant relationships can be found in some detail in Appendix II. These expressions were coded in BASIC on a Commodore computer to generate the correct settings for any given movement. Two main computer programs were developed that would give the cross–over and photomultiplier coordinates for any given starting position of laser, one for horizontal (Bacscat 321) and the other one for vertical (Bacscat 341) beams. (Appendix IV).

In order to achieve these alignments, the positions of two of the three components (laser, reactor, detector) had to be adjustable. A decision was made for convenience to mount the photomultiplier on one traverse system. This meant that a decision had to be made whether it was more effective to move the laser or the reactor. A second traversing system, besides enabling movement in three orthogonal directions of space, should also be able to have angular moment (for measurements at different positions of baffles relative to the cross–over position, for the same x, y, z coordinate).

It was decided to mount the reactor on the second traversing system, while the laser remained stationary. The advantages of such a configuration were that angular movements would be much easier to achieve (reactor could be mounted on a turntable), as also would vertical movement. If the laser beam axis and the photomultiplier's pinhole were on the same elevation, then only the reactor traverse needed z–movement to obtain all possible focusing positions. In addition, a way of mounting baffles in the reactor and rotating

them in a controlled manner was devised, making redundant the need for a turntable to mount the reactor on.

A heavy–duty traverse was available with the following characteristics: 80 x 350 mm travel distance in the XY–plane with a minimum resolution of 0.025 mm in both directions, and 700 mm travel distance for vertical movement with a minimum resolution of 0.1 mm.

The photomultiplier's maximum traverse specifications, obtained from the two computer programs Bacscat 321 and 341, were found to be 200 mm in the Y–axis and 100 mm in the X–axis. Also very important was the minimum resolution on photomultiplier movement necessary to ensure that the cross–over was always well inside the pinhole (d = 200 μm); this was 0.01 mm. Two independent stages were bought from Unislide, Time and Precision Ltd. (United Kingdom) with 164 and 240 mm travel distances and with a minimum vernier division of 0.01 mm.

The reactor was mounted on a heavy–duty traverse using large lead weights to balance its weight and give the arrangement complete stability. The photomultiplier was mounted on the top of the X–Y stages, which were in turn supported on a heavy metal base to give mechanical stability to the system.

3.3.9 Initial alignment procedure for LDA

The initial alignment of the LDA in the chosen geometry was of crucial importance, since it would affect all subsequent measurements. Therefore great care was taken in making sure that the photomultiplier and

laser were at 90° to each other, that the reactor was placed at the centre of the coordinate system so defined and that the laser beam's axis was on the same height as the photomultiplier's pinhole (Figure 3.23).

The laser was placed on a sturdy table and made perfectly level by adjustments to its four legs. Since the alignment procedure would be very difficult with two converging beams, it was decided to temporarily remove the beam splitter and use the single beam for alignment purposes.

The first task was to direct the laser beam towards the reactor, along a diameter, that is, through the axis on which the stirring shaft is mounted. The following procedure was used to achieve this:

(i) The glass reactor was removed.

(ii) The deck–plate to which the reactor was attached was made perfectly horizontal, using its three adjustable nuts (Figure 3.24).

(iii) An auxiliary rod exactly fitting the hole for the stirring shaft was machined, having the lower end shaped as a half cylinder, and the flat surface polished.

(iv) The auxiliary rod was fitted into the hole of the stirring shaft with the flat polished surface of the half cylinder facing the laser. The laser position was adjusted until the reflection of the incoming laser beam returned back on itself and was at the centre of the flat section. This ensured that the laser was directed along the X–axis and going through the origin of the coordinates (Figure 3.25).

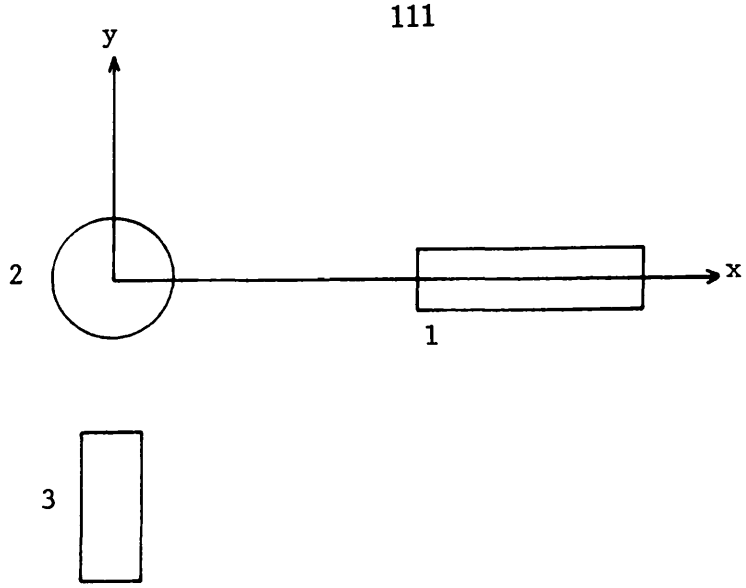


Figure 3.23 Schematic view of LDA arrangement

1. Laser
2. Reactor
3. Photomultiplier

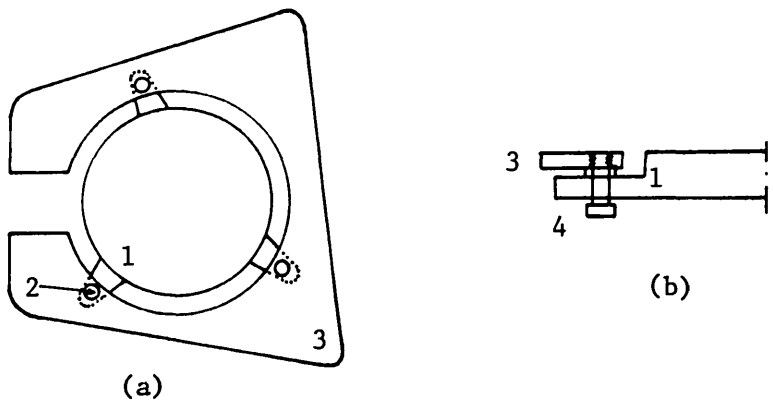


Figure 3.24 Schematic Diagram of Deck–plate and adjustable nuts

(a) Top view
(b) Side view
1. Deck–plate
2. Clearing hole for nut
3. Reactor platform
4. Nut

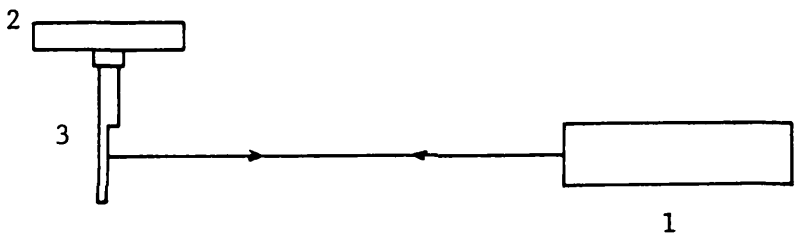


Figure 3.25 Positioning of laser along x–axis

1. Laser
2. Deck–plate
3. Auxiliary Rod

(v) The auxiliary rod was turned by 45° towards the photomultiplier (with the lens removed to have the pinhole accessible). The position and height of the photomultiplier were adjusted until the reflected laser beam was directed along the axis of the photomultiplier, falling onto the pinhole.

The checking procedure for this part of the alignment involved using the photomultiplier's traversing system to move the Y– and X–axis (in the latter case also moving the reactor traverse by an equivalent distance to maintain their relative positions). If the laser beam was always falling inside the pinhole, then the alignment was correct and no further changes were necessary.

(vi) The beam splitter was put back into the laser arrangement, the lens was fitted into the photomultiplier and an auxiliary rod used having a matt black flat surface. With the beam splitter and converging lens in position, the reactor frame was adjusted such that the cross–over point of the two laser beams (50 cm away from the converging lens) was exactly at the centre of the reactor. At this point, it did not matter if the reactor had to be slightly moved because the photomultiplier could be moved accordingly, since they had already been aligned relative to each other. The best way of judging if the reactor was at the centre of coordinates and hence that the two laser beams were crossing exactly at that point, was by looking through the photomultiplier's eyepiece, focusing sharply the image of the cross–over, and blocking each beam at a time. If only a reduction in intensity was observed, the photomultiplier was looking at the cross–over.

(vii) This completed the alignment procedure. As a final check, the glass reactor was mounted and filled with distilled water, still with the auxiliary rod in place of the stirring shaft. This was then used to compare the observed cross–over position with that predicted by the computer programs. With the laser beams in the horizontal plane then, according to computer program Bacscat 321, the cross–over should be as in air in the alignment procedure, that is, in the centre of the reactor. This was confirmed. When the laser beams are in the vertical plane, then the cross–over coordinates are predicted to be X = –1.78 cm and Y = 0 cm, which was also verified. If the photomultiplier (or the reactor) traverse were moved by ± 0.1 mm along the X–axis, that was sufficient to loose the cross–over image on the pinhole, i.e. adjustments must be made with a precision better than ± 0.1 mm.

(viii) The predictions of the computer programs were confirmed in real measurements by the quality of both the live display and the probability distribution function and also by doing a check on the background measurement of the two separate beams (by blanking one of them) and on the two beams together. The background of the separate beams should be very close to each other, but smaller than the value for the two beams together. This check ensures that the photomultiplier is looking at the cross–over and was always done before any measurements. If, due to the glass surface imperfection, the live correlogram and the probability distribution function were not of the required quality, for the predicted photomultiplier's location, then small local manual adjustments were made to optimise the quality and strength of the signal.

References to Chapter Three

[1] G. Venkatraman, "The effect of different agitation conditions on batch suspension polymerisation," M.Sc. Thesis, University of London (1983).

[2] C. Cole, M. Thompson, 3rd Year undergraduate project, University of London (1983).

[3] "Principles and Practice of Laser Doppler Anemometry", F. Durst, A. Melling, J. H. Whitelaw, Academic Press, (London) 1981.

[4] E. Jakeman, "Photon Correlation", in "Photon Correlation and Light Beating Spectroscopy", H. Z. Cumins, E. R. Pike, (Editors), Plenum Press (London), 1973, page 75.

[5] R. G. Brown, E. R. Pike, "Laser Doppler Anemometry" in "Optical Transducers and Techniques in Engineering Measurement", A. R. Luxmoore (Editor), Appl. Science Publisher, (London), 1985, page 239.

[6] T. S. Durrani, C. A. Greated, "Laser Systems in Flow Measurement," Plenum Press (New York), 1977.

[7] E. R. Pike, "Introduction to Photon Correlation Spectroscopy and Velocimetry", in "Photon Correlation Spectroscopy and Velocimetry", H. Z. Cumins, E. R. Pike (Editors), Plenum Press, (London), 1976, page 3.

[8] E. R. Pike, "Introduction to Photon Correlation Spectroscopy and Velocimetry", in "Photon Correlation Spectroscopy and Velocimetry", H. Z. Cumins, E. R. Pike, (Editors), Plenum Press, (London), 1976, page 23.

[9] Malvern Instruments Manual

[10] F. M. White, "Viscous Fluid Flow", McGraw Hill, (London), 1974, page 123.

CHAPTER FOUR

SUSPENSION POLYMERISATION EQUIPMENT

The suspension polymerisation experiments were all carried out in a 1–litre Büchi (Büchi AG, Uster, Switzerland) glass autoclave. The reactor was mounted on a sturdy frame to avoid vibration, and agitation was provided via a magnetically–driven motor to avoid sparks and danger of explosion when dealing with flammable materials. A three–phase motor was used, 50 Hz, with differential gear, infinitely variable from 0–2000 min^{-1}, adjusted using a manual dial and speed scale. Photographs of the reactor and motor assembly can be seen in Figure 4.1.

The glass reactor was capable of withstanding up to 12 bar in pressure and 473 K in temperature. It was held by 8 bolts against a stainless–steel top plate fitted with four entry ports. Two of these entry ports were used for safety measures: in one of them there was a bursting disc that was set to blow at 12 bar if there was an undesirable pressure rise inside the reactor; and in another one there was a pressurised pipette containing an aqueous solution of inhibitor (hydroquinone) that could be injected into the autoclave via valve II. Figure 4.2 shows a schematic diagram of the apparatus, while Figure 4.3 presents a close–up photograph of the deck–plate attachments.

The temperature was initially measured by a thermometer inserted into a stainless–steel sleeve which protruded inside the reactor, acting like a baffle. This thermometer was used in the first few polymerisations, but it was soon abandoned in favour of a thermocouple wire which run flush against the vessel wall and induced minimal flow disturbance, besides

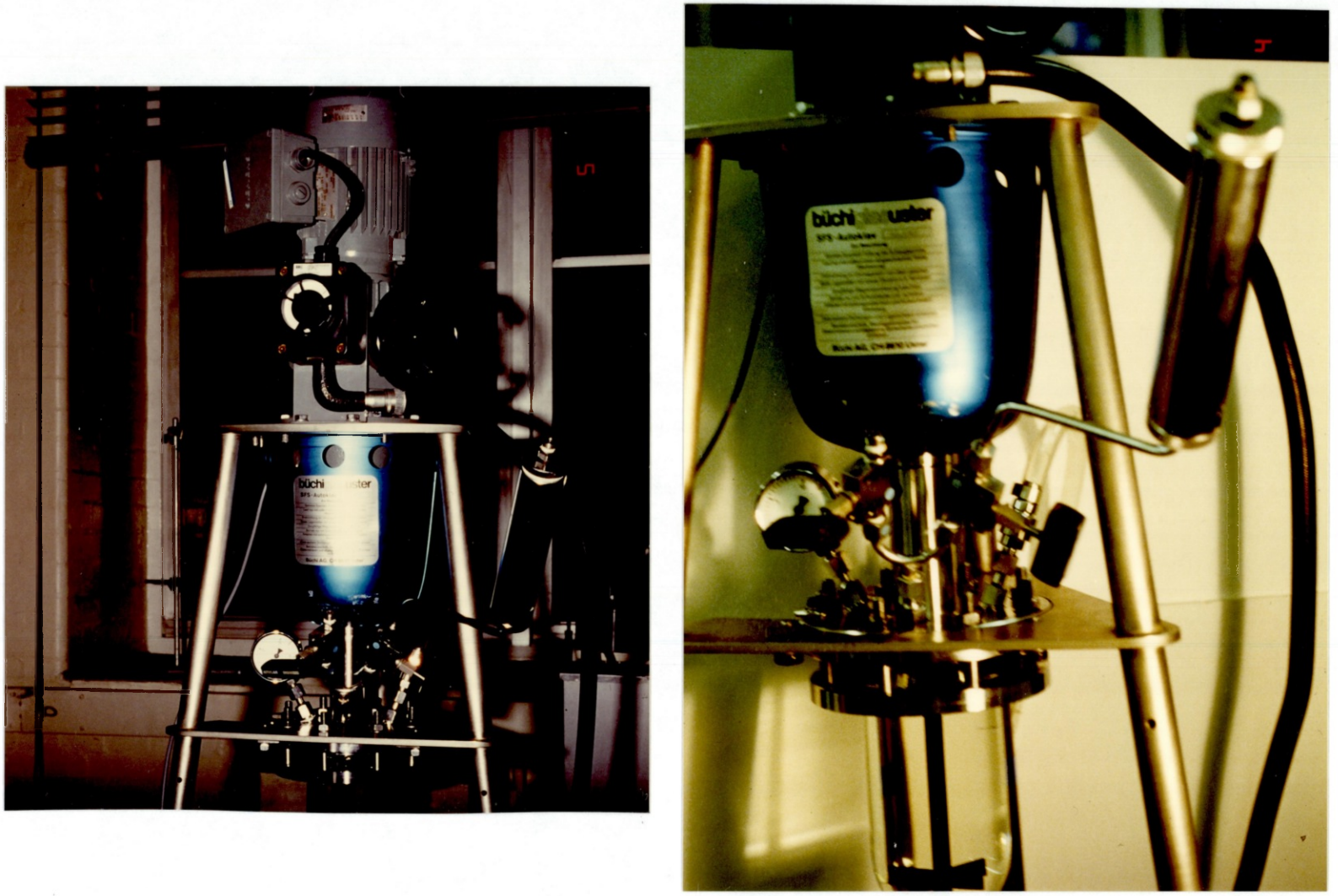


Figure 4.1 Photographs of reactor and Motor assembly

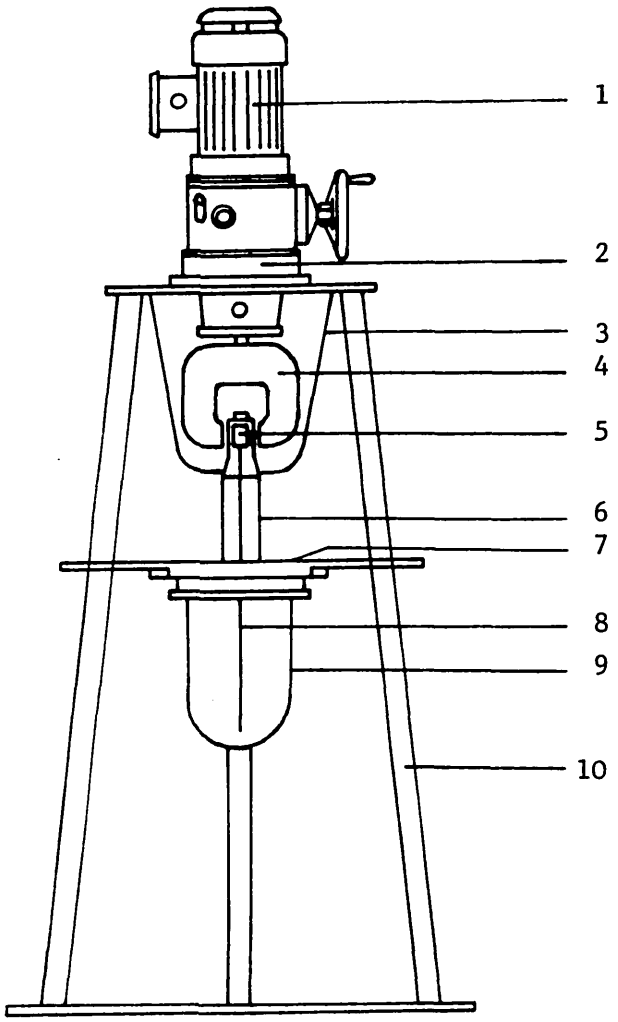
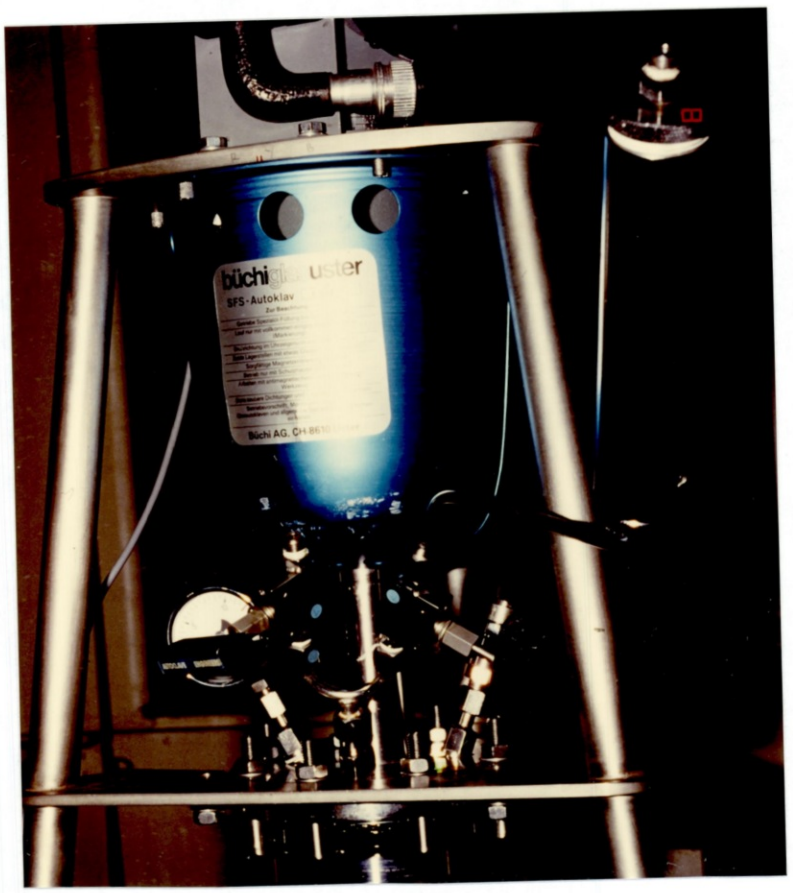
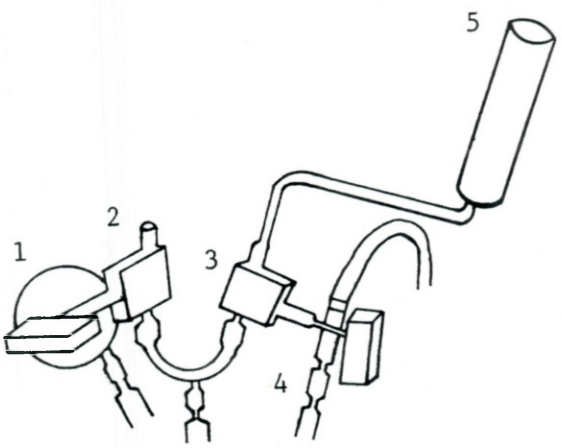


Figure 4.2 Schematic diagram of reactor assembly

1. 3–Phase Motor ; 2. Differential Gear
3. Magnet casing ; 4. Permanent Magnet
5. Rotor ; 6. Stirrer Dome
7. Deck–plate ; 8. Stirring shaft
9. Reactor ; 10. Reactor stand





1. Pressure gauge
2. Valve I (Nitrogen Inlet)
3. Valve II
4. Bursting disc arrangement
5. Pipette (containing inhibitor)

Figure 4.3 Photograph of deck–plate attachments

having a higher accuracy in temperature measurement. The thermocouple was connected to a BBC microcomputer, via an appropriate interface. A pressure gauge (1–12 bar and later 1–1.4 bar) monitored the pressure inside the reactor.

The glass reactor could be equipped with a removable glass jacket through which hot water from a thermostatic bath circulated in a closed system, as shown in Figure 4.4. This layout allowed for the possibility of a fast cooling of the reactor contents whenever needed, as well as the normal heating needs when a polymerisation reaction was proceeding, enabling the temperature to be kept within ± 0.5°C.

4.1 Reactor Geometry

The agitator geometry could be easily modified by inserting different agitators on to the stirring shaft. Amongst the agitators supplied with the reactor there was a two–bladed paddle (50 x 35 mm) that was initially used, and this arrangement is henceforth referred to as the "simple geometry" (Figure 4.5).

The other agitator used was a four–bladed paddle (63 x 11mm) that was constructed in the Departmental Mechanical Workshop and this arrangement will be referred to as the "complex" geometry (Figure 4.6).

With this latter geometry baffles could also be used and two baffles of triangular section were placed at 180° to each other, as shown in Figure 4.7. Two sets of baffles with different lengths were manufactured: 86 and 112 mm. The baffles were held from a baffle disc which consisted of a stainless–steel disc (3 mm thick) that fitted on the top of the reactor,

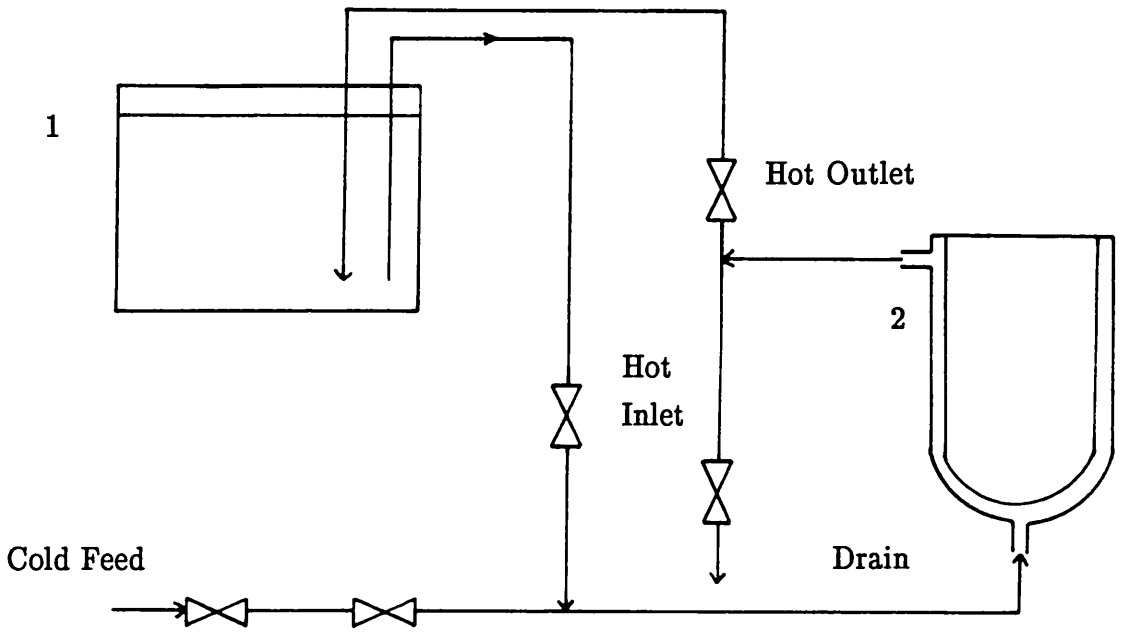


Figure 4.4 Heating/Cooling system for glass reactor

1. Thermostatic Bath
2. Jacket

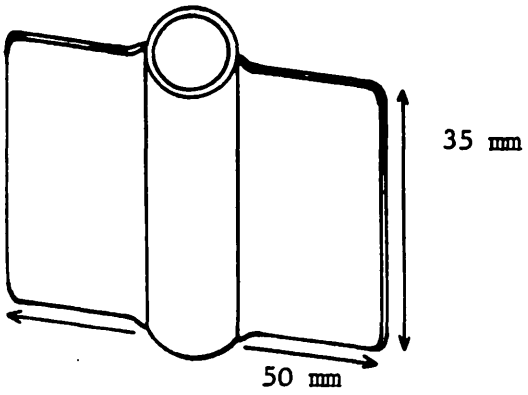


Figure 4.5 2–bladed paddle used in "simple" geometry

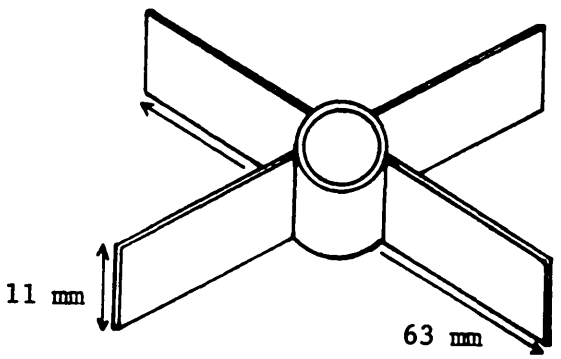


Figure 4.6 4–bladed paddle used in "complex" geometry

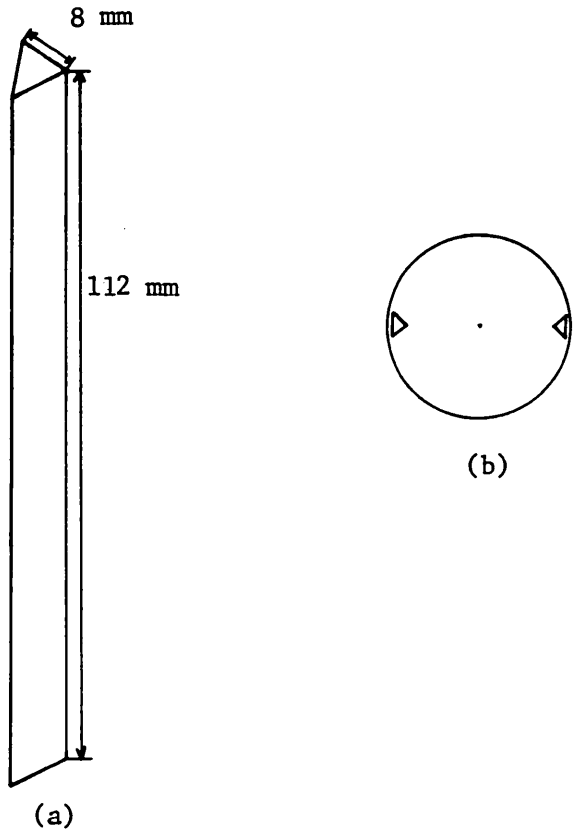


Figure 4.7 Baffle used in complex geometry
(a) Side view

(b) Top view of reactor showing mounting position of baffle relative to reactor wall.

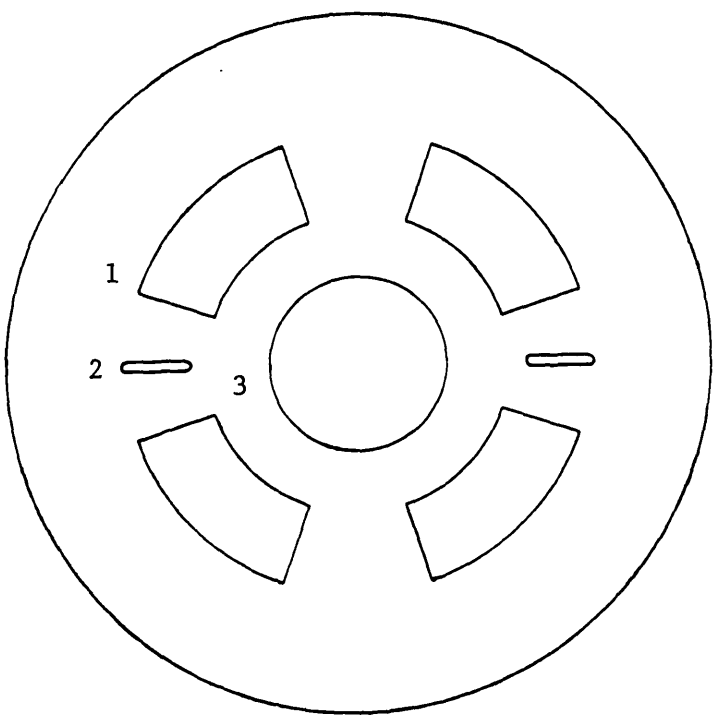


Figure 4.8 Baffle disc

1. Holes to clear entry ports
2. Fixing slots for baffles
3. Central hole to clear stirring shaft

between the glass and the deck–plate (Figure 4.8). The seals were provided by a rubber and a reinforced asbestos disc at the interfaces between the deck–plate and the baffle disc, and the baffle disc and glass reactor, respectively.

4.2 Experimental Procedure

Several operations had to be carried out prior to the start of any experiment. These involved removing the inhibitor from commercial styrene, recrystallising the initiator and dissolving the suspending agent.

Commercial styrene (BDH Chemicals, England; minimum assay 99.0%) had hydroquinone added to stabilise it, and this had to be removed before reaction, by washing with an equal amount of 0.5 M sodium hydroxide solution. The operation was repeated three times, after which styrene was washed again three times with distilled water to remove any traces of the alkaline solution. The last wash's water was tested with litmus paper to ensure neutral pH of the washed styrene.

The initiator: 2,2′–azo–bis–2–methyl–propionitrile (AIBN) (BDH Chemicals Ltd., England; minimum assay 97.6%) was recrystallised from hot methanol and the resulting filtered solution was left in the fume cupboard to allow methanol to evaporate and obtain the pure AIBN crystals.

The dissolution of the suspending agent: polyvinyl alcohol (BDH Chemicals, England: Mw $\simeq$ 125,000, 87–89% degree of hydrolysis or Gohsenol: GH23–Nippon Gohsei, Japan: 86.5–89% degree of hydrolysis) was done *in situ*. The required amount of distilled water was poured into the

reactor and then, with little agitation, the PVA was added. Stirring was increased until approximately 300 rpm and the polymer was left to swell at room temperature, for approximately 1 hour. Then the heating was switched on and hot water started circulating through the jacket. Heating continued until the temperature had reached 50°C, after which it was switched off, but the stirring was continued for a further period of about 1 hour. Any remaining small lumps of undissolved PVA dissolved during this heating period, before any other components were added.

These operations were always performed the day before a polymerisation reaction was to take place. The thermostatic bath (Techne Cambridge Ltd., England, Fail Safe Tempunit) was left on a time switch to start overnight, in order to allow the temperature to be at the desired value, usually 80°C.

When the temperature was steady at the required reaction temperature, the agitator was switched on at a speed lower than the operating one (about 100 rpm lower), and a slow flow of nitrogen was passed over the surface of the water for 10 minutes to remove oxygen. Then the necessary amount of purified styrene was added (150 ml, for a 20% phase ratio and $^3/_4$ full reactor), the agitator speed was increased to the operating value, and the flow of nitrogen was continued for another 5 minutes. The initiator was then added to the reactor, and the system closed to the atmosphere.

The reaction was allowed to proceed for about eight hours, during which the temperature and pressure were regularly monitored. After that period of time had elapsed, the temperature was decreased by flowing cold water through the jacket until room temperature was obtained (it was

usually necessary to wait for about 45 minutes for this to occur). The reactor was then opened to the atmosphere and its contents emptied into a beaker.

The first separation method attempted, filtration, did not prove satisfactory, due to clogging of the filter pores or formation of a low permeability filter cake, which resulted in a batch filtration time of almost three days. Centrifugation was found to be a very satisfactory alternative separation method. A Beckman centrifuge (model J2–21) was used and a first centrifugation was performed at 12,000 rpm for 95 minutes. The supernatant liquid was sucked from the centrifuge bottles and the polymer was removed. As this supernatant liquid was not completely clear, a second centrifugation, also at 12,000 rpm and for 95 minutes, was done to make all the fine particles settle. The resulting supernatant liquid was clear, which was then sucked and filtered through a sinter filter No. 3 (pore size 16–40 μm), to ensure that all particles had been removed. The polymer was dried in an oven at 40^{0}C for several hours.

This separation process had to be discontinued after some time due to the unavailability of the centrifuge. Since no other centrifuge capable of handling reasonable volumes at a time was available in the Department, alternative steps had to be taken. The new separation process involved letting the particles settle under gravity for 24 hours, after which the resulting supernatant liquid would be sucked off, and the polymer removed and dried in the already described manner. The supernatant liquid was slightly translucent, indicating that some very fine particles were lost in this alternative process. However, all particle size measurements were performed on the reaction mixture as it came out of the reactor. In this way it was ensured that the particle size distribution was related to the

whole contents of the reactor and any possible minor loss in the separation process was not affecting the sizing results.

CHAPTER FIVE

POLYMER CHARACTERISATION TECHNIQUES

The properties that can be determined for any polymer are many and varied, ranging from physical to chemical characteristics. However, in this study we were only concerned with those properties that might be modified by the effects of agitation conditions on the suspension polymerisation of styrene. Taking into consideration the nature of suspension polymerisation: liquid droplets dispersed, by agitation, in a continuous phase, the first and most obvious characteristic of the resulting polymer to be influenced and monitored is particle size distribution. The mean particle size and the full particle size distribution are going to be directly influenced by the agitation variables in the system: type of agitator, its geometry, presence or absence of baffles and agitator speed.

Another polymer property commonly determined in these kind of studies for polyvinyl chloride is polymer porosity. However, polystyrene suspension polymerisation produces pearl-like, non-porous particles and so such a measurement was not relevant to this polymer.

The other polymer characteristics to be followed are molecular weight distribution and conversion. To date there is no report of a direct link between molecular weight distribution and agitation conditions in suspension polymerisations.

The way in which the molecular weight distribution might be affected by agitation can be better understood if we remember that each droplet in a suspension polymerisation acts like a mini-bulk batch reactor.

Hence, if agitation (and the presence of stabilising colloid) cannot maintain a stable dispersion, the consequence for molecular weight distribution can be that of a quick broadening in the distribution curve, due to the onset of the gel effect [1]. However, even if agitation is enough to maintain a stable system, but the droplet size distribution is shifted towards the higher end of the size range of a normal suspension polymerisation, then heat transfer within each droplet and at the droplet/water interface might play a role. As the reaction proceeds and viscosity within each droplet increases, heat transfer with the cooling, dispersing medium (water) can be more difficult due to the bigger droplet radius and so a more broad molecular weight distribution curve might be expected. Related to the effect of agitation is the effect of heat transfer. If the rate of heat transfer removal is not uniform throughout the whole reactor, then there are going to be zones within the reactor which have different temperatures and these local temperature variations tend to broaden the molecular weight distribution.

5.1 Measurement of Particle Size Distribution

The particle size distribution analysis is the crucial polymer characteristic to reflect the effects of agitation conditions on suspension polymer properties, as already mentioned. The technique used for such an analysis should be able to give reliable information on the full particle size distribution, for both solid particles and liquid droplets, if possible.

A literature search[2–5] indicated that the two most used methods of obtaining a particle size distribution in such kinds of studies were:

(i) Sieve analysis, and

(ii) Coulter Counter.

Sieve analysis is a mechanical technique and was the first particle size distribution technique to be considered. However, it was soon abandoned, since it would constitute a poor choice, both in terms of selectivity and convenience of analysis.

The Coulter Counter technique is a method of determining both the number and the size of particles suspended in an electrolyte, by forcing them to pass through a small orifice on either side of which is immersed an electrode. As particles go through the orifice, there are changes in resistance that generate voltage pulses whose amplitude are proportional to the volume of the particles. The pulses are amplified, sized and counted, allowing the size distribution of the suspended phase to be determined.

This technique is very sensitive to vibration and electrical noise, and the instrument available in the Department was a single channel model, which meant that each channel (size range) had to be determined individually. This meant that a full particle size distribution of any one sample was very time–consuming, which made us abandon this technique as a possible means of obtaining all our sizing analyses.

The method used throughout this work was a Malvern Particle Size Analyser which enables a 16– or 32–channel (size range) distribution to be obtained in much less time than the Coulter Counter and is suitable for both solid particles and liquid droplets.

5.1.1 Measuring principle of Malvern Particle Size Analyser

The measuring principle of a Malvern 2600 Particle Size Analyser is based on the forward diffraction of light from a dispersed suspension, and a

block diagram of this instrument is shown in Figure 5.1.

A low–power laser beam is directed towards an appropriate sample cell, where the particles, whose particle size distribution is desired, are contained. The incident light is diffracted by the particles to yield a diffraction pattern. As particles enter and leave the illuminated area the diffraction pattern changes, always reflecting the instantaneous size distribution. So, by integrating over a suitable period of time, a representative sample of particles is used in constructing the final measured diffraction pattern. The angle of diffraction is related to particle size (the smaller the particle, the greater the angle of diffraction) and the intensity of diffracted light at any angle is a measure of the mean projected areas of particles of a specific size. The diffracted light is collected by a lens, which focuses it on a multi–element photo–electric detector placed on the focal plane of the lens, as seen in Figure 5.2. The analogue signal produced is proportional to the incident light intensity. This detector is directly interfaced to a computer, which performs the necessary integrations. Non–linear least square analysis is used to find the size distribution which fits better the measured diffraction pattern. The resulting size analysis is basically volumetric.

This instrument was suitable for solid particles as well as for droplets, and two sample cells were available. The solid particles arrangement consisted of a recirculating cell with a 2 mm gap between the two optical windows and material was pumped to and from an agitated tank, with a capacity of 1.2 l. Since this set–up was clearly unsuitable for droplets, due to passage through the recirculating pump, which would change the particle size distribution of deformable droplets, a small batch cell with a light path of 14.3 mm was used. Mild agitation was provided

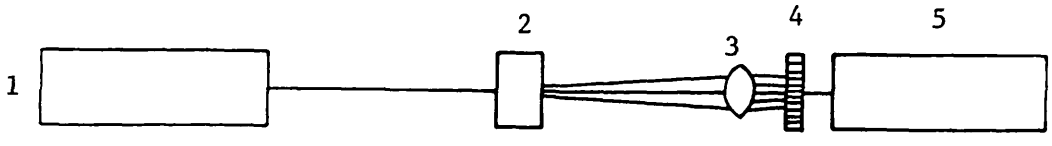


Figure 5.1 Block diagram of Malvern Particle Size Analyser

1. Laser tube
2. Sample cell
3. Lens
4. Detector
5. Signal processing system

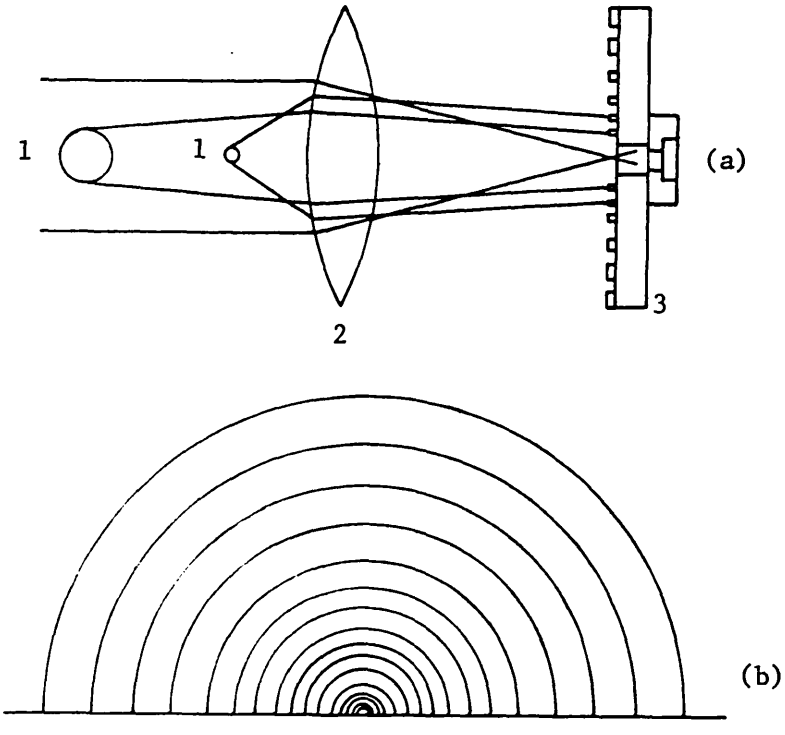


Figure 5.2 Schematic diagram of (a) diffraction of light by particles and (b) front view of detector
1 – Particle; 2 – Lens; 3 – Detector

via a small magnetic stirrer to ensure circulation in the cell, but preventing disruption of the particle size distribution of the material to be examined. According to the nature of the sample one of these two cells was used: the recirculating cell with a light path of 2 mm for solid polymer particles and the small cell with a light path of 14.3 mm for liquid droplets of monomer or of a mixture of monomer and polymer, before reaching final conversion. The agitated tank for solid particles could also be subjected to ultrasound, to break up any aggregates present, which was the case with polymer samples in this work once they had reached the solid state.

The choice of lens depended upon the required range of particle size. Three lenses were available:

(a) Focal length = 300 mm; size range = 5.8–564.0 μm;

(b) Focal length = 100 mm; size range = 1.9–188.0 μm;

(c) Focal length = 63 mm; size range = 1.2–118.0 μm.

The 300 mm focal length lens was used in all measurements, since it covered the desired size range of the samples.

The analysis of the results could be done either by fitting to a two–parameter analytical function (Rosin–Ramnler, log–normal or normal functions) or by a model–independent analysis. The latter mode was always chosen, since it could measure multi–moded size distributions with high resolution.

5.1.2 Experimental procedure

The required lens and cell were fitted into the apparatus according

to the size range and type of sample to be analysed, and the particulars referring to the sample were entered into the microcomputer. The optic alignment was then checked, with only distilled water in the cell. The detector position was adjusted such that the incident laser beam was falling inside the central detector ring, indicating that no diffraction was taking place. The background was measured and adjusted.

Then the sample could be added to the cell. If it was a dry, solid material, then it was advisable to add a wetting agent (a heavy alcohol) to the distilled water (prior to any background reading) to improve suspension of particles. The sample was added a little at a time, until the video display, at sample inspection, was at the accepted level of obscuration:

$$\text{obscuration} = 1 - \frac{\text{light energy transmitted by sample}}{\text{incident light energy}}$$

Suitable values were between 0.25 and 0.35.

The sizing measurement of the sample could then start, after which the results were calculated and displayed.

The result of the analysis was presented as the cumulative volume (weight) undersize and volume frequency for 16 or 32 size classes. In addition, a full range of derived diameters could be tabulated, and the distribution could be presented in standard sieve sizes. It could also be transformed to a surface area, linear or number weighting distribution.

5.1.3 Comparison of results between Malvern Instrument and Coulter Counter

The reliability of results given by the Malvern Instrument was tested against a polymer sample (suspension polyvinyl chloride) whose particle size distribution was known from ICI's multi–channel Coulter Counter. The size distribution of this sample was well within the range of both instruments and it was commonly used for testing the reliable operation of the Coulter Counter. Figures 5.3(a) and (b) present the cumulative and differential undersize volume curves for the polymer sample run in the Malvern Particle Size Analyser and in ICI's multi–channel Coulter Counter. The results agreed closely and the average diameter also compared well: $\bar{d}$ = 132 μm and $\bar{d}$ = 138 μm for the Coulter Counter and Malvern analysis, respectively. However, the spread of the polyvinylchloride sample distribution (taken between 15% and 85% of the whole distribution) was much smaller (60 μm) than the corresponding value for typical polystyrene samples in this work (200–300 μm).

5.2 Measurement of Molecular Weight Distribution

The molecular weight of a polymer cannot be expressed by a unique value, as simple molecules can, but rather by a distribution curve of individual polymer molecules with different chain length. This arises from the random nature of polymerisation reactions. We can draw curves of number molecular weight distribution (or number chain length distribution) or of weight molecular weight distribution (Figures 5.4(a) and (b)).

These molecular weight distribution curves can be determined by the experimental technique of gel permeation chromatography (GPC), which

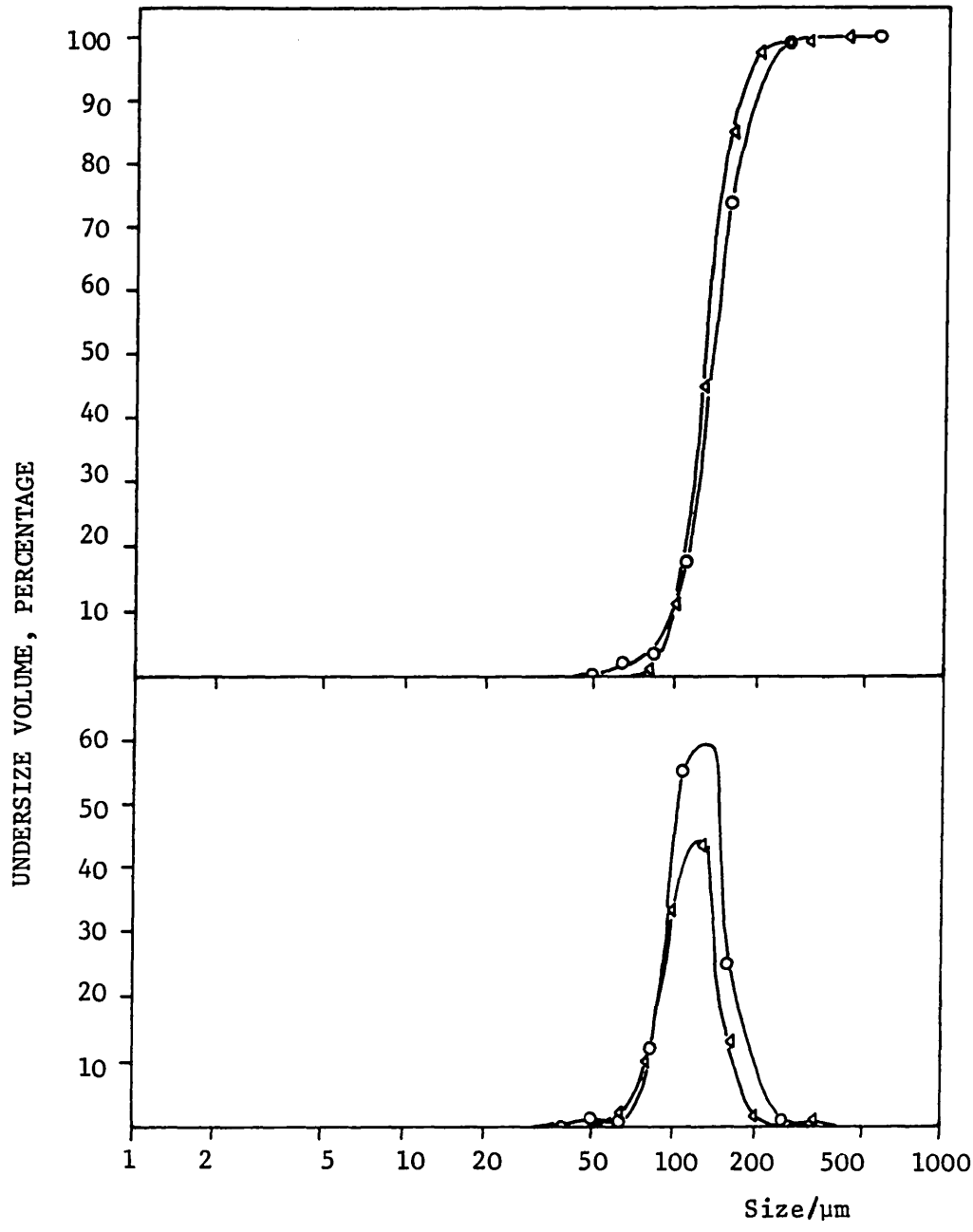
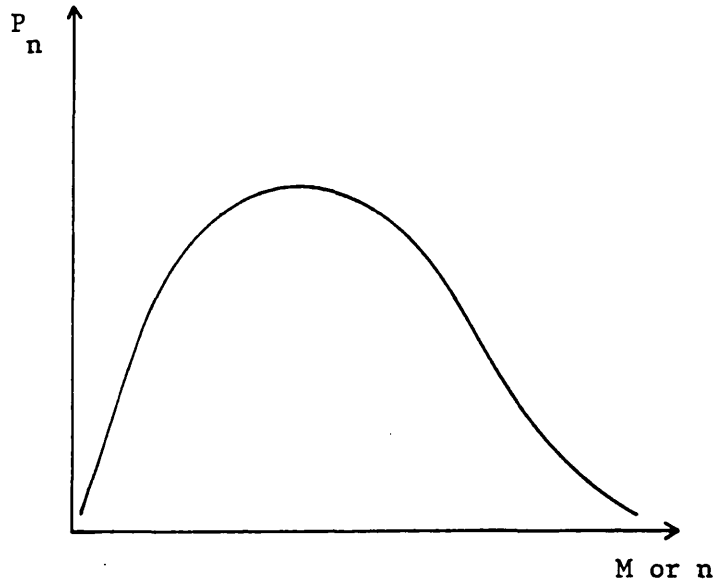
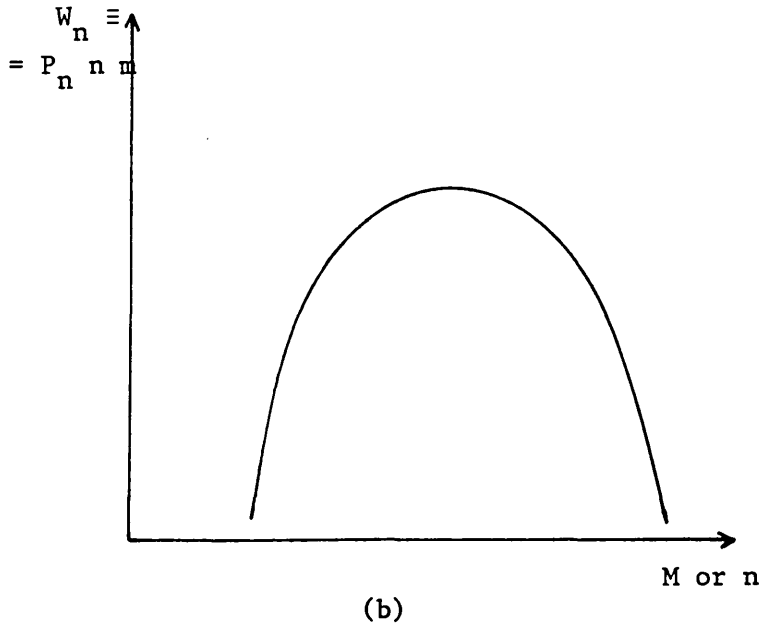


Figure 5.3 (a) Cumulative and
(b) Differential undersize volume curves
for a test polymer sample

○ Using Malvern Particle Size Analyser
◁ Using I.C.I. Multi–channel Coulter Counter



(a)



(b)

Figure 5.4 (a) Number molecular weight distribution curve
(b) Weight molecular weight distribution curve

where P_n is the concentration of a polymer of chain length n,
m is the molecular weight of monomer,

W_n is the weight of a polymer of chain length n.

is, however, not suitable for all polymers, but can be employed for polystyrene, the polymer used in this study. Less convenient molecular weight techniques for polymers are light scattering, viscosity measurements and colligative properties (e.g. osmotic pressure), which only give average values.

There are several average values that can be quoted in relation to a polymer, and most common are the number average, M_n, and the weight average, M_w, molecular weight, that can be defined by[1]:

$$M_n = \frac{\sum_{j=1}^{\infty} m\,j\,P_j}{\sum_{j=1}^{\infty} P_j} = \frac{\sum_{j=1}^{\infty} M_j\,P_j}{\sum_{j=1}^{\infty} P_j} = m\,\bar{\mu}_n \qquad (5.1)$$

where $\bar{\mu}_n$ is the number average chain length, or the degree of polymerisation.

$$M_w = \frac{\sum_{j=1}^{\infty} M_j\,w_j}{\sum_{j=1}^{\infty} w_j} = \frac{\sum_{j=1}^{\infty} m^2 j^2 P_j}{\sum_{j=1}^{\infty} m\,j\,P_j} = \frac{\sum_{j=1}^{\infty} M_j^2\,P_j}{\sum_{j=1}^{\infty} M_j\,P_j} = m\,\bar{\mu}_w \qquad (5.2)$$

where $\bar{\mu}_w$ is the weight average chain length.

The ratio of these two quantities is the polydispersity, Z_p, and represents the broadness of the distribution curve:

$$Z_p = \frac{M_w}{M_n} = \frac{\bar{\mu}_w}{\bar{\mu}_n} \qquad (5.3)$$

The polydispersity is usually equal or bigger than 1, and can have values from two to fifty for commercial polymers.

The method of gel permeation chromatography involves separating the different polymer molecules according to their size. This is done in columns filled with porous beads having different pore sizes, usually 10–250 nm. A polymer sample is dissolved in a suitable solvent which is also used as the elution liquid which flows continuously down through the columns. When the dissolved polymer sample is injected into the column, the bigger molecules have great difficulty in penetrating the pores, whereas the smaller molecules can go inside the pores, hence taking more time in going through the columns. This process results in an effective separation of the sample according to molecule size, with larger molecules appearing first and smaller ones at the later stage. A detection system measuring refractive index variations is used to monitor concentration changes in the effluent. If the experimental variables: temperature, flow rate, concentration, are kept constant for a same system, then the retention volume, that is, the volume of solvent that has to be eliminated from the system, between sample injection time and the time it appears in the effluent, is only a function of the molecular size of the polymer. A calibration curve can then be made for a polymer system, by injecting samples of that polymer with low polydispersity and known molecular weight, and measuring the retention volume. This curve is usually linear for molecular weights within the range 10^3–10^7 and can then be used to obtain the molecular weight distribution curve of a new sample.

5.2.1 Experimental procedure

The molecular weight measurements were carried out on a Gel

Permeation Chromatograph (Applied Chromatography Systems Ltd.) located in the Department of Chemical Engineering at Imperial College, or at ICI Petrochemicals and Plastics Division, Runcorn. The solvent used was tetrahydrofuran stabilised with 1% quinol (BDH Chemicals Ltd., England) and the elution flow rate was always set at 1.0 $ml.min^{-1}$. The concentration of the polymer samples was about 2% (weight by volume) and 0.05 $ml.ml^{-1}$ of 1% toluene in tetrahydrofuran were added as an internal reference. The injection volume was kept constant at 0.1 ml by means of an injection coil. All measurements were carried out at room temperature and a period of 2–3 hours warm–up time of solvent and column was allowed to prevent baseline drift. In Figure 5.5 a typical chromatogram is presented.

To convert this chromatogram to the required molecular weight averages, the calibration curve of the columns used was needed. Figure 5.6 shows the calibration curve relative to the columns used in the measurements.

The height of the chromatogram, at any given elution volume, is directly proportional to the weight of polymer, i.e. $M_j\ P_j$. The corresponding molecular weight, M_j, for that elution volume can then be obtained from the calibration curve. The number average, M_n, and the weight average, M_w, molecular weight can be evaluated using expressions (5.1) and (5.2), respectively.

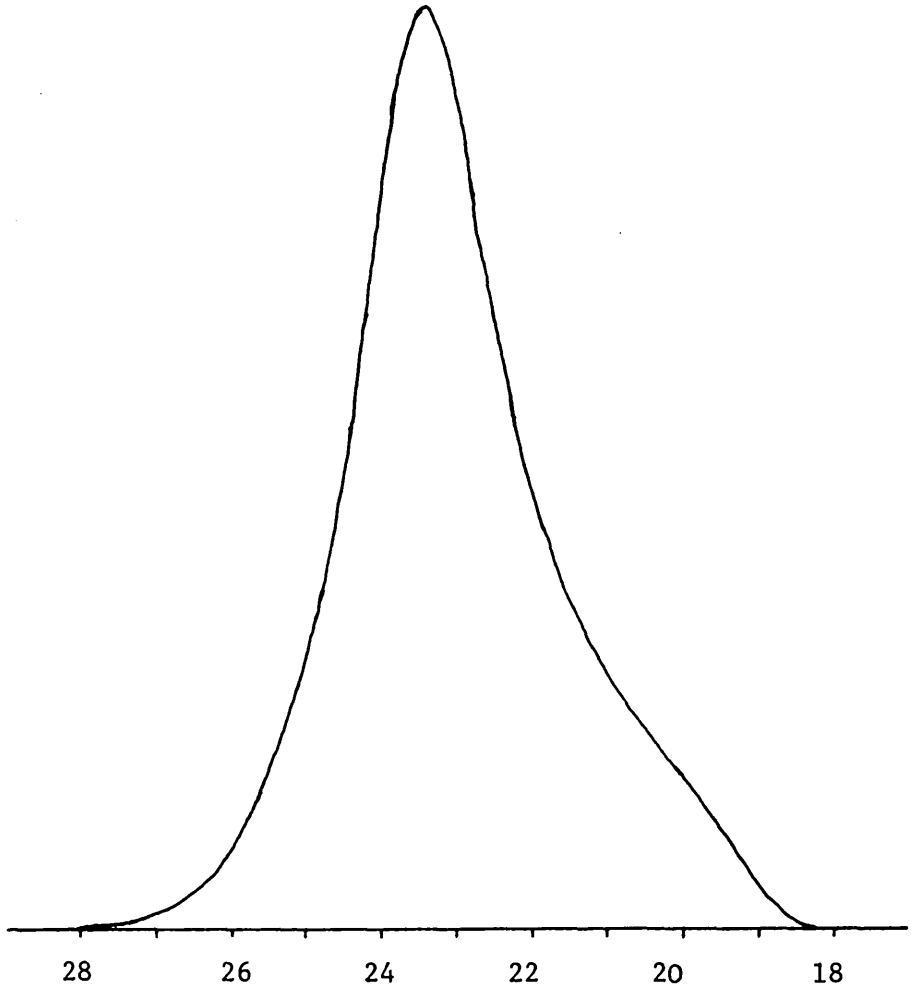


Figure 5.5 Typical gel permeation chromatogram for polystyrene samples

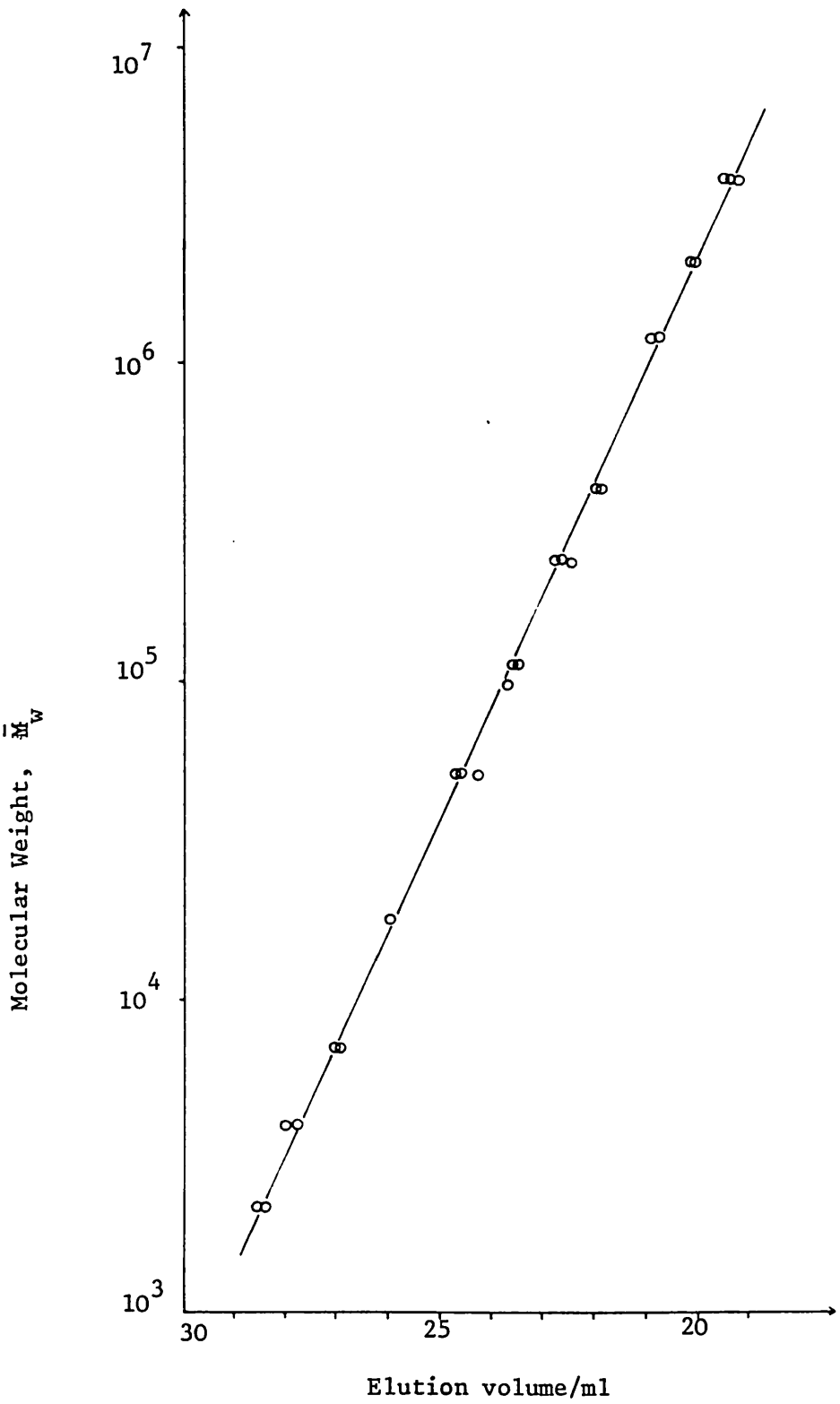


Figure 5.6 Calibration curve for gel permeation chromatography

References to Chapter Five

[1] "Principles of Polymer Systems", F. Rodriguez, McGraw–Hill, (New York), 1982.

[2] M. H. Lewis, G. R. Johnson, "Agitation Scale–Up Effects during VCM Suspension Polymerisation", J. Vinyl Tech., 3(2), 102–106 (1981).

[3] H. Hopff, H. Lüssi, P. Gerspacher, E. Hammer, "Zur Kenntnis der Perlpolymerisation", Chemie–Ing. –Techn., 11, 1085–1089 (1964).

[4] R. Schröder, B. Piotrowski, "On particle formation during suspension polymerisation of styrene", Ger. Chem. Eng., 5, 139–146 (1982).

[5] F. Langner, H-U. Moritz, K–H. Reichert, "Reactor Scale–Up for Polymerisation in Suspension", Chem. Eng. Sci., 35, 519–525 (1980).

CHAPTER SIX

EXPERIMENTAL RESULTS

The results concerning flow and polymerisation experiments as well as the polymer characteristics are presented in this chapter. As already mentioned the flow was characterised in the same vessel and under the same conditions as polymerisation reactions were carried out. In this way the polymer properties can be directly related to the flow characteristics and the linking of the two sets of information can give a more profound understanding of the complex phenomena involved in suspension polymerisation reactions.

The first section to be presented will compare the results of this work with existing correlations between mean particle diameter and agitation parameters such as stirrer speed for styrene suspension polymerisation, and serves to illustrate their deficiencies.

Next, the second part deals with a more detailed analysis of the results for the 2–bladed paddle ("simple") geometry and the final third section reports findings with the 4–bladed paddle ("complex") geometry. These sections show how the details of the polymer product characteristics can be understood in terms of a more comprehensive analysis of the flow characteristics which form the link between agitation conditions and the nature of the polymer product.

6.1 Preliminary Comparison of Results with Existing Correlations

Before examining the results of this work in some detail it is instructive to briefly examine how existing correlations for just one of the

derived parameters of the polymer products, mean particle size, compare with the measured values.

The literature reports several correlations between mean particle size and stirrer speed, N_s, as mentioned earlier in chapter 2. Two of the most relevant studies in this field are those from Calderbank [1] and Reichert [2]. The first work gives an equation for the mean drop diameter, d_{32} (Sauter mean diameter), for liquid–liquid dispersions (equation (2.1) in page 43).

$$d_{32} = 0.224\ D\ We^{-0.6} \left[\frac{V}{D^3}\right]^{0.4} P_o^{-0.4} \left[\frac{H}{1-H}\right]^{-0.5} \left[\frac{\mu_d}{\mu_c}\right]^{0.25} \qquad (6.1)$$

Reichert's work on polymerising styrene in suspension reports that the mean particle diameter, $d_{50\%}$, has a two region dependency with stirrer speed

$$d_{50\%} \simeq N_s^{\,b} \qquad (6.2)$$

where b has the values –3.0 and –0.3 if stirrer speed is smaller than 300 rpm or higher than 450 rpm, respectively. These values are referred to a paddle stirrer, without baffles, in a 1.5l reactor with a diameter to height ratio of two.

The Calderbank equation can be used to predict the Sauter mean diameter for the various agitation conditions used in this work, which can be compared with our own experimental results. This is done in Table 6.1.

Table 6.1 Sauter mean droplet diameter from Calderbank equation and from experiments in this work.

$d_{32}/\mu m$	Predictions from Calderbank			Experimental values		
	2–Bladed Paddle	4–Bladed Paddle		2–Bladed Paddle	4–Bladed Paddle	
RPM		No baffles	Baffles		No baffles	Baffles
200		256.3	133.9		220 (19.6)	168.5 (22.2)
300	250.4			(42.3)		
350	208.2			(49.5)		
400	177.2	116.6	58.3	(33.4)	103 (21.6)	93.6 (20.4)
500	135.7			(30.2)		

(Values in parenthesis refer to samples subjected to ultra–sound treatment).

The predicted values were calculated using the following data:

$D_{2\text{–bladed paddle}} = 5.0 \times 10^{-2}$ m $\qquad$ $D_{4\text{–bladed paddle}} = 6.3 \times 10^{-2}$ m

$V = 0.750 \times 10^{-3}$ m^3 $\qquad$ $\mu_{H_2O} = 1$ CP

$\rho = 10^3$ kg.m^{-3} $\qquad$ $\mu_{styrene} = 1.5$ cP

$\sigma = 4.0$ mN.m^{-1} [3] $\qquad$ H = 0.25

$P_{o\ \text{unbaffled case}} = 1.2$ [4] $\qquad$ $P_{o\ \text{baffled case}} = 6.1$ [4]

Figures 6.1 (a) and (b) present the deviations of sauter mean diameter of the Calderbank equation from the present experimental results with stirrer speed for the complex and simple geometry, respectively.

The Calderbank equation is an overestimate for the unbaffeld case of the complex geometry, although the baffled situation exhibits a reversal of the position of the two curves, and hence we can not generalise as to whether Calderbank underestimates or overestimates the Sauter mean diameter. The application of ultra–sound treatment to the size distribution of both geometries, reverting to a size distribution resembling that existing before the aggregation process, greatly reduces the Sauter mean diameter (curves 5, 6, 7) as compared with the Calderbank predictions. Even in non–aggregating conditions this equation is an overestimate of the Sauter mean diameter.

If a mean particle diameter dependence with stirrer speed of the same type as that presented in equation (6.2) is used to fit the current experimental results for the simple geometry, then the exponent b increases from –0.95 to

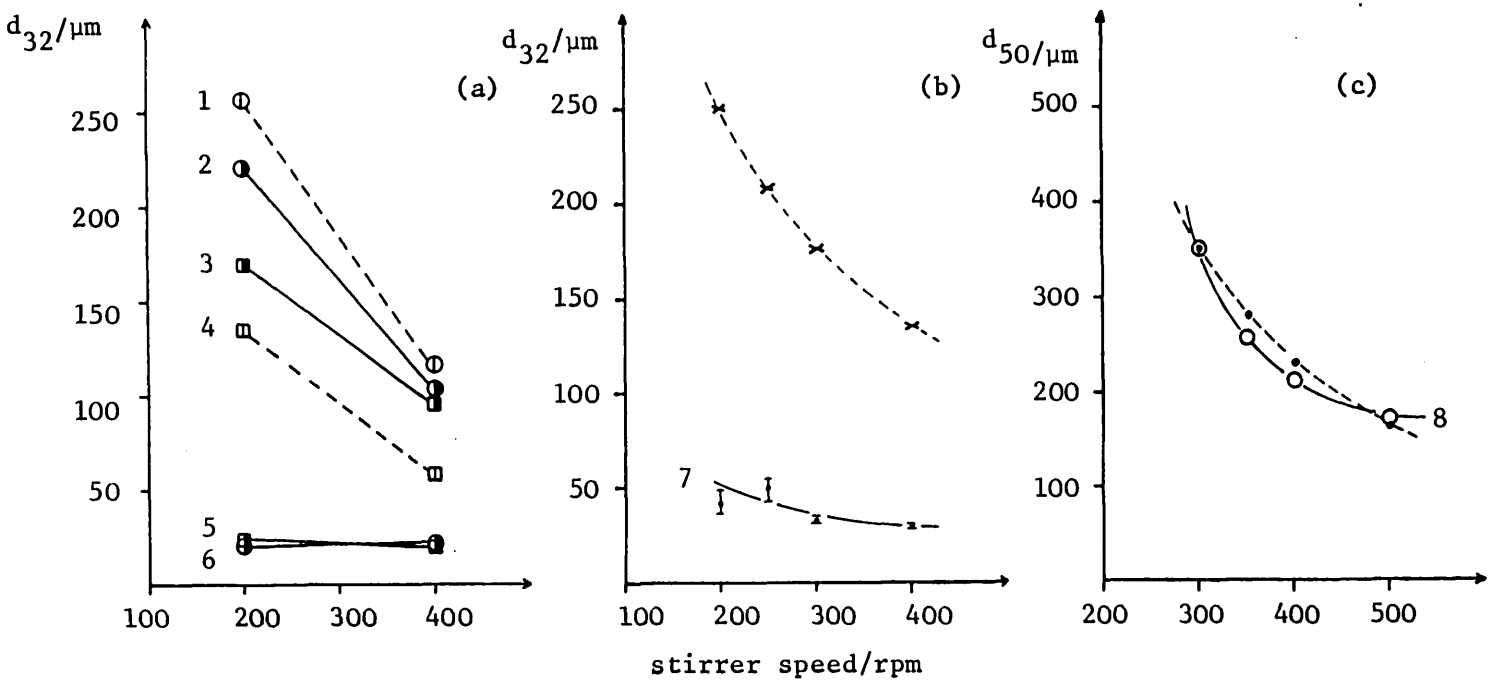


Figure 6.1 Comparison of experimental results and predictive models of mean particle size as a function of stirrer speed

(a) Sauter mean diameter for complex geometry (b) Sauter mean diameter for simple geometry
(c) $d_{v/50\%}$ for simple geometry

——— solid lines: experimental points – – – dashed lines: prediction according to Calderbank equation

– • – dash – point lines: Prediction according to $d \sim N_s^{-1.47}$

1,2,6,7,8 – No baffles 3,4,5 – Baffles 5,6,7,8 – After ultra–sound treatment

–2.05 as stirrer speed decreases. This trend is in agreement with Reichert's equation, although the actual values are very different, being closer to those reported in [5] for a high stabilizer concentration, where b was –1.47. If this value of b is used to generate a curve of mean particle diameter, $d_{50\%}$, versus stirrer speed, using the experimental result at 300 rpm as the starting point – Figure 6.1(c), then fair agreement is found with our experiment results.

It is evident from the lack of concensus shown in this brief comparisons that the current level of understanding and prediction is still far away from providing a complete picture of the complex phenomena involved in a suspension polymerisation process. The Calderbank equation, by assuming that the droplet size will be determined by the balance between the turbulent nature of agitation that causes break–up and the material properties opposing this, surface tension and viscosity, can give a good first estimate of the initial droplet diameter, but it does not take any account of the changing surface and rheological properties of the polymerising droplets. There are also a certain number of other factors that have not been taken into account in this approach.

One of the first factors that should be considered is that the details of the complete particle size distribution are often more important in determining the product characteristics than a simple mean particle or droplet diameter. There are reports of bimodal distributions in the literature [5] (which was also found to be the case of this work), which makes it less meaningful to define a single mean particle size. Certainly, one mean diameter will not be sufficient to characterise more complex size distributions.

The Calderbank equation and similar approaches assume that the

initial monomer droplet size distribution is attained rapidly and is reflected unaltered in the polymer product. This approach ignores the possibility of the existence of agglomeration/aggregation processes that will change drastically the particle size distribution during the course of a long polymerisation.

Hence correlations such as these tell nothing about the time evolution of the particle size distribution. Usually this evolves from the initial stages of reaction, until a stable size distribution has been achieved, reflecting the dynamic equilibrium between coalescence and break–up processes. Such factors should also be considered in a more complete approach.

The effect of baffles in the system is only reflected by the Power number in the Calderbank equation (6.1). This dimensionless number is a gross flow characteristic that is unlikely to be able to reflect all the fine changes in flow that occur when baffles are introduced, and how these affect the product, especially in a coalescing system.

Another physically important factor which is not explicitly included in lumped agitation parameter approaches is the circulation time, t_c, defined here as the time for a polymerising droplet which originates in the high turbulent region near the agitator to return to this zone after an excursion into the more quiescent upper zones. This is just the parameter reflected in many of the data presented earlier in this chapter. In fact, of course, there are a whole range of t_c values for any given system and it is the distribution of circulation time which will most certainly influence the resulting particle size distribution. For instance, a narrow distribution of t_c will probably be associated with a narrower particle size distribution, since the particles will have a more uniform flow history.

This list of additional factors not included in the standard correlations reinforces the need for a more global understanding of the suspension polymerisation process from the point of view of flow and property characterisation, which we will attempt in the next two sections.

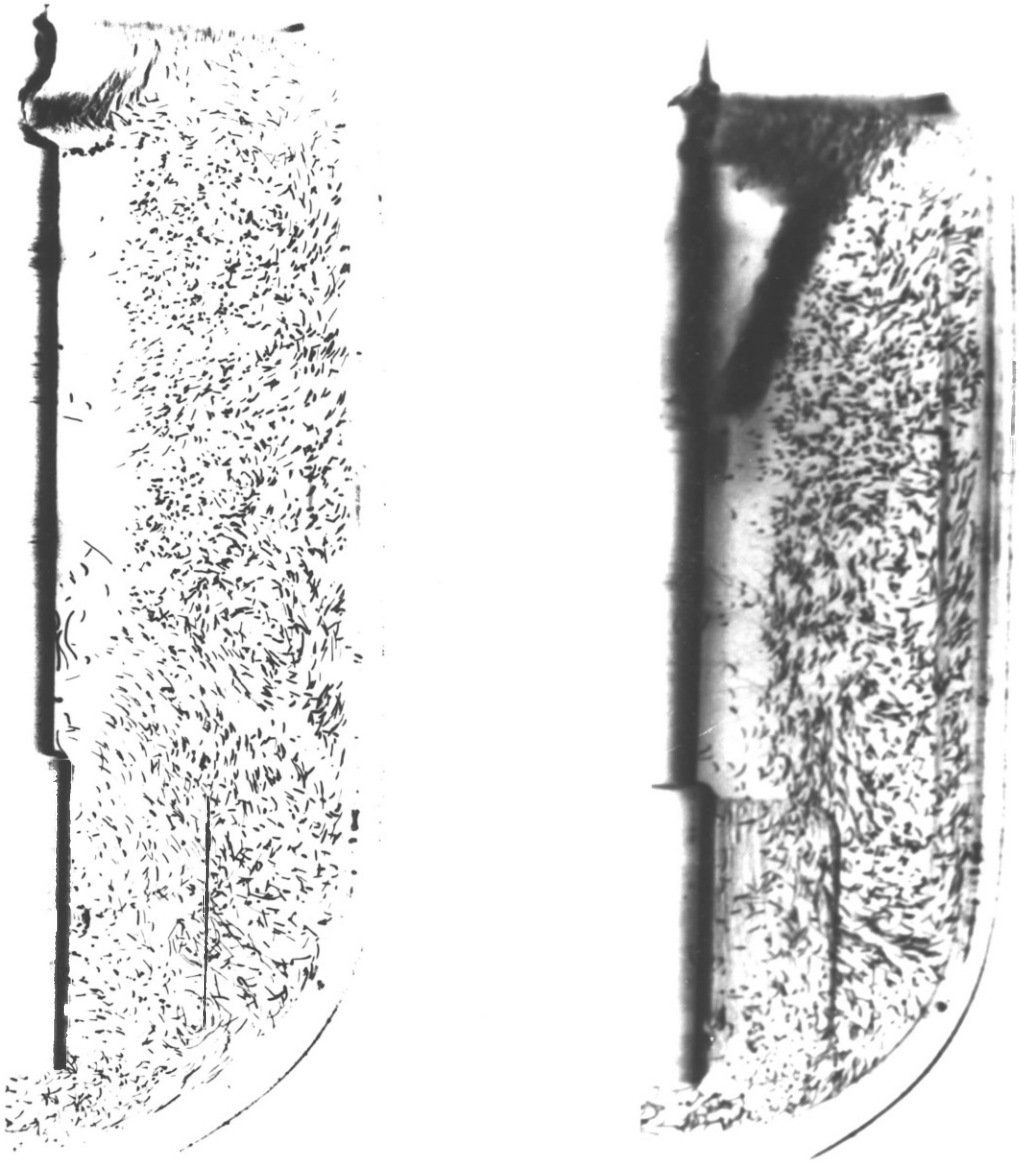
6.2 2–bladed Paddle ("Simple") Geometry

For the 2–bladed paddle geometry the flow was first characterised using static streak photography, dynamic video monitoring and laser doppler anemometry. Subsequently polymerisation experiments were performed under these well characterised flow situations and the resulting polymer characterised in terms of its particle size and molecular weight distribution.

6.2.1 Flow characterisation Experiments

(a) Static streak photography

The experiments done in this section covered a wide range of stirrer speeds, ranging from 150 to 400 rpm. The flow patterns obtained for this range of stirrer speeds were essentially identical. The photographs shown in Figures 6.2 (a) and (b) represent typical vertical flow patterns for the 2–bladed paddle at 150 and 300 rpm, respectively. These photographs show that fluid is thrown out by the paddle, going up near the wall and coming down by the shaft. Also a considerable part of the fluid never reaches the top, reversing its direction and by–passing the surface. Some vortices are sometimes seen next to the agitator, their occurrence probably being a function of blade position during exposure time. The fact that the flow patterns look similar even though absolute velocities double indicate that, at least on this level of detail (gross circulation patterns), the agitation process is still very much the same. No qualitative difference can be found, although quantitatively velocities change in the autoclave, as reflected by streak length.



(a) (b)

Figure 6.2 Streak Photograph of vertical flow patterns in simple geometry, at
(a) 150 rpm
(b) 300 rpm

(b) Dynamic video monitoring system

At the start of the experiments the scanning time had to be chosen in order to give a statistically meaningful results, i.e. to ensure that the counting had lasted long enough to have adequately sampled all aspects of the flow follower's history. Scanning times were varied from 5 to 30 minutes, at a stirrer speed of 150 rpm, and the variable under question was the percentage of time spent in each zone (zones 1 to 5, increasing from top to bottom of reactor) – Figure 6.3. These results show that at this stirrer speed the flow follower spends an almost equal amount of time in the middle zones of the reactor (2,3 and 4), in a percentage very close to 20%, but the time spent at the bottom zone, (5), of approximately 35% is much higher that that at the top zone, (1) which is around 8%. The fact that the middle zones exhibit percentage of time close to 20% is in close agreement with the statistics of a random mixing process: therefore if one is prepared to wait for long enough then, on average, the flow follower should spend the same amount of time in any of the different zones of the reactor. As these data do not show any particular trend with increasing scanning time, except for a smaller spread in the results, a scanning time of 6–10 minutes was chosen for the majority of the work.

The experiments covered a range of stirrer speeds from 150 to 300 rpm and in Figure 6.4 the percentage of time spent in each zone is plotted as a function of stirrer speed. At this stage it may be worth remembering that zones are fixed in the screen and that it was always arranged such that the bottom zone – (5) started just above the paddle. As the stirrer speed increases, the vortex becomes deeper, and when defining the scanning area for each particular speed, the upper boundary line had to be just below the lowest height of vortex. Taking into consideration these two facts, the two top zones become gradually unavailable for scanning, thus the existence of results for part of zone. The results of Figure 6.4 show a slight increase in the

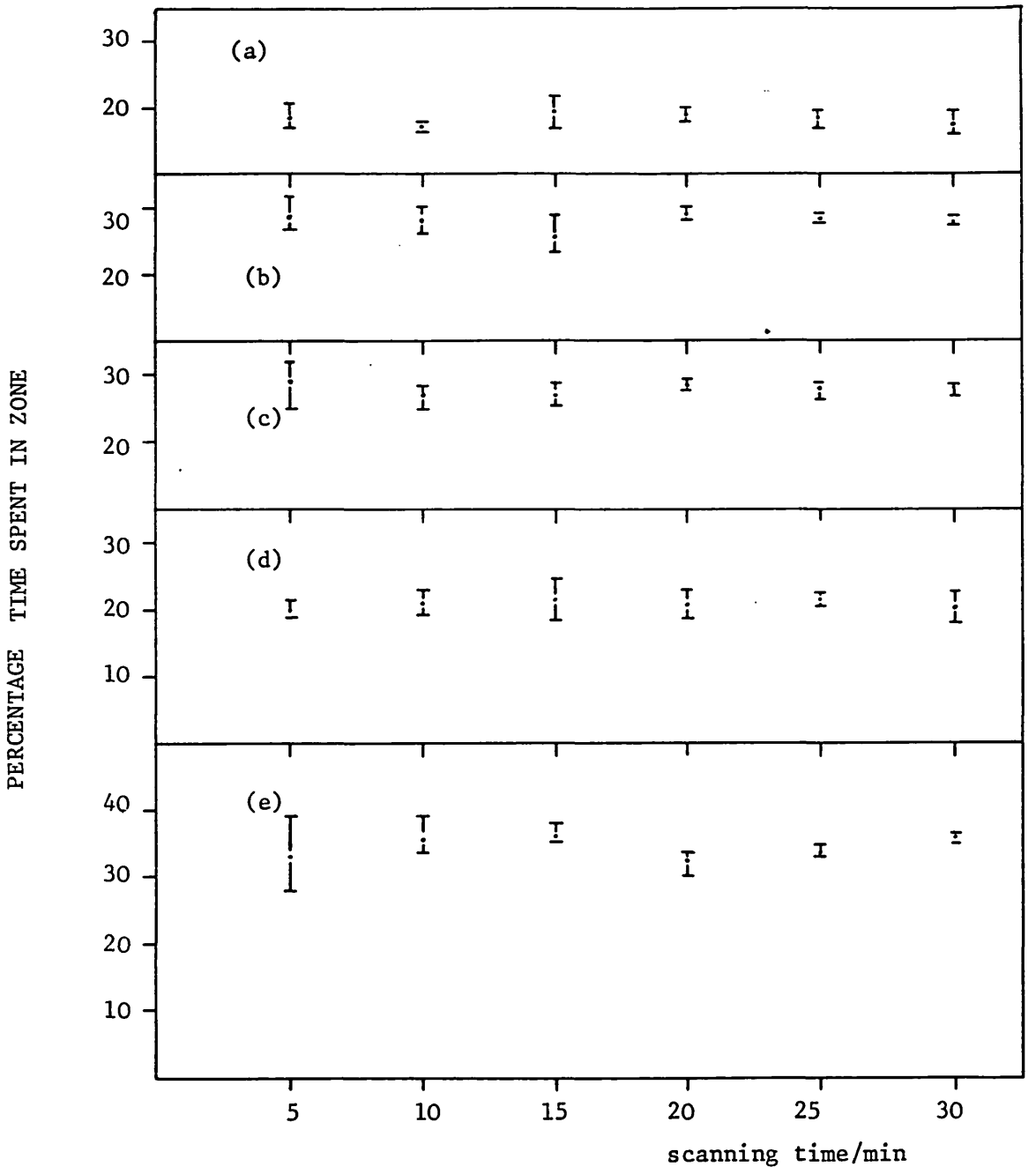


Figure 6.3 Variation of scanning time for 2–bladed paddle, at 150 rpm

zone 1 was not completely available for measurements

(a) zone 1 (b) zone 2
(c) zone 3 (c) zone 4
(e) zone 5

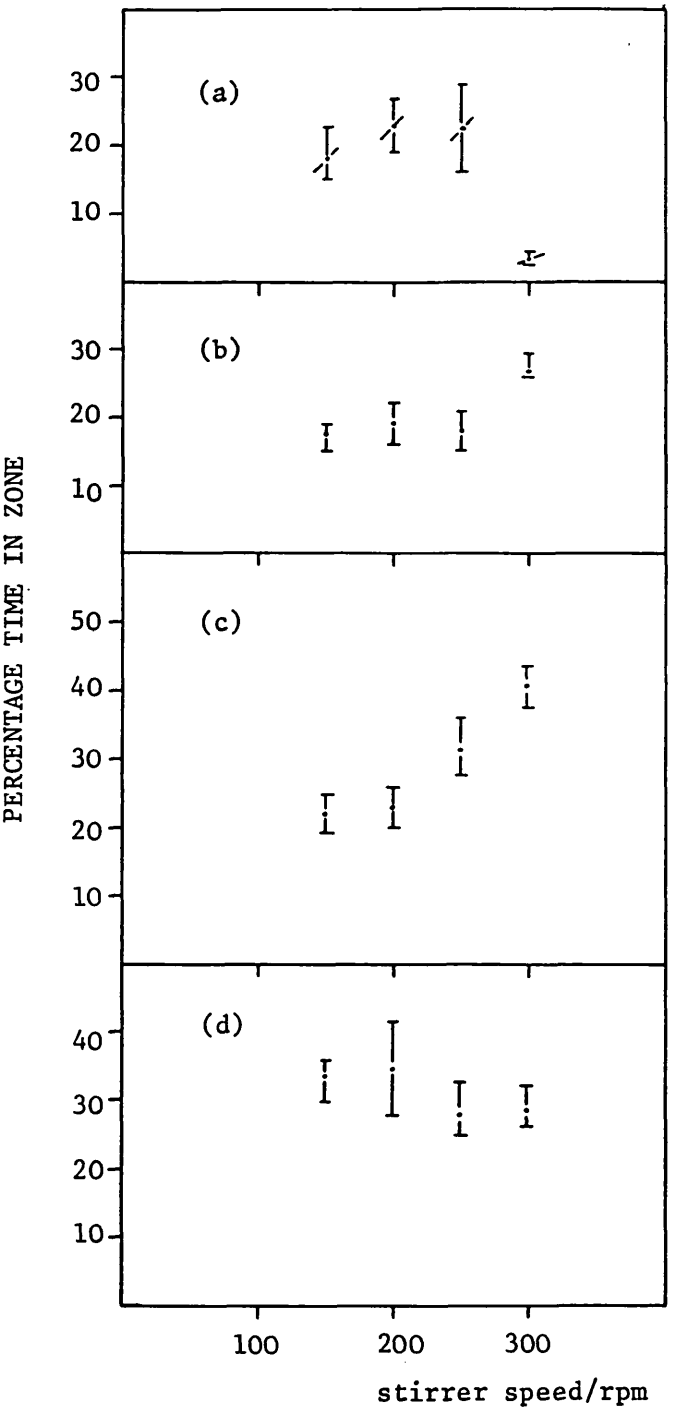


Figure 6.4 Variation of percentage time spent in zone with stirrer speed for 2–bladed paddle

$\overset{I}{\not I}$ denotes measurement in part of zone (due to vortex intrusion)

(a) zone 2 (b) zone 3
(c) zone 4 (d) zone 5

percentage of time spent in zone (3), above 250 rpm; this increase becomes more pronounced and starts at an earlier stirrer speed, 200 rpm, in zone (4). The percentage of time spent in the bottom zone (5) does not seem much affected by the increase in stirrer speed, although a small decrease might be noted. In this geometry the flow follower spends a considerable proportion of its time in the agitator zone, which does not seem to change much with the variation in stirrer speed.

A different kind of information can be obtained from this flow characterisation technique by looking at the probability of direction change at any zone for 150 rpm and during 25 minutes, when the flow follower can either reverse its direction or continue its path Figure 6.5. The data show that the middle zones (2)–(4) have similar values for the probability of going down and turning up of approximately 0.15, and the reverse probability of going up and turning down is almost 0.3 for the same three zones: (2)–(4). The top and bottom zone values are somewhat different from those in the central zones because particles entering either have a high probability of changing direction before leaving because they are approaching either the free liquid surface or the reactor base. Hence for example, for zone one (near the liquid surface) there is a very high probability (0.7) of an upward travelling particle turning over to move downwards in the reactor, but very little chance (0.2) of a downward moving particle moving up again before it leaves this zone. The short time effect of stirrer speed on the probability of direction change can be seen in Figure 6.6, for a scanning time of 10 minutes. There seems to be a small stirrer speed effect with the probability of reversal when going up increasing as stirrer speed increases in zones (2) and (3), but becoming less pronounced and reaching an almost steady value of 0.38 for zones (3) to (5). The probability of going down and turning up seems to

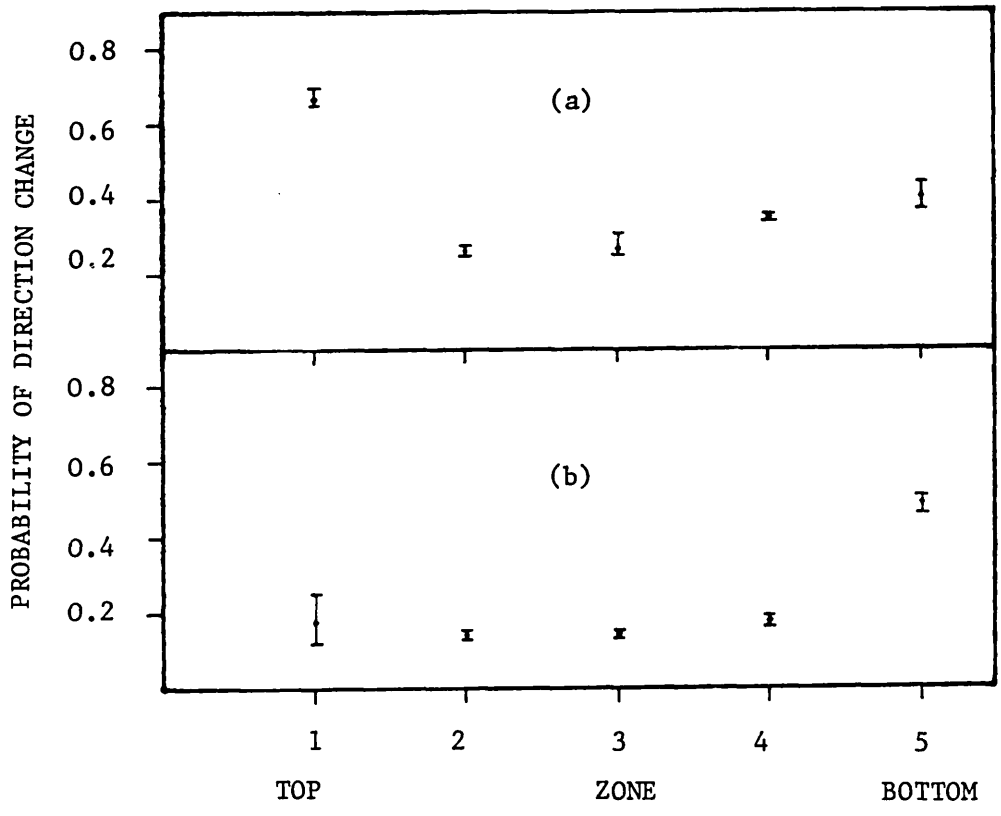


Figure 6.5 Probability of direction change at zone, for 2–bladed paddle, at 150 rpm for 25 minutes

(a) Going up and turning down
(b) Going down and turning up

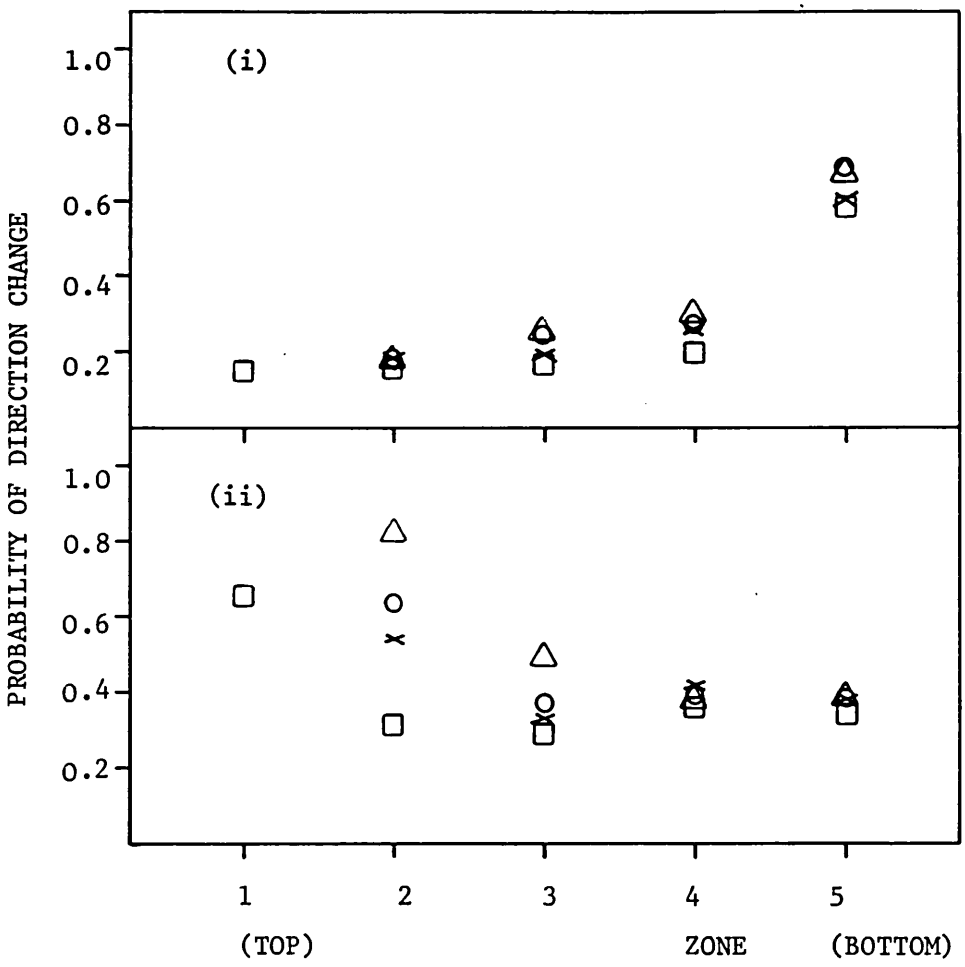


Figure 6.6 Variation of probability of direction change at zone with stirrer speed, for 2–bladed paddle, for 10 minutes

(i) Probability of turning up when coming down
(ii) Probability of turning down when coming up

□ 150 rpm ×200 rpm
○ 250 rpm △300 rpm

have a similar although much reduced stirrer speed effect and as expected is at its highest for the bottom zone (5) If these values of probability of direction change in each zone were to be used to predict a flow pattern, the emerging one would consist of fluid going up by the wall and coming down by the shaft, with some degree of by–passing before fluid would reach the liquid surface and also some degree of recirculation in each zone, which is in agreement with the earlier qualitative view of streak photography. However, we have now quantified to some extent the dynamics of the by–pass and local recirculation flows.

(c) Laser Doppler Anemometry

The components of velocity measured were the vertical and the y–component of velocity, the latter being identical to the tangential velocity since the measuring volume was always positioned on a diameter. The other component of velocity in the XY spatial plane is the radial velocity, which was not measured in this work.

The positions where the LDA measurements were made form a vertical grid along a diameter of the reactor, coincident with the x–axis, as shown in Figure 6.7. The origin of the vertical coordinate was chosen to be at the top edge of the agitator blade.

The experiments were carried out at 300 and 400 rpm and the results for the tangential, v_t, and vertical, v_z, velocities together with the associated values for turbulence intensity, I_R, are presented on Figures 6.8 to 6.11, respectively. Each point corresponds to an average of 2–3 measurements and the error bars refer to minimum and maximum values. The deep intrusion of the vortex prevented obtaining a complete velocity profile at the top region of the reactor.

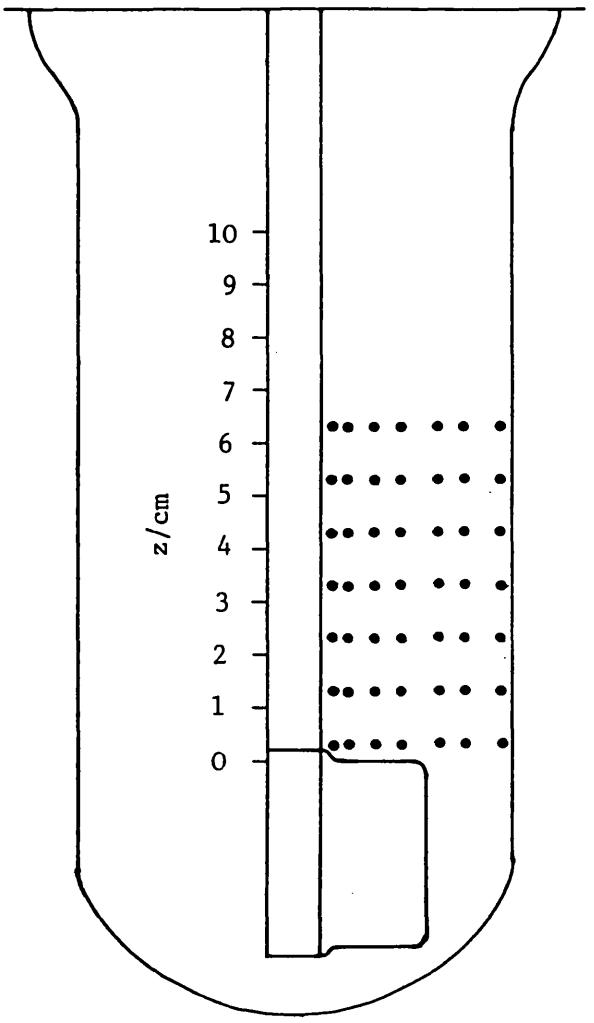


Figure 6.7 Measuring positions for LDA for 2–bladed paddle at the bottom of the reactor.

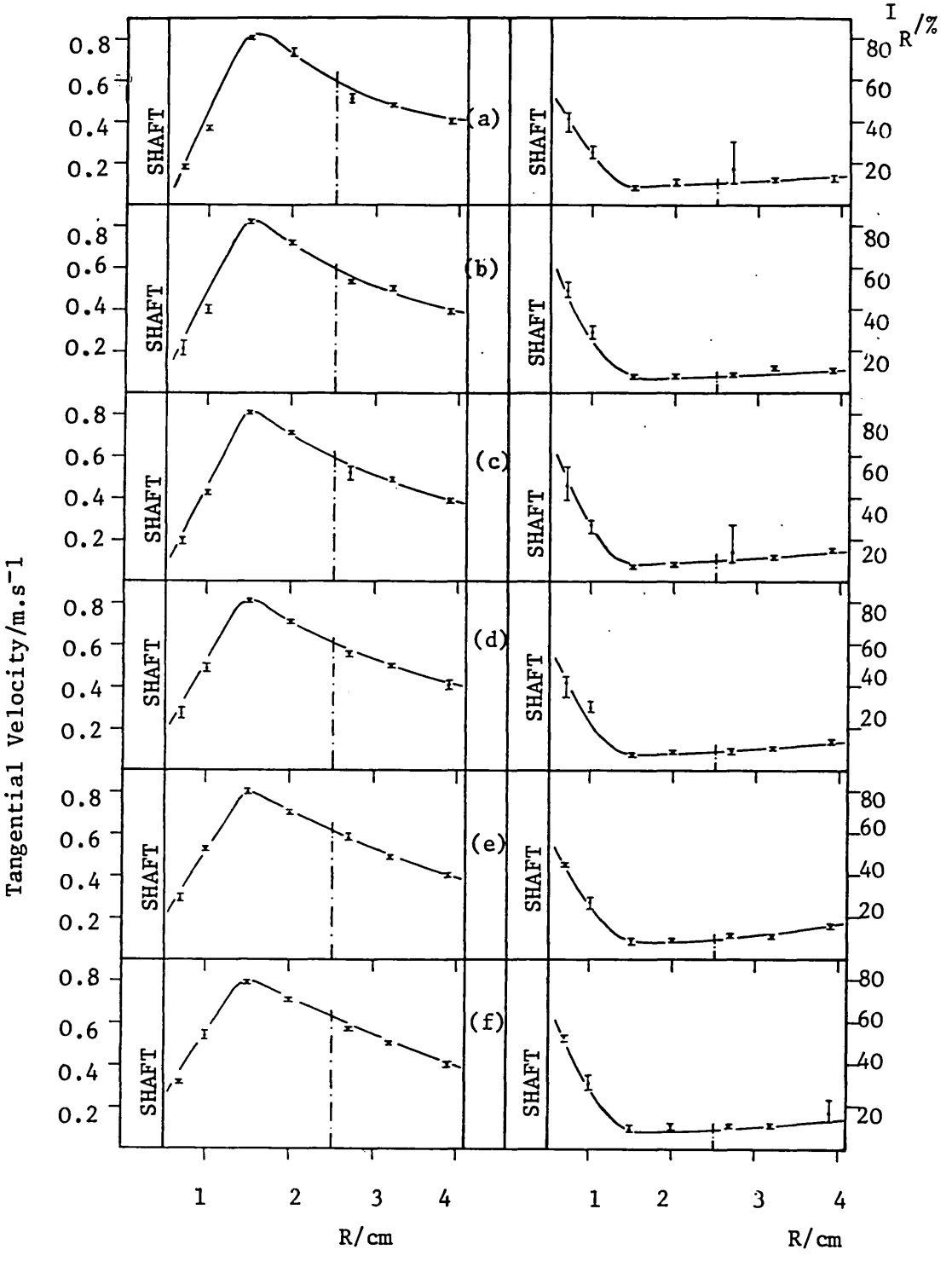


Figure 6.8 Tangential velocity profiles for 2–bladed paddle at the bottom of the reactor, at 300 rpm

(a) z = 6.3 cm (b) z = 4.3 cm
(c) z = 3.3 cm (d) z = 2.3 cm
(e) z = 1.3 cm (e) z = 0.3 cm

— • — • — Agitator tip position

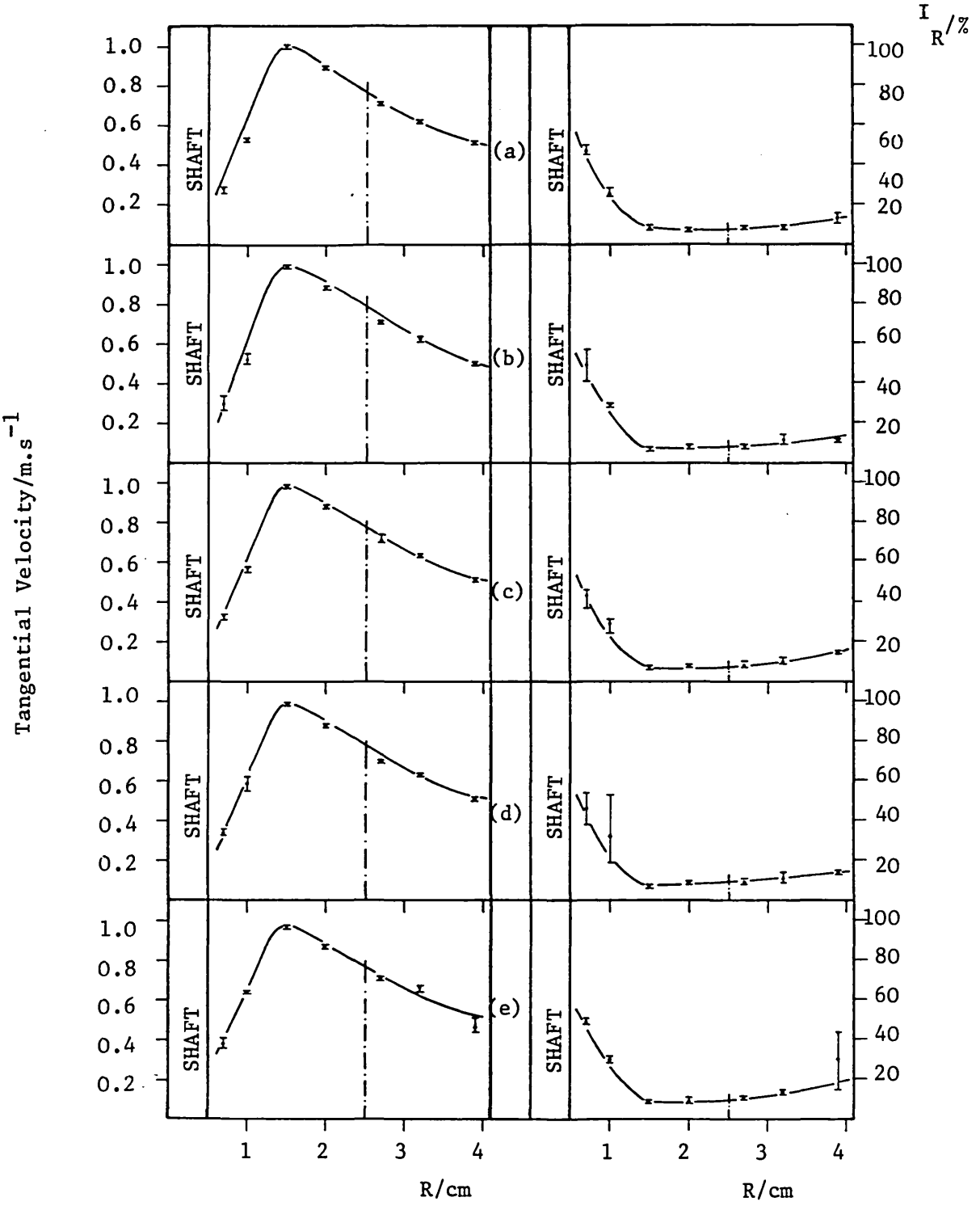


Figure 6.9 Tangential velocity profiles for 2–bladed paddle at the bottom of the reactor, at 400 rpm.

(a) z = 4.3 cm (b) z = 3.3 cm
(c) z = 2.3 cm (d) z = 1.3 cm
(e) z = 0.3 cm

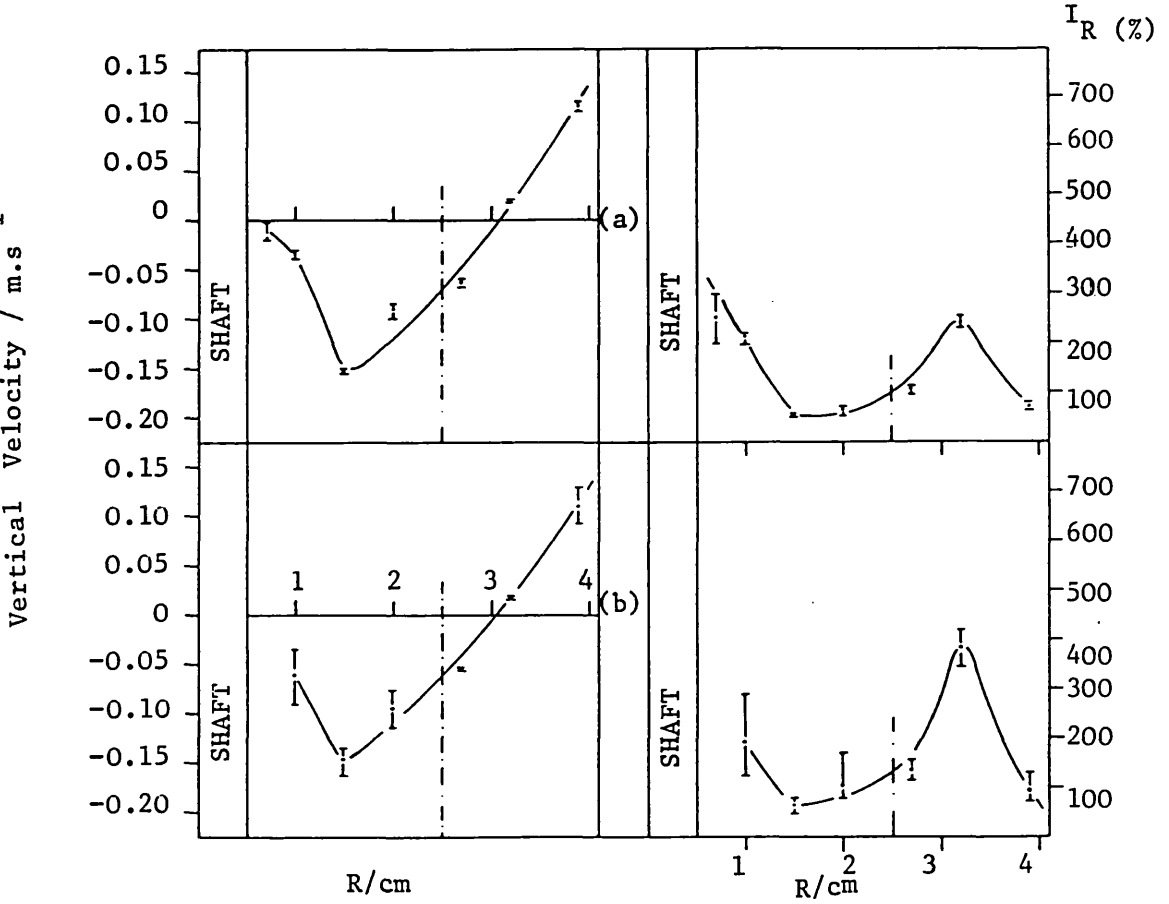


Figure 6.10 Vertical velocity profiles for 2–bladed paddle at 300 rpm

(a) z = 3.3 cm (b) z = 0.2 cm

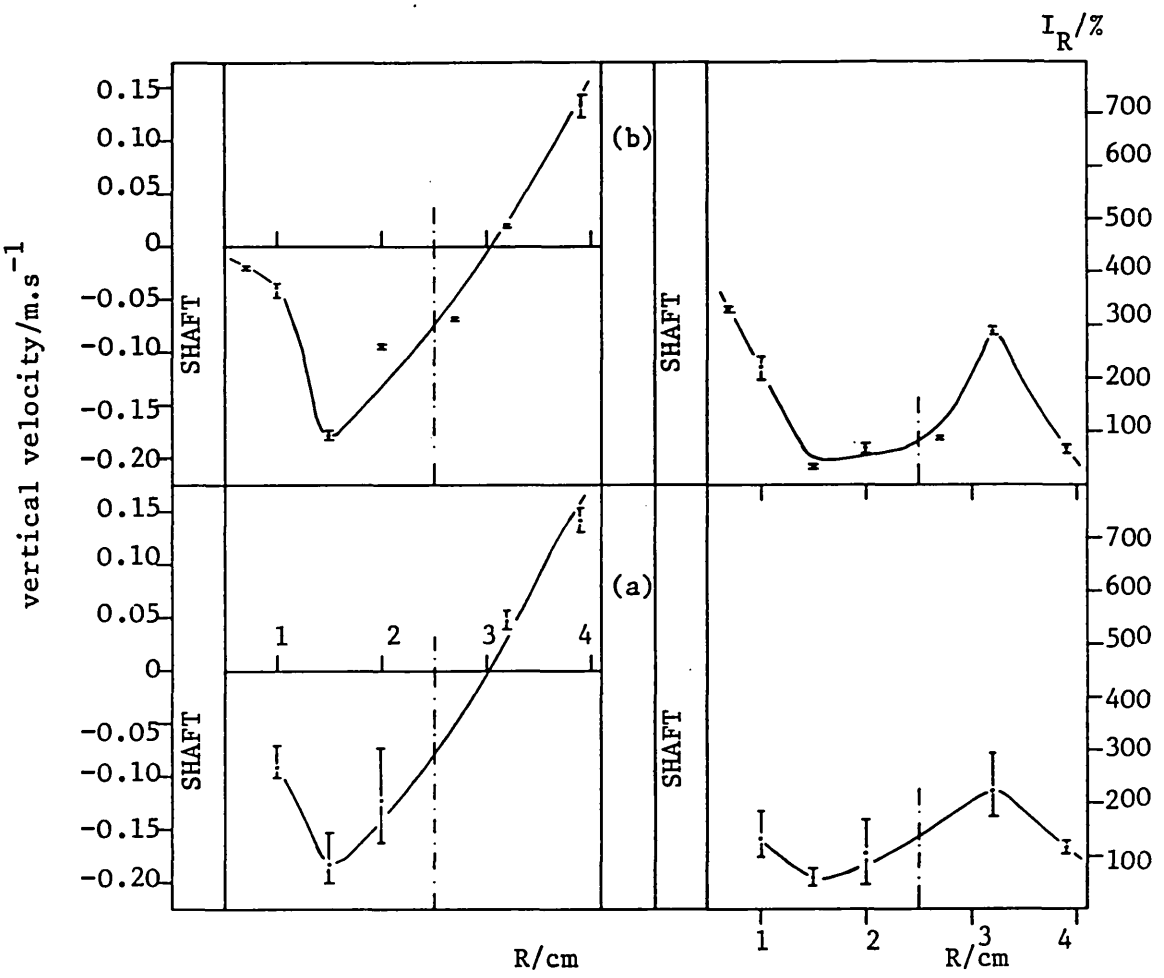


Figure 6.11 Vertical velocity profiles for 2–bladed paddle at 400 rpm.

(a) z = 0.2 cm (b) z = 3.3 cm

The tangential velocity profiles at 300 rpm, Figure 6.8, show the increase of this velocity component as distance from the shaft increases, peaking at around R = 1.5 cm, before the agitator tip (R = 2.5 cm), then gradually decreasing towards the wall of the reactor. There is no difference in the shape of the velocity profiles at the various heights in the reactor, even between just above the paddle and the top of the reactor. Velocity at paddle tip (R = 2.5 cm) is constant at all vertical distances: v_t = 0.59 – 0.60 $m.s^{-1}$. When the stirrer speed is increased to 400 rpm the tangential velocity profiles obtained, Figure 6.9, show very similar features to the ones at 300 rpm, the difference lying in the increased values of velocity. The value of velocity at agitator tip is now 0.75–0.77 $m.s^{-1}$, for all heights in the reactor, which means that tangential velocity at the agitator tip scales with stirrer speed.

The spread of velocities denoted by the turbulence intensity, I_R, is higher (40–60%) closer to the shaft, gradually decreasing and staying between 10 and 20% until the wall. This pattern remains unchanged with stirrer speed and vertical height in the reactor.

If a scale–up calculation based on tip speed is performed on the experimental results at 300 rpm, to find what would be the scaled–up values at 400 rpm, then these calculated velocity profiles are found to agree closely with the experimental ones for the whole of the vessel, within the experimental errors involved.

Regarding the velocity profiles for vertical velocity they were only performed for a more limited number of vertical positions in the reactor: one very close to the agitator blade (z = 0.2 cm) and about halfway towards the surface (z = 3.3 cm), as shown in Figure 6.7. The profiles presented in Figure 6.10, at 300 rpm, show downwards flow near the shaft, peaking at

R = 1.5 cm, reversing its direction at R = 3.0 cm and then upwards flow until the wall. Vertical velocities are about one tenth of the tangential velocities. There is no qualitative or quantitative difference when going higher in the reactor. Increasing stirrer speed to 400 rpm, the vertical velocity profiles obtained, Figure 6.11, show very similar characteristics to the ones at the lower stirrer speed: peaking in velocity and flow reversal are both at the same respective radial distances; only absolute values of velocity increase. Vertical velocity at the tip of the paddle is downwards being -0.065 ± 0.005 m.s^{-1} and -0.083 ± 0.005 m.s^{-1} at 300 and 400 rpm, respectively. Again, if a scale–up calculation is performed for vertical velocity, the profiles at both heights seem to scale–up on tip speed, within the experimental error.

The spread of velocity, I_R, is high (200–400%) near the shaft, decreasing to a value of about 50% towards the middle of the reactor, and then peaking (200–400%) near the radial distance where flow reversal occurs. This trend is constant for the two heights and the two stirrer speeds.

It is interesting to note that peaking occurs for the same radial distance for both the tangential and vertical velocities, halfway along the agitator radius, and that flow reversal occurs at R = 3.0 cm, radially outwards from the agitator tip. These observations allow a clear three–dimensional picture of flow to emerge, consisting of a central core of liquid where there is not much direct downwards flow, most of the fluid going round in a slow swirling motion, near the shaft; a rapid helix–spiralling motion down through the reactor, at the radial distance where the maxima coincide; and considerable upwards flow combined with swirling motion, from the flow reversal position outwards until the wall of the reactor. The spiralling motion which arises from these quantitative velocity measurements of

LDA had already been visually detected during the video monitoring experiments, when the flow follower was seen to come down in a helical movement, at about the same radial distance. The fact that flow reversal is combined with high values of turbulence intensity indicates a region of high shear and extension rates, where droplet elongation or even break–up might occur.

These quantitative results for velocity confirm the previous view by streak photography in which no qualitative. difference in vertical flow patterns was found as a function of stirrer speed over this range.

These vertical velocity profiles may be used to calculate the circulation time, t_c, defined in section 6.1 (see page 152) as the time for a polymerising droplet which originates in the high turbulent region near the agitator to return to this zone after an excursion into the more quiescent upper zones. Depending upon the path followed by each droplet, a whole distribution of circulation time values can be derived and in this work three circulation times were calculated:

(1) $t_{minimum}$, where the droplet/particle goes down at the maximum downwards velocity and comes up near the wall, at R = 3.9 cm;

(2) $t_{average}$, where the droplet/particle goes down at R = 1.3 cm and goes up at R = 3.5 cm (typical middle radial distances of the upwards and downwards sections of the reactor); and

(3) $t_{maximum}$, where the droplet/particle goes up at a radial distance 1.0 mm after flow reversal and comes down close to the shaft, at R = 0.7 cm.

The upwards path starts at the middle height of the reactor and ends at the lower vertical coordinate of the vortex (this was estimated as 2 mm above the highest complete radial scan possible, which was 6.3 and 4.3 cm at 300 and 400 rpm, respectively). The velocity was assumed constant within each section and the half distance of the two vertical scans was taken as the partition line between the two vertical sections.

The circulation times obtained for the simple geometry are presented in Table 6.2.

Table 6.2 Circulation time distribution for simple geometry

RPM	t_{min}/s	t_{av}/s	t_{max}/s	t_{max}/t_{min}
300	1.3	2.2	11.4	8.8
400	0.8	1.3	5.8	7.3

The various t_c averages show that increasing the stirrer speed reduced considerably the circulation time in the reactor, for all paths considered. The average t_c, is close to t_{min}, whereas t_{max} reflects the time taken for a long complete circulation loop in the reactor.

The results presented in Figures 6.8 to 6.11 refer to average velocities over 360° of blade revolution. Additional experiments were performed to see if any differences would be picked up as the agitator blade approaches or leaves the measuring volume. For this purpose a shaft encoder was used which only allows data collected from the photomultiplier to be correlated when the agitator blade is at specific, pre–determined positions relative to the measuring volume. The measuring positions were located on a radial coordinate, between the edge of agitator blade and the wall, as shown in Figure 6.12. The glass curvature at the bottom of the vessel prevented any

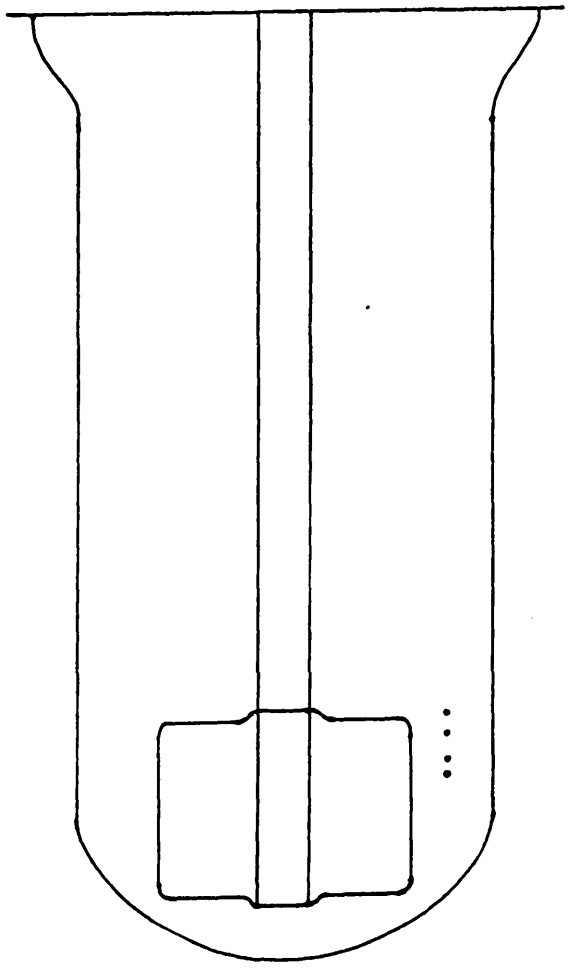


Figure 6.12 LDA Measuring positions with shaft encoder

measurements with a vertical coordinate lower than –1.1 cm. The shaft encoder was adjusted to allow data correlation at various angular positions before and after the cross over i.e. at different time delays before and after the stirrer passes through the azimuth of the measuring volume. When the shaft encoder was used, the experiment duration had to be increased considerably, since data correlation only occurs for a small proportion of each revolution. The results of the experiments with the shaft encoder are presented in Figure 6.13 for the tangential velocity, v_t, at a radial distance of R = 3.2 cm and a speed of 400 rpm. Measurements were taken at a variety of angular positions, but in Figure 6.13 are shown the two extreme cases where a difference might be expected to appear i.e. when stirrer blade is at 0° or 90° to the measuring volume, to compare with results without shaft encoder, for a full revolution of the paddle. Several repeat runs were performed and the errors are presented as two standard deviations (equivalent to 95% confidence limits). As no evidence of any correlation between blade position and velocity was found, these kind of measurements using the shaft encoder were not pursued further. The conclusion that can be taken from these measurements is that the 360° average represents the time invariant average and that fluid moves in a plug–like manner between the agitator blade and the wall.

This paddle geometry was used for a series of additional measurements to check the LDA system by examining the vertical symmetry of the flow when the paddle was positioned midway along the stirring shaft. Both the tangential and vertical velocity were determined at 200 rpm for a grid of positions across a diameter in the vessel: Figure 6.14. The origin of the vertical coordinate is taken as the middle of the paddle. The results for tangential and vertical velocity, on a horizontal and vertical slice are presented in Figures 6.15 to 6.18, respectively. Figure 6.15 shows that tangential

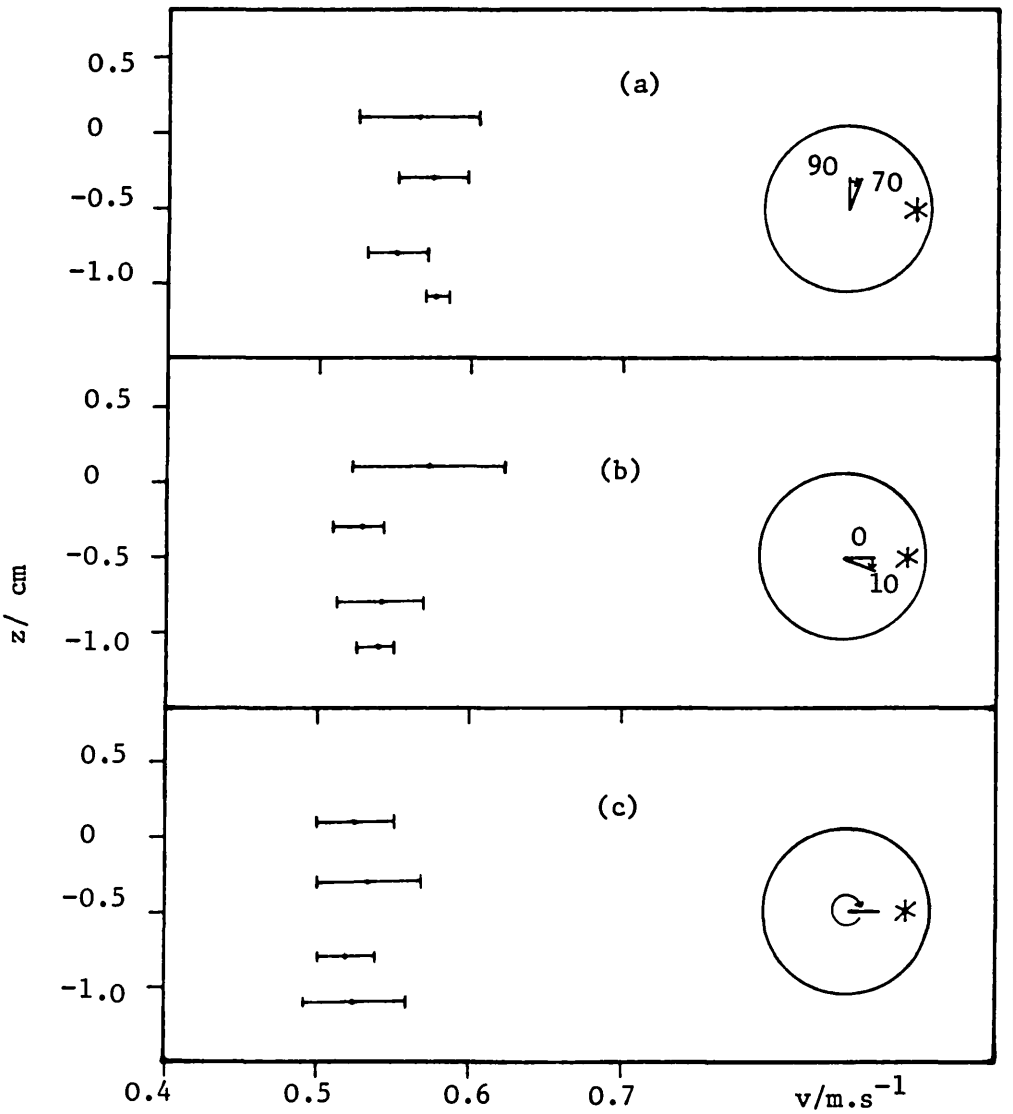


Figure 6.13 Tangential velocity measurements with and without shaft encoder, at R = 3.2 cm and 400 rpm, for the 2–bladed paddle geometry

* measuring position
(a) 10 ° sweep at 90 ° to cross–over
(b) 10 ° sweep at 0 ° to cross–over
(c) without shaft encoder

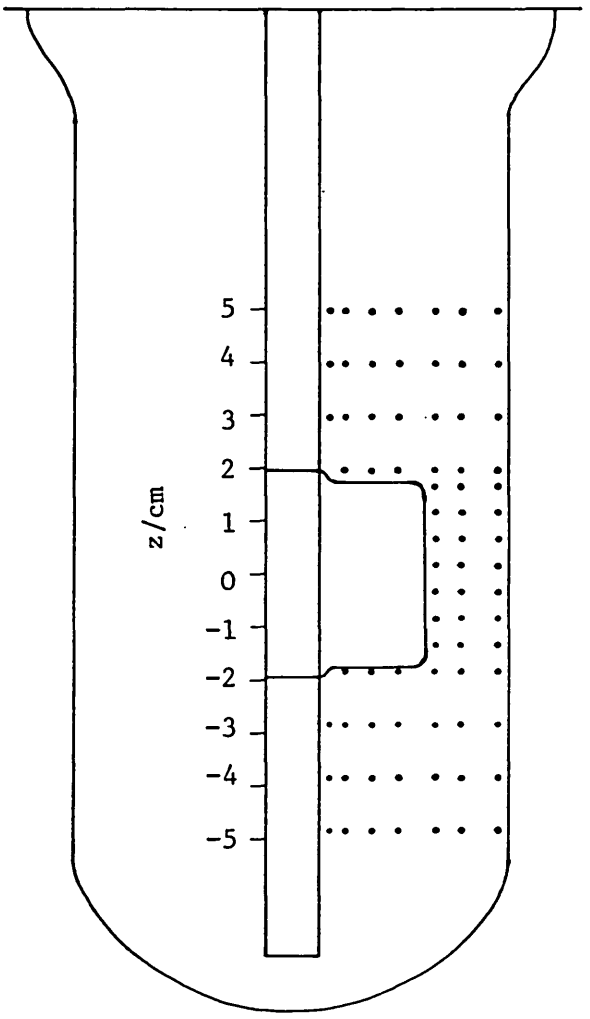


Figure 6.14 Measuring positions for 2–bladed paddle in the middle of the reactor

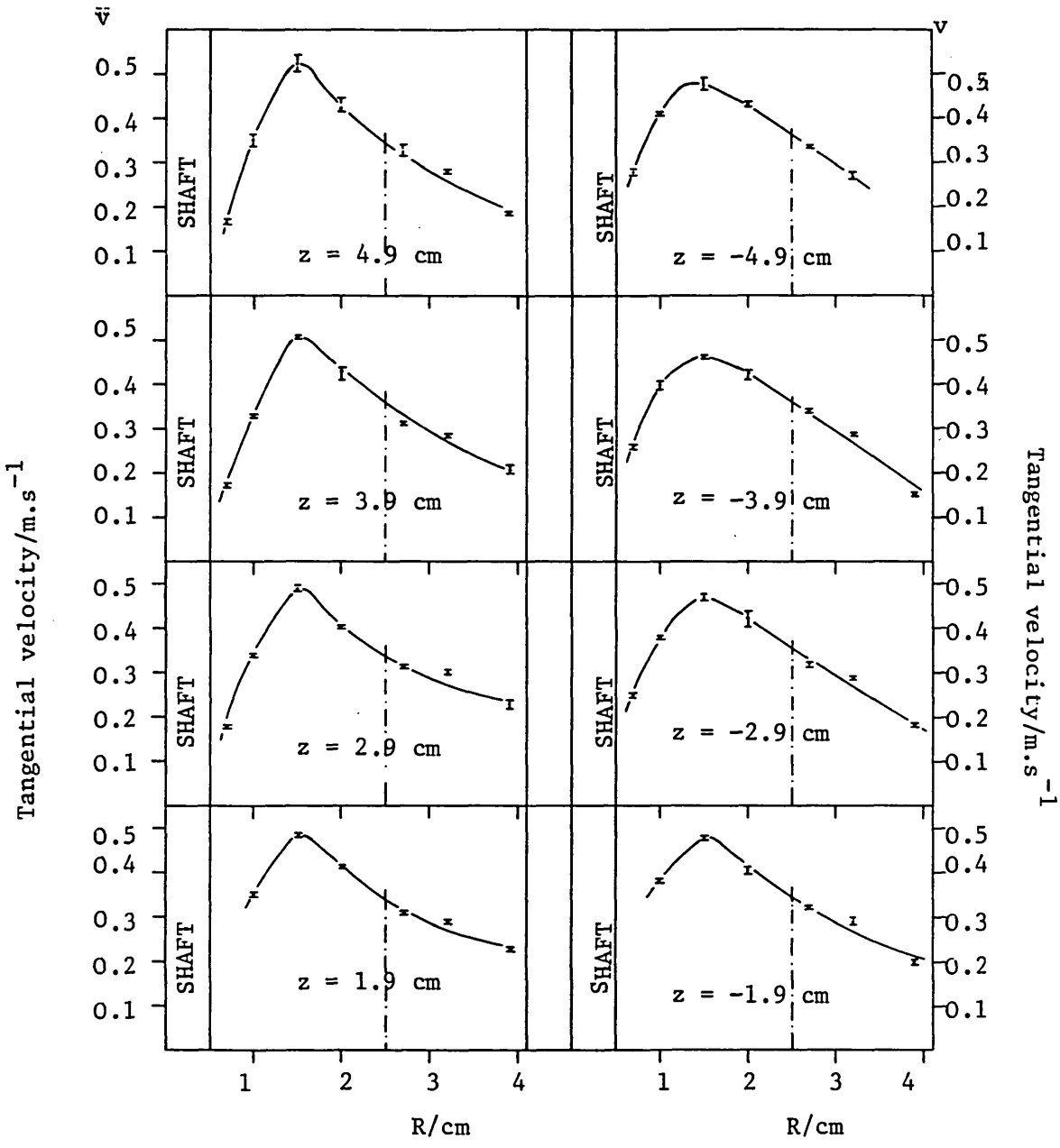


Figure 6.15 Tangential velocity profiles for 2–bladed paddle in the middle of the reactor at 200 rpm.

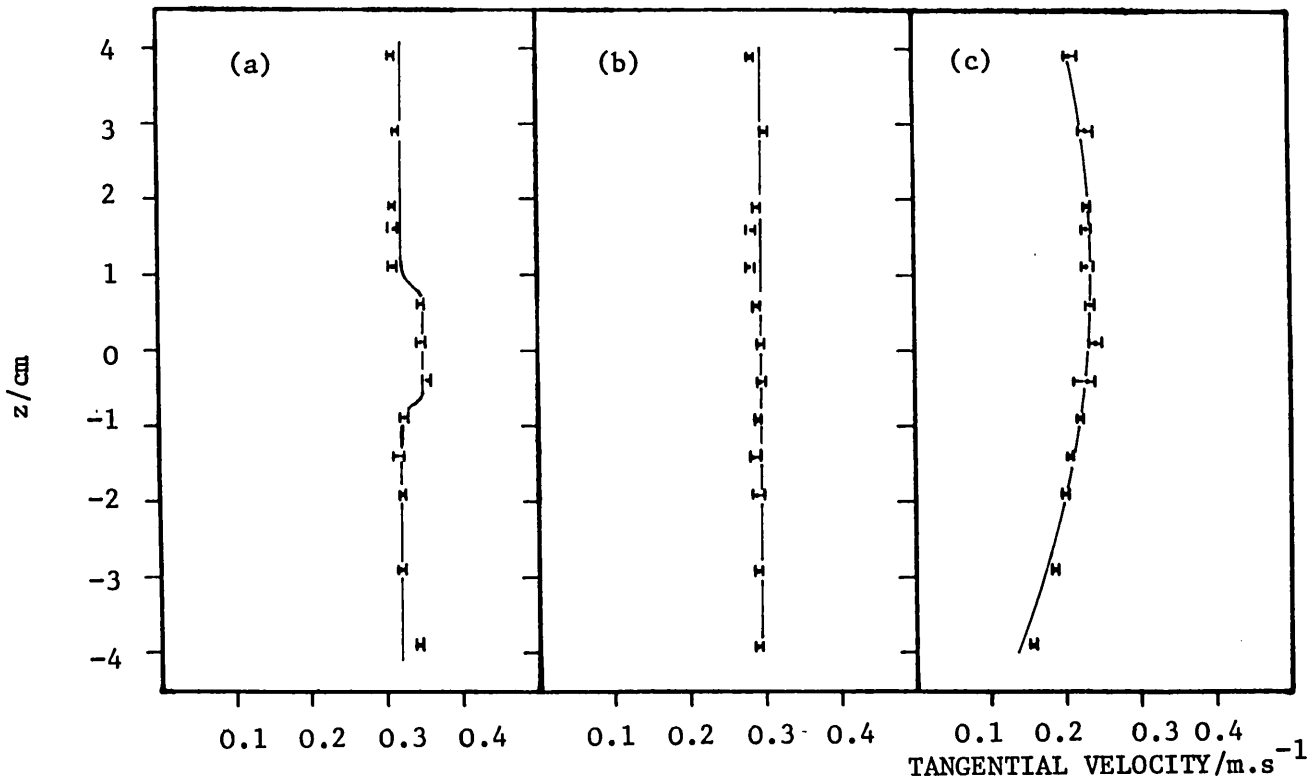


Figure 6.16 Tangential velocity profiles for 2–bladed paddle in the middle of the reactor, at 200 rpm, for various radial positions.

(a) R = 2.7 cm (b) R = 3.2 cm (c) R = 3.9 cm

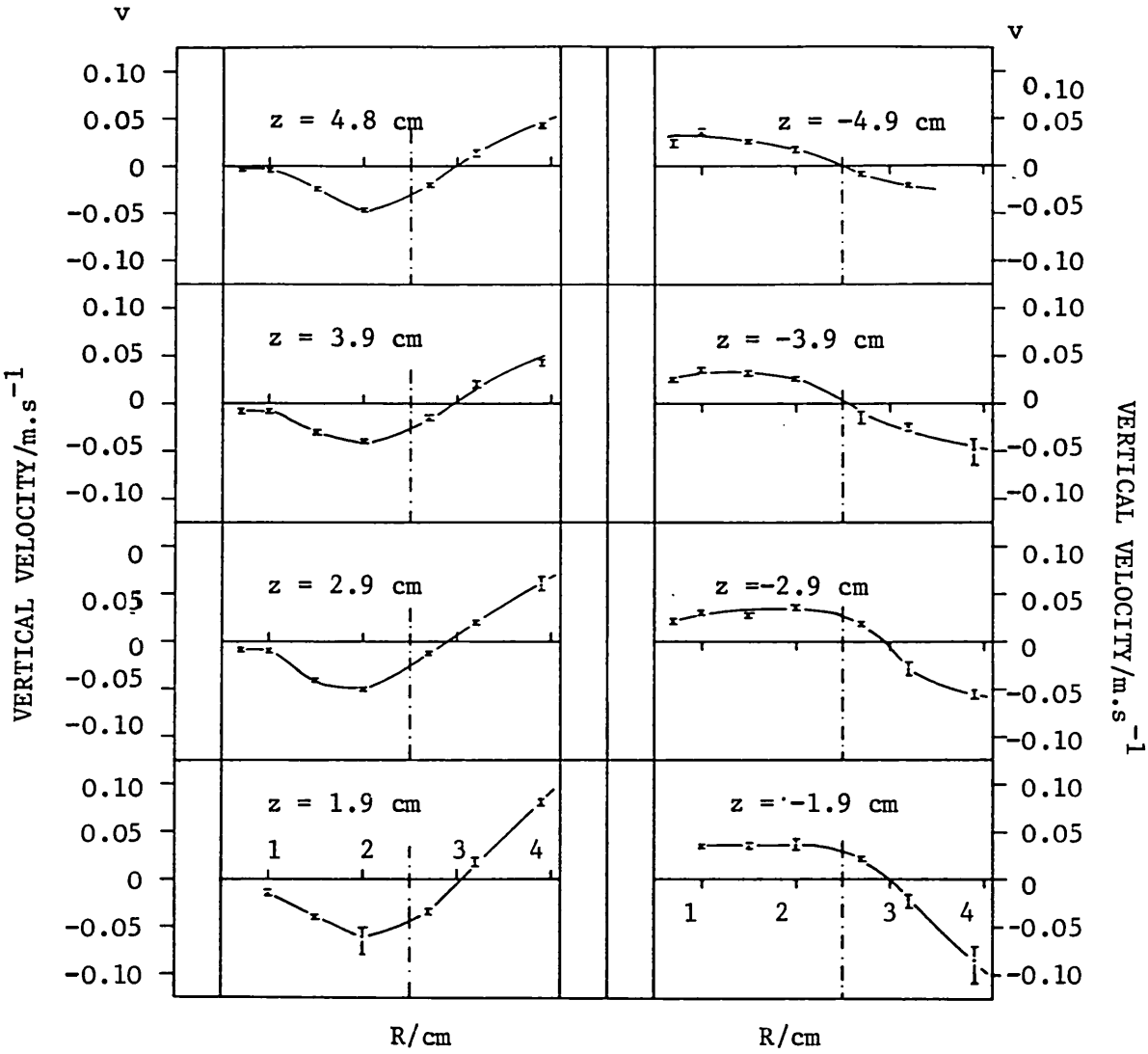


Figure 6.17 Vertical velocity profiles for 2-bladed paddle in the middle of the reactor at 200 rpm.

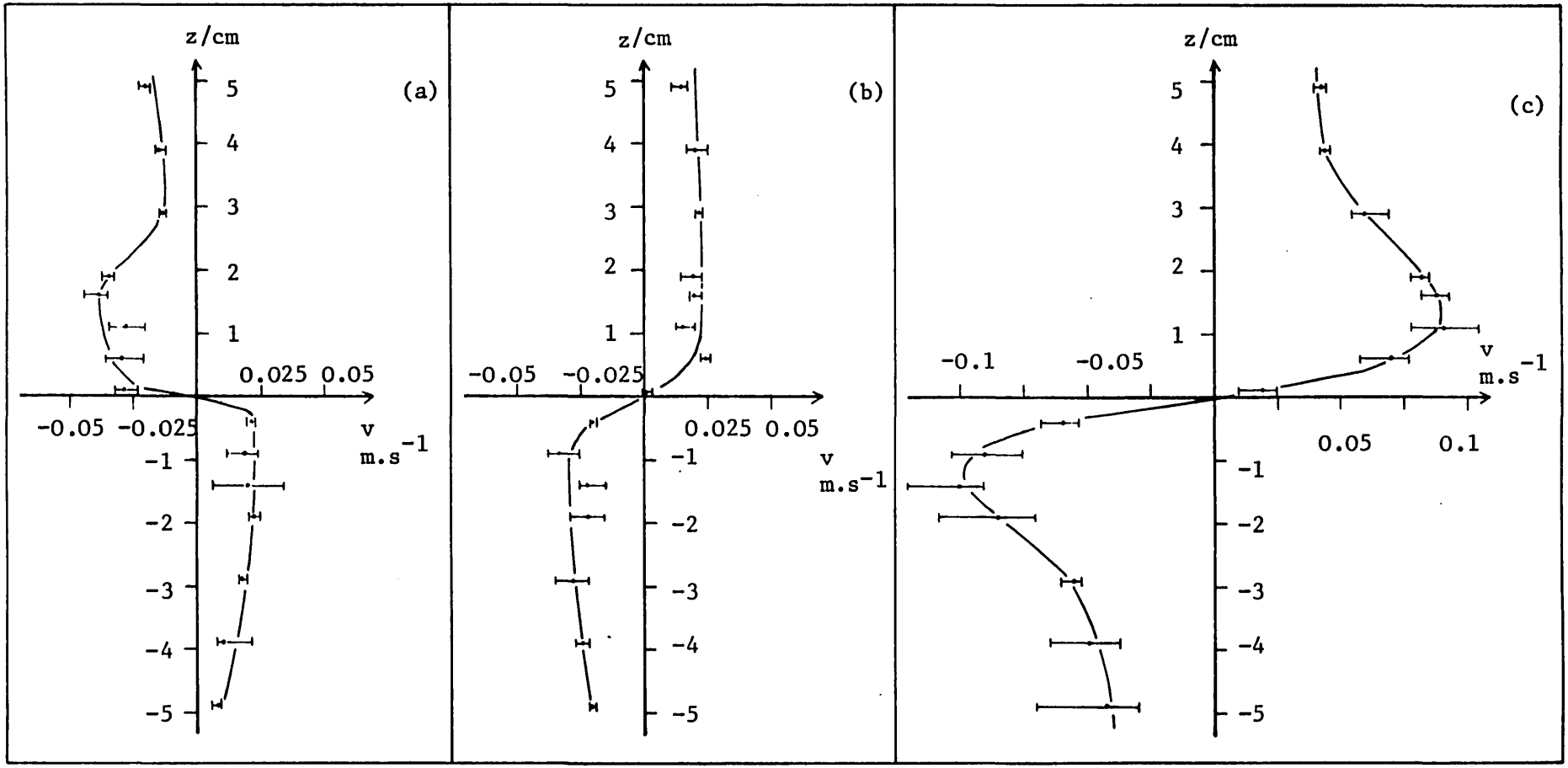


Figure 6.18 Vertical velocity profiles for 2–bladed paddle in the middle of the reactor, at 200 rpm, for various radial positions.

(a) R = 2.7 cm (b) R = 3.2 cm (c) R = 3.9 cm

velocity profiles above the paddle exhibit slightly sharper and larger peaks than the corresponding ones below the paddle. This could be due to surface influence (vortex) and bottom curvature of reactor. Peaking in velocity is always around R = 1.5 cm and tangential velocity at the agitator tip seems fairly constant at all heights, perhaps with a slight increase on moving vertically away from the paddle. These tangential velocity profiles scale with the previous results for the corresponding profiles with the paddle at the bottom of the reactor, at 300 and 400 rpm, with peak velocity close to the tip speed (V_{tip} = 0.523 $m.s^{-1}$) at this stirrer speed (200 rpm).

The measurements done on vertical slices of the reactor at various radial locations, Figure 6.16, show that at R = 2.7 cm tangential velocity is at maximum at the middle region of paddle height, suggesting that close to blade edge fluid movement is mostly like a plug of fluid going round the reactor, the maximum reflecting the agitator's influence due to its pumping power. On moving towards the wall, at R = 3.2 cm, the influence of the agitator dies out and fluid motion is plug like, revealed by the very flat profile found at this radial distance. As wall is approached, R = 3.9 cm, fluid is still moving in a plug–like motion, but wall drag, bottom curvature and surface influence yield a slight curvature for this tangential velocity profile. On the basis of these tangential velocity profiles one can say that vertical symmetry holds in the reactor.

Regarding vertical velocity profiles in the radial direction, Figure 6.17, downwards velocity above the paddle shows a peak occurring at R = 2.0 cm, with flow reversal at R = 3.0 cm; while below the paddle there is no peak in v_z, and flow reversal is observed at R = 2.5 cm, in the lowest heights of the reactor, whereas it happens at R = 3.0 cm higher up in the reactor. The vertical slices cut done for this component of velocity, v_z, Figure 6.18, show

the expected trend: flow reversal is around R = 3.0 cm, the flattest of the observed profiles happens at R = 3.2 cm, as with tangential velocity, and more pronounced variations with vertical height are seen closer to blade and wall. From this evidence it can be concluded that there is considerable asymmetry in vertical velocities in contrast with the earlier evidence of vertical symmetry on the basis of tangential velocity.

The picture of flow that emerges from these results is one where close to shaft there is little vertical movement either below or above the paddle and fluid is going round the reactor in a mainly swirling motion. At R = 1.5–2.0 cm there is some spiralling motion down the reactor, above the paddle, while this might not be present, or in lesser extent, below the paddle. As radial distance increases, fluid movement is mostly plug–like, especially for the middle distance between agitator edge and wall, with upwards movement close to wall for positive vertical heights and downwards movement for negative vertical heights.

6.2.2 Suspension Polymerisation Experiments

(a) Choice of polymerisation recipe

The first suspension polymerisation experiments carried out for the simple geometry were devised to get experience running the equipment and to test the response of the system to experimental parameters. Initiator concentration, [I], and stirrer speed, N_s, were varied before a more systematic study of variation of suspending agent concentration started, in order to choose the best value of suspending agent concentration for observing the effects of agitation conditions.

The suspending agent chosen was polyvinyl alcohol supplied by BDH chemicals, MW = 125,000, which yielded polymer having the desired size characteristics ($\bar{d} < 1000$ μm). In Table 6.3 the conditions under which these first polymerisations were carried out are presented. Unless otherwise stated stirrer speed was 400 rpm, the initiator concentration was 10 $g.l^{-1}$ (based on dispersed phase volume) and based on values published in the literature [5], the suspending agent was polyvinyl alcohol (BDH chemicals, MW = 125,000). Its concentration was based on continuous phase volume, the phase volume of styrene was 0.25, chosen not to have very concentrated dispersion, based on a recipe suggested by Reichert [2].

Table 6.3 Experimental conditions for polymers 1–12, using the 2–bladed paddle

POLYMER	[PVA] /$g.l^{-1}$	Comments
1	2.5	
2	2.5	Initiator concentration = 5 $g.l^{-1}$
3	2.5	Stirrer speed = 300 rpm
4	1.875	
5	1.25	
6	0.938	
7	0.625	
8	0.413	
9	0.313	
10	0.156	Stable particles, but $\bar{d} > 560$ μm
11	0.078	Stable particles but $\bar{d} > 560$ μm
12	0.0	Agglomeration occurred

Standard conditions : phase volume of styrene = 0.25 ;
initiator concentration = 10 $g.l^{-1}$; reactor 3/4 full.

The system was found to be stable for a low suspending agent concentration (0.078 $g.l^{-1}$), even though the polymer produced was out of the desired size range ($\bar{d} < 560$ μm) a constraint set by the range of the available particle size analyser (see page 135). The key role played by the presence of a suspending agent in maintaining a stable suspension was demonstrated by run 12 without any suspending agent. The results showed that a stable dispersion could not be maintained, with droplets sticking to the walls of the reactor after 30 minutes from the start of the reaction, and a major agglomeration occurring at about 3 hours. A dynamic equilibrium between coalescence and break–up maintained solely by agitation is therefore not a stable condition in this particular reacting system.

The effect of the variation of suspending agent concentration on the full particle size distribution and on their mean diameter (based on a volume distribution), $d_{50\%}$ is presented in Figures 6.19 and 6.20, respectively. The particle size distribution of polymers 9 to 11 is not shown, since they were too coarse to be used in the sizing instrument available (Malvern Particle Size Analyser), even for the 300 min focal lens (Sizing Range : 5.8 – 564.0 μm). Polymers 2 and 3 are not included since they deviate from the standard conditions but their particle size distribution is presented in Figure 6.21. From the size distributions shown in Figure 6.19 all, except polymer 1, have most of the particles in the upper size band : 262–564 μm, although the mean diameter of polymers 1 and 2 are not very different (Figure 6.20). On the basis of these results the suspending agent concentration chosen to carry out polymerisations at various stirrer speeds was 2.5 $g.l^{-1}$.

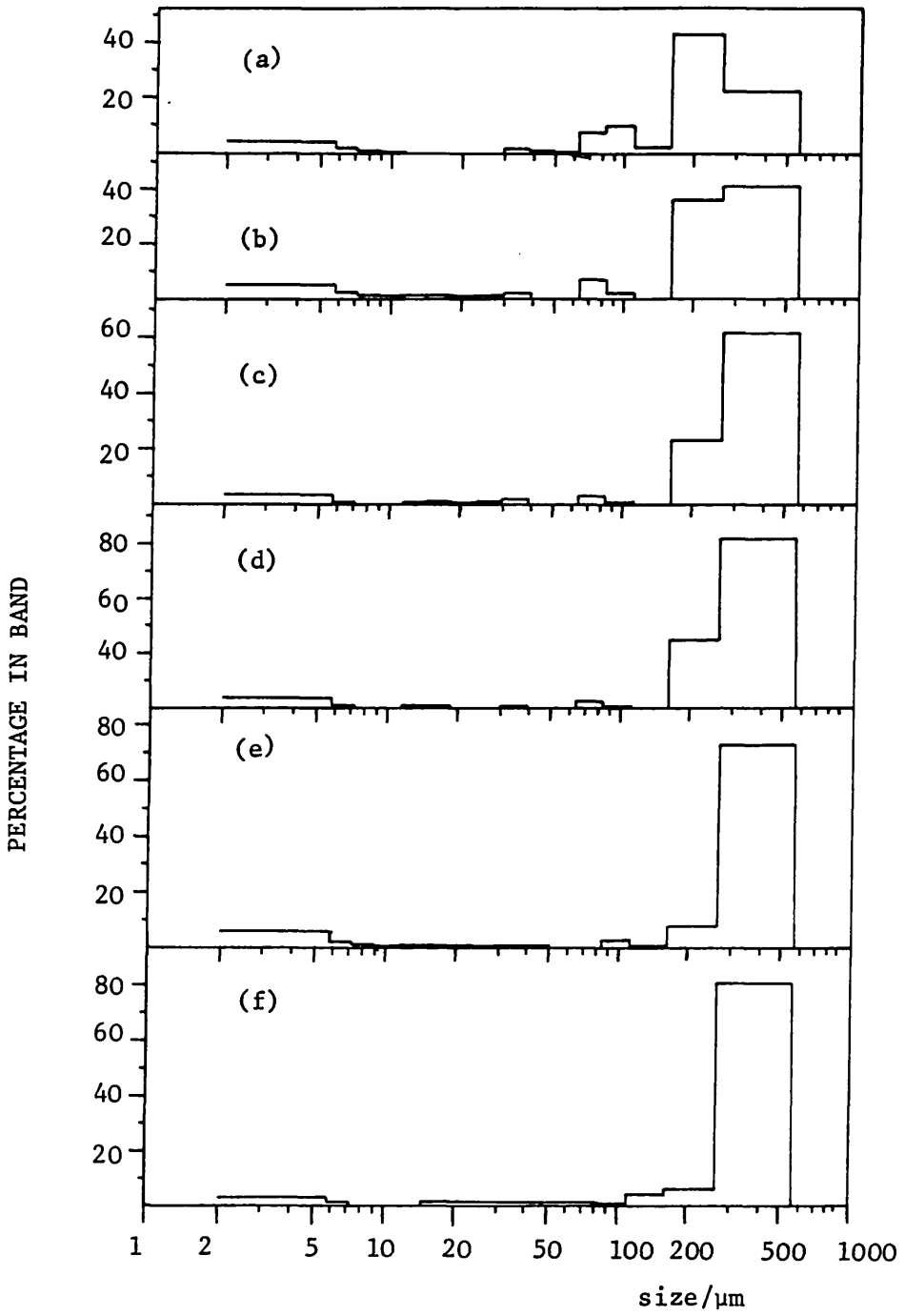


Figure 6.19 Effect of the variation of suspending agent concentration on the particle size distribution of polystyrene, at 400 rpm, for 2-bladed paddle geometry

(a) PS1 – 2.5 g.l^{-1} PVA (b) PS4 – 1.875 g.l^{-1} PVA
(c) PS5 – 1.25 g.l^{-1} PVA (d) PS6 – 0.938 g.l^{-1} PVA
(e) PS7 – 0.625 g.l^{-1} PVA (f) PS8 – 0.413 g.l^{-1} PVA

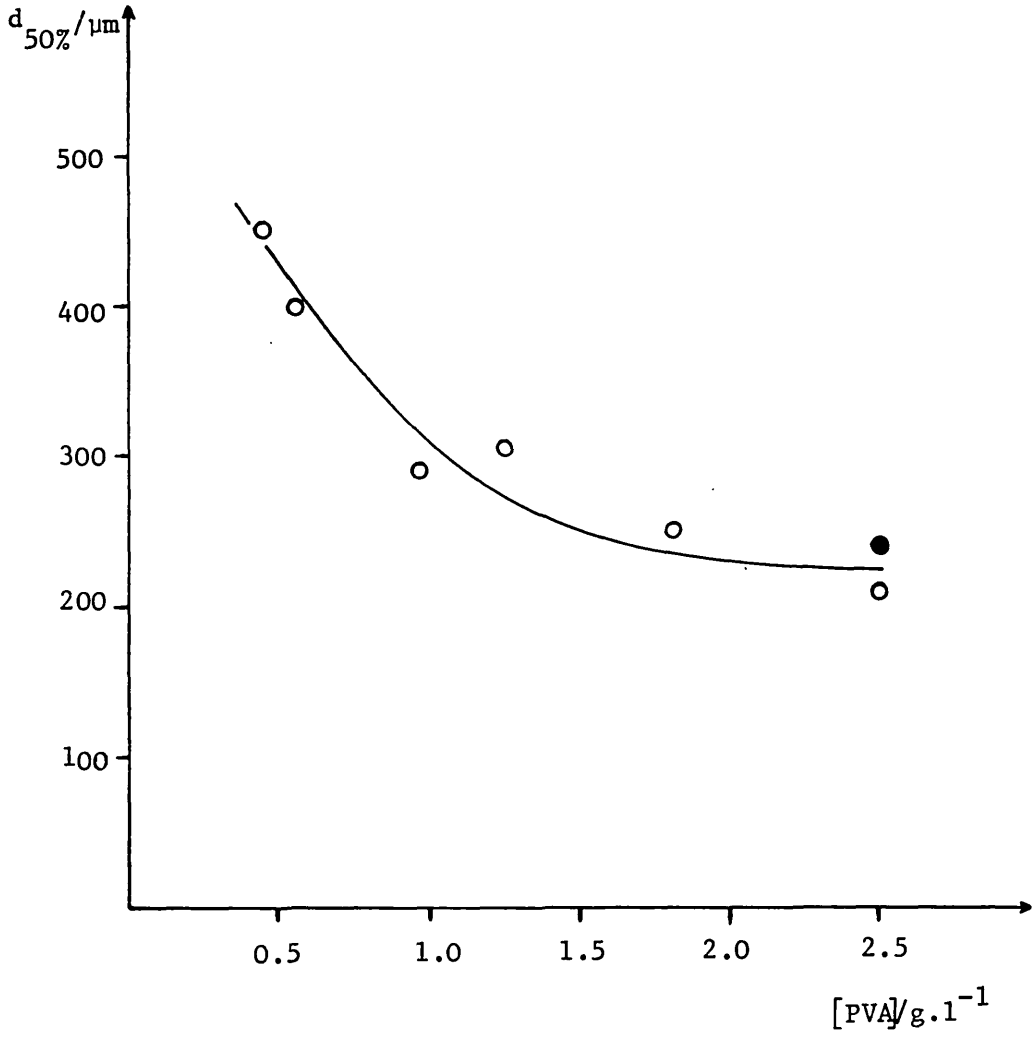


Figure 6.20 Effect of variation of [PVA] on 50% mean diameter for 2–bladed paddle at 400 rpm.

● Value corresponding to Polymer 2, whose [I] was one half of all others.

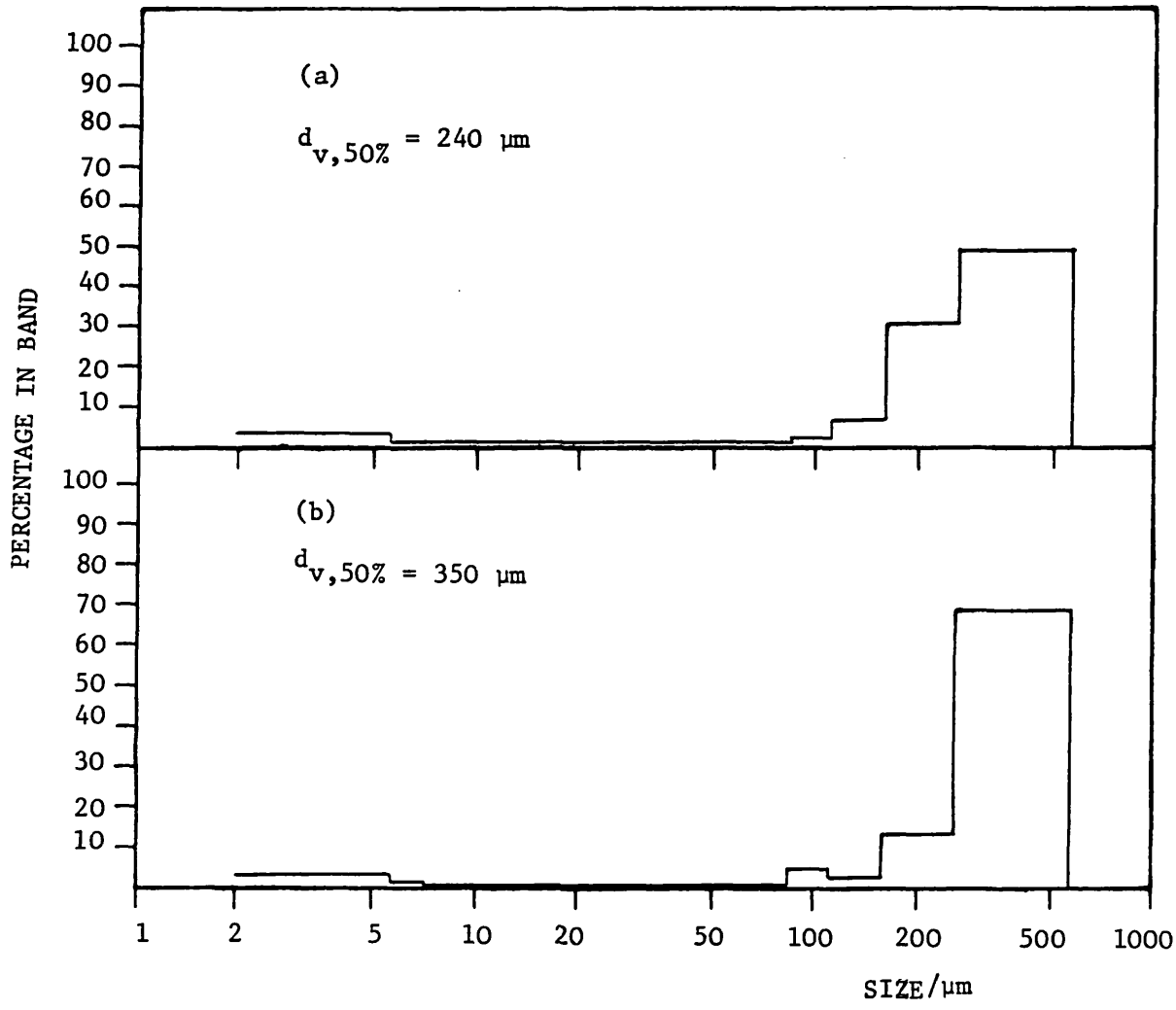


Figure 6.21 Particle size distribution of Polymer 2 and 3 in 2-bladed paddle geometry

(a) Polymer 2 – $[I] = [I]/_2$ of all other runs; 400 rpm; 2.5 $g.l^{-1}$ PVA

(b) Polymer 3 – Run done at 300 rpm ; 2.5 $g.l^{-1}$ PVA

Halving the initiator concentration, while maintaining all other conditions constant shifted both the particle size distribution and mean diameter of polymer 2 (Figure 6.21) compared to polymer 1 (Figures 6.19 and 6.20).

At this stage the temperature measuring device was changed from a bulky thermometer pocket to the less instrusive thermocouple wire as described in Chapter 4.

The suspending agent was changed from a BDH brand to a Gohsenol type which is more widely used in commercial suspension polymerisations. Trial experiments indicated that GH 23 was the best type of Gohsenol to be used, corresponding to a high molecular weight polyvinyl alcohol (48–56 cP for a 4% aqueous solution). No optimisation of concentration was done for GH 23, since it yielded a very similar polymer, in terms of particle size distribution, mean particle size, number and weight average molecular weight and polydispersity, as the BDH material under the same experimental conditions. Polymers 1 and 15 (see next sections) are those whose properties were compared. Also, it was desired to change stirrer speed and a well protected system was necessary at the higher speed range, to ensure the product was still stable and within the sizing conditions at smaller values of stirrer speed.

(b) Variation of stirrer speed

The next series of polymerisations involved changing the stirrer speed while keeping all the other experimental variables constant. The agitation conditions used are shown in Table 6.4.

Table 6.4 Variation of stirrer speed for 2–bladed paddle polymerisations

POLYMER	STIRRER SPEED/rpm
3	300
13	300
14	350
15	400
16	500

Experimental conditions: Phase volume of styrene = 0.25; Reactor 3/4 full; initiator concentration = 10 $g.l^{-1}$; suspending agent concentration = 2.5 $g.l^{-1}$; suspending agent = Gohsenol 23, except for Polymer 3, where it was BDH brand.

The polymers produced consisted of aggregates as it can be seen in Figure 6.22, for Polymer 3 (at 300 rpm). Under microscope observation (30 x magnification) the polymer product revealed clusters of individual translucent beads (2–4 beads per aggregate, typically) bound by some very fine ($\bar{d} < 5.8$ μm) whitish particles, besides single beads. These aggregates are quite loose, as they all disintegrate to individual beads, after 15 s treatment by ultrasound in the Malvern sample cell.



Figure 6.22 Photograph of polymer 3 showing the presence of aggregates

Scale in cm
Magnification 3.6:1

A typical temperature and pressure profile is shown in Figure 6.23. The reactor temperature profile shows a slight peak after about 3 hours, which coincides with the time when solid particles start to be seen inside the reactor. As the polymerisation reaction proceeds, the initial translucent and low viscosity monomer droplets evolve into more cloudy and viscous monomer–polymer droplets. When viscosity has reached a critical level, the onset of the gel effect within each polymerising droplet is likely to cause a sudden rise in droplet temperature, due to the increased polymerisation rate and poor heat dissipation. Also, local heat transfer problems due to sticking to the thermocouple wire could add to the gel effect and therefore the slight peak in temperature will be observed. Once all particles have become solid–like, a steady–state between heat generation in droplets and heat dissipation by the dispersing medium is achieved and temperature remains stable.

6.2.3 Polymer characterisation

(a) Particle Size Distribution

The size distribution presented for this geometry were obtained after a 15 s ultra–sound treatment in the Malvern sample cell, since the Malvern Particle Size Analyser was unable to produce a representative and reliable size distribution for the polymer aggregates as they came out of the reactor.

The effect of the variation of suspending agent concentration, [S], on the full particle size distribution and on the mean diameter has already been presented in the previous section (Figures 6.19 and 6.20).

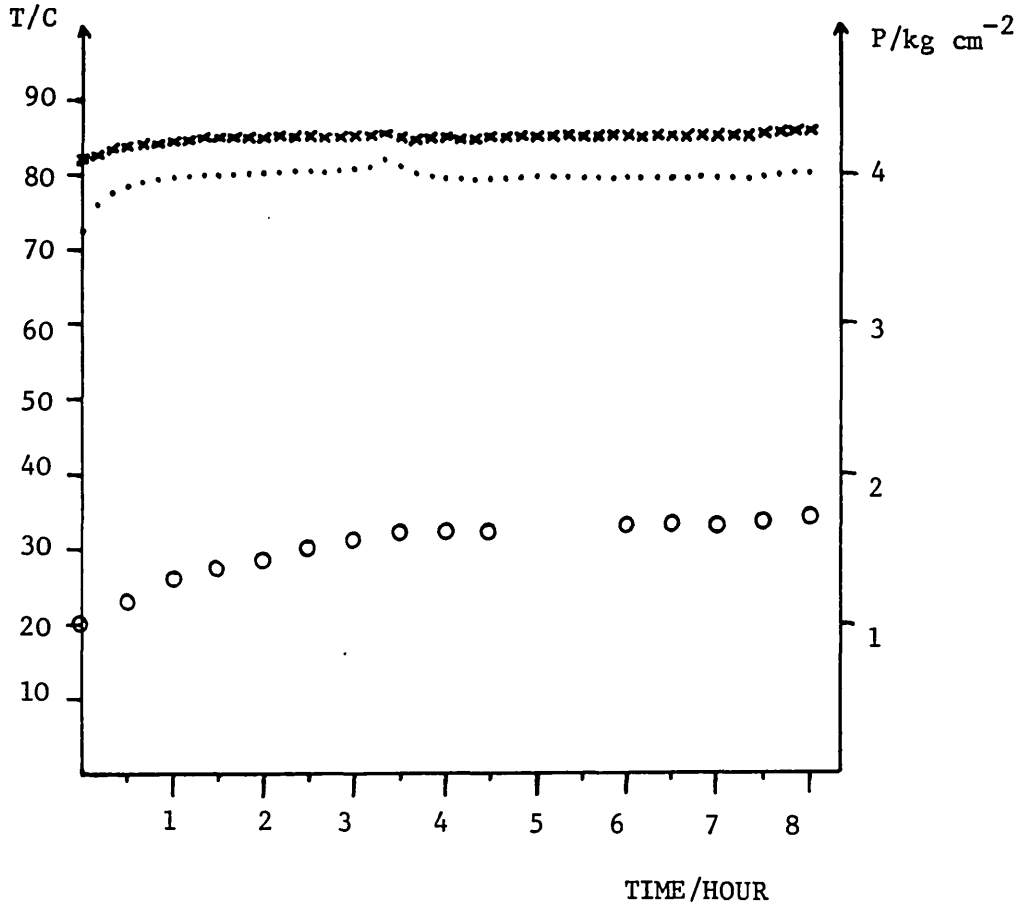


Figure 6.23 Temperature and pressure profiles during a typical polymerisation reaction

× bath temperature
● reactor temperature
○ pressure

The results refering to the variation of stirrer speed for fixed [S] can be seen in Figures 6.24 and 6.25, where the full particle size distribution and the $d_{50\%}$ and Sauter mean diameter are shown, respectively. The distributions obtained show a significant trend of decreasing mean particle size and shifting the full particle size distribution to smaller values with increasing stirrer speed. At 300 and 350 rpm the majority of particles lies within the higher size range: 564–262 μm, whereas it decreases to the next size band at 400 rpm (although there are still a fair number of bigger particles), and one step further down at 500 rpm. A second, secondary small peak seems to arise in all cases, at $d \simeq 100$ μm from 300–400 rpm and at $d \simeq 60$ μm for 500 rpm. A higher resolution size distribution (32 size range) can be used to reveal more clearly the bimodal structure of the particle size distribution – Figure 6.26, which shows the reduction of the average size of both the main and secondary peaks with stirrer speed. The amount of fine particles seems steady between 300–400 rpm at approximately 5%, with only a slight increase at 500 rpm (about 8%). These fine particles are the ones responsible for holding together the beads in the aggregates acting like a glue and could come from a certain degree of emulsion polymerisation in the continuous medium or could be due to physical aspects of flow, such as droplet break–up mode or high shear flow in particular areas in the reactor. The presence of these fine particles will be discussed in more details in the next section dealing with the 4–bladed paddle geometry (see page 254). The mean particle size, $d_{50\%}$, shows a smooth decreasing curve with the increase in stirrer speed, seeming to reach a plateau where a further increase in tangential and vertical velocity would not cause a steep decrease in mean particle size. The Sauter mean diameter is several orders of magnitude smaller than $d_{50\%}$, probably due to the presence of very fine particles, and does not seem to very much with stirrer speed.

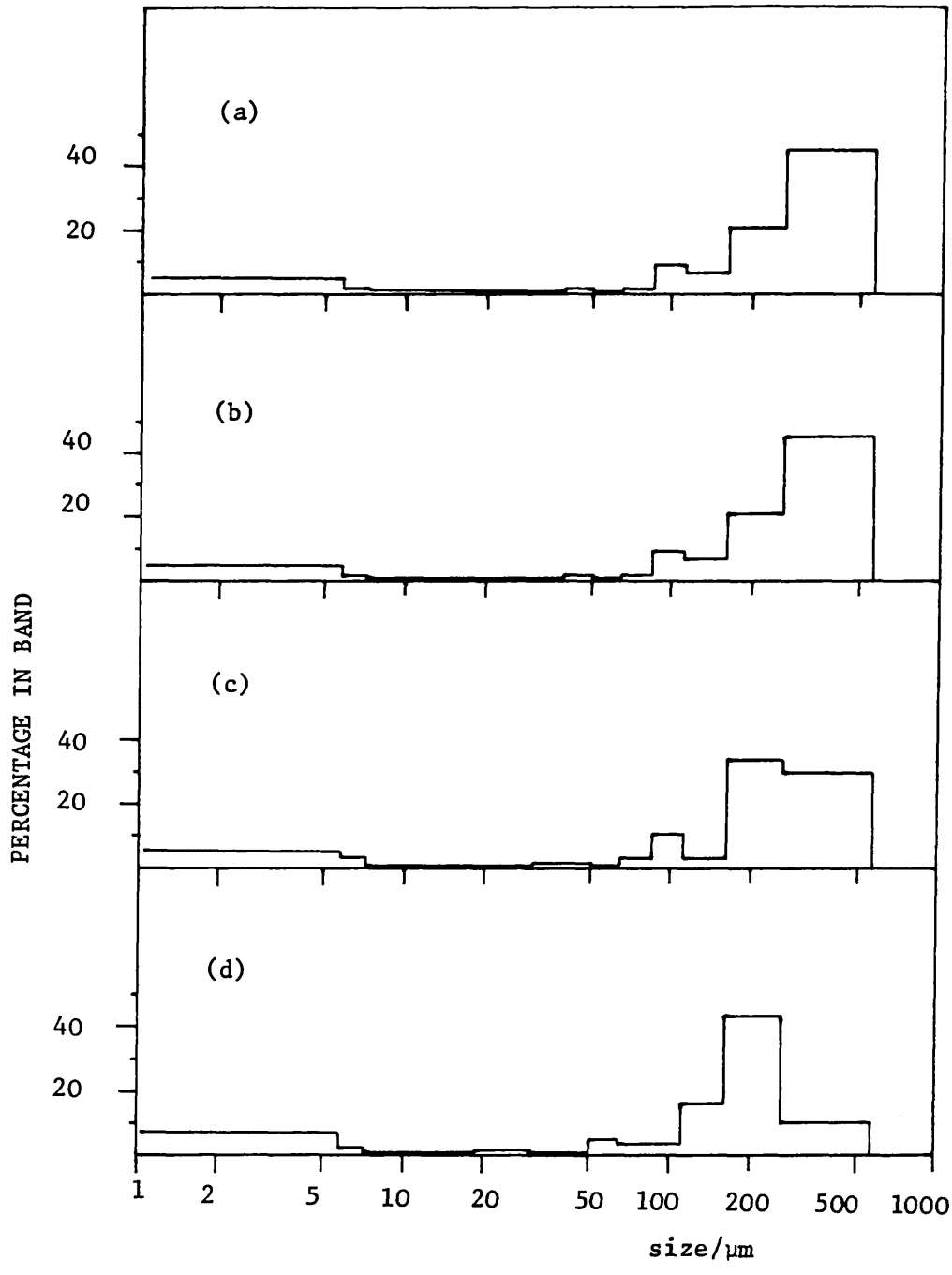


Figure 6.24 Effect of the variation of stirrer speed on particle size distribution for 2–bladed paddle

(a) PS13 – 300 rpm (b) PS14 – 350 rpm
(c) PS15 – 400 rpm (d) PS16 – 500 rpm
(2.5 $g.l^{-1}$ of PVA)

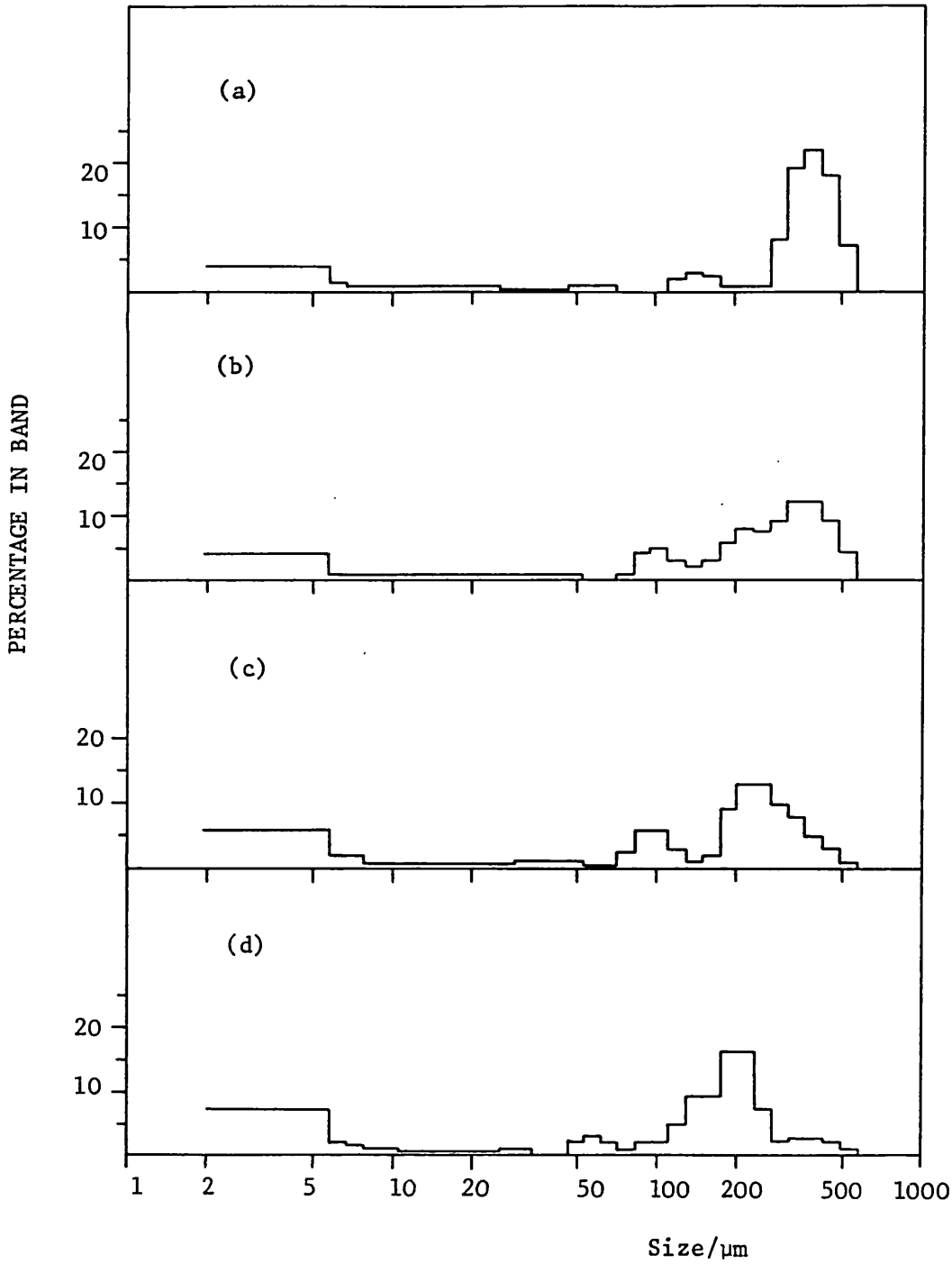


Figure 6.25 High resolution particle size distribution of polymers obtained at different stirrer speeds in 2–bladed paddle geometry

(a) PS13 – 300 rpm (b) PS14 – 350 rpm
(c) PS15 – 400 rpm (d) PS16 – 500 rpm

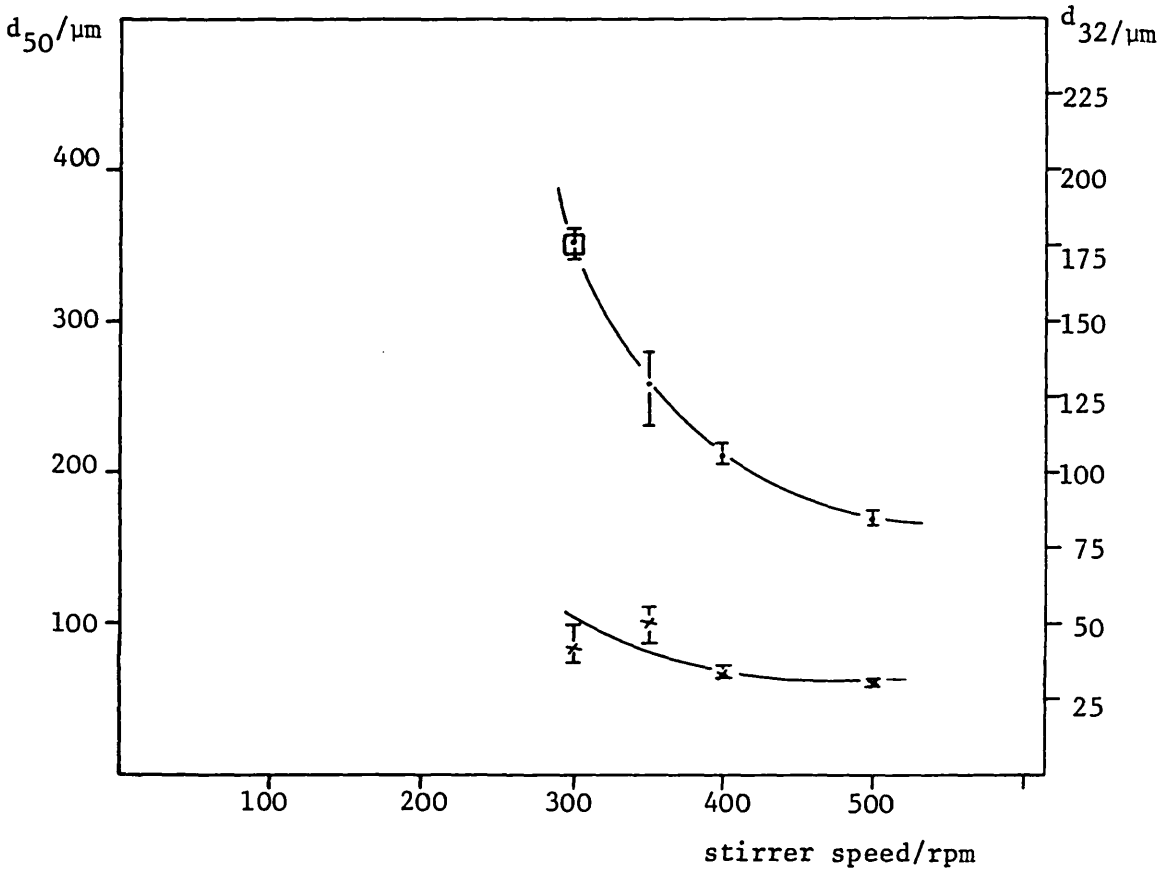


Figure 6.26 Variation of 50% mean and Sauter mean diameter with stirrer speed, for 2–bladed paddle with 2.5 $g.l^{-1}$ PVA.

□ d_{50} for Polymer 3, using PVA from BDH, instead of GH23
I d_{50}
⧗ d_{32}

(b) Molecular weight Distribution

The results for the number, weight average molecular weight and polydispersity of polymers 1–16 are presented in Table 6.5.

Table 6.5 Table of results for molecular weight distribution of polymers 1–16.

POLYMER	M_n x 10^{-4}	M_w x 10^{-5}	Z_p	RPM
1	3.7	1.2	3.2	400
2	7.3	2.2	3.0	400
3	3.6	1.2	3.3	300
4	4.2	1.1	2.7	400
5	3.5	0.97	2.8	400
6	3.8	1.1	2.8	400
7	3.5	0.96	2.7	400
8	4.2	1.1	2.7	400
9	4.3	1.2	2.7	400
10	4.2	1.2	2.9	400
11	4.0	1.0	2.6	400
12	3.4	0.85	2.5	400
13	4.4	1.5	3.5	300
14	4.2	1.3	3.2	350
15	3.7	1.2	3.3	400
16	5.4	2.1	3.8	500

Polymerisations carried out at 80 C.

The polymer exhibiting the highest number average molecular weight is number 2, which corresponds to the one whose initiator concentration has been reduced to one half of all other experiments. This effect was expected from the known influence of initiator concentration on molecular weight: the number average chain length, $\bar{\mu}_n$, is proportional to $[I]^{-\frac{1}{2}}$ [6], which means that a decrease in initiator concentration will cause an increase in M_n. The weight average molecular weight, M_w, is also higher, while the polydispersity remains unchanged.

The theoretical values for the two molecular averages and polydispersity were calculated assuming styrene polymerisation proceeded by a free–radical chain mechanism with initiation, propagation and combination termination, and an isothermal reaction at 80 C. The generating function approach [7] was used to obtain the momemts of the distribution. The rate constants at 80 C were taken from the literature [8]. The theoretical values for M_n, M_w and Z_p, together with the averaged experimental values (except those from Polymer 2), quoted with 95% confidence limits, are presented in Table 6.6.

Table 6.6 Table of results for experimental and theoretical values for molecular weight distribution of polymers 1, 3–16.

	Theory	Experiments
M_n	2.36×10^4	$(4.0 \pm 0.51) \times 10^4$
M_w	3.81×10^4	$(1.2 \pm 0.29) \times 10^5$
Z_p	1.62	2.98 ± 0.38

Both the experimental number and weight average molecular weight are higher than the theoretical ones, although M_n is of the same order of magnitude. The higher experimental value of M_w is probably reflecting the autoacceleration or gel effect, which happens within each polymerising droplet when a critical value of viscosity has been reached. As a droplet viscosity increases, chain mobility is reduced and the termination reaction is decreased by 1 or 2 orders of magnitude, whereas the propagation reaction is not so much affected. Since M_n is proportional to $k_t^{-\frac{1}{2}}$, where k_t is the rate constant for the termination reaction, an increase in this average is expected although to a lesser extent than in the weight average molecular weight. The increase in the experimental values of polydispersity is also a direct reflection of the gel effect.

The introduction of error limits in the experimental values of M_n, M_w and Z_p show that all polymers, except polymer 2 (lower [I] – already mentioned) and polymer 16 (corresponding to a stirrer speed of 500 rpm) fall within the 95% confidence range. Therefore, no significant trend in MWD could be found either with stirrer speed or suspending agent concentration.

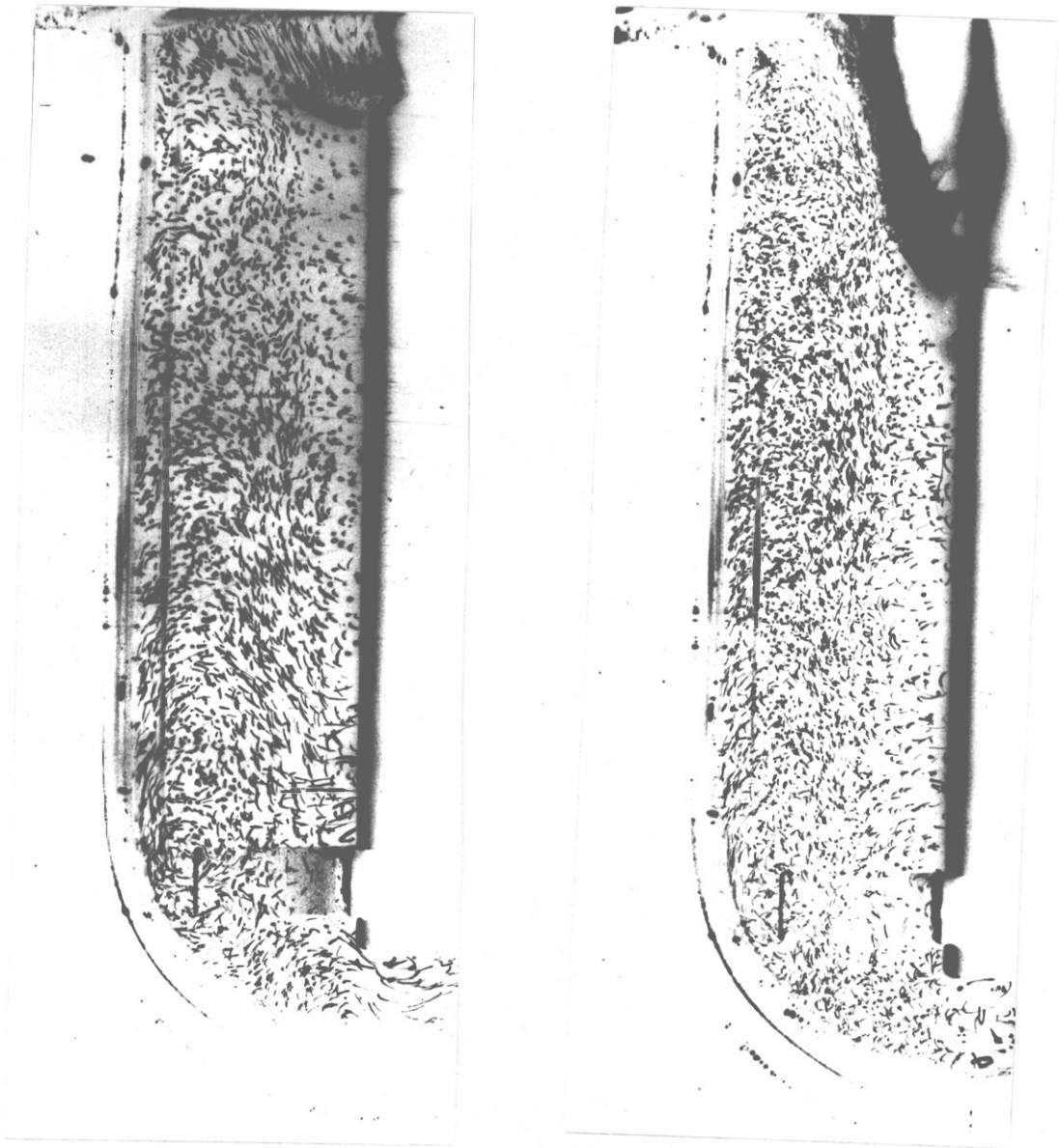
6.3 4–Bladed Paddle ("Complex") Geometry

The 4–bladed paddle ("complex") geometry was characterised in a similar way to the 2–bladed paddle. Besides the normal polymerisation runs for the well characterised flow situations, a series of runs at different polymerisation temperatures was planned to try to explain the sudden onset of aggregation during the polymerisation process, which happens in both geometries.

6.3.1 Flow Characterisation Experiments

(a) Static streak photography

The experiments done covered a range of stirrer speeds, from 150 to 300 rpm and 600 rpm, with and without baffles. Two sets of baffles with different lengths (86 and 112 mm) were used at 90° to the light plane and the long baffles were also examined at about 10° to the illuminated plane of light. In Figures 6.27(a) and (b) are shown typical photographs of vertical flow patterns obtained with the 4–bladed paddle, without baffles at 150 and 300 rpm, respectively. No difference could be detected in the flow patterns with stirrer speed. Again, as in the case of the previous geometry, fluid is thrown out by the paddle, going up near the wall and coming down by the shaft. As with the 2–bladed paddle there is considerable by–passing of fluid before it reaches the liquid surface. The dramatic effect of the introduction of baffles upon the vertical flow pattern can be seen in Figure 6.28 where the right hand side corresponds to a non–baffled vessel and the left hand side shows the same vessel, at the same stirrer speed, 150 rpm, but with the 86 mm baffles inserted at 90° to the light plane. The presence of baffles causes a considerable increase in the amount of vertical motion (long streaks) upwards



(a) (b)

Figure 6.27 Streak photograph of vertical flow patterns for the 2–bladed paddle, without baffles, at
(a) 150 rpm
(b) 300 rpm

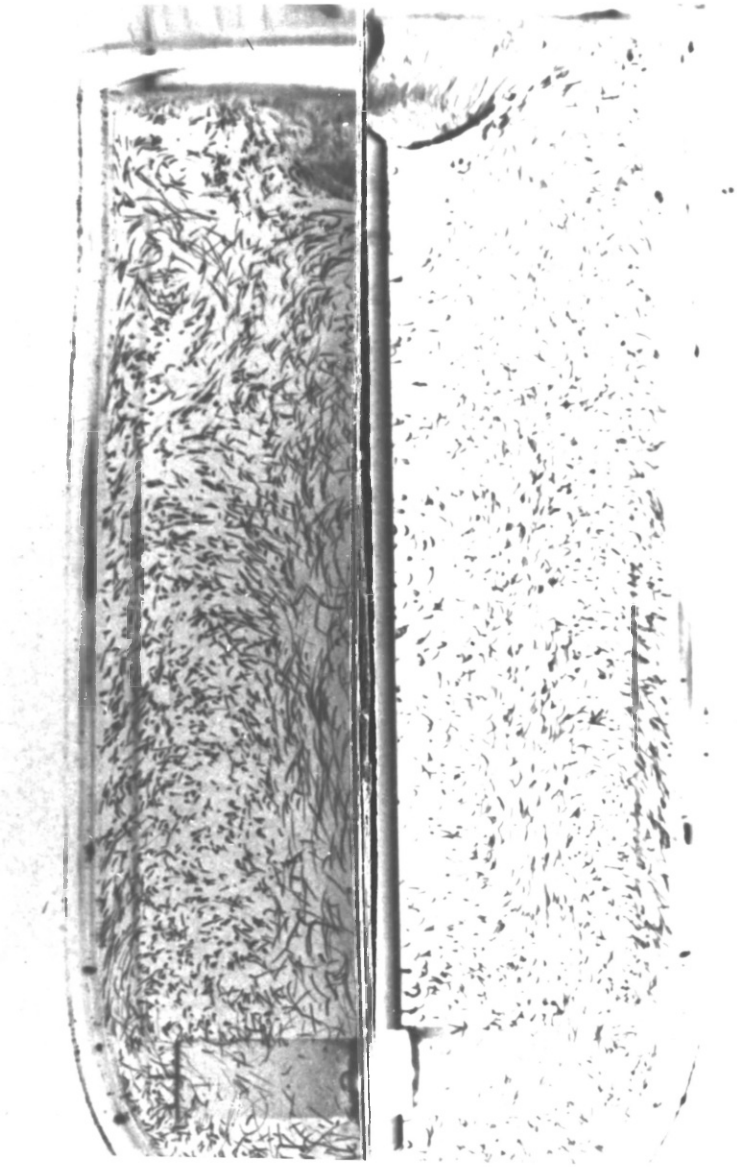


Figure 6.28 Streak photograph of vertical flow patterns for the 4–bladed paddle, with and without baffles, at 150 rpm

Left hand side – with 86 mm baffles
Right hand side – without baffles

near the wall and down by the shaft. As was the case without baffles, this represents a typical photograph, as no significant change with stirrer speed was noted.

The influence of baffle length was investigated with the set of longer baffles: 112 mm, also placed at 90° to the light plane. Figure 6.29 shows the photographs of vertical flow patterns at 150 rpm with the two sets of baffles: the longer (112 mm) baffles on the left hand side, and the shorter (86 mm) baffles on the right hand side. As it is clear from this photograph no difference can be detected between the two baffles; this remained the case for all the other stirrer speeds used. To conclude the experiments with this flow technique, the relative position of the baffles to the incoming plane of light was changed from 90° to about 10°. Figure 6.30 presents the photographs of vertical flow patterns with the 112 mm baffles at 90° (left hand side) and 10° (right hand side) at the same stirrer speed, 150 rpm. As previously no difference between the two conditions is present at this or any other stirrer speed.

This set of experiments using static streak photography showed that on the macroscale of the agitation process no discernable difference could be detected in vertical flow patterns between the two geometries: 2– and 4–bladed paddle. Furthermore, with the latter geometry no significant difference was present with the two different length baffles, even at a different position relative to the light plane. The major effect comes from the introduction of baffles in the reactor. From these considerations, the two other flow characterisation techniques only used the longer (112 mm) baffles, when baffles were included.

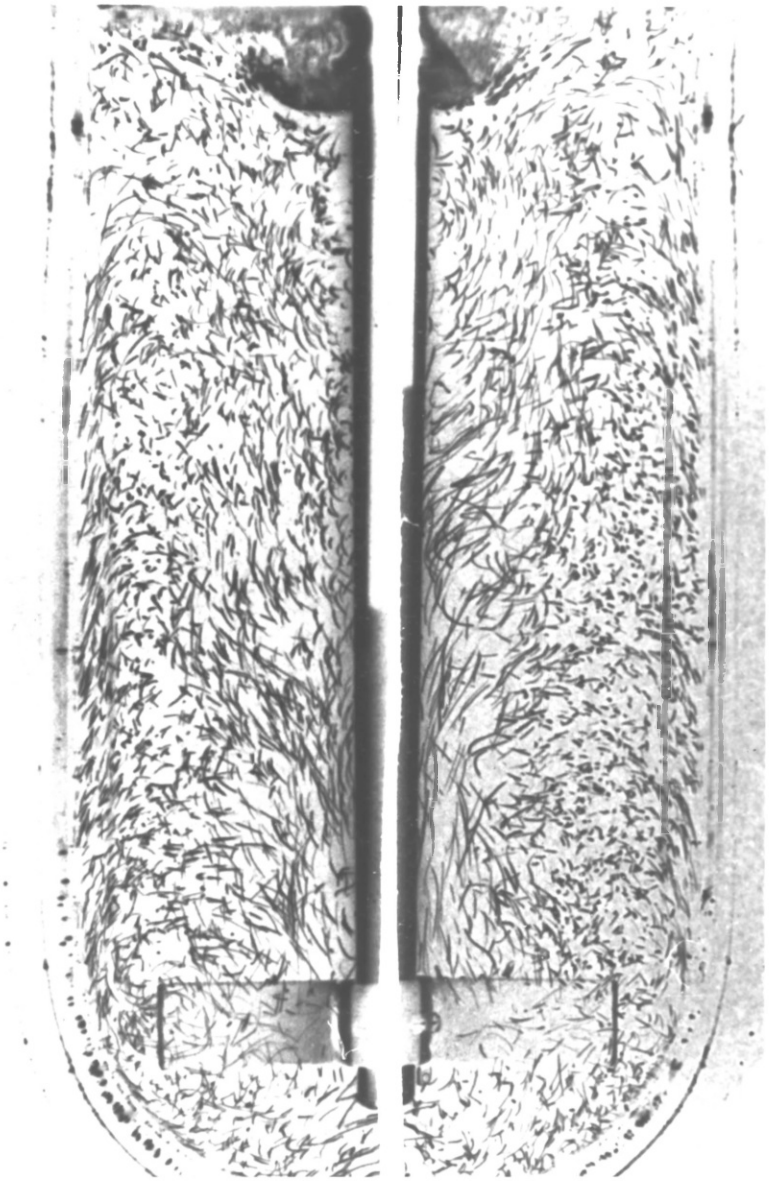


Figure 6.29 Streak photograph of vertical flow patterns for the 4–bladed paddle, with 86 and 112 mm baffles, at 150 rpm

Left hand side – with 112 mm baffles
Right hand side – with 86 mm baffles

(Baffles can be seen at shaft)

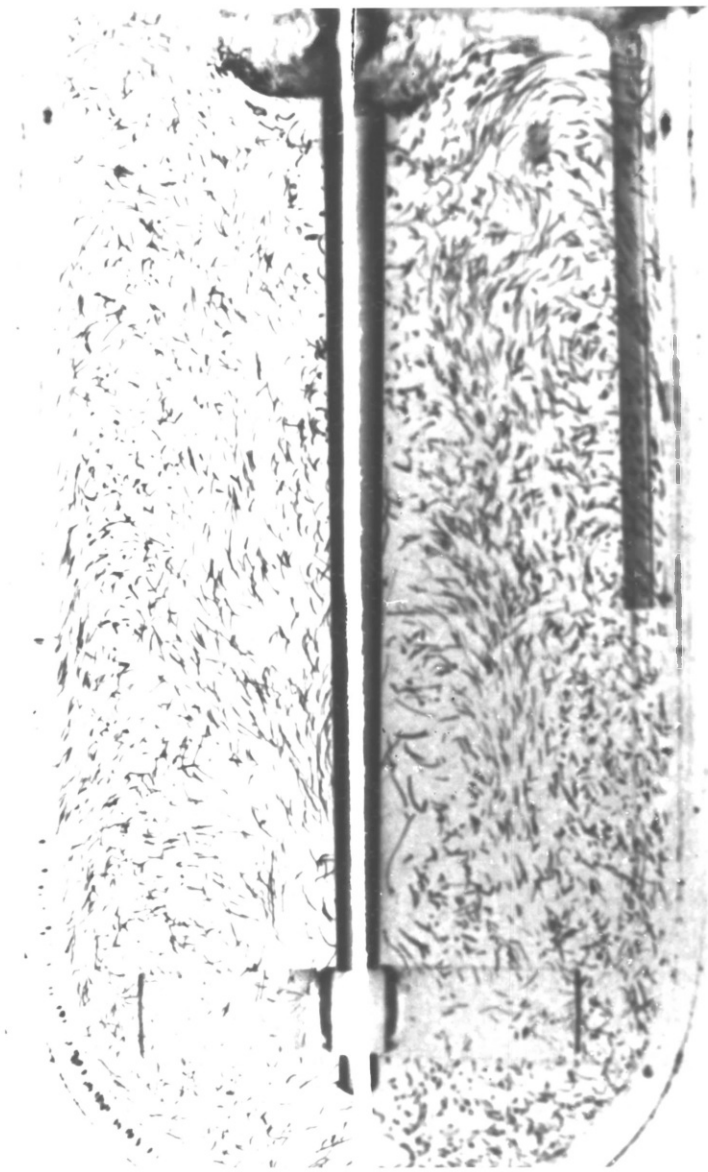


Figure 6.30 Streak photograph of vertical flow patterns for the 4–bladed paddle with 112 mm baffles, at 150 rpm, and at 90 ° and 10 ° to the light plane

Left hand side – 90 ° to the light plane
Right hand side – 10 ° to the light plane

(b) Dynamic video monitoring

The flow follower, video monitoring experiments were done without and with baffles (112 mm long) for stirrer speeds between 150 and 300 rpm. Figure 6.31 presents the percentage of time spent in each zone as a function of stirrer speed for the unbaffled vessel.

The results show that the percentage of time spent in the bottom zone decreases with stirrer speed, whereas it increases in the three upper zones. Although the top zone is not completely available for detection, even at the lower end of the stirrer speed, preventing correlation of time in zone with rpm, it is worth noticing that the flow follower spends there a fraction of time comparable with that in zone (5), at the bottom of the reactor, for stirrer speeds below 200 rpm. This evidence suggests that at low values of stirrer speed the flow follower will be trapped for quite some time in the two extreme regions of the reactor: below and near the agitator, and by the vortex. These two zones present quite different flow characteristics: the agitator is a high shear, elongational region where the droplets can be broken–up, and the vortex has a high rotational flow, where coalescence is more likely to occur.

The increase in stirrer speed reduced both these tendencies and the flow follower will not spend that much time near the agitator (its pumping power has increased) and by the vortex, but it will be more evenly distributed in the middle of the vessel. The probable consequences for a suspension polymerisation experiment are that at low stirrer speeds it will take more time for an equilibrium droplet size distribution to be attained, since any droplet breakage occurring by the paddle has a lot of time to be restored by coalescence near the top of the reactor. Increasing stirrer speed reduces the time near the agitator, but this effect can be balanced by the increase in

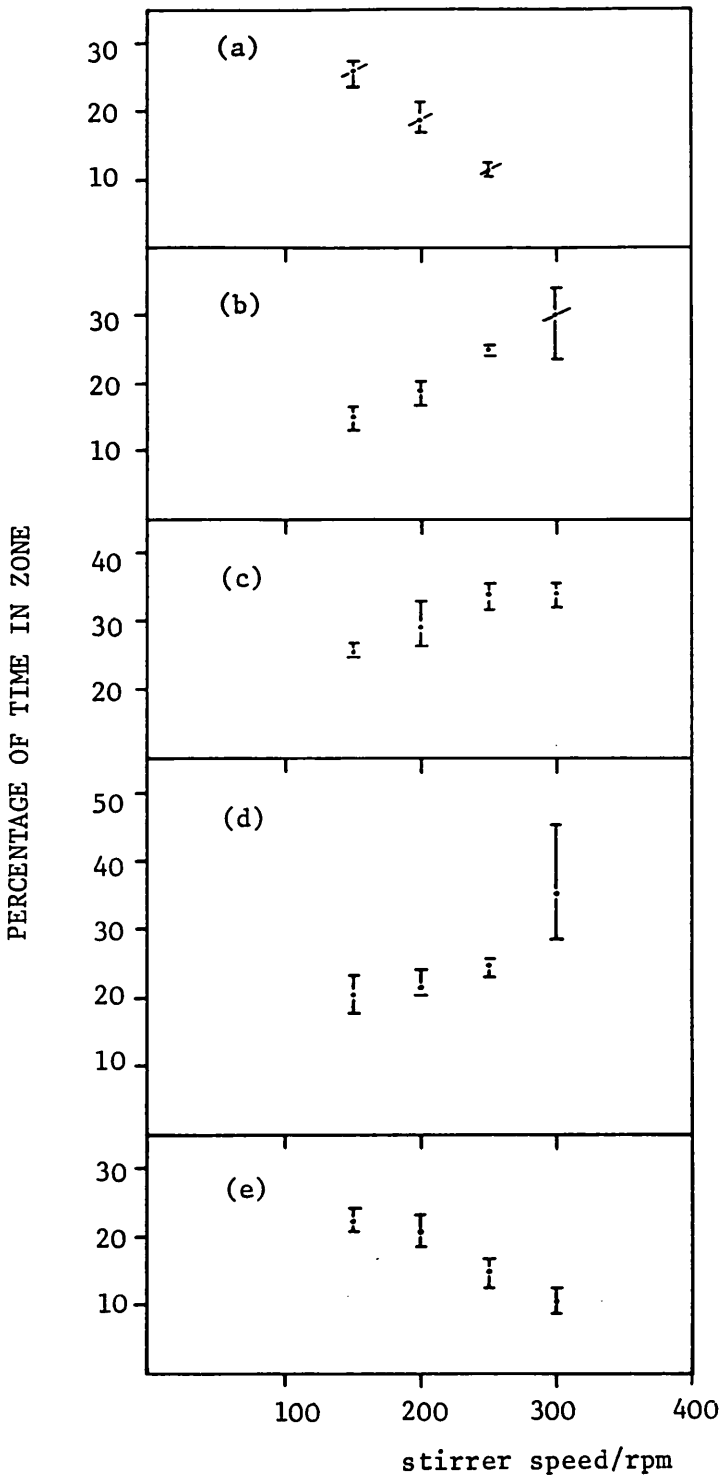


Figure 6.31 Variation of percentage time in zone versus stirrer speed for 4–bladed paddle, without baffles

I denotes measurement in part of zone (due to vortex intrusion)

(a) zone 1 (b) zone 2
(c) zone 3 (d) zone 4
(e) zone 5

elongational rate, the decrease in circulation time and the decrease of time near the top of the reactor. The combination of these effects will cause the particle size distribution to shift towards lower values.

This residence time behaviour compares well with the one for the 2–bladed paddle, except for the bottom zone where the percentage of time spent there, in the 2–bladed case was not very strongly dependent on stirrer speed.

The effect of the introduction of baffles can be seen in Figure 6.32. As expected from the earlier evidence of streak photography, considerable differences in behaviour arise between the two cases, lowering the amount of time the tracer particle spends in zone (5) – (bottom) and (1) and (2) – top, and increasing the time in the middle region of the reactor. The reduction in zones (1) and (2) may be due to the decrease in swirl motion and vortex that trapped the flow follower into these top zones in the unbaffled case. The variation of fractional residence time with stirrer speed in zone (3) is much like it was without baffles. By contrast for zone (4), there is a decreasing trend with stirrer speed. The difference in zone (4) may be explained by the fact that the baffle protrudes into this zone and might cause some local flow disturbances.

Baffling the reactor has a similar effect on the circulation characteristics as an increase in stirrer speed, and might therefore be expected to produce the same kind of end results in a suspension polymerisation. Increasing both factors should mean that the dynamic equilibrium of the droplet population is achieved faster and the particle size distribution is shifted towards smaller values. Whether baffles will cause a more pronounced effect at the lower or the higher speed range is not immediately apparent from this

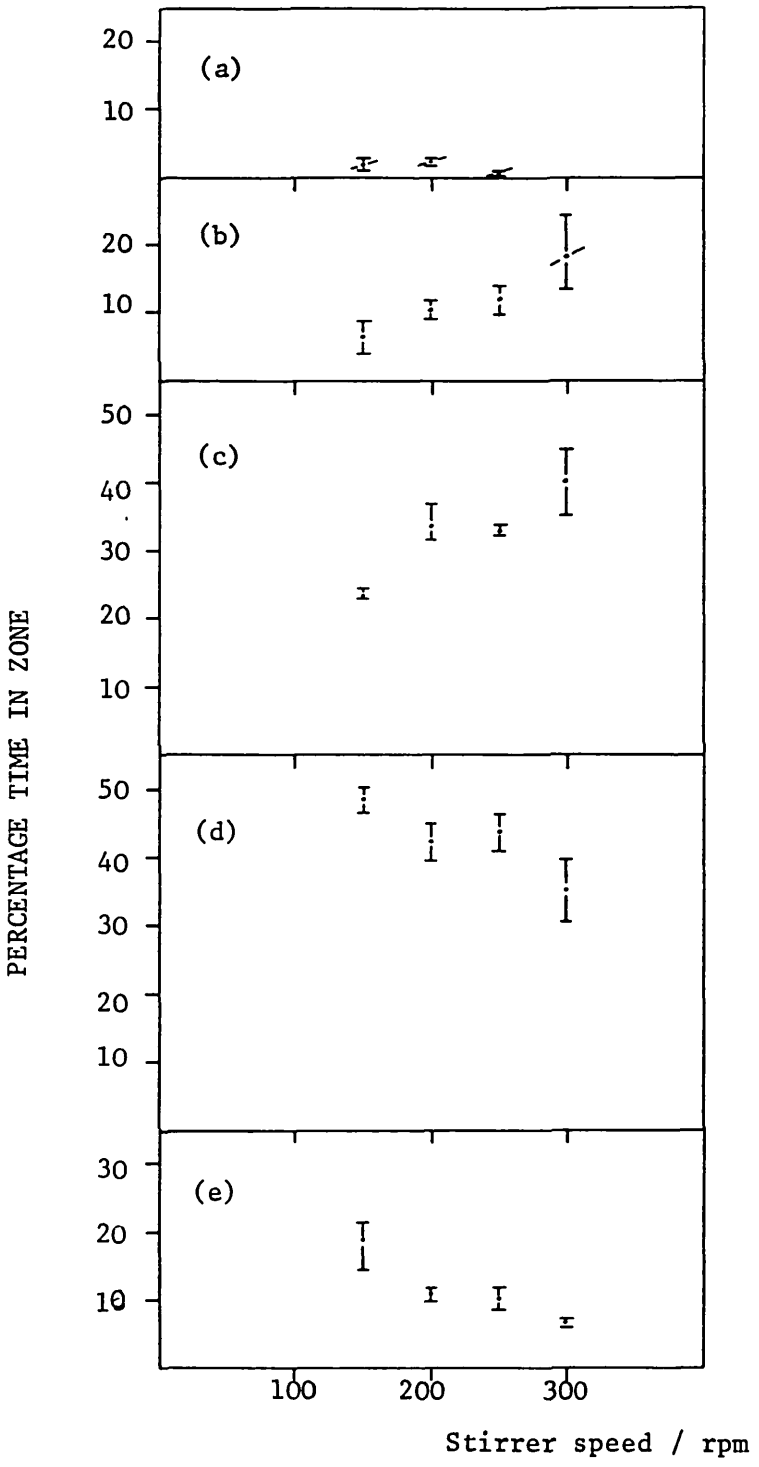


Figure 6.32 Variation of percentage time in zone with stirrer speed, for 4–bladed paddle, with 112 mm baffles.

(a) zone 1 (b) zone 2 (c) zone 3 (d) zone 4 (e) zone 5

kind of flow information. To answer this question we need to examine the flow in more detail using LDA.

The argument that on a statistical basis, if one is prepared to count for long enough, the amount of time the flow follower spends in any particular zone of the reactor should be equal, is in apparent contradiction with the evidence just presented. In a suspension polymerisation reaction the crucial events happen in the first few hours when the droplets still have a low enough viscosity to be influenced by the different shear and extension conditions present in the various zones of the reactor. Once they have reached a critical viscosity it is very difficult for break–up or even coalescence to take place between polymerising droplets. For this reason it is important to look at the more short term differences between these agitation conditions. The residence time history of the flow follower over relatively short time scales is expected to reflect that of the particles in the suspension process.

The other output from this flow characterisation technique is the probability of direction change within each zone, which can be seen in Figures 6.33 (a) and (b) for the 4–bladed paddle at 150 rpm, for 25 minutes without and with baffles, respectively. To compare these results one must again confine attention to the middle zones (2)–(4), since zones (1) and (5) are distinct in that these are zones where there is always flow reversal. This information is directly linked with the flow structure obtained with a certain paddle. It can also give some information about flow stability in the middle zones of the reactor.

Without baffles the results show that it is more likely for the droplet to change direction when going up (~ 40%) than when coming down (~ 30%). When baffles are introduced, the probability of direction change when going up

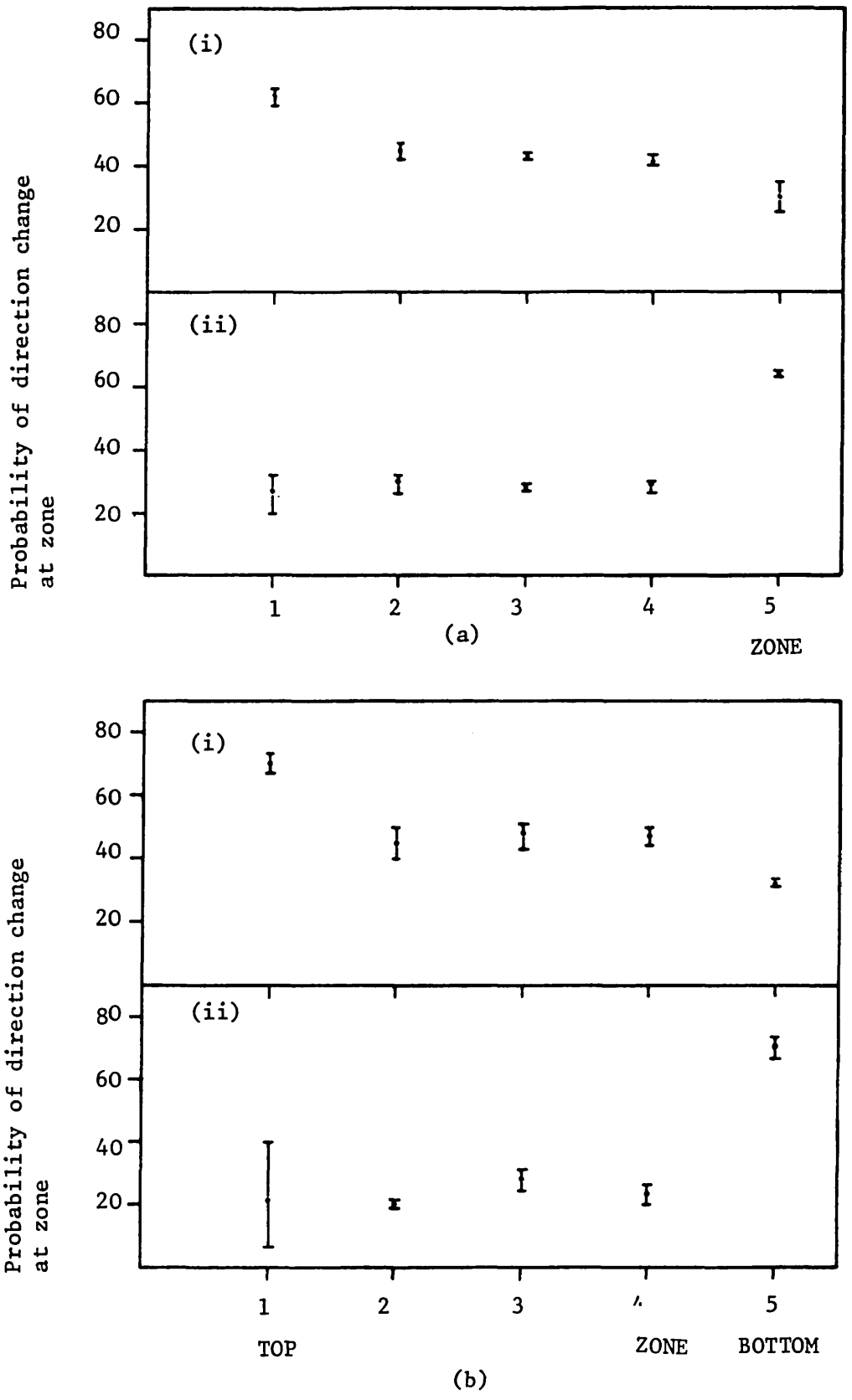


Figure 6.33 Probability of direction change at zone for 4–bladed paddle with and without baffles, at 150 rpm, for 25 minutes

(i) going up and turning down
(ii) going down and turning up
(a) without baffles
(b) with 112 mm baffles

increases slightly from the values without baffles. The short time effects of stirrer speed on the probability of direction change for this geometry can be seen in Figures 6.34(a) and (b), for the unbaffled and baffled case. The probability of going up and turning down is now exhibiting a decreasing trend from top to bottom of reactor, revealing an increasing probability of by–pass of the liquid surface as we go higher in the reactor. The introduction of baffles increases the probability of short circuiting the liquid surface which is evident from the steeper curve obtained for the probability of flow reversal when going up. In both cases there is not a clear stirrer speed effect. The other probability of flow reversal, i.e. turning up when coming down exhibits a reverse behaviour, being at its highest in the bottom of the reactor, as expected. Again baffles seem to cause a more marked variation and there is a small stirrer speed effect. The picture of flow that emerges corresponds to a flow structure where there is recirculation in each zone ("by–passing"), even quite low down in the reactor. This flow pattern agrees closely with the earlier evidence from streak photography, but quantifies the dynamics in a way which is not possible using an essentially instantaneous view of the flow.

The short time effects reveal that there is not much difference in flow structure between the unbaffled case of both geometries, while the probability of by–pass of the liquid surface seems to increase with the introduction of baffles. If there is more frequent short–circuiting of the surface of the liquid, then droplets will come more frequently to the agitator zone, and a particle size distribution shifted to smaller size range might be expected.

(c) Laser Doppler Anemometry

The components of velocity measured were, as in the case of the 2–bladed paddle, the tangential, v_t, and vertical, v_z, components. The

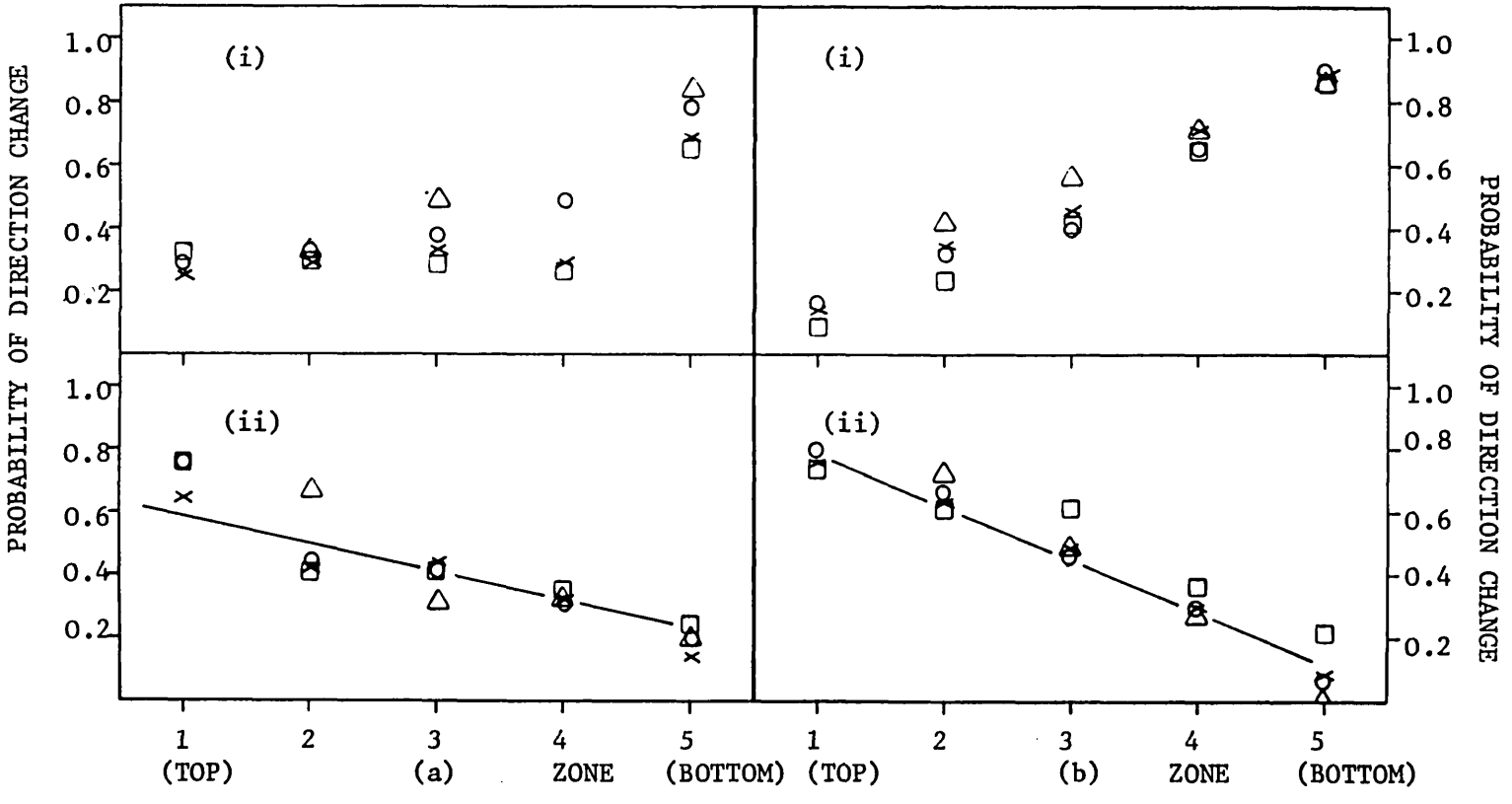


Figure 6.34 Variation of probability of direction change at zone with stirrer speed, for the 4–bladed paddle, for 10 minutes.

(a) without baffles (b) with baffles
(i) Probability of turning up when going down
(ii) Probability of turning down when going up

□ 150 rpm × 200 rpm
○ 250 rpm △ 300 rpm

measuring positions can be seen in Figure 6.35 and they form a vertical grid along a diameter of the reactor, coincident with the x–axis. The positions were chosen such that the highest vertical coordinate in the reactor, at each stirrer speed, was just below (1–2 mm) vortex position at stirring shaft, to still enable a full radial scan. The lowest vertical position was coincident for the two speeds, $z = 0.6$ cm, determined by geometrical constraints of the reactor. The two resulting available heights were then divided into equal spacing.

The experiments were carried out at 150 and 400 rpm, each without and with baffles, and the results for the tangential velocity, v_t, and vertical, v_z, velocities together with the corresponding values for turbulence intensity, I_R, are presented in Figures 6.36 to 6.43. The values quoted are averages of three to five individual measurements and the uncertainty refer to maximum and minimum values.

We look first at the results for the tangential velocity at 150 and 400 rpm without baffles, Figures 6.36 and 6.37, respectively. At 150 rpm a two maximum situation arises ($R_1 = 2$cm and $R_2 \simeq 3.5$ cm) in the lower part of the reactor ($z \leq 2.1$ cm), being more pronounced closer to the agitator ($z = 0.6$ cm). This gives an almost flat radial profile in v_t. In the upper part of the reactor ($z \geq 5.1$ cm) the variations in v_t with radial distance, R, become more marked, a single peak in the velocity profile developing at a radial distance of $R \simeq 2.0$ cm, well before the edge of the agitator blade (which was at $R = 3.15$ cm, shown as a dash–point line). This peaking in velocity becomes more pronounced in the higher regions of the reactor, but never as sharp as with the two–bladed paddle. Maximum tangential velocity, $v_{t\ max} \simeq 0.4$ m.s^{-1} is smaller than the tip speed at this stirrer speed, $V_{tip} = 0.495$ m.s^{-1}.

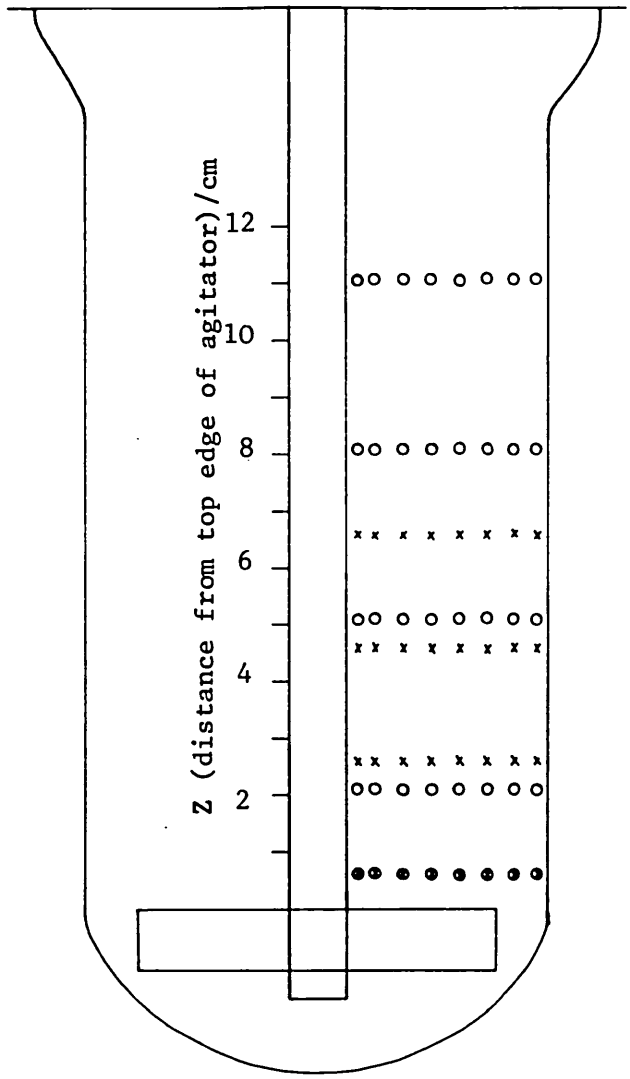


Figure 6.35 Measuring positions in LDA for the 4–bladed paddle
○ – at 150 rpm
× – at 400 rpm

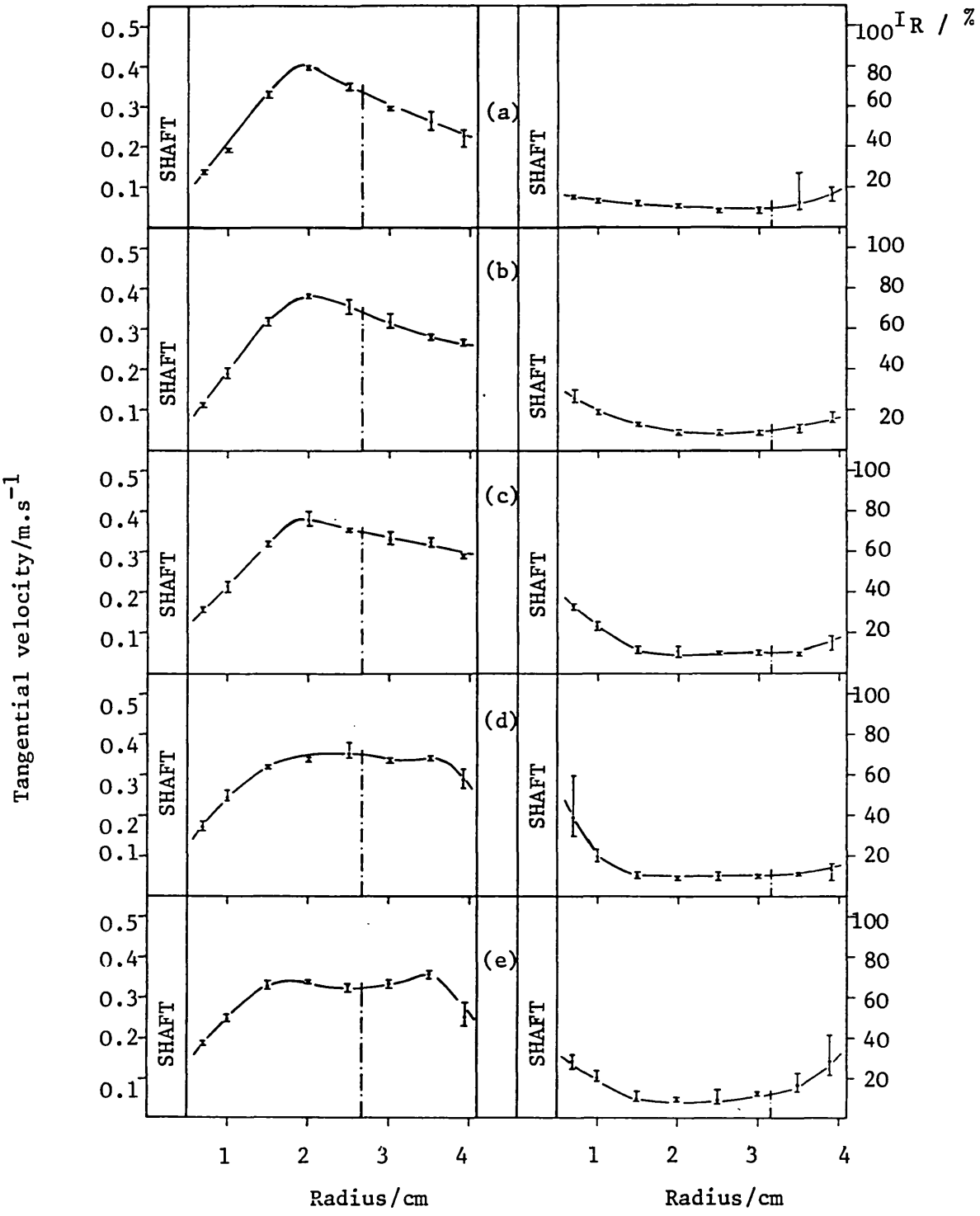


Figure 6.36 Tangential velocity profiles for the 4-bladed paddle, at 150 rpm, without baffles

(a) z = 11.1 cm (b) z = 8.1 cm
(c) z = 5.1 cm (d) z = 2.1 cm
(e) z = 0.6 cm

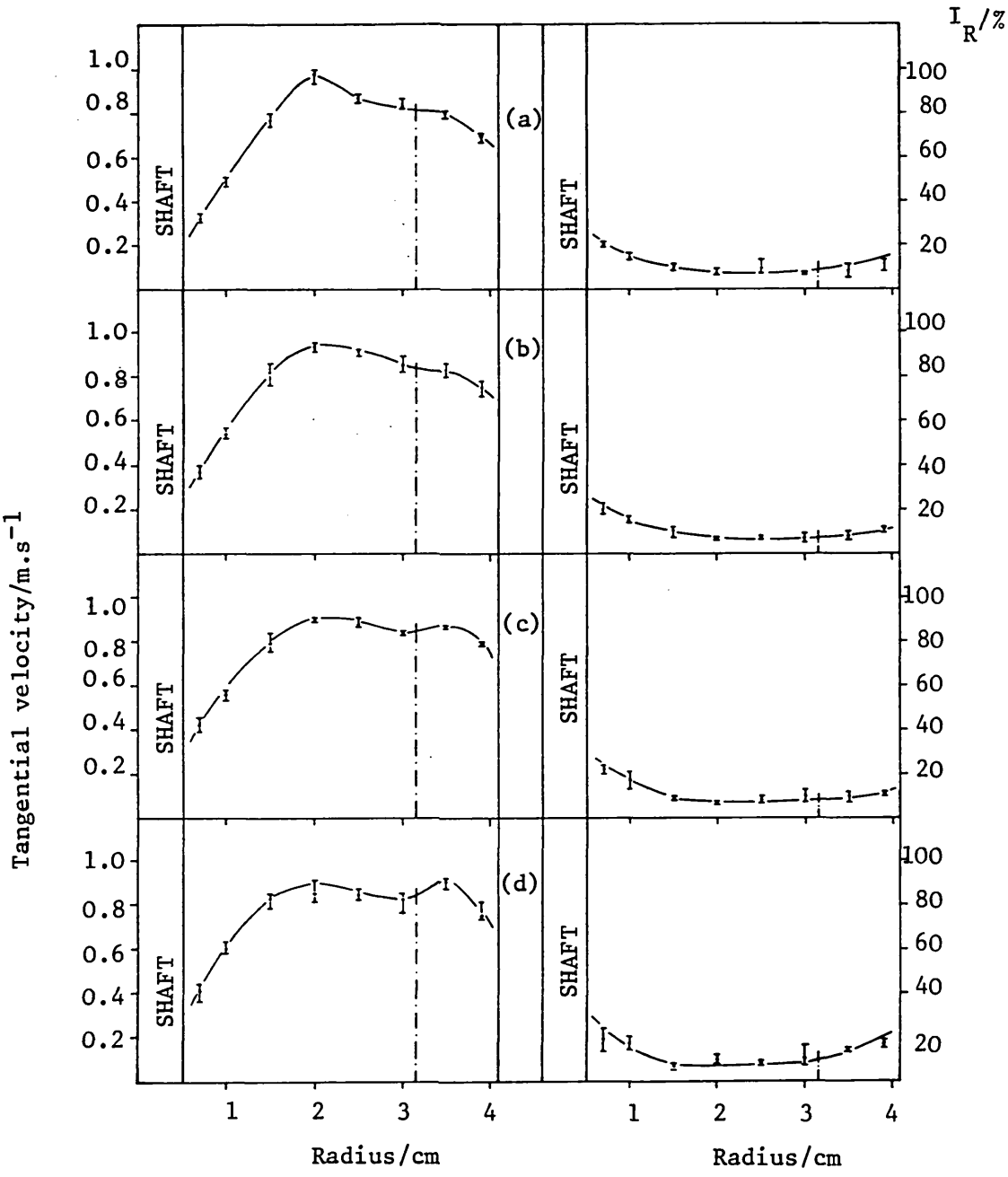


Figure 6.37 Tangential velocity profiles for the 4–bladed paddle, at 400 rpm, without baffles

(a) z = 6.6 cm (b) z = 4.6 cm
(c) z = 2.6 cm (a) z = 0.6 cm

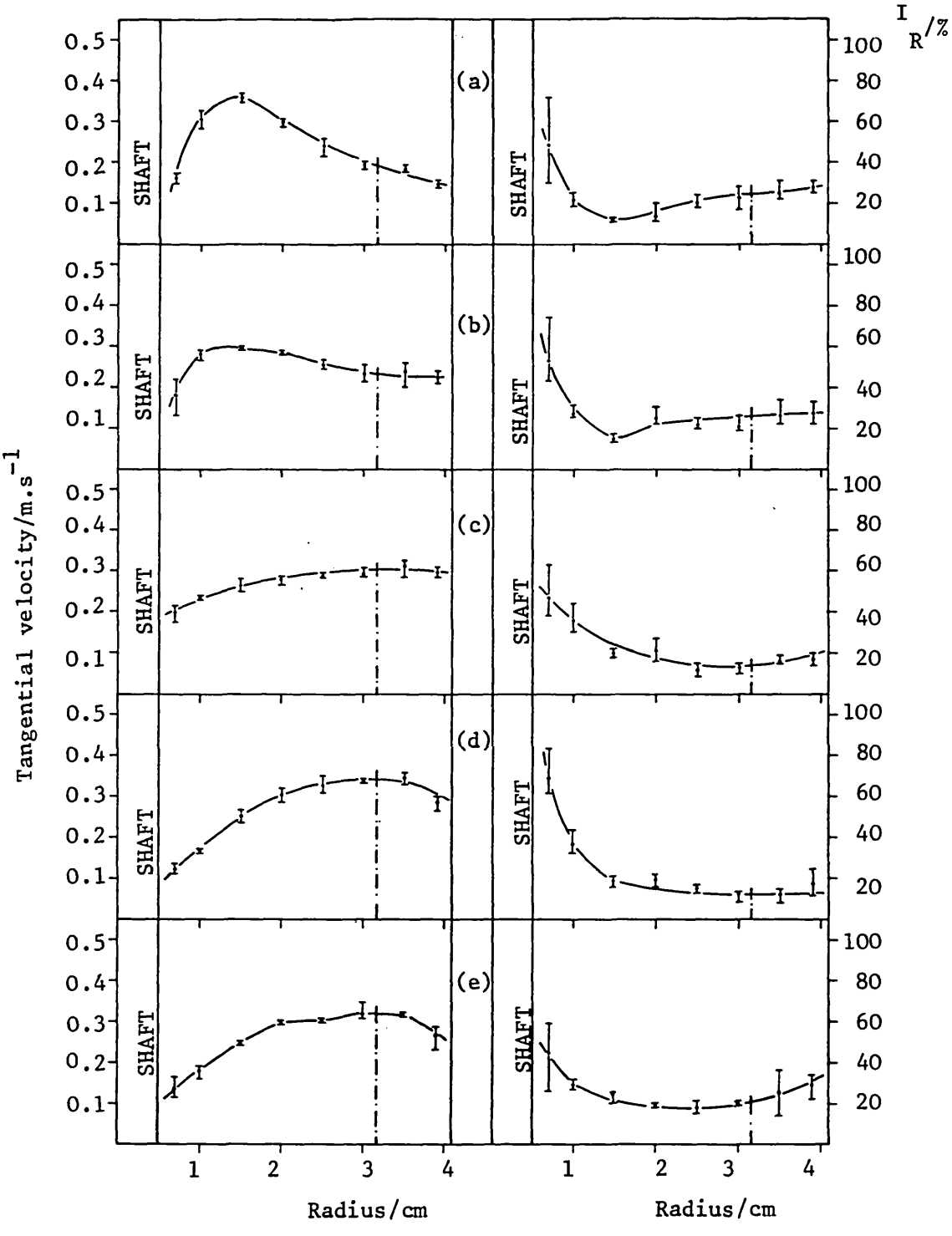


Figure 6.38 Tangential velocity profiles for the 4–bladed paddle, at 150 rpm, with baffles

(a) z = 11.1 cm (b) z = 8.1 cm
(c) z = 5.1 cm (d) z = 2.1 cm
(e) z = 0.6 cm

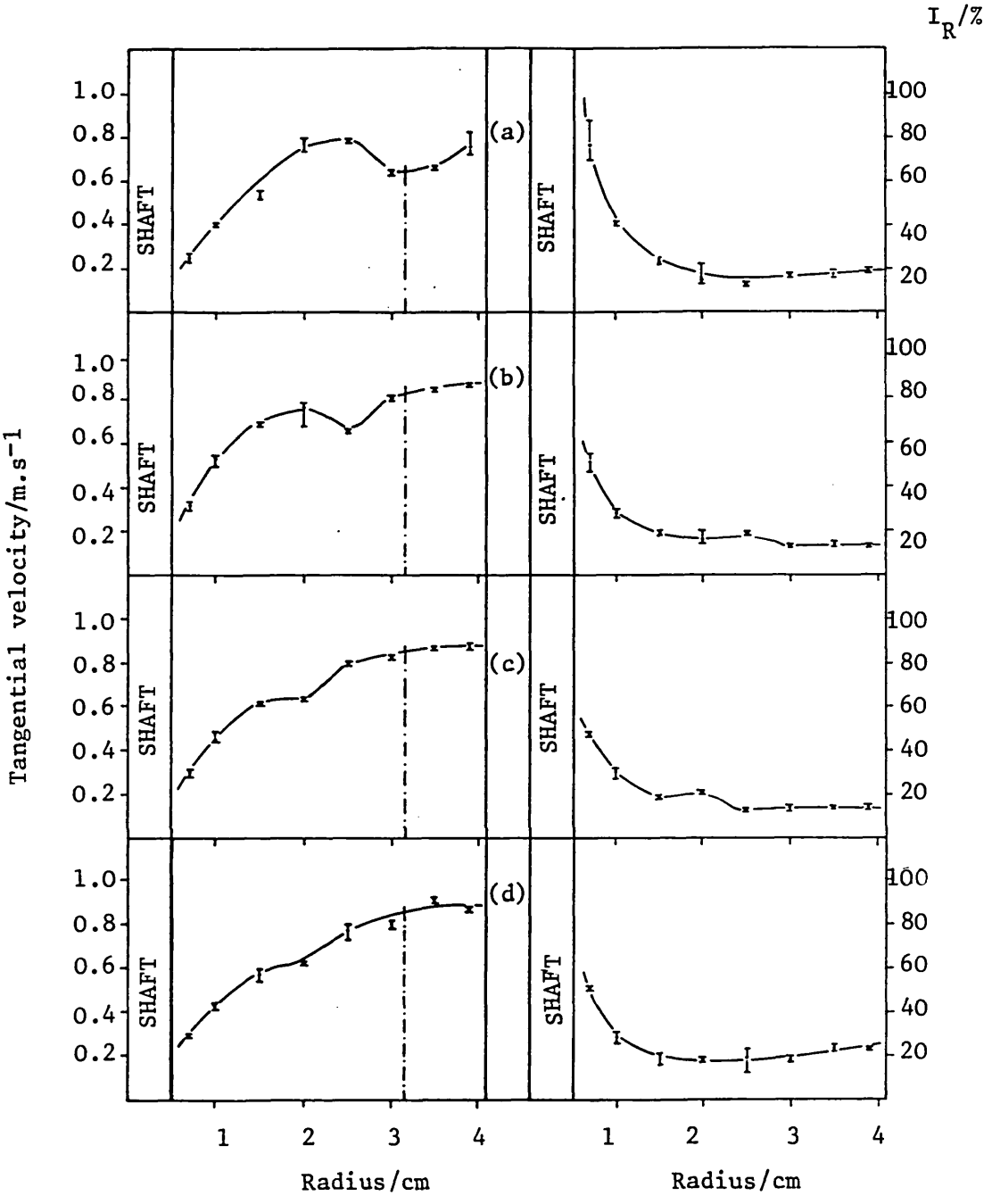


Figure 6.39 Tangential velocity profiles for the 4–bladed paddle, at 400 rpm, with 112 mm baffles.

(a) z = 6.6 cm (b) z = 4.6 cm

(c) z = 2.6 cm (d) z = 0.6 cm

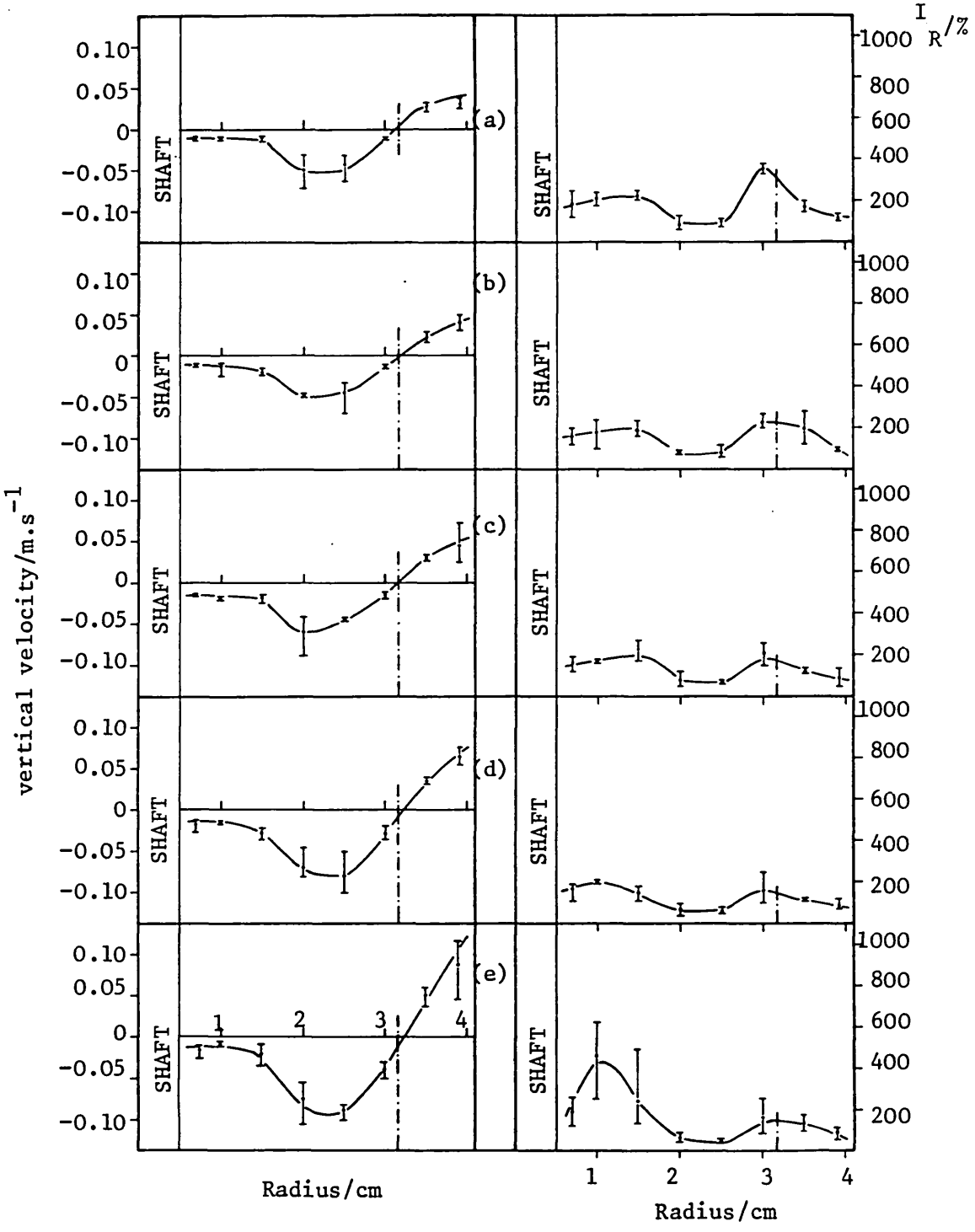


Figure 6.40 Vertical velocity profiles for the 4-bladed paddle, at 150 rpm, without baffles

(a) z = 11.1 cm (b) z = 8.1 cm

(c) z = 5.1 cm (d) z = 2.1 cm

(e) z = 0.6 cm

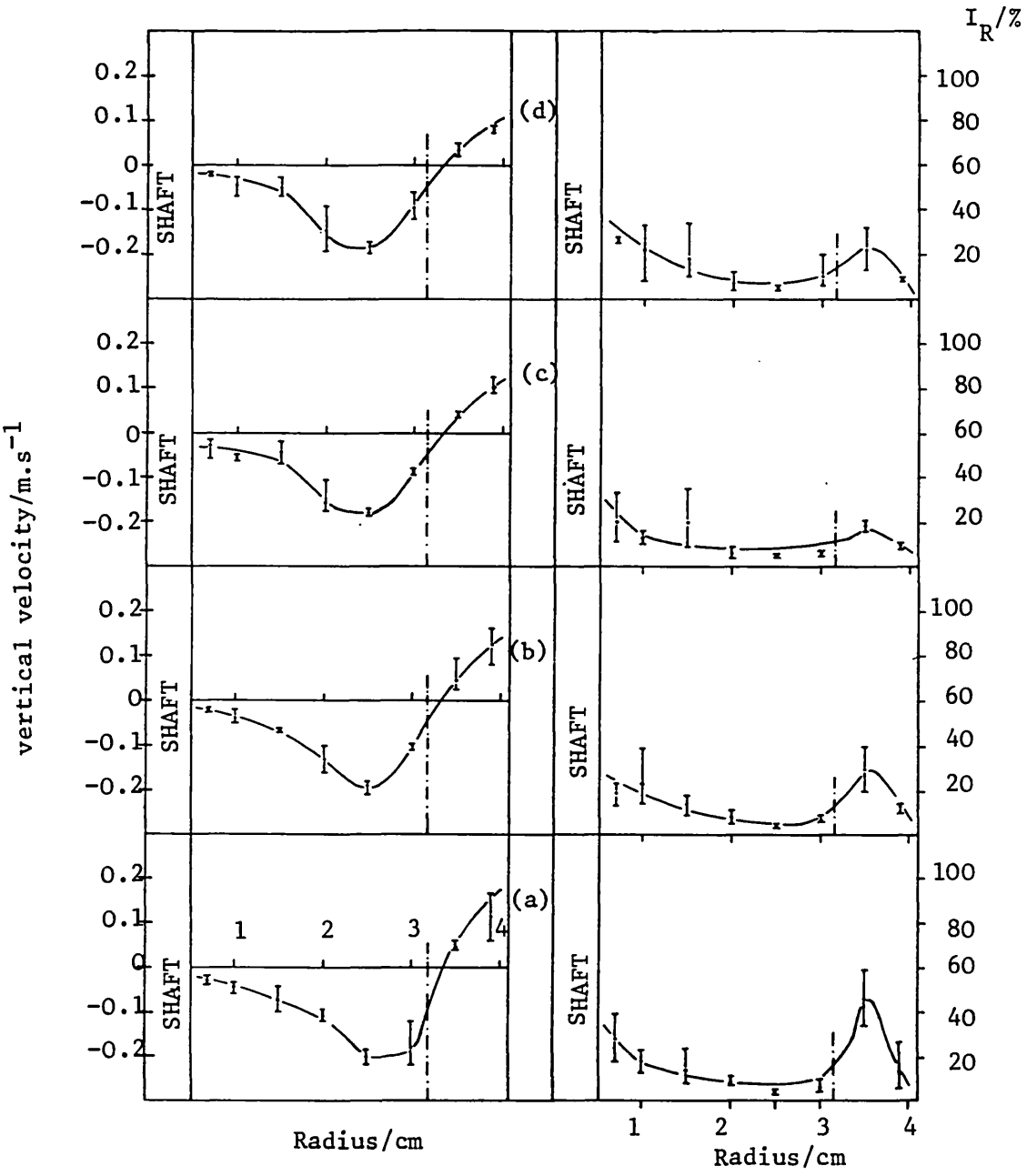


Figure 6.41 Vertical velocity profiles for the 4–bladed paddle, at 400 rpm, without baffles.

(a) z = 0.6 cm (b) z = 2.6 cm
(c) z = 4.6 cm (d) z = 6.6 cm

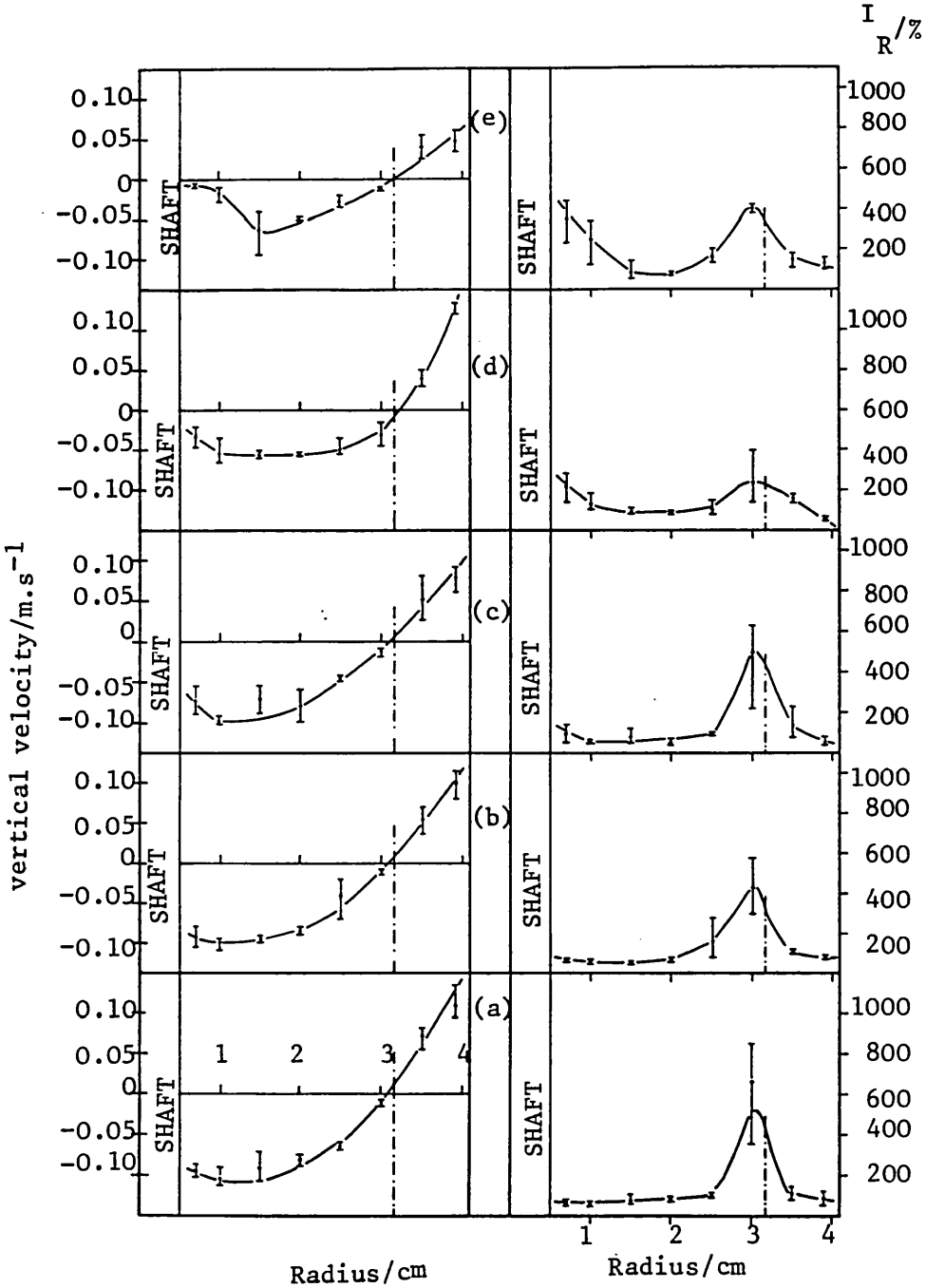


Figure 6.42 Vertical velocity profiles for the 4–bladed paddle, at 150 rpm, with 112 mm baffles

(a) z = 0.6 cm (b) z = 2.1 cm
(c) z = 5.1 cm (d) z = 8.1 cm
(e) z = 11.1 cm

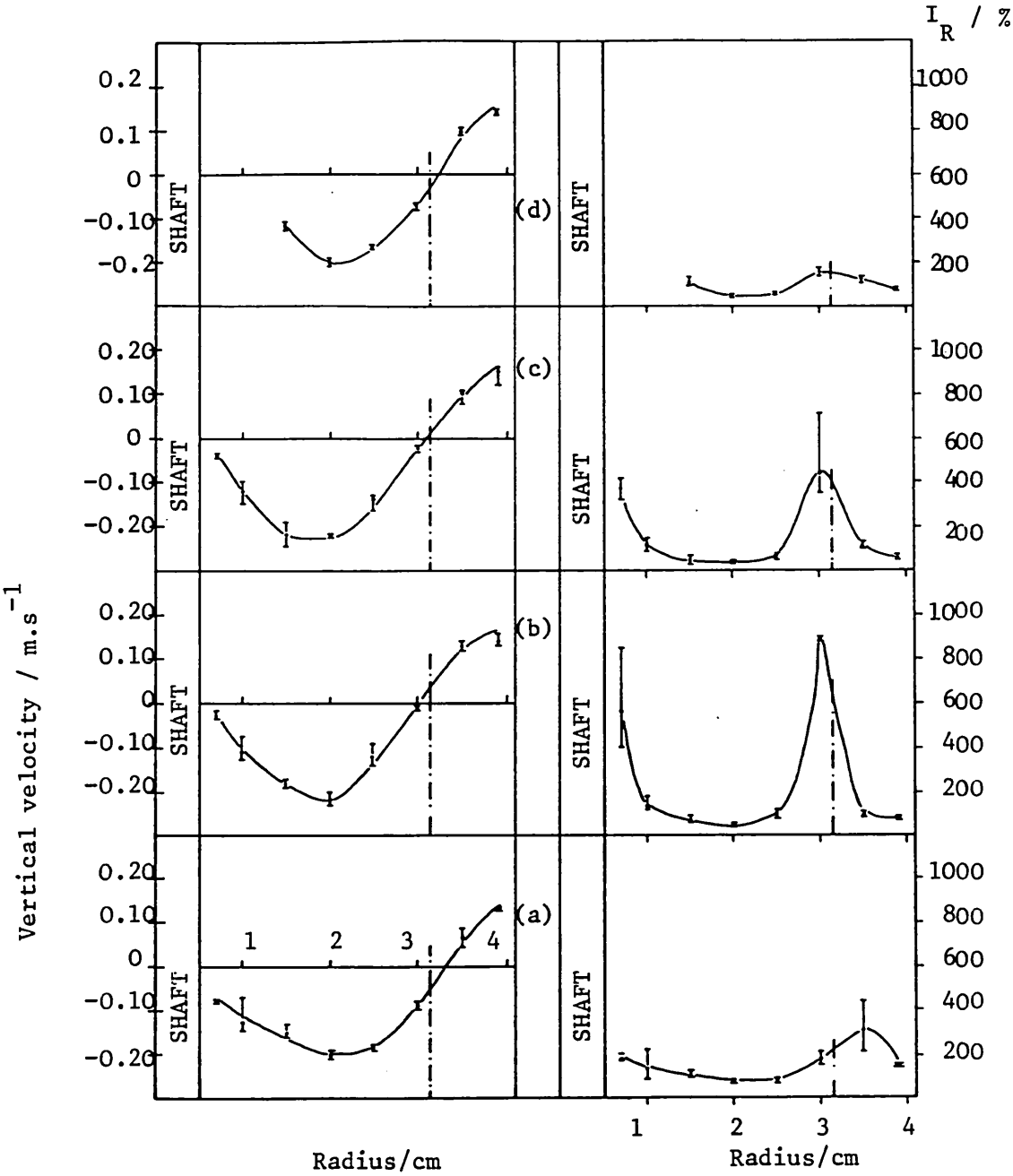


Figure 6.43 Vertical velocity profiles for 4–bladed paddle, at 400 rpm with 112 mm baffles
(a) z = 0.6 cm
(b) z = 2.6 cm
(c) z = 4.6 cm
(d) z = 6.6.cm

The turbulence intensity, I_R, is higher (20–40%) close to solid surfaces i.e., stirring shaft and wall, denoting more velocity fluctuations than in the middle of the reactor, where a stable value of 10% is obtained. These profiles are not much affected by vertical height in the reactor, although slightly higher values near shaft and wall are found closer to the paddle.

At the higher stirrer speed, 400 rpm (Figure 6.37), the velocity profiles are very similar to the ones at 150 rpm in the lower part ($z \leq 2.6$ cm) of the reactor, with a two maximum, relatively flat, curve ($R_1 \simeq 2.0$ cm and $R_2 \simeq 3.5$ cm). However, as distance from the agitator increases the second maximum, at $R_2 = 3.5$ cm, decays considerably becoming a hardly noticeable "bump", still at the same radial distance. These velocity profiles, at 150 and 400 rpm, agree closely in shape in the bottom section of the reactor, whereas dissimilarities arise in the top section. Again, the maximum tangential velocity, $v_{tmax} \simeq 1.0$ m.s^{-1}, is smaller than the tip speed at this stirrer speed, $V_{tip,400\ rpm} = 1.32$ m.s^{-1}.

If the same kind of scaling–up calculations based on tip speed, as mentioned earlier for the 2–bladed paddle (see page 169) are performed on the experimental results at 150 rpm, then the calculated velocity profiles agree closely near the paddle, although the discrepancies higher in the reactor still fall within the experimental error.

The turbulence intensity, I_R, at this stirrer speed shows the same trend with radial distance as at 150 rpm, but velocities are more stable and the maximum value only reaches 20%, at wall and shaft, and 10% at intermediate radial distance.

Next we consider the influence of baffles upon these velocity profiles:

Figures 6.38 and 6.39. Baffles (112 mm long) were introduced inside the reactor at 90 ° to the measuring grid and the previous measurements were repeated. The decrease in magnitude of the velocities at the two stirrer speeds and at all elevations in the reactor is evident and as expected from knowledge of the effect of baffles on tangential velocity of a radial–type impeller. At the lower stirrer speed , 150 rpm, and at the bottom of the reactor, z = 0.6 cm, the two maximum situation still persists, although less pronounced. A very flat velocity profile appears at z = 5.1 cm, which is just above the baffle tip; and the peaking in velocity only starts to appear at z = 8.1 cm, for a radial distance of R = 1.5 cm, much closer to the shaft than without baffles.

At 400 rpm there is a distinct change in the velocity pattern. The velocity profiles at all heights in the reactor exhibit a curious depression, which is small in magnitude and close to a radial distance of R = 2 cm in the lower part of the vessel, but gradually increases in magnitude and moves towards the wall of the reactor, reaching R $\simeq$ 3.0 cm. This behaviour is clearly dissimilar from the corresponding one without baffles and to the baffled situation at much lower speeds. The fluid velocity, v_t, is here at a maximum near the reactor wall.

It is interesting to note that the turbulence intensity, I_R, has increased near the shaft and the wall, as compared with the unbaffled case, and for the two stirrer speeds. This behaviour reflects the higher spread of velocities near solid surfaces when baffles have been introduced.

Turning now to vertical velocity, v_z, the velocity profiles at 150 rpm (Figure 6.40) do not show much difference with distance away from the agitator, only a decrease in the magnitude of the downwards flow in the bulk

of the vessel and upwards velocity by the wall. There is very little amount of downwards flow until a radial distance of R = 1.5 cm; peaking in velocity occurs between R = 2–2.5 cm; and flow reversal happens very close to the agitator tip.

The velocity profiles at the higher stirrer speed, 400 rpm, shown in Figure 6.41 are similar in shape at all heights in the reactor and also to the ones at 150 rpm, allowing for the obvious increase in magnitude. However, there are a few differences: downwards flow becomes more significant closer to the agitator shaft, at R $\simeq$ 1.0 cm, and peaking in velocity is shifted towards the right, at R $\simeq$ 2.5 cm.

The turbulence intensity, I_R, is high near the shaft and agitator tip, reflecting the fact that large velocity fluctuations occur, either in magnitude or in sign, when flow is reversed. Peak values reach 500%,at 150 and 400 rpm, near the agitator, but not much difference is detected with vertical height at both speeds.

The introduction of baffles should have the biggest influence on vertical velocity and that is confirmed in the results presented in Figures 6.42 and 6.43 (see Figures 6.40 and 6.41). At 150 rpm there is a marked increase in downwards flow very close to the agitator shaft by a factor of 5 to 6, in the lower sections of the reactor ($z \leq 2.1$ cm), and by a factor of 3 to 4 in the middle of the reactor. Very flat downwards flow profiles are obtained, with no peaking in velocity. The difference from the unbaffled case reduces at the the top of the reactor, where peaking in downwards flow reappears, although closer to the shaft (R $\simeq$ 1.5 cm) than in the non–baffled vessel. The increase in upwards flow is not so significant, except at z = 8.1 cm, where it increases by a factor of 3.

At 400 rpm, Figure 6.43, the introduction of baffles increases the amount of downwards flow, but to a lesser extent than at 150 rpm. There is still a peak in downwards velocity, which is broader and at a lower radial distance, R = 2.0 cm, than in the unbaffled case, with peak velocity remaining unchanged. There is a slight increase in upwards velocity at all heights, except close to paddle.

The turbulence intensity, I_R, is high near shaft and agitator tip, with exceptionally high values (800–900%) occurring for the baffled case at 400 rpm in the middle heights of the reactor. The other curves are similar for both the baffled and unbaffled reactor at both stirrer speeds.

The physical picture that emerges from these LDA measurements consists of a central core of fluid slowly going down but mainly swirling around the shaft, a fast spiralling down motion at R = 2.0 – 2.5 cm and then upwards movement, together with swirling motion, from flow reversal until the wall of the reactor. This three–dimensional view of the flow is valid for 150 and 400 rpm, without baffles and 400 rpm with baffles. In the case of the baffled reactor, at 150 rpm, the spiralling motion is absent and fluid movement is more plug like, with downward movement in the central core more pronounced than in all other cases.

This detailed quantitative flow characterisation by LDA is showing that the introduction of baffles is likely to cause the greatest influence on the particle size distribution of the polymerisation performed at the lower stirrer speed, since the major differences in the shapes of velocity profiles (both tangential and vertical) were found to happen at 150 rpm. This fact is the reflection of the greater efficiency of transfer of radial to vertical flow in the baffled reactor at the lower stirrer speed, 150 rpm.

These detailed velocity profile differences will change the circulation times and zone exchange frequencies of polymerising particles and should in turn be reflected on the balance between break–up and coalescence seen in the product particle size distributions. The vertical velocity profiles were used to obtain various circulation times in the reactor, as has already been done for the 2–bladed paddle (see page 171). The same assumptions were considered and Table 6.7 presents the circulation times for the 4–bladed paddle.

Table 6.7 Distribution of circulation times for 4–bladed paddle

RPM	Baffles	t_{min}/s	t_{av}/s	t_{max}/s	t_{max}/t_{min}
150	———	4.3	11.8	19.4	4.5
	Baffles	2.8	4.6	13.5	4.8
400	———	1.0	3.1	5.6	5.6
	Baffles	0.8	1.5	4.7	5.9

The results show that both stirrer speed and baffles decrease the various circulation time averages and confirm the earlier evidence that baffles were expected to cause the greatest influence at the lower stirrer speed. A droplet will come more often to the high elongational flow region of the agitator, and will therefore have more chances to be broken–up. A particle size distribution shifted towards smaller diameters might then be expected.

The introduction of baffles increases quite sharply the downwards velocity close to the shaft and also the upwards velocity by the wall. Near the wall this increase in velocity will increase the shear rate of the droplets past the stationary surface. This may cause severe droplet break–up, possibly with the formation of very small droplets. If these small droplets are below the actual diameter for coalescence, then an increase of droplet population at

the smaller size range might occur.

The high turbulence intensity values found for vertical velocity, at flow reversal, for the baffled case and especially at 400 rpm, reflects a region of highly localised extensional flow in the turbulent eddy structure. This could lead to droplet break–up, in addition to the high shear, extension rate region by the paddle, or close to the wall.

The knowledge of these detailed velocity profiles may also be used to calculate shear rate, $|\dot{\gamma}|$, based on the tangential or vertical velocity, so that actual values can be quoted for certain regions in the reactor. These calculations were done assuming velocity at wall was zero, and in Figures 6.44 and 6.45 are presented the shear rate values $|\dot{\gamma}|$, at both stirrer speeds based either on the tangential, v_t, or vertical velocity, v_z, respectively. Table 6.8 summarises the averaged shear rates for the bulk of the vessel and the wall region at both stirrer speeds, with and without baffles.

Table 6.8 Average shear rate for 4–bladed paddle, for the various agitation conditions.

RPM	Baffles	Average Shear Rate, $\|\dot{\gamma}\|/sec^{-1}$ Based on tangential velocity		Based on vertical velocity	
		Wall	Bulk	Wall	Bulk
150	———	130	25	32	10
	Baffles	125	25	54	10
400	———	374	50	58	20
	Baffles	433	50	76	20

These results show that the average shear rate at the bulk of the

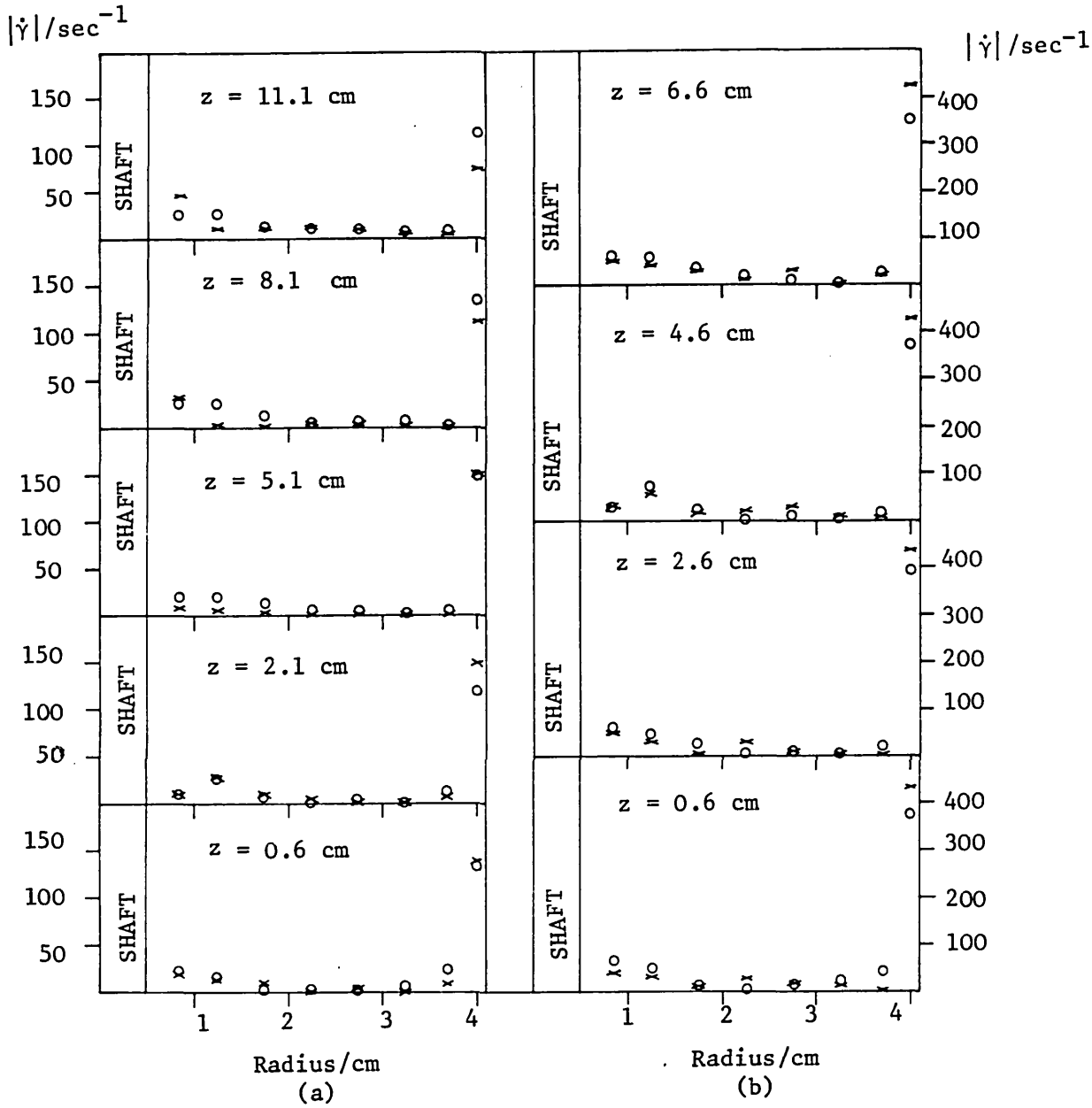


Figure 6.44 Shear rate profiles based on tangential velocity for 4-bladed paddle at

(a) 150 rpm
(b) 400 rpm
○ No baffles
× Baffles

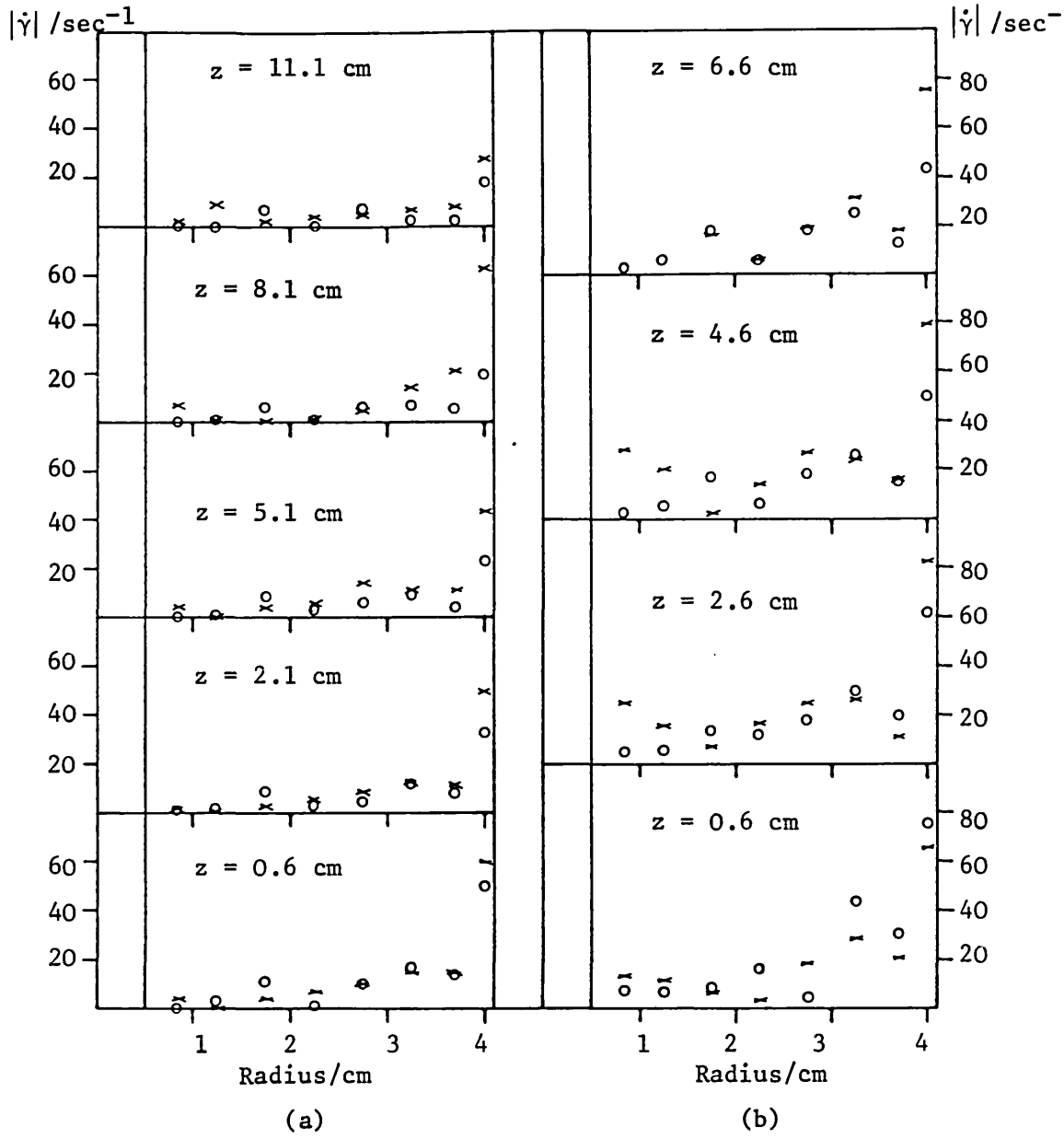


Figure 6.45 Shear rate Profiles based on vertical velocity for 4–bladed paddle at

(a) 150 rpm
(b) 400 rpm

o No baffles
× Baffles

vessel are always lower (10–35%) than at the wall and do not change with the introduction of baffles at both stirrer speeds. The wall shear rates show significantly increased values when baffles are present, with the biggest increase found for 150 rpm in the vertical direction.

(d) Comparison between "Mixflow" solution and LDA data.

It may be interesting to compare our measured velocity profiles using LDA with an existing computer prediction for a similar geometry.

A computer simulation of flow in a reactor agitated by a 4–bladed paddle and containing baffles was carried out using the program Mixflow [9]. This model assumes the agitator to be a source of energy and power and maps out velocity profiles within the reactor. All these components of velocity (axial, radial and tangential) are derived and presented as vector at several heights in the reactor and at different angular positions of agitator blade with respect to baffle position.[10]

To compare the two sets of results, radial and vertical positions were converted into percentage of total height to try to match the two grids as closely as possible.

The experimental values of vertical velocity correspond to a time average, whereas in the "Mixflow" solution the axial velocity is presented at different angular positions of blade versus baffle position. Therefore, for each grid position, the values at the various angular positions were averaged.

The generated "Mixflow" tangential and vertical velocity profiles are presented in Figures 6.46 and 6.47, respectively.

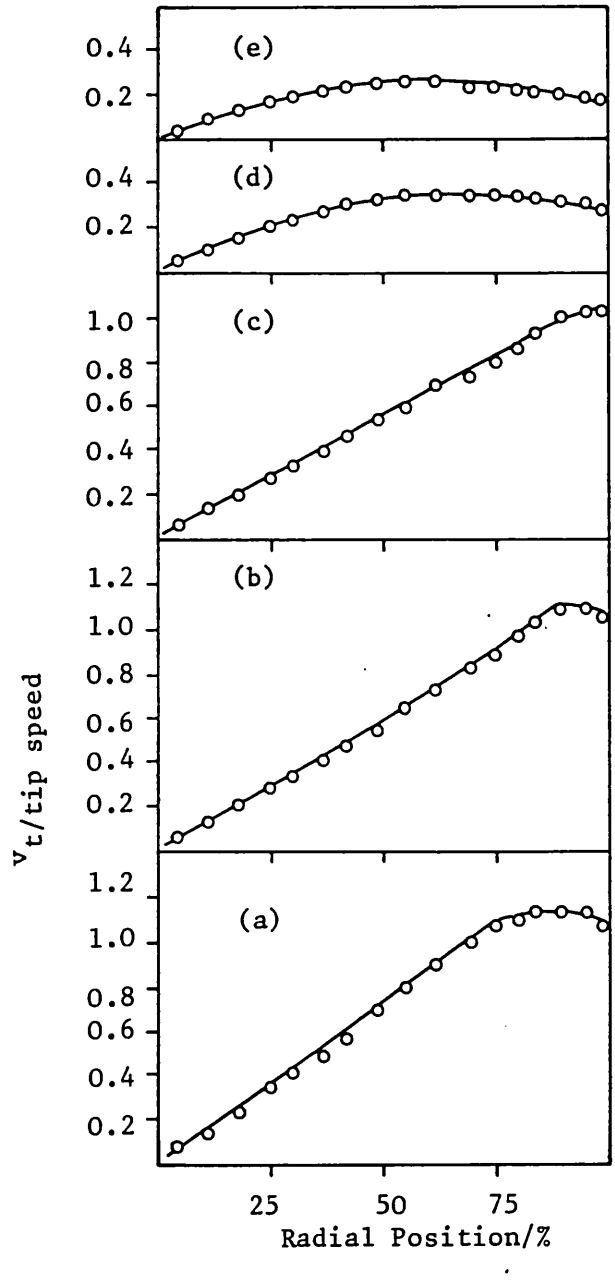


Figure 6.46 "Mixflow" Simulation Profiles of tangential velocity

(a) z = 5.7% of total height (b) z = 26.8% of total height

(c) z = 33.6 of total height (d) z = 70.5% of total height

(e) z = 97.2% of total height

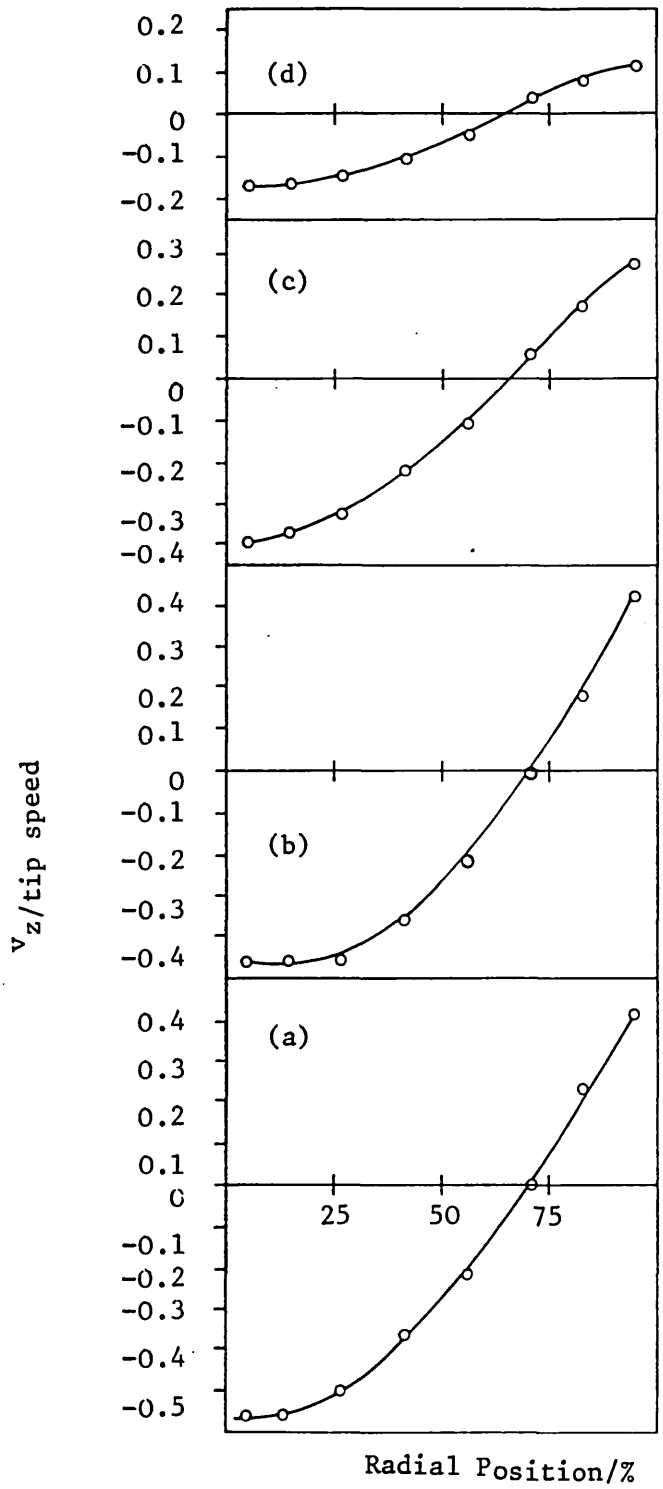


Figure 6.47 "Mixflow" simulation profiles of vertical velocity

(a) z = 15.2% of total height
(b) z = 37.6% of total height
(c) z = 54.9% of total height
(d) z = 81.2% of total height

Looking first at the tangential velocity profiles, Figure 6.46, they are much steeper than the corresponding experimental values (see Figures 6.38 and 6.39) for vertical heights below 70% of total height, with the maximum velocity exceeding the tip speed. The upper reactor profiles, above 70% of total height, exhibit very flat curves, only reaching 30% of the corresponding tip speed. No difference can be found in the shape of the velocity profiles immediately above or below baffle tip. The measured tangential velocity profiles show a more marked changing pattern with increasing vertical height, with a dividing line at baffle tip, where an extremely flat velocity profile was obtained at 150 rpm. Also, experimental maximum velocities are always below the corresponding tip speed and therefore the reduced Mixflow data, v_t/V_{tip}, do not superimpose on the experimental profiles quantitatively especially near the agitator tip.

Regarding vertical velocity, Figure 6.47, the generated "Mixflow" profiles seem to compare reasonably well with the experimental ones (see Figures 6.42 and 6.43), except at the top region of the reactor where no peak in downward velocity is found. As for tangential flow, the ratio of v_z/V_{tip} is always higher than in the measured profiles.

6.3.2 Suspension Polymerisation Experiments

(a) Choice of Polymerisation Recipe

The polymerisation recipe for this geometry was optimised in terms of suspending agent concentration. All other variables remained the same as in the case of the 2–bladed paddle: the initiator was AIBN at a concentration of 10 $g.l^{-1}$ (based on dispersed phase volume), the phase volume of styrene was 0.20, the reactor was 3/4 full (the batch volume was 750 ml) and the

suspending agent was Gohsenol GH23, as before.

A range of suspending agent concentrations were tested at 400 rpm, from a value of 2.5 $g.l^{-1}$ to 3.67 $g.l^{-1}$. The results of such polymerisations are presented in Table 6.9.

Table 6.9 Variation of suspending agent concentration for 4–bladed paddle polymerisations

T/C	POLYMER	[PVA]/$g.l^{-1}$	Comments on stability of system
80	17	2.5	unstable
78	18	2.92	stable, but big granules present
78	19	3.125	stable
80	20	3.33	stable
78	21	3.67	stable, but larger than usual aggregates

Polymerisation conditions:
PVA – Gohsenol (GH–23) ; AIBN – 10 $g.l^{-1}$; 400 rpm
20% styrene ; reactor 3/4 full ; 8 hour reaction

The first PVA concentration tried, 2.5 $g.l^{-1}$, did not yield a stable system, even though this same concentration had been successfully used with the 2–bladed paddle at 500 rpm, which corresponds to a tip speed of V_{tip} = 1.31 $m.s^{-1}$ very close to the value V_{tip} = 1.32 $m.s^{-1}$ for this present geometry at 400 rpm.

The particle size distributions of the whole contents of the reactor for polymers 18–21 are shown in Figure 6.48. As in the case of the previous geometry, the final polymer consisted of single beads and aggregates, with most of the particles in the upper size band (262–564 μm) and there was not much difference between the aggregates of the various polymers. If these

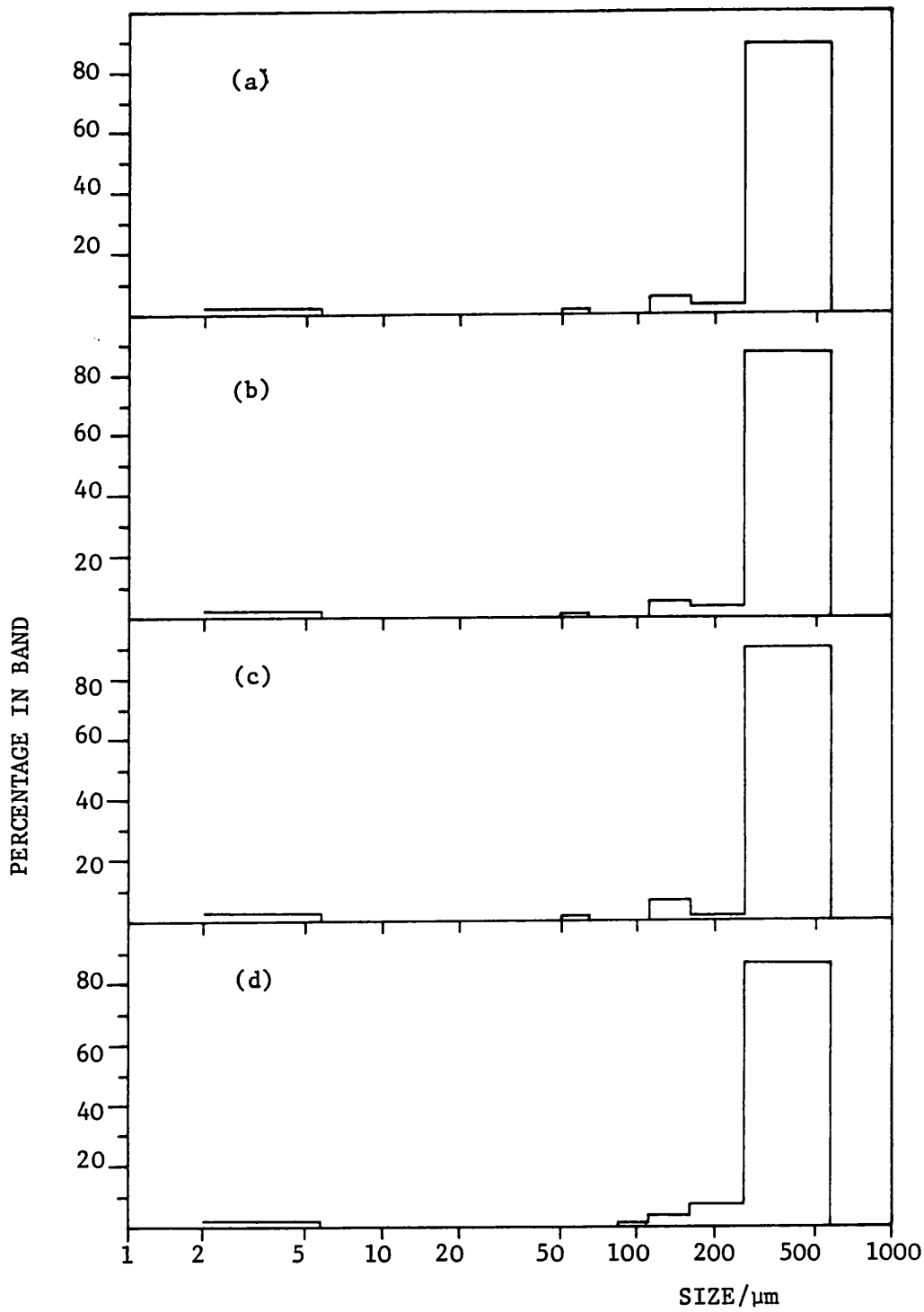


Figure 6.48 Effect of suspending agent concentration on the particle size distribution of polystyrene obtained with 4–bladed paddle, at 400 rpm

(a) [PVA] = 2.92 $g.l^{-1}$ (PS18) (b) [PVA] = 3.125 $g.l^{-1}$ (PS19)

(c) [PVA] = 3.33 $g.l^{-1}$ (PS20) (d) [PVA] = 3.67 $g.l^{-1}$ (PS21)

aggregates were subjected to ultra–sound treatment in the Malvern Sample Cell, then they broke down into individual beads within 60 second. This was confirmed by visual microscope examination. The particle size distribution of the broken down polymer samples can be seen in Figure 6.49, where three size regions can be distinguished: the majority of the particles lie within the range 100–564 μm, an intermediate size arises between 5.8 and 100 μm, with a much smaller proportion of particles, and then fine particles below 5.8 μm. This particle size distribution contrasts with the one for the aggregates, without the ultra–sound treatment, Figure 6.48, where the majority of the particles are in the 100–564 μm size range, and mostly in the upper size band (262 –564 μm), with a smaller amount of fine particles, below 5.8 μm.

The results of Figure 6.49 show that the size distributions of Polymers 18–20 are similar, with the most populated band at 112.8–160.4 μm, whereas this band is shifted to the next size range (160.4 – 261.7 μm) for Polymer 21, which corresponds to the highest PVA concentration. The presence of big granules ($\bar{d} \simeq 1000$ μm) in Polymer 18, indicated that the system was not entirely stable, but the next higher concentration of suspending agent – 3.125 $g.l^{-1}$ (Polymer 19) yielded a stable system, without over protection, which was chosen as the best PVA concentration to carry out further work.

As already mentioned the polymer obtained consisted of single beads plus some aggregates, which in the case of Polymer 19 consisted of 5–7 individual translucent beads, typically, stuck together by some whitish fine particles. Also these aggregates seemed to be bonded more strongly than in the previous geometry, judging by the increased ultra–sound time (60 s, instead of 15 s) needed to break them down into individual beads. This behaviour could be due to the smaller particle size in the 4–bladed paddle geometry compared to that in the 2–bladed paddle case, for the same stirrer

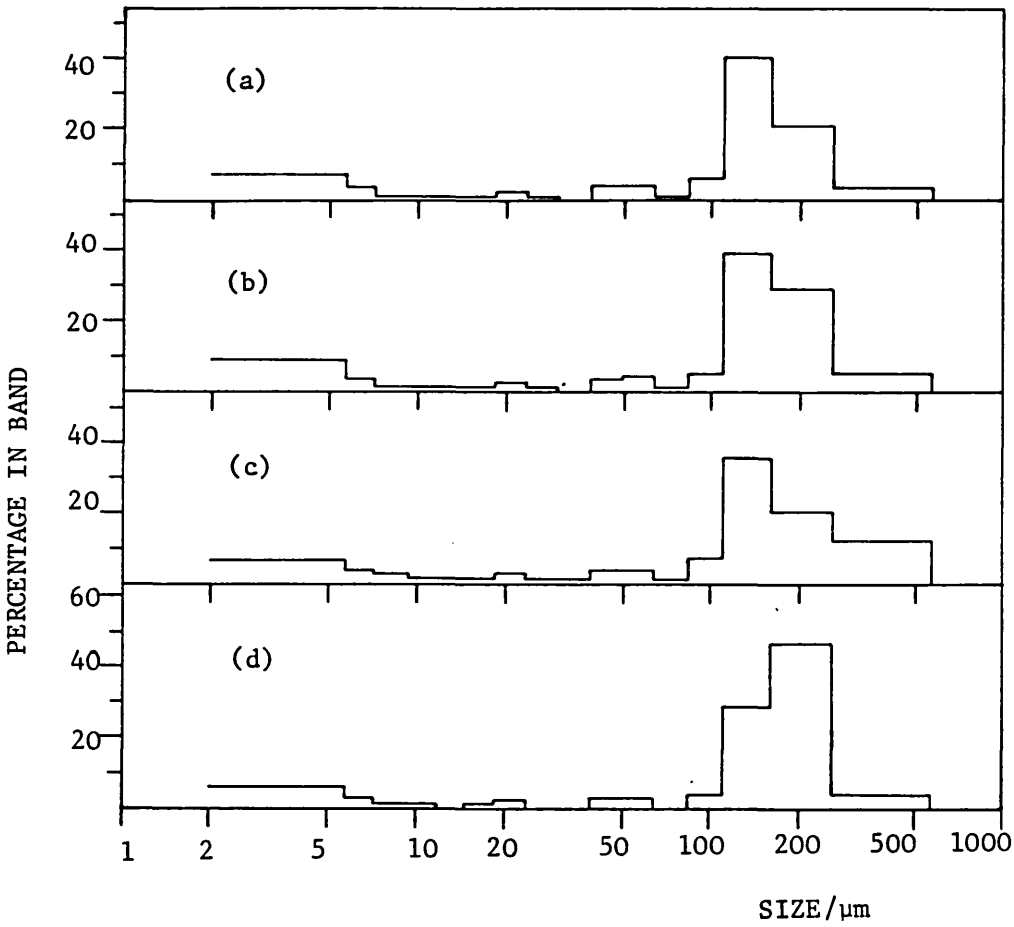


Figure 6.49 Effect of suspending agent concentration on particle size distribution of polystyrene obtained with 4–bladed paddle, at 400 rpm, but when subjected to 1 min ultra–sound treatment.

(a) [PVA] = 2.92 $g.l^{-1}$ (PS18) (b) [PVA] = 3.125 $g.l^{-1}$ (PS19)
(c) [PVA] = 3.33 $g.l^{-1}$ (PS20) (d) [PVA] = 3.67 $g.l^{-1}$ (PS21)

speed, which produces a higher contact surface area for aggregation.

The instability of the system at 2.5 $g.l^{-1}$ (Polymer 17) producing agglomeration is explained by the smaller average diameter ($\overline{d} \simeq 140$ μm) of the main peak in the case of the complex geometry at 400 rpm (and hence significant larger particle surface area), as compared with a similar system at the same tip speed (500 rpm) for the simple geometry ($\overline{d} = 175$ μm). This evidence may suggest that for the same tip speed a droplet on the complex geometry will have a higher frequency of transit through the agitator zone, since this is the reactor's region where most of the droplet break–up process is likely to occur.

(b) Variation of agitation conditions : stirrer speed and baffling

The agitation conditions examined here were not exactly the same ones under which flow characterisation had been carried out. Stirrer speeds of 200 and 400 rpm, both with and without baffles, where chosen for the polymerisation experiment; the value of 200 rpm instead of the 150 rpm used in the flow experiments was due to the fact that at 150 rpm monomer dispersion was not sufficient and all the styrene was gathered by the shaft. This prevented any successful polymerisation run at 150 rpm and it was necessary to move to the nearest stirrer speed capable of achieving effective monomer dispersion, which was 200 rpm. This small difference is not expected to have a major effect.

These polymerisation runs were also devised to obtain further information about the evolution of the particle size distribution with time and samples were taken from the reactor at several time intervals. The sampling

technique employed consisted of using a 25 ml glass pipette with a bore of 3 mm that was introduced into the reactor through an available entry port and withdrawing samples by suction To prevent subsequent droplet coalescence in the sample, especially during the initial stages of polymerisation, the samples (V ≃ 10 ml) were immediately transferred into a bottle containing 10 ml of an aqueous solution of PVA (0.5%, by weight). The sudden temperature change from 80 °C to room temperature ensured that no further reaction would take place.

Table 6.10 presents the agitation conditions used in the suspension polymerisations with the 4–bladed paddle.

Table 6.10 Agitation conditions for suspension polymerisation of styrene in complex geometry.

POLYMER	STIRRER SPEED	BAFFLES	T/C
22	200	———	80
23	200	112 mm	80
24	400	———	78
25	400	112 mm	80

Polymerisation conditions
PVA = GH–23 : 3.125 $g.l^{-1}$
AIBN = 10 $g.l^{-1}$
20% styrene
3/4 full reactor
8 hour reaction

The particle size distribution results are described in section 6.3.3 (a) below.

6.3.3. Polymer and Process characterisation

(a) Particle Size Distribution

The evolution of the particle size distribution of polymers 22 to 25, corresponding to the various agitation conditions presented in Table 6.10 can be seen in Figures 6.50 to 6.59, respectively.

Looking first at the results at 200 rpm, without baffles, Figure 6.50, the initial size distribution at t = 0 h shows that the majority of the droplets had diameters above 160 μm. The proportion of droplets with bigger diameter decreased with time and after 1.5 hours the main peak between 260 and 560 μm had dropped from 60% to approximately 25%. At the same time, a smaller, secondary peak had been established around 20 μm and some very fine particles (d < 5.8 μm) had also been formed. One hour later, t = 2.5 h, the system seemed to be stable, with the relative positions of the two peaks constant, although the peak at ~ 20 μm had become much larger than the one centred on 350 μm. The proportion of fines (d < 5.8 μm) seemed unchanged. At this stage, the particle size distribution exhibited was probably the result of a dynamic steady–state equilibrium between break–up and coalescence. At around 3 hours this dynamic steady–state equilibrium became markedly disturbed, presumably by a sharp decrease in the rate of particle break–up. Net aggregation occurred and a major change was noted: the particle size distribution shifted towards larger diameters with most of the particles being compressed into a main peak at 260–560 μm. This peak accounted for 90% of the whole distribution. After this step change the particle size distribution remained essentially frozen until the end of the polymerisation. If the contents of the whole reactor were subjected to ultra–sound treatment in the Malvern Sample Cell for a period of 5 minutes, then a particle size

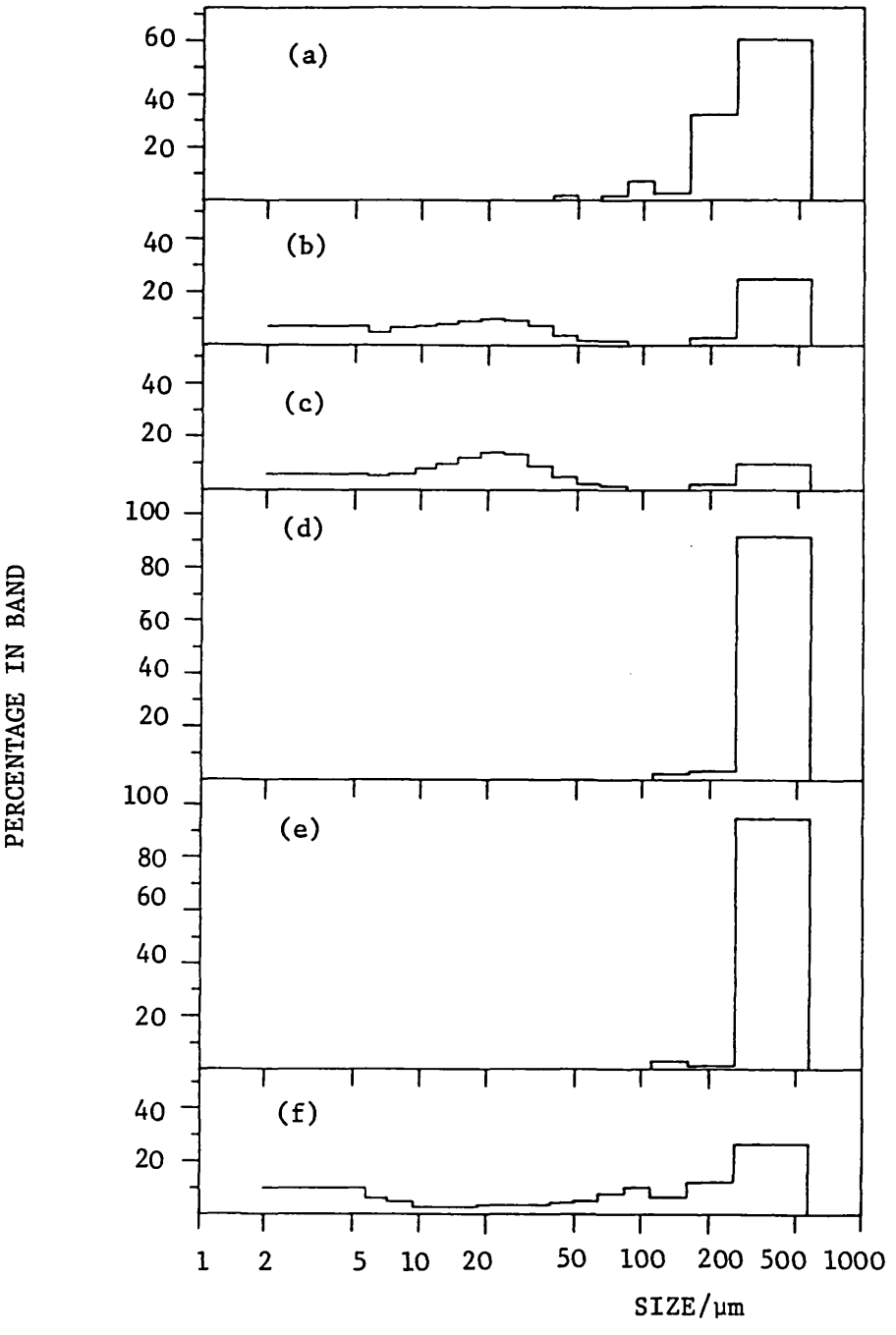


Figure 6.50 Evolution of particle size distribution as a function for suspension polymerisation of styrene at 200 rpm, without baffles, with 4–bladed paddle.

(a) t = 0 h
(b) t = 1.5 h
(c) t = 2.5 h
(d) t = t_{agg} = 2.77 h
(e) t = 8 h
(f) t = 8 h (after ultra–sound treatment)
Temperature = 80 C

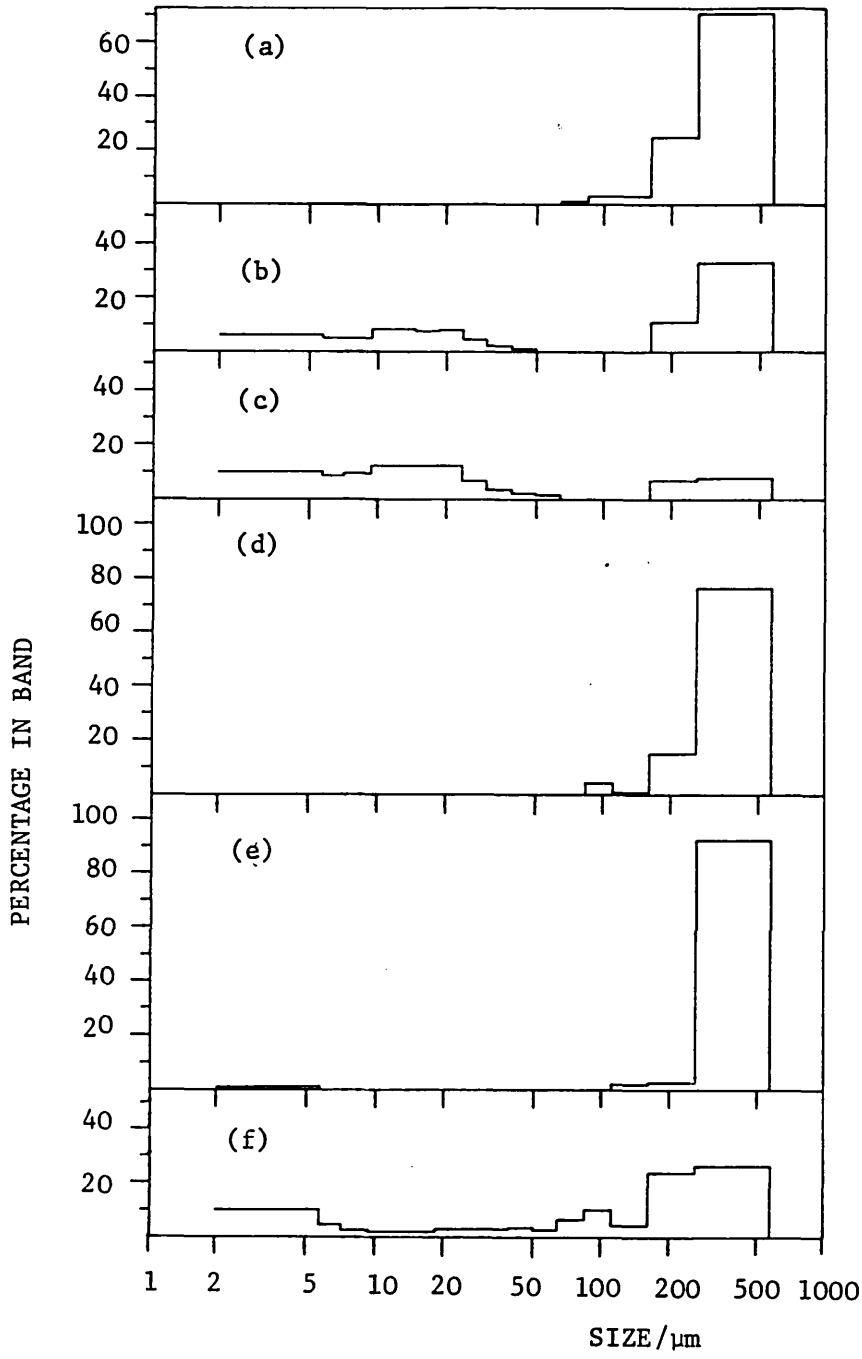


Figure 6.51 Evolution of particle size distribution with time for suspension polymerisation of styrene, with 4–bladed paddle, at 200 rpm, with 112 mm baffles.

(a) t = 0 h
(b) t = 1.5 h
(c) t = 2.5 h
(d) $t = t_{agg} = 2.73$ h
(e) t = 8 h
(f) t = 8 h (after ultra–sound treatment)
Temperature = 80 C.

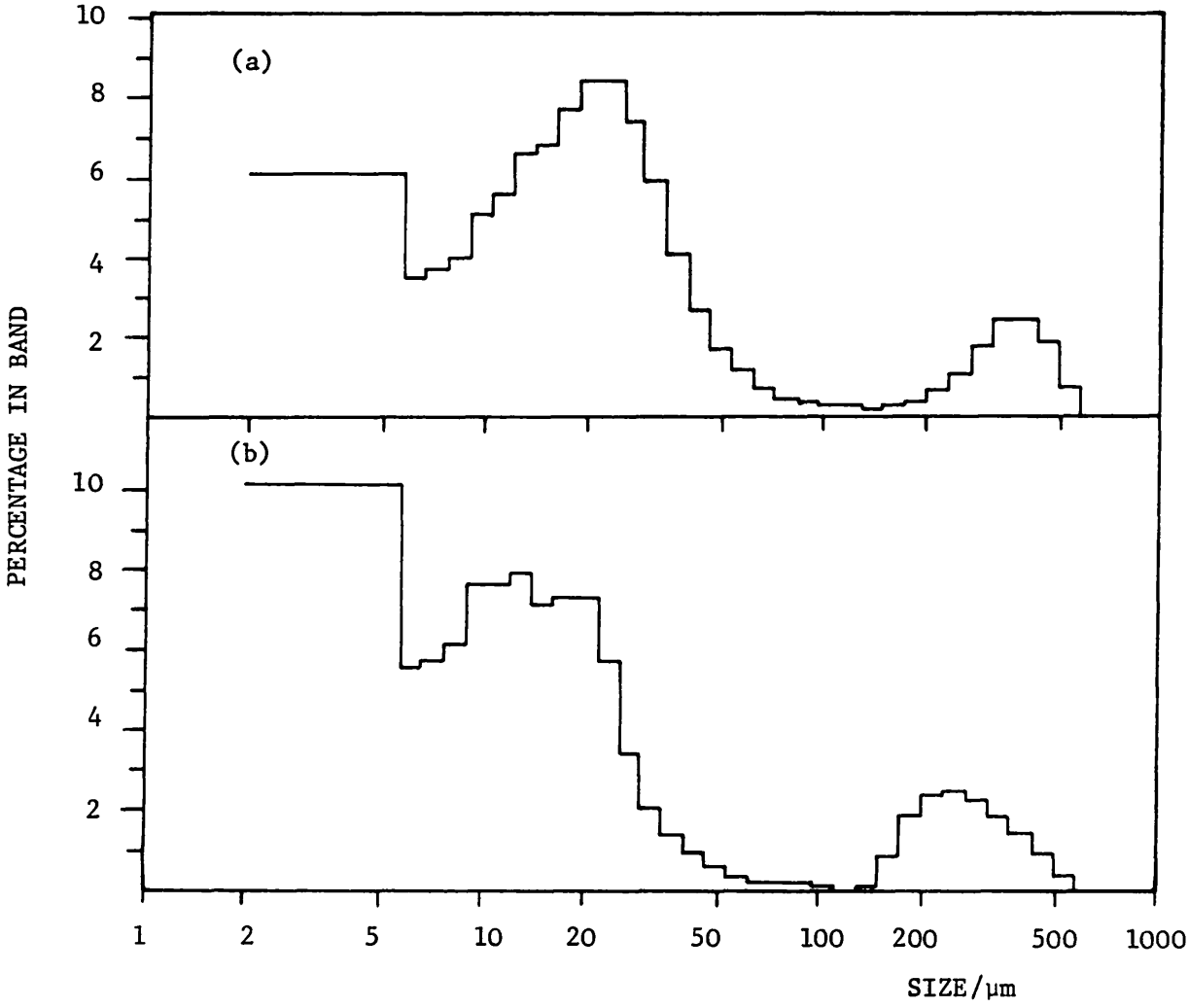


Figure 6.52 High resolution particle size distribution at t = 2.5 h for the complex geometry at 200 rpm, with and without baffles

(a) Polymer 22 – 200 rpm – no baffles
(b) Polymer 23 – 200 rpm – 112 mm baffles

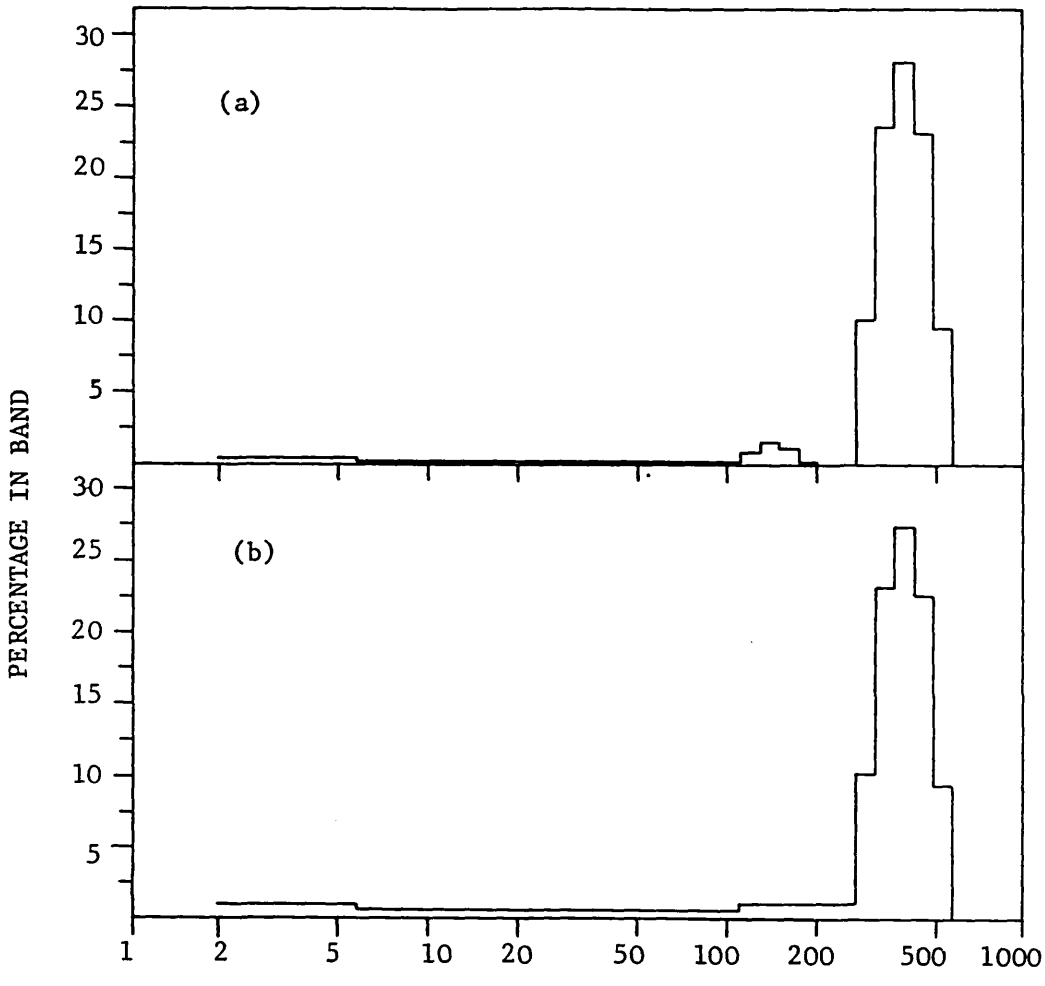


Figure 6.53 High resolution particle size distribution for the final product, for the complex geometry, at 200 rpm

(a) without baffles
(b) with baffles

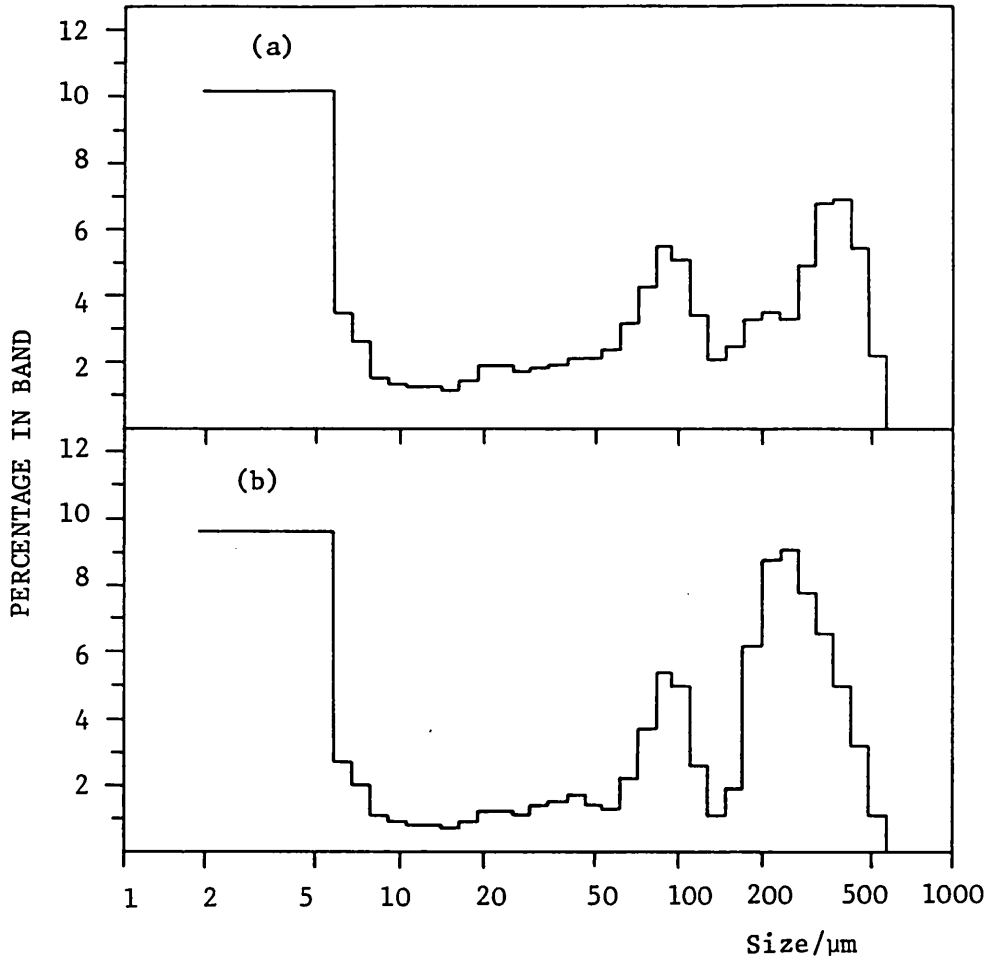


Figure 6.54 High resolution particle size distribution for the final product, after ultra–sound treatment, for the complex geometry, at 200 rpm
(a) without baffles
(b) with baffles

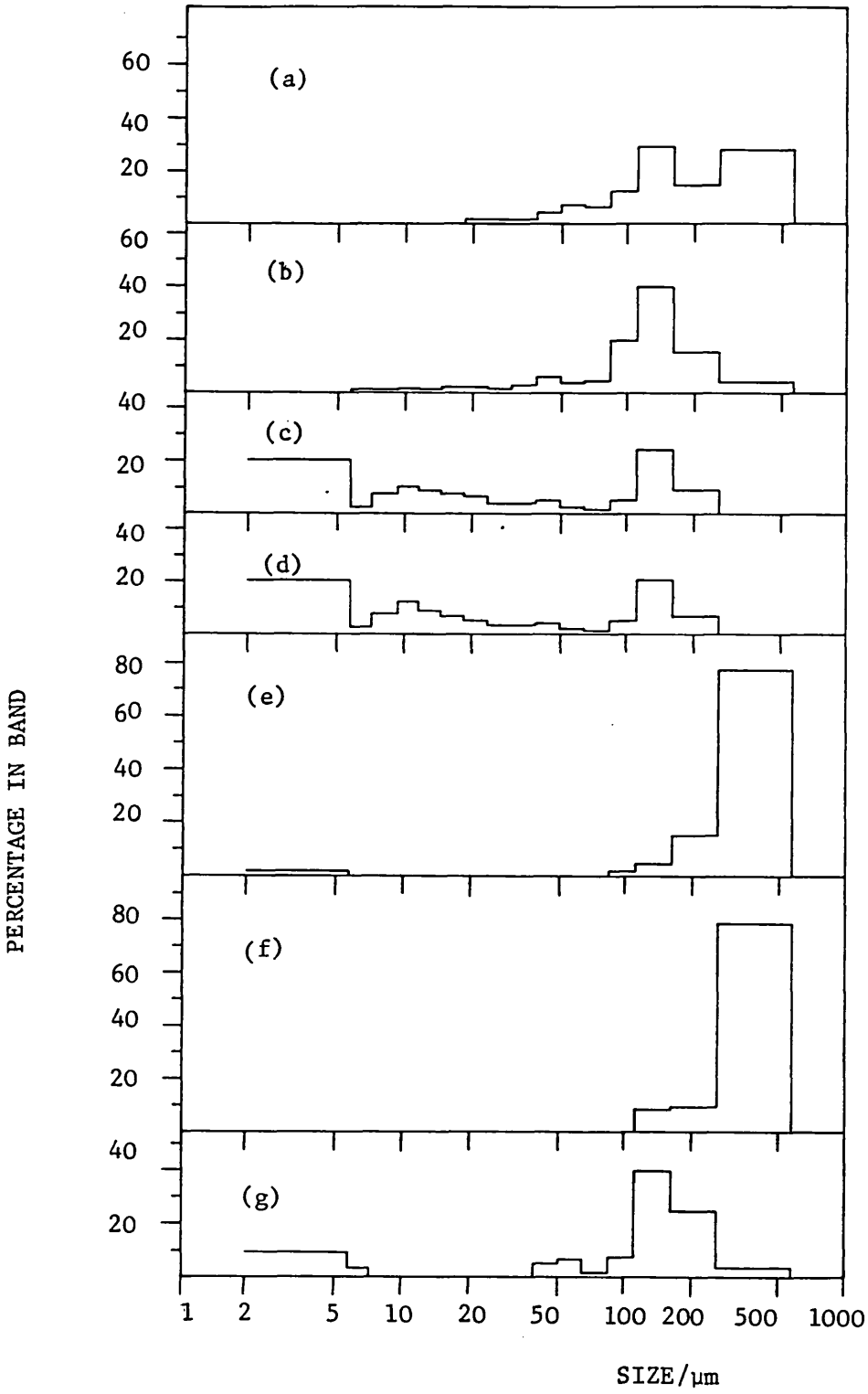


Figure 6.55 Evolution of particle size distribution with time for styrene suspension polymerisation with 4–bladed paddle, at 400 rpm, without baffles.

(a) t = 0 h (b) t = 0.5 h
(c) t = 1.5 h (d) t = 2.5 h
(e) $t = t_{agg} = 3.17$ h (f) t = 8 h
(g) t = 8 h (after ultra–sound treatment)
Temperature = 78 C

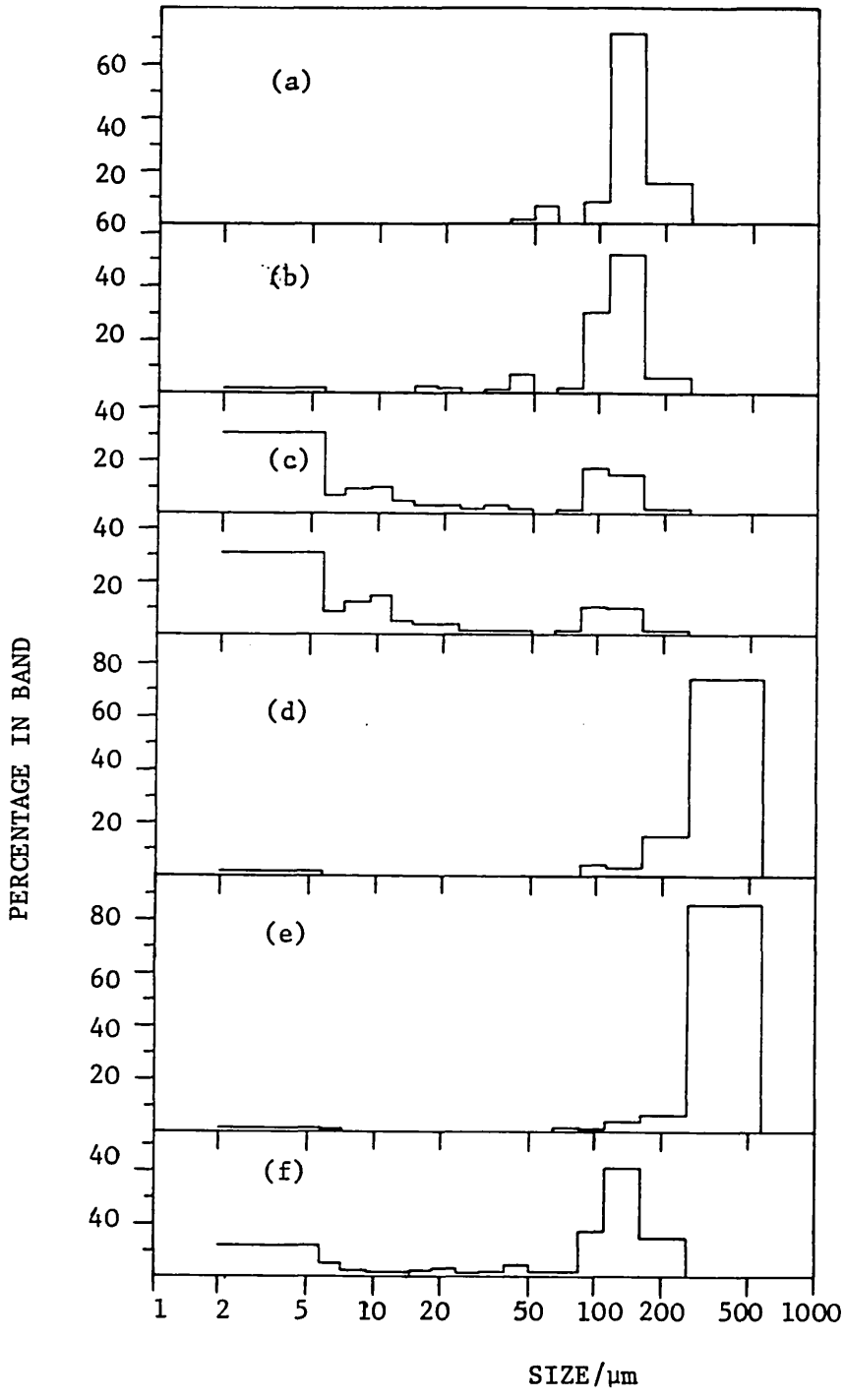


Figure 6.56 Evolution of particle size distribution with time for suspension polymerisation of styrene with 4–bladed paddle, at 400 rpm, with 112 mm baffles.

(a) t = 0 h (b) t = 0.5 h

(c) t = 1.5 h (d) t = 2.5 h

(e) $t = t_{agg} = 2.83$ h (f) t = 8 h

(g) t = 8 h (after ultra–sound treatment)

Temperature = 80 C

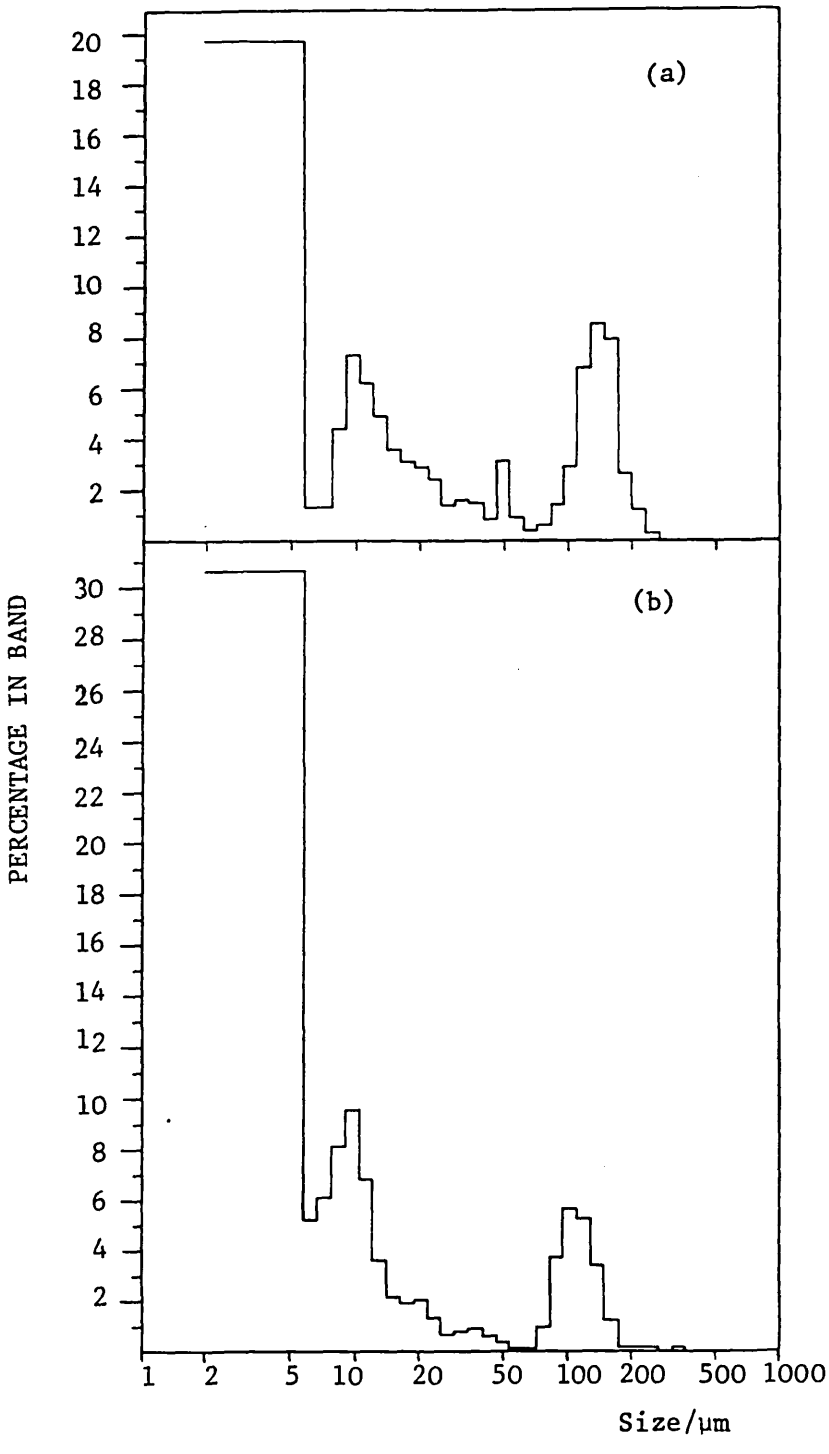


Figure 6.57 High resolution particle size distribution at t = 2.5 h for

(a) Polymer 24 – 400 rpm – no baffles
(b) Polymer 25 – 400 rpm – 112 mm baffles

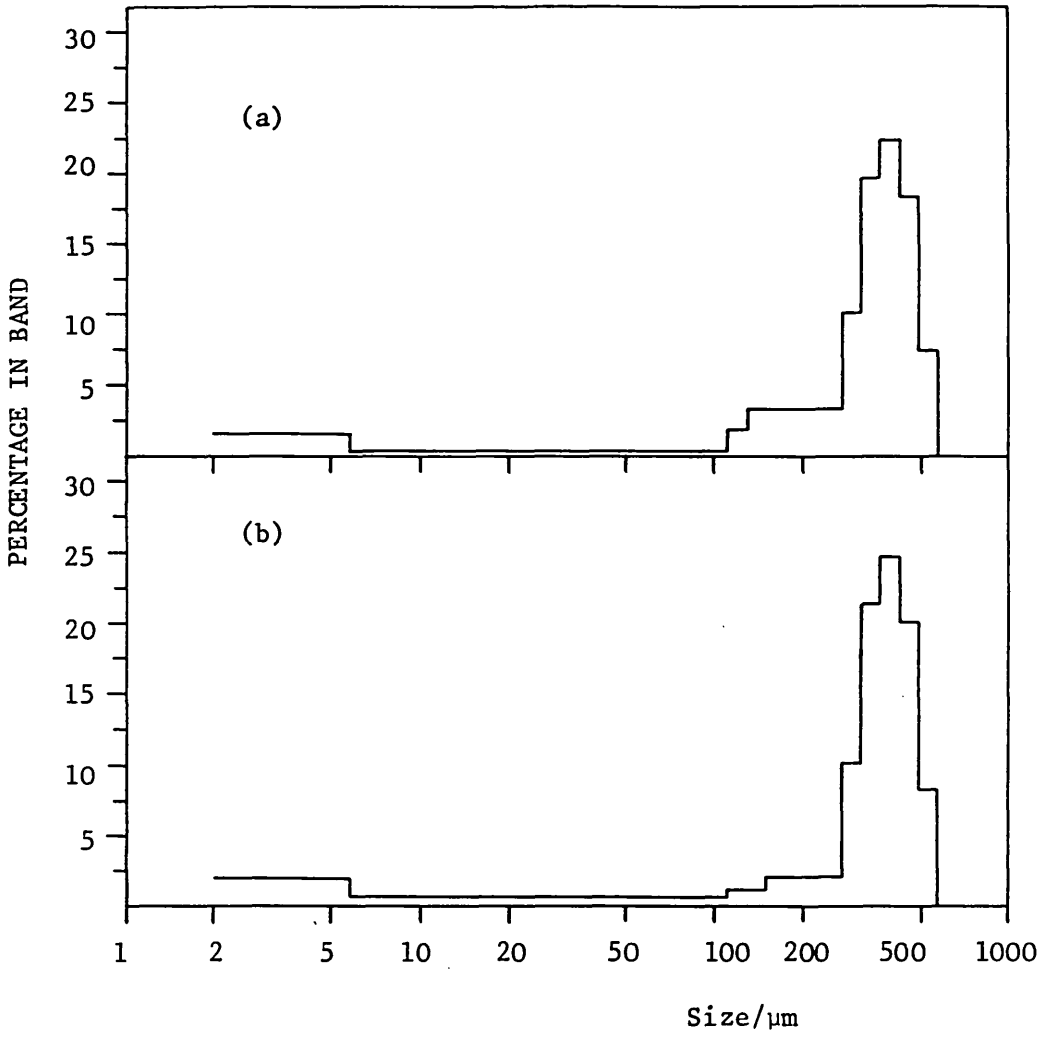


Figure 6.58 High resolution particle size distribution for the final product, for the complex geometry, at 400 rpm

(a) without baffles
(b) with baffles

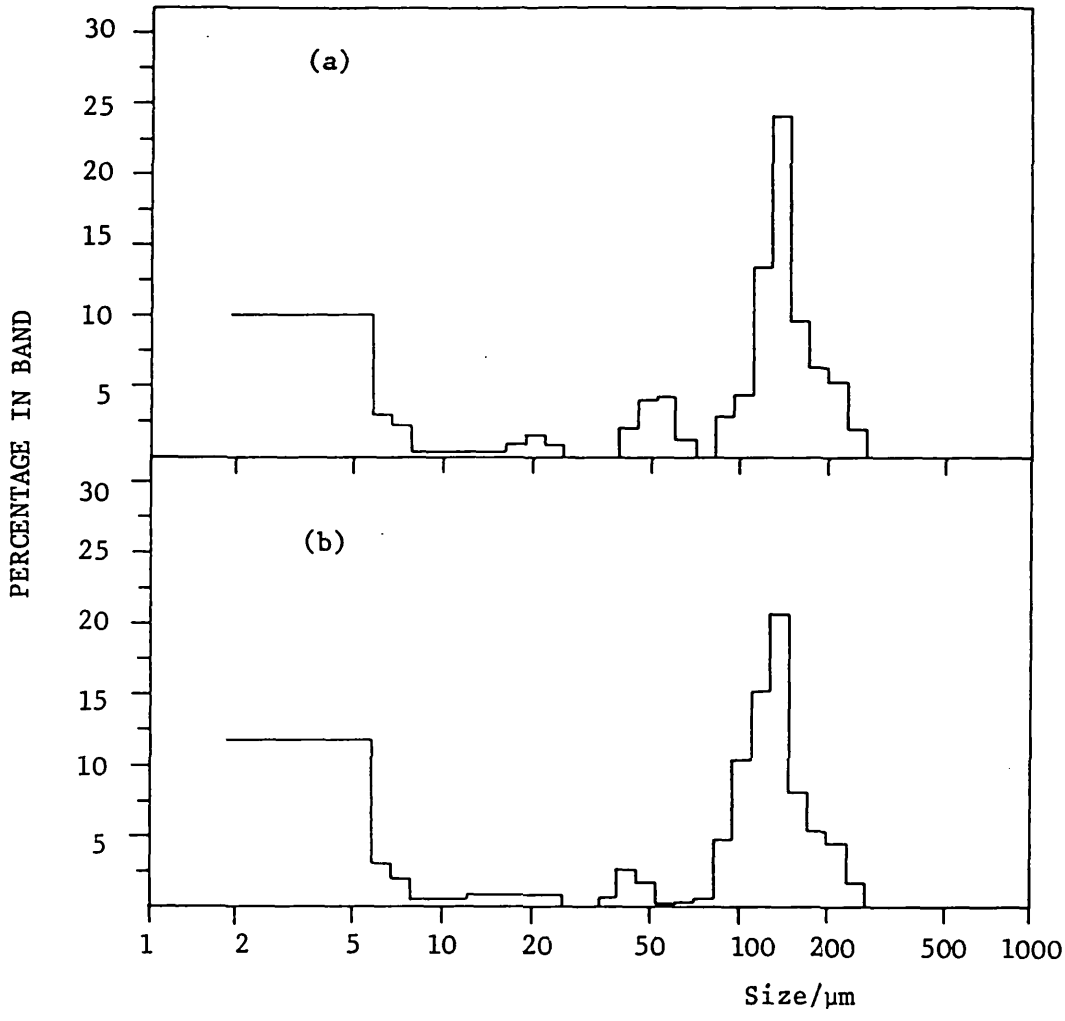


Figure 6.59 High resolution particle size distribution for the final product, after ultra–sound treatment, for the complex geometry, at 400 rpm

(a) without baffles
(b) with baffles

distribution very similar to the one at t = 2.5 h was obtained. This partial reversibility of the PSD (particle size distribution) seemed to support the suggestion (and visual microscope observation) that the onset of aggregation was based on a relatively weak physical interaction of coherent particles, rather than a chemical attachment or a true coalescence in which they loose their identity.

If baffles were introduced, the resulting PSD, Figure 6.51, at all sampling times seemed to be very similar to the previous ones without baffles. This behaviour appeared to be in contradiction with the expected consequences of the flow characterisation results, where a considerable increase in vertical flow (especially downwards) and decrease in tangential velocity were found, leading to smaller circulation times (see Table 6.7). In this case, a droplet would return more frequently to the high shear/elongational flow region by the paddle (see Table 6.8), with more opportunities to break–up, hence a smaller mean diameter might be expected. In Figures 6.52 to 6.54 (a) and (b) are shown the higher resolution particle size distributions (32 size range) at t = 2.5 h, t = 8 h (no ultra sound) and t = 8 h (after ultra sound) for the non–baffled and baffled reactor, respectively. These figures revealed that in fact there were small but significant shifts to lower particle sizes when baffles were introduced, consistent with the argument mentioned above. For example, at t = 2.5 h (Figure 6.52), the peak at the higher size range occured at a smaller diameter for the baffled diameter: d_1 = 250 μm than for the unbaffled reactor; d_1 = 365 μm. The mean size of the other peak in the smaller size range had also decreased, from d_2= 22 μm to d_2 = 13 μm.

At the higher stirrer speed, 400 rpm, without baffles, Figure 6.55, the initial droplet size distribution had a different shape than that at 200 rpm. There were two equal size peaks at 112–160 μm and 260–560 μm. The peak

at 260–560 μm starts being broken–up, and at t = 0.5 h was very much reduced, while the peak at 112–160 μm increased in volume fraction. At t = 1.5 h the higher size band had disappeared completely and very fine particles, d < 5.8 μm, had been formed, as well as the intermediate family at approximately 10 μm. The peak at 112–160 μm seemed stable. This size distribution was essentially unchanged after t = 2.5 h, showing that the dynamic equilibrium (see page 6.62) had already been established at t = 1.5 h, which was earlier than in the case at the lower stirrer speed. The earlier occurrence of the dynamic steady–state equilibrium between coalescence and break–up at 400 rpm, than at 200 rpm had already been suggested by the previous flow characterisation results from the dynamic video monitoring system (see page 6.39), whereby an increase in stirrer speed was found to cause a decrease in time by the agitator and vortex, and a faster equilibrium droplet size distribution was therefore expected.

At around 3 hours the aggregation process starts to dominate and the same comments are applicable as at 200 rpm. Comparing the results at those two tip speeds, without baffles, the rate at which the dynamic equilibrium was achieved was higher for the higher tip speed; the two distributions are similar, although shifted towards smaller size range at the higher stirrer speed. This behaviour was expected from the results of flow characterisation : higher velocities, both vertical and tangential, mean that the polymerising droplet will have smaller circulation times (see Table 6.7) in the reactor, hence going past the agitator region more often and being broken–up at a higher rate.

Introducing baffles caused the faster initial disappearance of droplets at the higher size range, Figure 6.56, although the shape of the latter distributions seemed very similar. The amount of fines, d < 5.8 μm, seems to increase and the distribution is slightly shifted towards smaller size range than in the case

of the unbaffled vessel. Again, the dynamic equilibrium seemed to be reached after 1.5 h. At this higher stirrer speed baffles have their strongest influence on the initial stages of the polymerisation, when they are effective in the process of droplet break–up i.e. they reduce the average diameter quickly. Afterwards, their effect on the rate of achieving dynamic equilibrium was slight, since this was also established by t = 1.5 h, as in the unbaffled case. Again, a high resolution size distribution can be used to compare the PSDs at t = 2.5 h, t = 8 h (no ultra–sound) and t = 8 h (after ultra–sound) : Figures 6.57 to 6.59 (a) and (b) for the unbaffled and baffled vessel respectively. The mean diameter of the peak at higher size for the unbaffled vessel, d_1 = 140 μm, was higher than the corresponding one for the baffled case, d_1 = 104 μm; while the peak of the secondary distribution remained unchanged, although somewhat narrower, for the PSD at t = 2.5 h (Figure 6.56). Similar shifts in particle size can also be recognised for the other distributions at t = 8 h with and without ultra–sound treatment (Figures 6.58 and 6.59).

These results show the extent to which baffles influence the particle size evolution in a suspension polymerisation. Baffling has caused its most dramatic effects upon the polymerisation runs at the lower stirrer speed, which was expected from the LDA results, where major differences had arisen in the velocity profiles with and without baffles.

The polymerisations carried out at both stirrer speeds reveal the existence of fine particles (d < 5.8 μm), which increase considerably when baffles were introduced, either at 200 or 400 rpm. This evidence suggests that their formation is linked with flow characteristics in the reactor. The presence of fine particles (d < 5.8 μm) was also reported by Tehrani [11] when polymerising styrene in suspension in a flow cell, using the same system.

These particles were absent when non–polymerising droplets were subjected to model flow yields (extensional or rotational) and hence attributed to a chemical effect. A chemical effect, namely self–seeded emulsion polymerisation might be responsible to a certain extent. However, it is also likely that droplet break–up near the agitator proceeds with the formation of tiny satellite droplets, as described in [12] and [13] where it was found that big and viscous drops are more easily pulled out into liquid threads (which then burst with satellite droplet formation) than small and inviscid drops. Such a mechanism for droplet break–up could account for the presence of such small drops, which are smaller than the critical diameter for coalescence, and whose volume fraction increases during the period when droplet break–up is still possible. The observed increase in the amount of fines when baffles are introduced, either at 200 or 400 rpm, could also be explained by the higher shear ratio at the wall, causing severe droplet break–up (see page 228). Hence, wall surface "smoothness" could play an important role in the coalescence/break–up balance.

The decrease of polymerisation temperature to 75.5 °C and the resulting increase of time of aggregation is highlighted in Figure 6.60, where the evolution of the PSD with time, from the achievement of the dynamic equilibrium onwards, can be seen. At t = 2.5 h the size distribution is essentially the same at t = 1.5 h and very similar to the one shown in Figure 6.55, with the same agitation conditions, but at a different temperature (T = 78 °C). One hour later, t = 3.5 h, the decrease in the rate of droplet break–up is starting to manifest its influence, with the band at 260–560 μm increasing its volume fraction, and 7 minutes later (t = 3.63 h) the PSD had suffered a step change, with most of the particles falling in the higher size band. This PSD remained frozen until the end of the reaction (t = 8 h),

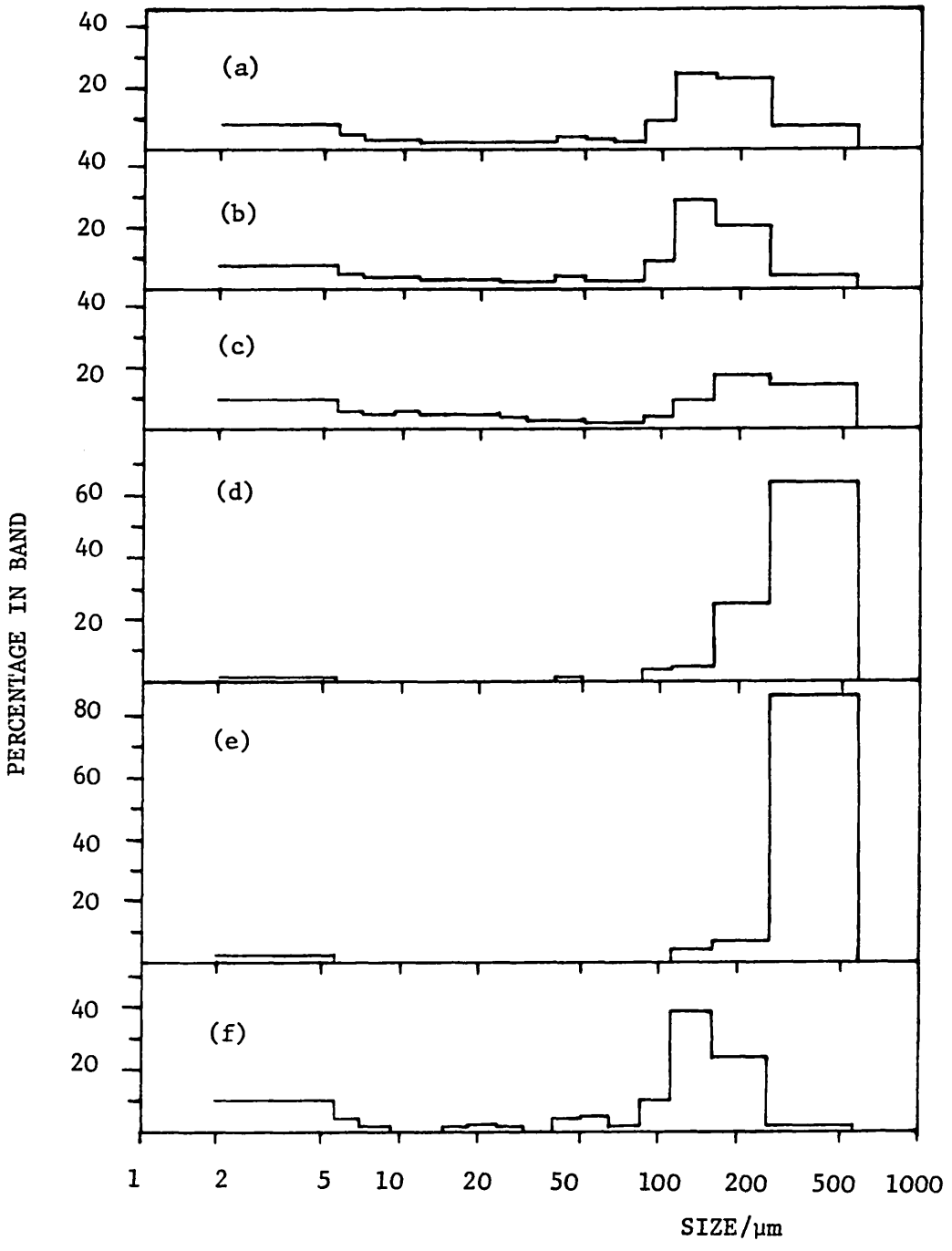


Figure 6.60 Evolution of particle size distribution with time for styrene suspension polymerisation, with 4–bladed paddle, without baffles, at 75.5 C

(a) t = 1.5 h (b) t = 2.5 h
(c) t = 3.5 h (d) t = t_{agg} = 3.63 h
(e) t = 8 h (f) t = 8 h, after ultra–sound treatment

which could be partially reversed to one corresponding to t = 2.5 h, after 5 minute ultra sound treatment in the Malvern Sample Cell.

This strong dependence of time of aggregation with polymerisation temperature and the rapid onset of the aggregation process are discussed further in the next section.

(b) Suspension Process Characterisation

The results presented in this section in which polymerisations were carried out at various temperatures were planned to explore the onset of aggregation in the polymerisation process, since polystyrene is usually described as a non–aggregating system.

In the previous experiments it was verified that aggregation appeared at some particular stage, after which the PSD remained frozen until the end of the reaction. This process settled in rather quickly and it could be visually detected as the reaction mixture changed from a milky suspension to one where solid particles could be seen. Also, at this moment, a small size in temperature, about 1–2 °C, was detected in the bath temperature for a given jacket temperature (see Figure 6.23).

In the suspension polymerisation process the relevant factors that are going to determine the droplet coalescence/aggregation behaviour are:

(i) The droplet deformability, determined essentially by the viscosity, which decreases as conversion increases, and

(ii) the surface adhesion characteristics, due to the presence of adsorbed colloid at its surface, which may go through a maximum as conversion is increased. This maximum is probably related to the increase in the viscoelastic nature of the droplet at the same time interval as

surfactant protection starts to become less effective, due to loss, degradation or copolymerisation.

The initial droplet population, mainly monomer and some growing polymer, is a mobile liquid, highly deformable, due to the low monomer viscosity and hence, they are prone to both coalescence and break–up. The flow regions where coalescence can occur are the ones where weak shear flows are more predominant, i.e. where there is a low shear rate (see Figures 6.44 and 6.45 and Table 6.8). Typical coalescence regions are the upper zones near the liquid surface, where most of the droplet coalescence might occur. If this coalesced droplet has a diameter above the maximum stable diameter for the flow conditions near the agitator, then if it goes into a region of extensional flow, e.g. near the agitator blade, then it can be easily broken–up into smaller droplets. At this stage the adsorbed colloid is evenly distributed at the surface of the droplet, the surface adhesion characteristics of the droplet are still not very high, and if two droplets come into close contact they might coalesce, or move apart if their collision energy was not sufficient to exceed the coalescence energy barrier.

As polymerisation proceeds, the droplets have a higher molar fraction of polymer, due to monomer conversion, and they could be described as a viscous liquid, more resistant to deformation, while their surface characteristics change as well, increasing it adhesive properties. The increase in adhesion could be explained by the increasing viscoelastic nature of the droplet material and by surfactant loss, consumed by copolymerisation with growing polymer or even degradation. The coalescence and break–up of droplets becomes increasingly difficult and at the droplet glass transition temperature, T_g, when they change from a viscous liquid to a deformable, sticky solid, the break–up process is no longer possible due to the rapid increase in droplet viscosity.

However, the surface characteristics of the droplet change more gradually and although true coalescence can no longer take place, an aggregation process is possible whereby two droplets can stick together, retaining their own identity, due to the high adhesive conditions at their surface. The aggregation process stops when droplets become stiff solids.

We may attempt to quantify this behaviour in the following manner. A suggested mechanism relates this evolution of properties to the fact that at each time during the reaction, a well–mixed droplet (monomer plus growing polymer) has its own glass transition temperature, $Tg_{1,2}$, which will vary according to conversion. Assuming the simplest mixing rule:

$$Tg_{1,2} = Tg_1 \, X \; + Tg_2 \, (1-x) \qquad (6.3)$$

where T_g is the glass transition temperature.
x is the conversion
1 refers to the pure monomer
2 refers to the pure polymer, and
1,2 refers to the polymerising droplet.

then $Tg_{1,2}$ varies linearly with conversion, from that of pure styrene to pure polystyrene in the manner seen in Figure 6.61. At the beginning of the polymerisation, the reaction temperature will typically be above $Tg_{1,2}$ of the droplet and both coalescence and break–up can occur. At the very end of the reaction, the droplets are almost pure polystyrene and the reaction temperature is below $Tg_{1,2}$ of the droplet. They now consist of high modulus, glass–like solids and both aggregation and break–up are very slow, if not impossible. At an intermediate stage the $Tg_{1,2}$ of the droplet will equal the reaction temperature. It is very likely that break–up will stop at a slightly lower

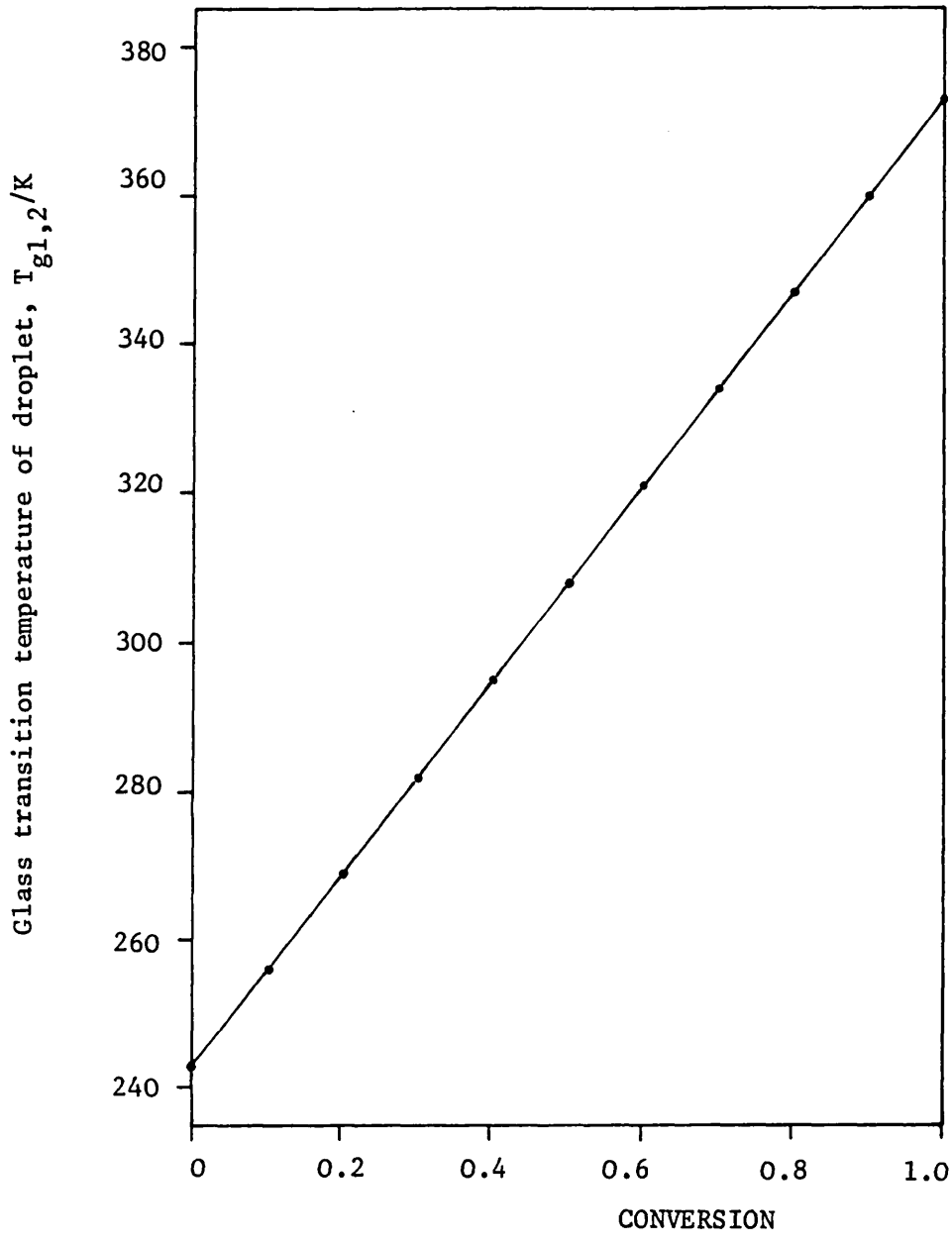


Figure 6.61 Glass transition temperature of droplet (monomer and polymer) versus conversion

viscosity than coalescence/aggregation, i.e. it is more difficult to divide a highly viscous fluid, even in the regions of high elongational flow, than to make them come together due to their surface adhesive properties, which were also assumed to change sharply at T_g. Then, at this stage net aggregation will take place and give the appearance of a sudden onset, as observed.

A set of polymerisation experiments were carried out to test the proposed mechanism, at a stirrer speed of 400 rpm, without baffles. The evolution of the particle size distribution was followed by the periodic sampling method. The time at which the dynamic equilibrium was shifted in favour of aggregation, t_{agg}, was noted by careful visual observation of the polymerising medium and also by the occurrence of a small exotherm detected by the thermocouple. Table 6.11 presents the conditions of this series of polymerisation runs at various temperatures, together with the corresponding times of aggregation, t_{agg}, and conversion, x_{agg}, while Figure 6.62 shows the corresponding temperature profiles.

Table 6.11 Polymerisation Temperatures, t_{agg} and x_{agg} for suspension polymerisations of styrene in complex geometry.

POLYMER	T/C	T_{agg}/h	x_{agg}
26	71	4.95	0.777
27	75.5	3.63	0.812
18,19,21,24	78	3.15	0.831
17,20,22,23,24	80	2.81	0.848
28	86	1.95	0.895

Experimental conditions: 400 rpm; no baffles; PVA = GH23–3.125 $g.l^{-1}$
AIBN = 10.$g.l^{-1}$; 20% styrene ; 3/4 full reactor ; 8 h reaction.

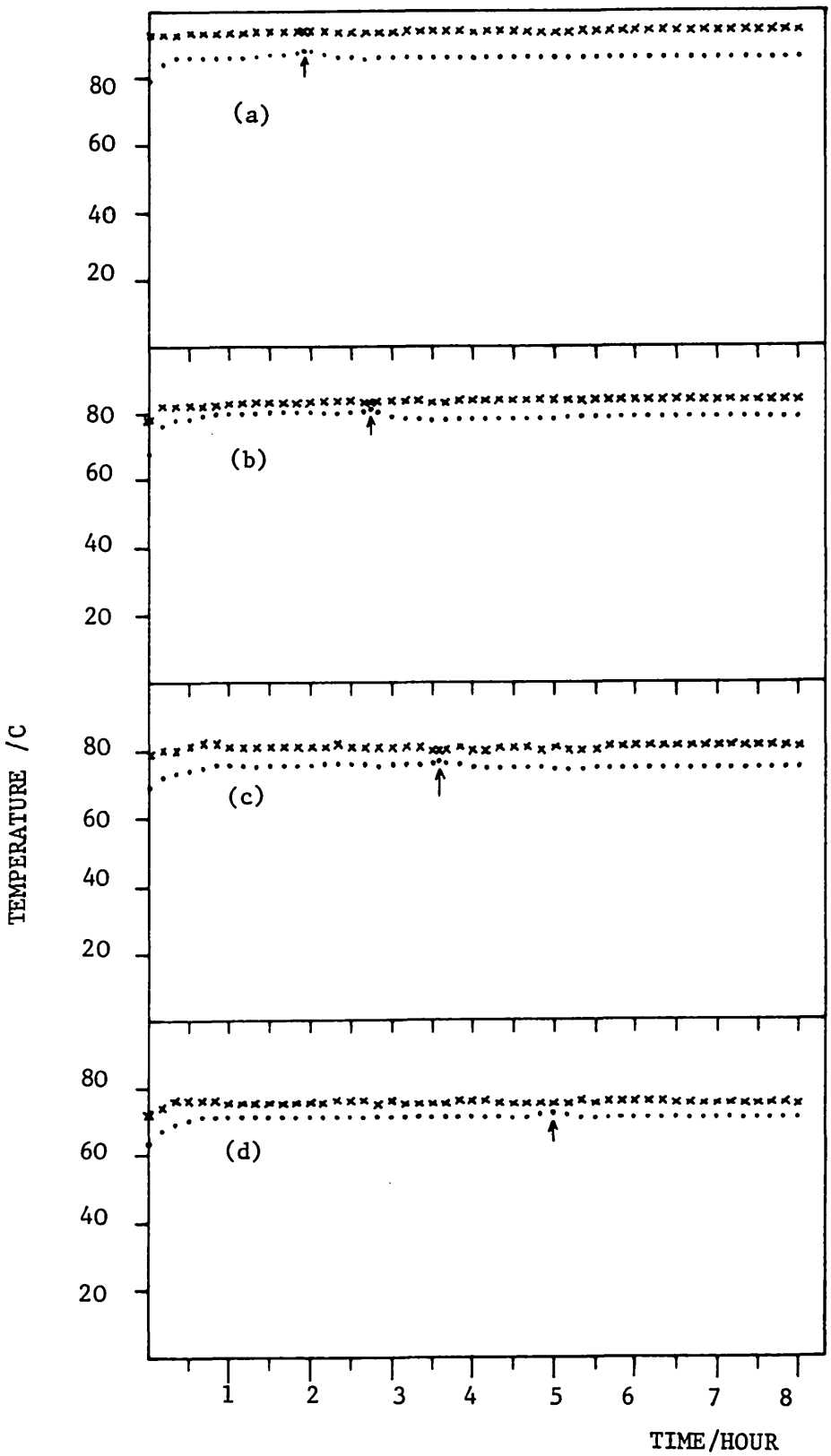


Figure 6.62 Temperature profiles for polymerisation performed at different temperatures

><refer to jacket temperature
•refer to batch temperature
(a) 86 C ; (b) 80 C (c) 75.5 C (d) 71 C

The variation of time of aggregation as a function of polymerisation temperature can be seen in Figure 6.63, exhibiting a smooth variation, which could be an indication of a true physical meaning behind this behaviour.

In order to check the validity of the suggested mechanism it was necessary to evaluate the conversion at time of aggregation and to compare this value with the corresponding conversion at which the $Tg_{1,2}$ of the droplet equals the temperature of reaction, assuming the previous mixing rule. Monomer conversion is obtained from the variation of monomer concentration against time. Here this was calculated assuming a simple free radial mechanism for the polymerisation of styrene (initiation, propagation and termination by combination) and that each droplet acts like a small batch reactor where bulk polymerisation is taking place. The detailed derivations and calculations can be found in Appendix III. Figure 6.64 presents the variation of temperature of polymerisation versus conversion at aggregation, x_{agg}, using the experimental values of t_{agg} and the calculated values from the proposed mechanism setting $T_{polymerisation} = T_{g1,2}$ at x_{agg}. The error bars correspond to a ± 20% error in the values of the individual rate constants, assuming no error in the time of aggregation deduced from the temperature profiles. The results for the experimental and calculated values are in close agreement which is consistent within the mutual uncertainties that can be ascribed to t_{agg}, values for the rate constants and $Tg_{1,2}$ due to deviations from the linearity law assumed in equation (6.3).

This strongly indicated that the proposed coalescenced/break–up mechanism, where the changes in the particular dynamic equilibrium are determined by both the flow history experienced by the particles and their evolving physical characteristics as conversion increases, is realistic for the polystyrene system studied here.

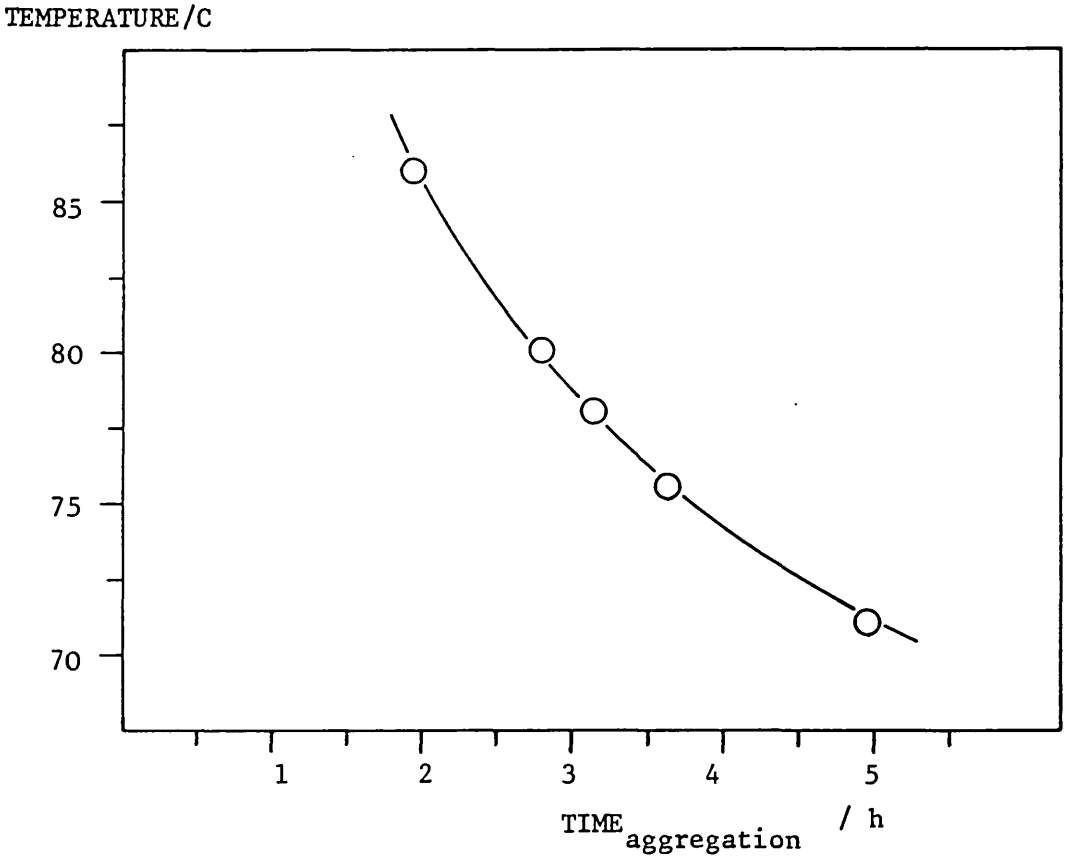


Figure 6.63 Variation of time of aggregation as a function of polymerisation temperature.

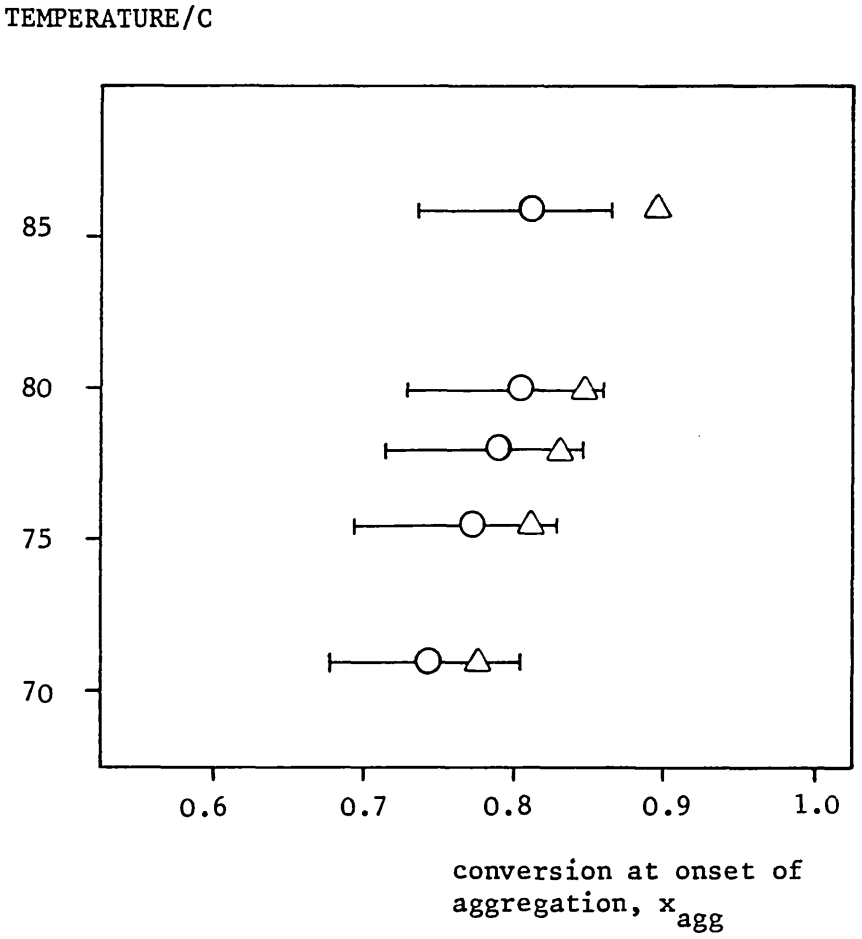


Figure 6.64 Variation of temperature of polymerisation versus conversion at onset of net aggregation.

○value deduced from polymerisation
△model value

(c) Molecular Weight Distribution

The results for the molecular weight distribution of the polymers obtained with this geometry are presented in Table 6.12.

Table 6.12 Molecular weight distribution for polystyrene obtained with 4–bladed paddle geometry.

POLYMER	T/C	RPM	$M_n \times 10^{-4}$	$M_w \times 10^{-5}$	Zp
17	80	400	(a)	(a)	(a)
18	78	400	4.2	1.2	3.1
19	78	400	4.3	1.4	3.2
20	80	400	4.2	1.2	2.8
21	78	400	4.1	1.3	3.1
22	80	200	4.9	1.9	3.9
23	80	200	4.2	1.7	4.0
24	78	400	4.2	1.2	2.9
25	80	400	3.9	1.1	2.9
26	71	400	6.6	2.3	3.4
27	75.5	400	5.2	1.8	3.5
28	86	400	5.3	2.0	3.7

(a) Not available – agglomeration occurred.

The number and weight average molecular weight of polymers 18–25 were expected to be very similar if agitation conditions did not influence molecular weight distribution (MWD), since they were all polymerised at the same temperature range: 78–80 °C. The averaged experimental values for M_n, M_w and Zp, quoted within 95% confidence limits, are presented in Table 6.13, together with the theoretical values for 80°C and 78°C (as already

calculated in section 6.2.3 (b) – page 197) and experimental values for the 2–bladed geometry, at the same temperature.

Table 6.13 Table of results for theoretical molecular weight distribution at 80°C and experimental values of simple and complex geometry.

	Theoretical values		Experimental Averages	
	78 °C	80 °C	Simple Geometry	Complex Geometry
M_n	2.37×10^4	2.36×10^4	$(4.0 \pm 0.51) \times 10^4$	$(4.2 \pm 0.3) \times 10^4$
M_w	3.86×10^4	3.81×10^4	$(1.2 \pm 0.29) \times 10^5$	$(1.4 \pm 0.3) \times 10^5$
Zp	1.63	1.62	2.98 ± 0.38	3.2 ± 0.5

These results show that the scatter amongst the molecular weight values of the different samples are all within the estimated error limits, except for Polymers 22 and 23 (200 rpm without and with baffles) where M_n, M_w and Zp are higher than the expected variation. These deviations observed at the lower stirrer speed might indicate that agitation conditions are playing some role in the MWD. As mentioned earlier (Chapter 5) there is no report of a direct link between agitation and MWD in suspension polymerisations, but it was noted then that an insufficient degree of agitation, although in a stable system, might have some consequences in the broadening of the distribution, due to mass transfer problems and the gel effect. This seems to be confirmed in the present case, at 200 rpm, where some clear broadening of the distribution arises, in contrast with other values, at the same polymerisation temperature.

The experimental values obtained with the complex geometry are slightly higher, but still close to the values for the simple geometry, with similar dispersion of results, as is evident from Table 6.13. Again, the experimental values are higher than the theoretical predictions for the

polymerisation temperature, indicating the probable presence of the gel effect (see page 198).

The values of the MWD for polymers 26 to 28 were expected to be different from all the others, since they correspond to various polymerisation temperatures. In order to compare these experimental findings with the theoretical predictions for MWD, the generating function approach [7] was used to obtain the moments of the distribution for the various temperatures, as in the case for the 2–bladed paddle (see page 198). The theoretical values for M_m, M_w and Zp at the polymerisation temperatures together with the corresponding experimental values are present in Table 6.14.

Table 6.14 Table of results for experimental and theoretical values of MWD for various polymerisation temperatures

T/C	Theory			Experiments		
	$M_n \times 10^4$	$M_w \times 10^{-5}$	Zp	$M_n \times 10^{-4}$	$M_w \times 10^{-5}$	Zp
71	2.72	4.51	1.7	6.6	2.3	3.4
75.5	2.42	4.02	1.7	5.2	1.8	3.5
80	2.36	3.81	1.6	3.9	1.1	2.9
86	2.40	3.89	1.6	5.3	2.0	3.7

The observed experimental trend for M_n and M_w goes through a minimum at 80°C which is also found in the theoretical values, although the variation is much smaller. The experimental behaviour for the polydispersity is quite different from what should be expected from the theory, which predicts no change with temperature. Again, all the experimental values are higher than the theoretical calculations, consistent with significant gel effects within the viscous polymerising droplets.

References to Chapter Six

[1] P. H. Calderbank, "Physical Rate Processes in Industrial Fermentation. Part I, The Interfacial Area in Gas Liquid Contacting with Mechanical Agitation," Trans. Instn. Chem. Eng., 36, 443–463 (1958)

[2] F. Langner, H.–U. Moritz; K.–H. Reichert, "On Particle Size of Suspension Polymers. II. Polymerising Two–Phase System," Ger. Chem. Eng., 2, 329–336 (1979)

[3] F. Langner, H.–U. Moritz, K.–H. Reichert, "Reactor Scale–Up for Polymerisation in Suspension", Chem. Eng. Sci., 35, 519–525 (1980).

[4] "Liquid Mixing and Processing in Stirred Tanks", F.A. Holland, F.S. Chapman, Chapman and Hall, (London), 1966, pages 33 and 35.

[5] R. Schröder, B. Piotrowski, "On Particle Formation During Suspension Polymerisation of Styrene", Ger. Chem. Eng., 5, 139–146 (1982)

[6] "Principles of Polymer Systems" F. Rodriguez, McGraw–Hill, (New York), 1982, page 68.

[7] W. H. Ray, R. Laurence, "Polymerisation Reaction Engineering", in "Chemical Reactor Theory" L. Lapidus, N. R. Amundsen (Eds.), Prentice–Hall, (New Jersey), 1977, page 532

[8] "Polymer Handbook", J. Brandrup, E. H. Immergut, (Eds), John Wiley and Sons, (London), 1975)

[9] A.H. Bolour–Froushan, "Prediction of Single Phase Turbulent Flow in Agitated Mixing Vessels", Ph.D. thesis, University of London (1986)

[10] A.F. Faraday, Private Communication

[11] M.A. Tehrani, "The role of agitation in suspension polymerisation processes", Report to the Department of Chemical Engineering and Chemical Technology, Imperial College, London, (1987)

[12] F. D. Rumşcheidt, S. G. Mason, "Particle Motions in sheared suspensions. 12. Deformation and Burst in Shear and Hyperbolic Flows, J. Colloid Int. Sci., 16, 238–261 (1961)

[13] S. Torza, R. G. Cox, S. G. Mason, "Particle motions in sheared suspensions. XXVII Transient and Steady Deformation and Burst of Liquid Drops", J. Colloid Int. Sci., 38(2), 395–411 (1972).

CHAPTER SEVEN

DISCUSSION AND CONCLUSIONS

7.1 Introduction

The results presented in the last chapter show the interaction between fluid movement in the reactor and the resulting particle size and molecular weight distributions. The use of these flow characterisation techniques, each with its particular view of the mixing process, enabled a more complete and global view of this complex situation to be established.

During the course of the study it has been possible to achieve a much better understanding of the detailed mechanism of droplet formation, of the aggregation process in polymerising systems and their relation to flow characterisation. This will be first illustrated by presenting a qualitative summary of the picture that emerges from the current work of the course of the suspension process, the flow history experienced by the droplets in suspension polymerisation reactors and how their properties evolve as polymerisation proceeds. This will be followed by models which quantify the links between agitation variables and flow kinematics on the one hand and the flow variables and polymer properties on the other.

7.2 Qualitative Model of Suspension Polymerisation

At the start of the polymerisation the bulk monomer, a low viscosity liquid, is dispersed into monomer droplets which absorb polymer at their surface to present coalescence. These droplets may experience coalescence or break–up depending

upon the particular region of the reactor they are in at a certain instant of time: break–up occurs mainly in the lightly localised high shear–elongational flow region near the agitator blade tips [1] (and may be near to the reactor walls), while coalescence is more probable in the lower shear flow region of the reactor near the liquid surface. The absorbed polymer at the surface of the droplet prevents, to some extent, coalescence of the droplets, and in the initial stages the rate of break–up is far higher than the coalescence rate, and an equilibrium droplet size distribution is rapidly reached.

However, as polymerisation proceeds the droplet viscosity increases due to the increased polymer fraction and the effectiveness of the polymer at the droplet's surface decreases either due to dissorption or physical/chemical incorporation into the polymerising droplet. These processes lead to changes in both the break–up and coalescence rates and to gradual shifts in the dynamic equilibrium between break–up and coalescence which control the particle size distribution. This equilibrium will be abruptly disrupted once the droplets' glass transition temperature (which increases with conversion as more polymer is formed) becomes equal to the reaction temperature, because at this point there is a rapid increase in the droplet viscosity. This greatly reduces the rate of break–up and eventually prevents further break–up from occurring. At the same time the surface adhesion characteristics of the particles increase markedly and for a short period aggregation (i.e. incomplete coalescence) can occur without this being followed by significant break–up. The particle size hence increases markedly, until the conversion becomes so high that the polymerising particles are sufficiently solid–like for aggregation to cease. The system then reaches a new equilibrium particle size distribution consisting of stable aggregates which neither accrete further material in the upper regions of the reactor nor break–up near the agitator.

While these dramatic physical property and size changes are occurring at droplet level, the droplets are circulating round the reactor and experiencing a variety of flow conditions in a cyclical manner. The final polymer characteristics will be the result of the interaction of the flow histories experienced by the particles with their changing rheological and adhesion characteristics.

The fluid circulation can be described as a central core of liquid slowly swirling around the stirrer shaft, a fast spiralling downwards motion at intermediate radial distances, flow reversal at a point close to the stirrer tip position and then a relatively smooth upwards movement from this flow reversal point until the wall is reached. This type of three–dimensional picture of flow was found for both the geometries studied, except at the lowest speeds for the 4–bladed paddle, with baffles, where the spiralling motion was absent and fluid movement was more plug like, with downwards movement in the central zone more pronounced than in all other cases.

The detailed flow profiles that were obtained by LDA were used to calculate circulation times, t_c, (see pages 171 and 227) in the reactor. The various averages: $t_{minimum}$, $t_{average}$ and $t_{maximum}$ reflect the way the polymerising droplet circulates within the reactor, from the highly turbulent flow region near the agitator to the more quiescent flow region near the top. The ratio of t_{max}/t_{min} should reflect the spread of the circulation time distribution (CTD) and a flow condition leading to a narrow CTD, where the droplets experience similar flow histories, should be expected to be associated with a narrow particle size distribution. The absolute value of an average circulation time indicates the frequency of return to the agitator, where break–up can occur, and hence a low value of t_c should lead to a smaller mean size, with the size distribution peak (s) shifted to lower values. Low

circulation times should also cause a more rapid achievement of the equilibrium size distribution; by coming more often to the agitator the break–up rate is increased and the droplets can reach their dynamic equilibrium size distribution sooner. The circulation times for the complex geometry show a decreasing trend with either an increase in stirrer speed or baffling. The effects of this on the resulting particle size distribution, viz shifting the whole distribution to lower size range (along with their mean values) in both cases are consistent with the above ideas. This will be quantified later in this Chapter.

Given the important physical significance of circulation time distribution, a single characteristic time may not be enough on its own to characterise the flow in the reactor completely, since not every droplet follows a complete path around the reactor, i.e. from the stirrer, up to the free surface and back again. In many instances, they were observed to by–pass the liquid surface by short–circuiting from upwards wall flow to downwards shaft flow at intermediate heights. Since $P_{reversal}$ is a measure of the probability of polymerising droplets by–passing the large circulation loops, larger P_{rev} should mean a broader CTD, i.e. more particles will short–circuit back to the stirrer at all heights. The increase in the proportion of droplets/particles that return to the agitator zone prematurely will also act to decrease the mean t_c. This will cause the easilier attainment of the dynamic equilibrium particle size distribution, a smaller mean size and a particle size distribution shifted to smaller values.

It has been shown that there was less degree of by–passing liquid surface in the unbaffled case of the complex geometry. It may therefore be expected that a particle size distribution shifted to lower size range will be obtained. This was indeed found to be correct: for both speeds in the complex geometry it was found that baffling caused a shift to a lower size range, as compared with the unbaffled situation.

7.3 Quantitative Models

Until now we have only presented a qualitative understanding of our results in terms of what is physically happening in the reactor as polymerisation proceeds. However, the present data can also be used to develop quantitative relationships:

(i) between the agitation variables (N_s, stirrer size, No. of blades, degree of baffling) and the reactor flow (flow kinematics) as characterised by fluid velocities and the circulation time distribution (which is in turn characterised by various circulation averages and the probability of reversal, P_{rev});

(ii) and between the flow kinematics [both globally around the reactor (circulation times) and locally in the vicinity of the stirrer (probability of break–up)] and the polymer properties (particle size distribution and to a lesser extent molecular weight distribution).

The structure of these models is shown schematically in Figure 7.1

These models are based on several key features that will be discussed below:

(1) The reactor has two major zones: (a) a high shear/turbulent extension region near the agitator, and (b) a low shear, quiescent upper region (with may be an intermediate region near walls and/or baffles);

(2) The agitator acts as a pump circulating fluid around the reactor away from the break–up zone and back again. Its pumping efficiency will determine the circulation time distribution and this is affected by its geometry and speed as well as by reactor geometry and baffle characteristics. The agitator acts also as a break–up device for droplets in the trailing vortices at the blade tips, by extension, necking and eventual rupture [2], [3] and [4].

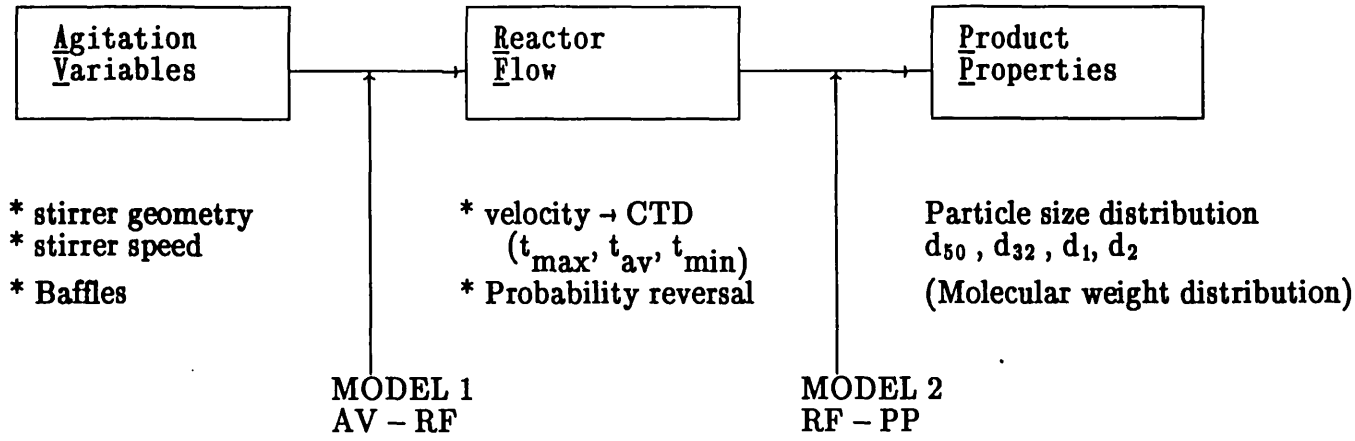


Figure 7.1 Schematic structure of quantitative models between agitation variables, reactor flow and polymer properties.

(3) The extent to which droplets or soft particles are broken up by the stirrer will depend on both these functions i.e. pumping efficiency as measured by the frequency of return to the stirrer zone (a) and the probability that a particle entering the agitator zone will be broken up before or on leaving, as measured by the number of potential sites at which such break–up may occur viz. the number of blade tips, N_b;

(4) Below a certain critical conversion, x_{crit}, polymerising droplets retain their identity in zone (b) as long as they are sufficiently large for the surfactant concentration used to give full surface coverage (or re–coalesce once their size has fallen below that corresponding to effective monolayer surfactant coverage) and then break–up in zone (a);

(5) Above x_{crit}, the polymerising particles aggregate in zone (b), but do not break–up in zone (a) unless t_c is smaller than t_{set}, where the latter is some critical time for particle fusion to become permanent;

(6) Above x_{perm}, no further break–up or aggregation occurs.

The models linking agitation variables, reactor flow characteristics and product properties were developed using the parameters referred in point (3): the frequency of return to zone (b) and the number of break–up sites in this zone. If we consider the maximum time, t_{max}, for a circulation loop in the reactor and take in account that there is a finite probability that some of the droplets will reverse their direction before reaching the top of the reactor, characterised by the probability of several P_{rev}, then since $(1–P_{rev})$ will be the probability of continuing straight into the next zone we can define an effective circulation time, t_{eff}:

$$t_{eff} = t_{max}(1–P_{rev}) \qquad (7.1)$$

t_{eff}^{-1} will be a measure of the frequency with which particles return to the near–agitator break–up zone:

The droplet break–up process occurs as it moves outwards along a blade face into the trailing vortices created at its tip; only those droplets in the immediate vicinity of a blade will be deformed/ruptured. A large number of droplets between the blades may simply be swept out of this zone and pumped round the reactor again without change. The probability of droplet break–up in this zone should therefore increase with the number of blades, N_b, since for a given droplet transit time at fixed stirrer speed the probability of blade/droplet contact increases with N_b. Hence, we acknowledge the fact that droplet break–up by rotating stirrers is a highly localised process, where efficiency is dependent on the number of potential sites at which vortices can form.

Hence the particle size distribution will therefore be determined by the circulation time distribution and the number of blades.

$$PSD = F(CTD, N_b) \tag{7.2}$$

More explicitly this model will lead to the prediction that particle size should scale directly with t_{eff} and inversely with N_b (i.e. less break–up, larger diameter, for higher t_{eff} and lower N_b):

$$d_{av} = f(t_{eff}, 1/N_b) \tag{7.3}$$

The simplest assumption that can be made is a linear relationship between the variables:

$$d_{av} = K\, t_{eff}/N_b \qquad (7.4)$$

The particle size distribution of a unimodal distribution can be characterised by a variety of mean diameters, such as $d_{50\%}$ or the Sauter mean diameter, d_{32}. However such parameters are not so meaningful in multimodal distributions, where we may attempt to use the arithmetic average of each individual peak as a more representative value.

The quantification of the first stage in the model, relating the agitation variables to the reactor flow characteristics is summarised in Table 7.1, for both the simple and complex geometries.

Table 7.1 Quantification of model between agitation variables and circulation time characteristics

Geometry	RPM	Baffling	t_{min}/s	t_{av}/s	t_{max}/s	P_{rev}	t_{eff}/s	N_b	t_{eff}/N_b/s
Simple (2–bladed paddle)	300	–	1.3	2.2	11.4	0.38	7.1	2	3.6
	400	–	0.8	1.3	5.8	0.38	3.6	2	1.8
Complex (4–bladed paddle)	150	–	4.3	11.8	19.4	0.4	11.6	4	2.9
	150	Baffles	2.8	4.6	13.5	0.46	7.3	4	1.8
	400	–	1.0	3.1	5.6	0.4	3.4	4	0.85
	400	Baffles	0.8	1.5	4.7	0.46	2.5	4	0.63

The circulation time distribution values were taken from Tables 6.2 (see page 171) and 6.7 (see page 227); while P_{rev} was considered as a global average, at zone 3 (middle of reactor), from Figures 6.6 (page 161) and 6.34 (page 212).

This Table shows the extent to which stirrer geometry, its speed and the degree of baffling affect typical characteristic times for circulation of fluid within the reactor.

If a power law correlation of the various t_c with stirrer speed is assumed:

$$t_c \propto N_s^a \qquad (7.5)$$

then the exponent a will vary with reactor geometry and baffling effect as presented in Table 7.2.

Table 7.2 Exponent of power law dependence of t_c with stirrer speed for the various reactor geometries

Geometry[a]	t_{min}	t_{av}	t_{max}
Simple	–1.69	–1.83	–2.35
Complex	–1.49	–1.36	–1.27
Complex (with Baffles)	–1.28	–1.14	–1.08

The strongest stirrer speed influence for all the t_c values is found for the simple geometry case, this effect is reduced in the complex geometry case and even further if baffles are introduced.

The variation of stirrer speed was minimum in P_{rev}, as already shown in Figures 6.6 and 6.34; only baffling caused a more significant change.

7.3.1 Product Particle Size Distribution

Since there are various stages in the polymerisation process, the linking of particle size distribution to reactor flow will be done for:

(a) The equilibrium size distribution, at t = 2.5h, for the 4–bladed paddle;

(b) The final aggregated product for the 4–bladed paddle; and

(c) The final product, treated with ultra–sound to break it up into its constituent primary particles, for both the 4– and 2–bladed paddle.

(a) Equilibrium Size Distribution

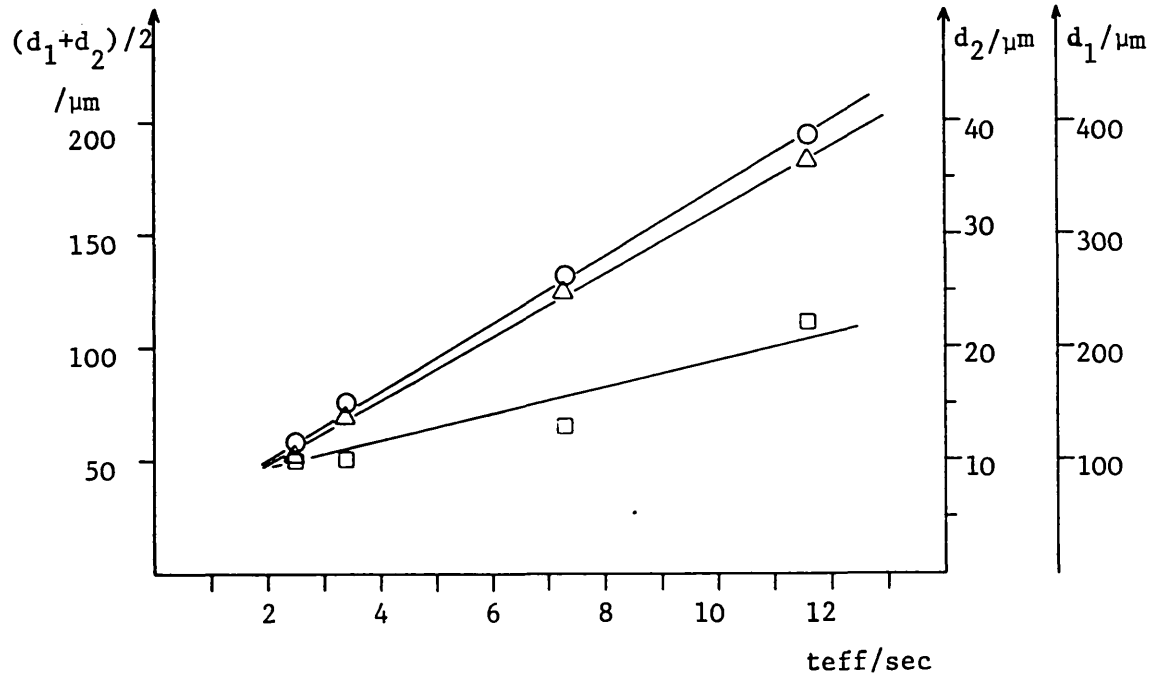
The relevant PSD data for the equilibrium size distribution, at t = 2.5h for the 4–bladed paddle was presented in Figures 6.52 and 6.57, and it is summarised below in Table 7.3.

Table 7.3 Mean diameter and width of primary (d_1) and secondary (d_2) peaks for PSD of complex geometry at t = 2.5h

RPM	Baffles	$d_1/\mu m$	Width (μm)	W/d_1	$d_2/\mu m$	Width (μm)	W/d_2	fines/%
200	—	365	217	0.60	22	25.1	1.14	6
	Baffles	250	247	1.00	13	16.4	1.26	10
400	—	140	62	0.44	10	6.3	0.63	20
	Baffles	104	66.3	0.64	11	4.3	0.43	30

(Width was taken at half height of each peak

The dependence of d_1, d_2 and $(d_1+d_2)/2$ with the effective circulation time, t_{eff}, is presented in Figure 7.2(a), while Figure 7.2(b) shows the variation of the percentage of fine particles ($d < 5.8\mu m$) with $1/t_{eff}$. The excellent correlations that



(a)

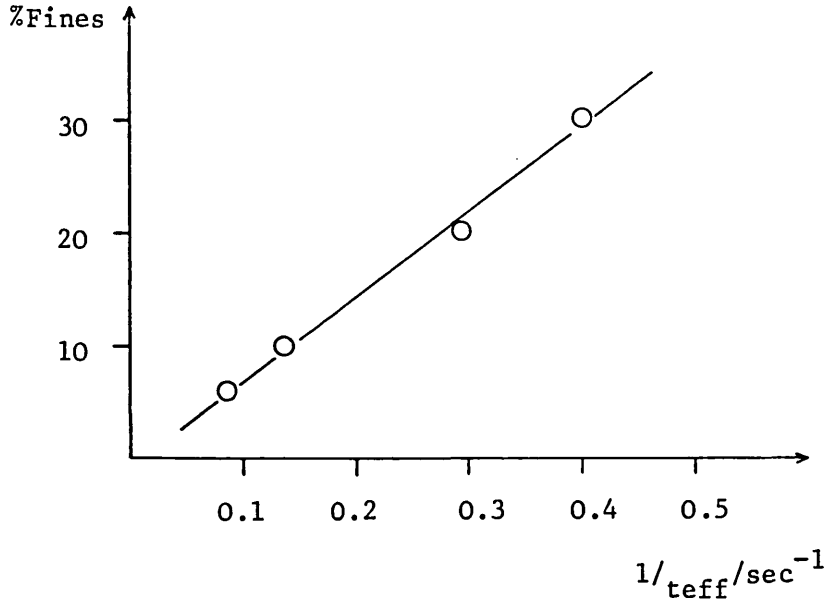


Figure 7.2 Correlations between PSD with effective circulation time for equilibrium size distribution, at t = 2.5 h, for 4–bladed paddle.

(a) For mean peak diameters versus t_{eff}

△ d_1 (primary peak) ○ $(d_1+d_2)/2$
□ d_2 (secondary peak)

(b) For percentage of fines versus $1/t_{eff}$

emerge demonstrate that the experimental results are consistent with the above model. Data for different agitator speeds and reactor geometries can be represented by the following single set of evaluations:

$$(d_1 + d_2)/2 = 14.8\, t_{eff} + 22.4 \quad (7.6)$$

$$d_1 = 28.3\, t_{eff} + 39.2 \quad (7.7)$$

$$d_2 = 1.3\, t_{eff} + 5.6 \quad (7.8)$$

$$\% \text{ fines} = 74.4\ 1/t_{eff} - 0.5 \quad (7.9)$$

The arithmetic mean of both peaks of the distribution appears to be a useful measure of mean size for bimodal distributions; its value is reduced by either stirrer speed or baffling. The increase of % fines with both stirrer speed and baffles, both of which decrease t_{eff}, is consistent with the previous hypothesis (presented in Chapter 6) that the fine particles are formed as satellite droplets each time a large droplet is extended and eventually breaks up in the trailing vortices at the stirrer blade tips. The more frequently droplets return to this zone, the higher the break–up rate, hence the greater the proportion of fine droplets and the smaller the mean size of both the large primary drops and the secondary drops formed from them.

The spread of sizes within each peak, scaled with respect to the peak diameter, W/d, is plotted against the spread of circulation times, taken as t_{max}/t_{min}, for this equilibrium size distribution in Figures 7.3(a) and (b). For the primary peak we see a good correlation between these parameters, although unlike for the mean values of diameter there is still a residual effect of the peak width on stirrer speed. For a given stirrer speed, the addition of baffles broadens the PSD through their broadening of the CTD. In the case of the secondary peak the

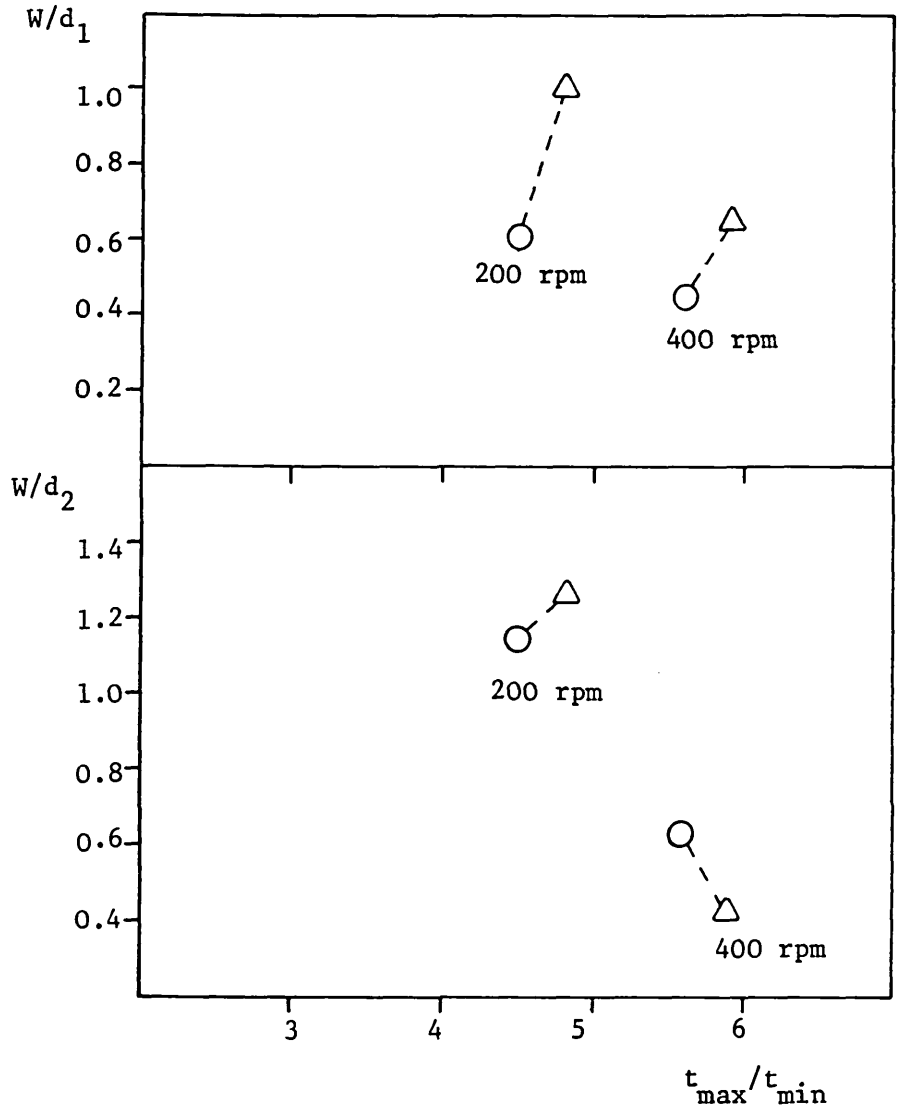


Figure 7.3 Correlation between the normalized spread of sizes within each peak with the breadth of the circulation time distribution for the equilibrium size distribution, for the 4–bladed paddle.

(a) primary peak
(b) secondary peak
○ No baffles
△ Baffles

correlation is similar but not so good, meaning that there are additional, and as yet unidentified, complexities in fully understanding the spread of the two peaks.

(b) Final Aggregated Product

The particle size distribution for this situation was shown in Figures 6.53 and 6.54 and the 50% mean diameter and the Sauter mean diameter for each of the polymer products are presented in Table 7.4. Their variation with the effective circulation time is shown in Figure 7.4.

Table 7.4 50% mean and Sauter mean diameter for final aggregated polymers in complex geometry

RPM	Baffles	$d_{50\%}$ (μm)	d_{32} (μm)	Width (μm)	W/d_{32}	d_{50}/d_{32}
200	—	382.9	220.3	175	0.79	1.75
	Baffles	379.5	168.5	175	1.04	2.25
400	—	357.5	102.7	175	1.70	3.48
	Baffles	368.0	93.6	175	1.87	3.93

(Width also taken at half height)

Both the d_{50} and d_{32}, correlate well with the effective time for circulation for different agitator speeds and reactor geometries. The volume mean diameter, d_{50}, does not depend strongly on t_{eff}, but the Sauter mean diameter (about half the corresponding values of d_{50}) exhibits a more marked variation with flow parameters. The data are represented by the following correlations:

$$d_{32} = 14.3\ t_{eff} + 57.7 \qquad (7.10)$$

$$d_{50} = 2.5\ t_{eff} + 356.9 \qquad (7.11)$$

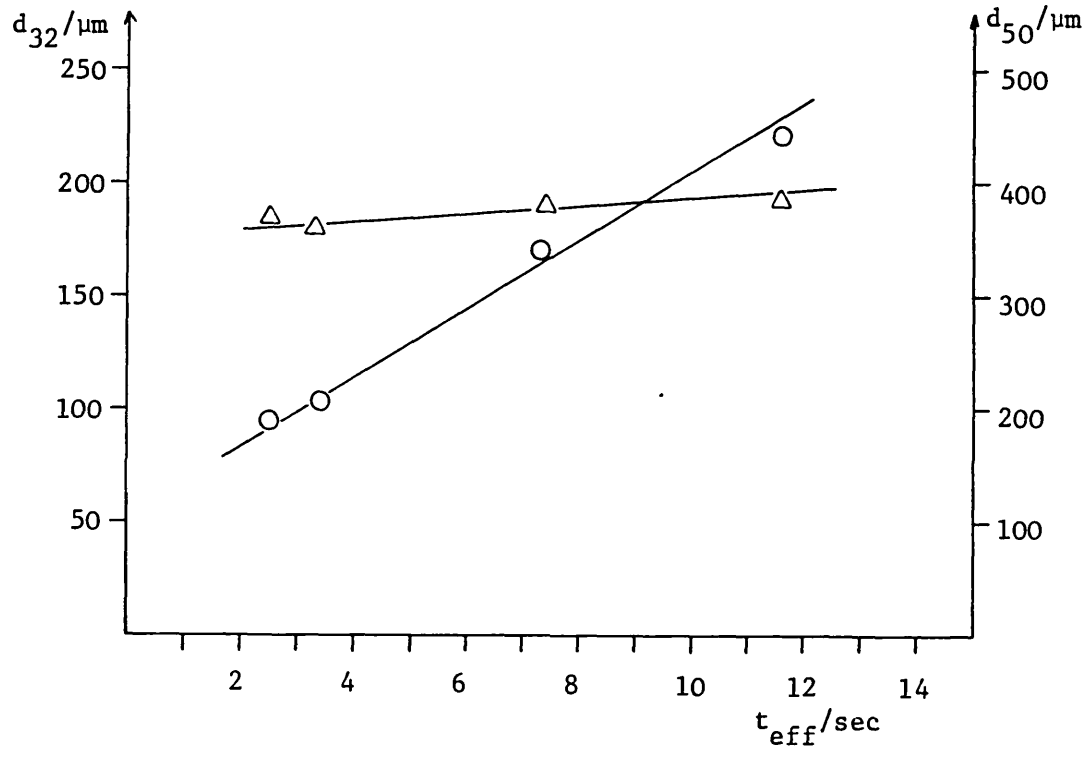


Figure 7.4 Correlation between the 50% mean and Sauter mean diameter of the final aggregated product with the effective circulation time, in the complex geometry case

△ $d_{50\%}$
○ d_{32}

Here the PSD is unimodal and we have used two measures of its breadth: the ratio of peak width over Sauter mean diameter, W/d_{32}, and the ratio d_{50}/d_{32}. In both cases there is an excellent correlation between the width of the peak and the breadth of the circulation times, which is presented in Figures 7.5(a) and (b):

$$W/d_{32} = 0.5\, t_{max}/t_{min} - 2.8 \qquad (7.12)$$

$$d_{50}/d_{32} = 1.4\ t_{max}/t_{min} - 4.5 \qquad (7.13)$$

Although we can understand the spread in PSD on the basis of the spread of circulation times for the aggregated product there is an additional mechanism which may come into play.

The aggregation process (where large aggregates are formed from d_1, d_2 primary particles and fines) takes place away from the agitator and we might postulate that if $t_c < t_{set}$, where the latter is some critical time for particle fusion to become permanent, then the aggregation becomes irreversible and after the critical conversion for aggregation (x_{agg}) is passed, particles returning to the agitator zone satisfying this criterion are not broken up, but remain intact. Hence, after x_{agg} is passed, and below x_{perm}, only if $t_c < t_{set}$ will break–up occur causing the PSD to be broadened by increasing the number of unaggregated particles or of smaller aggregates in relation to the larger aggregates. Therefore, in addition to effects due to the broadening of the CTD the extent to which some particles have $t_c < t_{set}$ may be relevant. The variation of the ratio width/d_{32} versus t_{eff} is shown in Figure 7.5(c). The width decreases with increasing t_{eff} until $\approx$ 6 sec, whereafter it appears to level off towards a limiting value at higher t_c. This suggests that there may be some contribution to the broadening due to the above mechanism, with t_{set} - 10 sec, although the distribution of circulation times still appears to be the dominant factor.

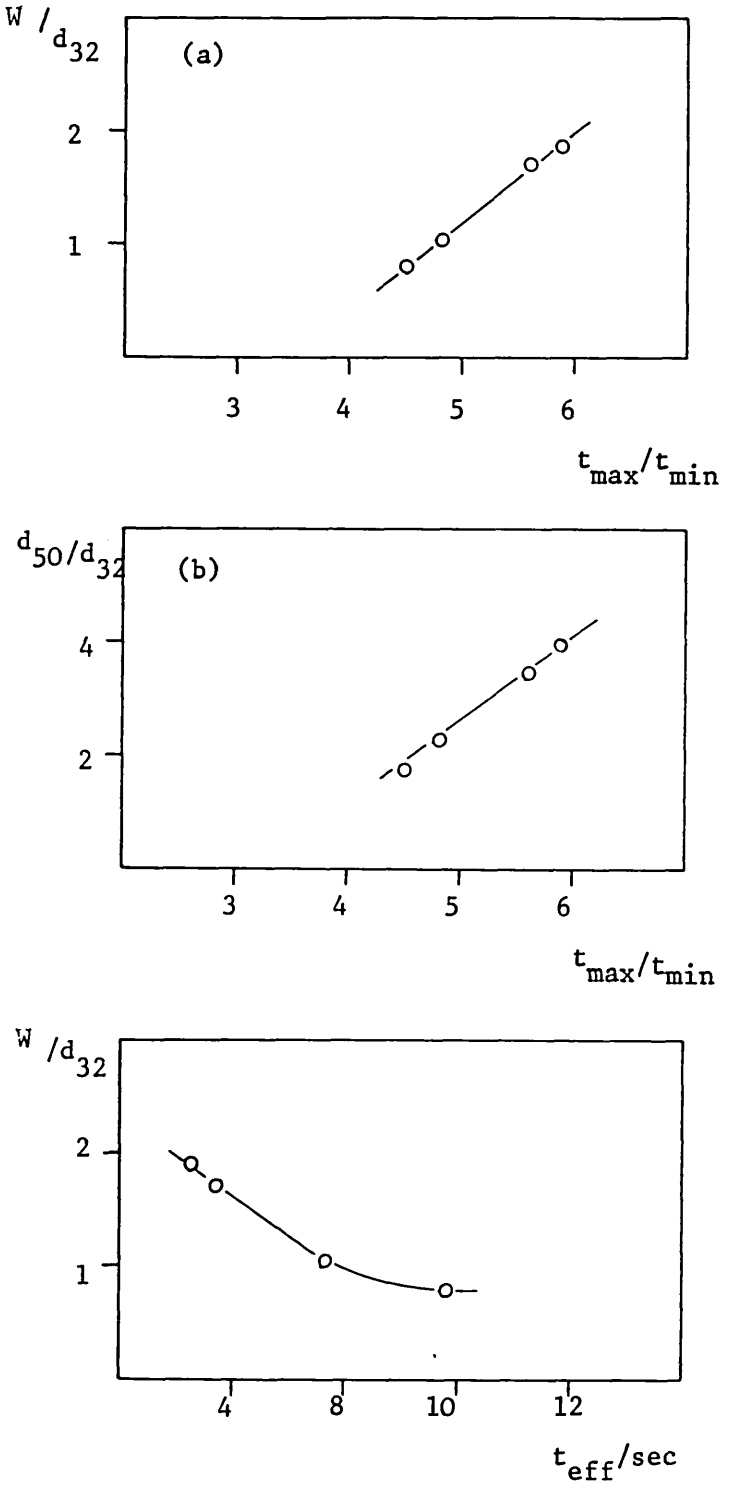


Figure 7.5 Correlations between breadth of distribution of final aggregated product with spread and effective circulation time, in the complex geometry

(a) $W/_{d_{32}}$ versus t_{max}/t_{min}
(b) d_{50}/d_{32} versus t_{max}/t_{min}
(c) W/d_{32} versus t_{eff}

(c) Final Product after Treatment with Ultra–Sound

The size distributions referring to both the simple and complex geometries have already been presented in Figures 6.25, 6.54 and 6.59 and the results are summarised below in Table 7.5.

Table 7.5 Table of results for PSD of final product after ultra–sound treatment, for 2–bladed and 4–bladed paddle.

RPM	Baffles	N_b	d_1 (μm)	Width (μm)	W/d_1	d_2 (μm)	width (μm)	W/d_2
200	—	4	366	217	0.59	89	67.4	0.76
	Baffles	4	252	247	0.98	89	39.6	0.45
300	—	2	391	175	0.45	139	62	0.45
400	—	2	236	189	0.80	97	24.5	0.25
	—	4	139	38	0.27	54	22.1	0.41
	Baffles	4	139	53.1	0.38	43	13.6	0.32

In this situation we have results for the two geometries to test the additional effect of changing agitator geometry. The model proposed earlier, expression (7.4), will be applied to quantify the effect of the flow parameters in product size properties expressed in terms of d_1, d_2 and $(d_1+d_2)/2$ – Figures 7.6(a) and (b), respectively. The excellent correlation obtained in Figure 7.6(b) $[(d_1+d_2)/2$ vs $t_{eff}/N_b)]$ illustrates the fit of the present model which rationalises the effects of variations in stirrer speed, stirrer geometry and reactor baffling on the PSD of the polymer product in terms of the flow kinematics. It confirms that the data can be rationalised in terms of a universal characterisation involving the CTD and the mechanism of droplet where the crucial parameter is the number of break–up locations, N_b. The correlations for the data are the following:

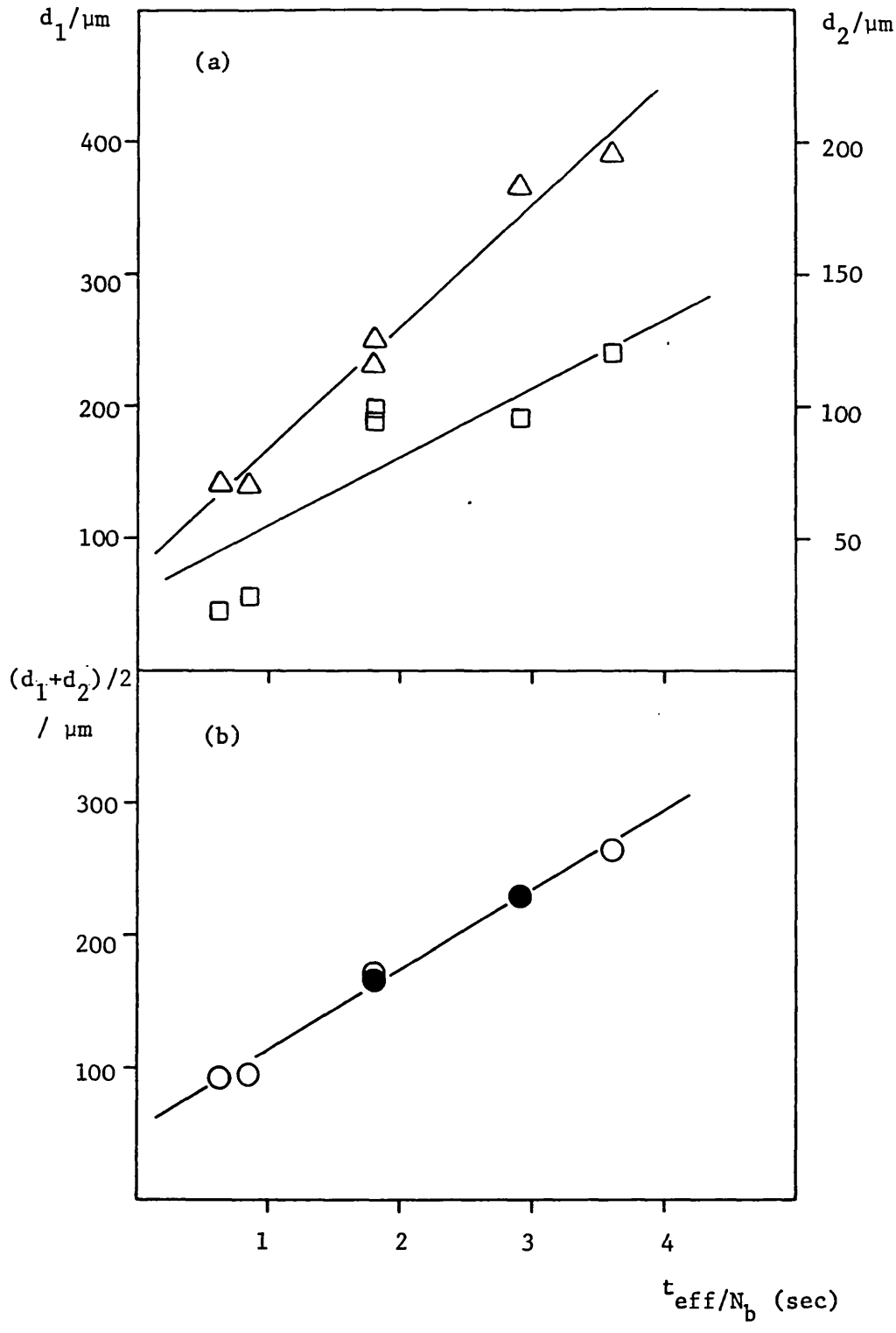


Figure 7.6 Correlation between the PSD of final product, after ultra–sound treatment with the ratio of the effective circulation time over number of blades, for the 2–bladed and 4–bladed paddle.

(a) Single Peak Diameters (b) Arithmetic Mean
△ d_1 (primary peak) ○ $(d_1+d_2)/2$ – 4–bladed paddle
□ d_2 (secondary peak) ● $(d_1+d_2)/2$ – 2–bladed paddle

$$d_1 = 92.7\ t_{eff}/N_b + 74.9 \quad (7.14)$$

$$d_2 = 27.2\ t_{eff}/N_b + 32.7 \quad (7.15)$$

$$(d_1+d_2)/2 = 60.0\ t_{eff}/N_b + 53.8 \quad (7.16)$$

It is interesting to note that the smallest particle that the model predicts it is possible to achieve has a diameter of $d \simeq 50\mu m$ (from the intercept at $t_{eff} = 0$), which coincides with the smallest particles observed in practice at $400\mu m$ for 4–bladed paddle (d_2 both with and without baffles). This would mean that even if particles return infinitely quickly to the break–up zone there may be a limiting size which is approached by these particles at $400\mu m$ (assuming the linear relationship on t_{eff} persists down to low t_{eff} values) due to the balance between hydrodynamic and surface tension forces. This droplet size range is very close to the one reported by Tehrani [5] in extensional flow (extensional rate of $40s^{-1}$) of suspended droplets in glycerol with polyvinyl alcohol as protective agent (interfacial tension = 1 mN m^{-1}).

The normalized width of these two peaks is represented as a function of t_{max}/t_{min} in Figures 7.7(a) and (b) for the primary and secondary peaks, respectively. For the primary peak, d_1, baffles seem to broaden the distribution but there is still a speed effect as in the similar case for the equilibrium size distribution at t = 2.5h, and there is not a complete tie–up between the 2–bladed and 4–bladed paddle results. The correlation for the secondary peak, d_2, is again not so good. The complete understanding of the width of the particle size distribution clearly requires more study.

7.3.2 Product Molecular Weight Distribution

So far, we have concentrated on understanding and quantifying the relation

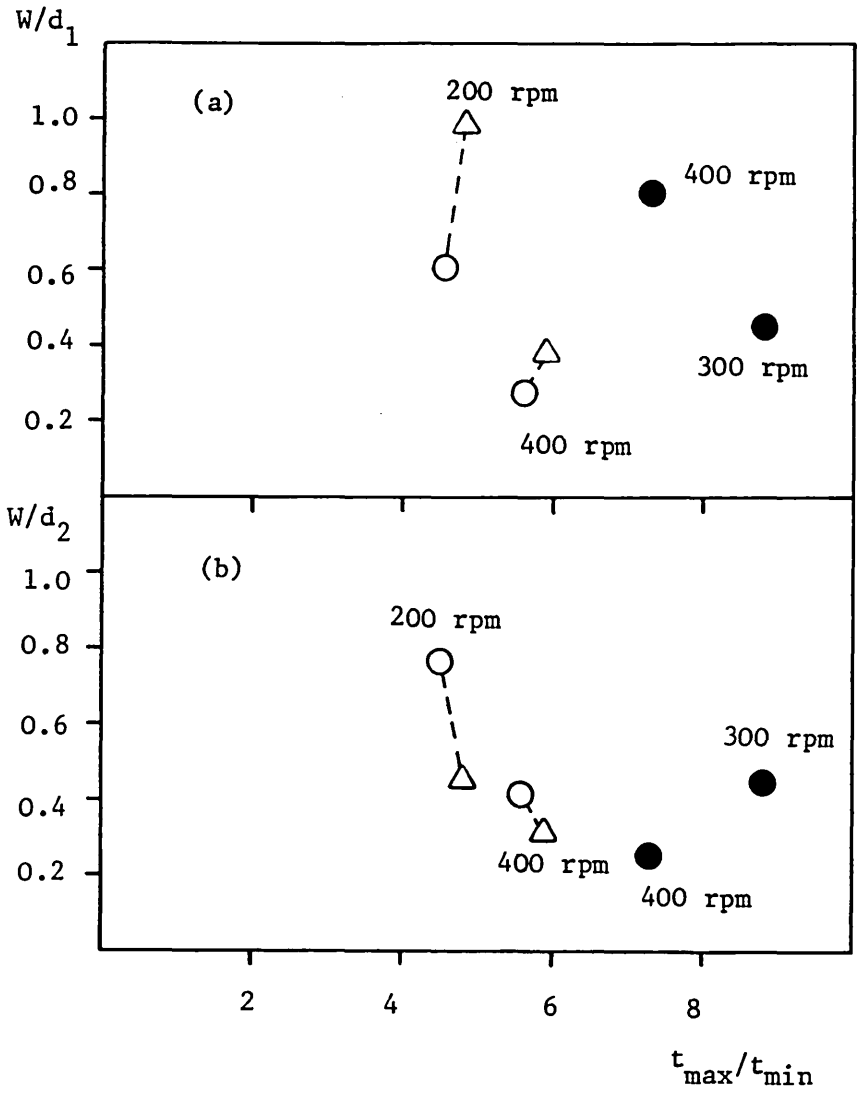


Figure 7.7 Correlation between the normalized spread of sizes within each peak with the breadth of the circulation time distribution, for the final product after ultra–sound treatment, for the 2–bladed and 4–bladed paddle.

(a) Primary peak
(b) Secondary peak

○ 4–bladed paddle, no baffles
△ 4–bladed paddle, baffles
● 2–bladed paddle

between the flow kinematics and the product PSD, which is the property for which major effects of the detailed flow characteristics are expected. The other important product property is molecular weight distribution, where the influence of flow is expected to be somewhat more indirect, through its effect on heat transfer, and how this controls the homogeneity of reactor temperature and the influence of the gel effect above certain conversions (see chapter 5, section 5.2).

The effect of agitation variables on the molecular weight distribution can be seen in Figure 7.8 where both the weight average molecular weight and the polydispersity are shown as a function of t_{eff}. As expected, the effects are small. However, there is significant increase in both $\overline{M}_w$ and Z_p with t_{eff}, which is consistent with a deterioration in convective heat transfer within the reactor as the rate of fluid circulation (and hence rate of contact with the temperature controlling fluid at the walls) decreases. This is consistent with the effects of temperature variations and the gel effect discussed earlier. Such effects must clearly be taken into account when close control of the MWD is required. The correlations are the following:

$$\overline{M}_w = 0.08\, t_{eff} + 1.0 \qquad (7.17)$$

$$Z_p = 0.1\, t_{eff} + 2.8 \qquad (7.18)$$

7.4 Concluding Remarks

The above analyses highlight the fact that it is possible by focussing on the details of the "flow" as the physical link between "agitation" and "product" to rationalise the behaviour of a large number of situations in terms of a few fundamental variables. However, we must not forget that the constants appearing in these correlations will vary with the fluids involved, the amount of stabilizer

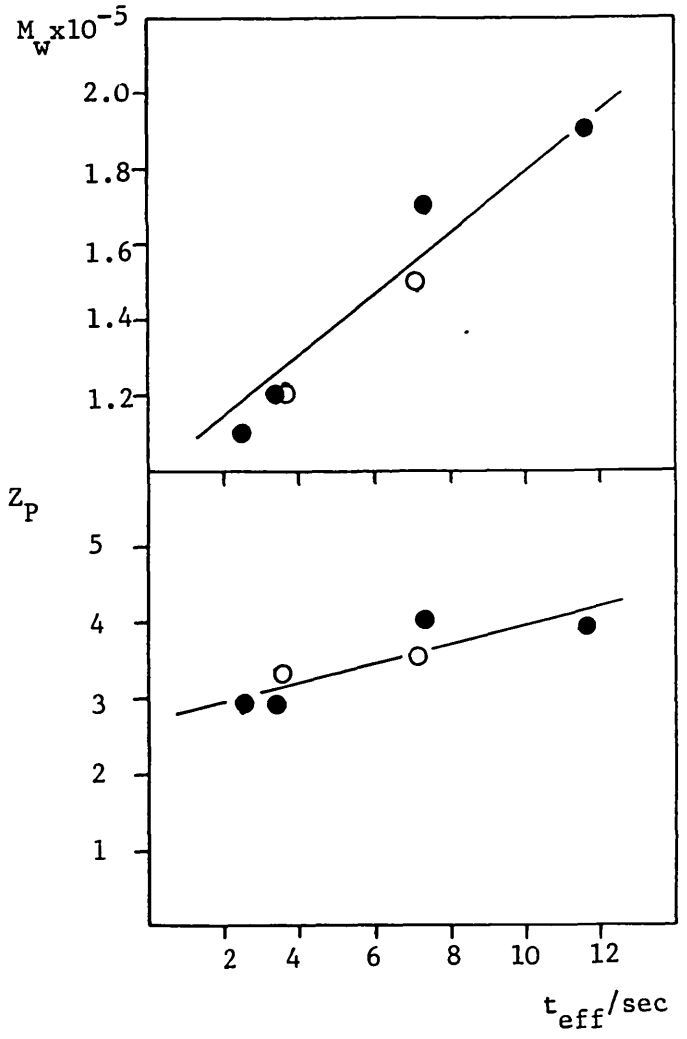


Figure 7.8 Correlation between the weight average molecular weight and polydispersity with the effective circulation time for the 2–bladed and 4–bladed paddle.

○ 2–bladed paddle
● 4–bladed paddle

used, etc., so their dependence on material properties like viscosity, surface tension, density, etc., which appear in the "agitation–size" correlations would need to be determined for wider range of conditions than were studied here to make this model more widely applicable. Therefore studies of the effect of varying material properties (of both polymer/monomer systems and different stabilizing surfactants) on the evolution of the PSD constitute a suggestion for further work.

We can now compare our particle size results with correlations proposed by other workers [6], [7], where a power law dependence of mean diameter versus stirrer speed is assumed, equation (2.7) (see page 48). If we try to fit this equation to the arithmetic mean of the two peak diameters for the final product, after ultra–sound treatment, then the exponent b will vary with geometry (b = –1.2 and – 1.6 for the 4–bladed and 2–bladed paddle, respectively) and with the introduction of baffles (b = –0.9). However, if we correlate the same sizing parameter with the appropriate flow parameter, such as t_{eff}/N_b, then a much smoother variation is observed and a complete fit is obtained for the different geometries and the baffling effect.

These models can be used in reverse order to define the reactor conditions necessary to obtain a desired specification. The required properties, essentially related to details of particle size and molecular weight distribution, can be entered into the "flow parameters–product properties" to obtain the flow parameters, in terms of t_{eff} or t_{eff}/N_b necessary for that purpose. Once that has been fixed, then we can go back to the "agitation variables–reactor flow" model and state the necessary conditions in order to produce the required fluid circulation characteristics: type of paddle (i.e. N_b), stirrer speed, and presence or absence of baffles. If more than one arrangement would be possible, then the final choice

would depend on other design considerations, such as heat transfer, power requirements, etc.

To finalise this chapter some comments about further work will be made. First, a more detailed statistical analysis of the data could extract more information, whereas some additional experiments covering more speeds, reactor geometries and polymerising systems would enlarge the present understanding and test the generality of the models suggested in this work.

It would be of great interest to characterise the flow by LDA at additional stirrer speeds e.g. much lower values of stirrer speed for the 2–bladed paddle and intermediate values for the 4–bladed paddle to fill in some gaps in the present models. The use of a different kind of impeller would enable the testing for different flow structures of our hypothesis that it is the CTD which is the major factor in determining the mean values and distribution of product properties in suspension polymerisation processes.

Regarding the quantitative glass–transition temperature model which showed the importance of surface material properties in aggregating polymerising systems, it could be further tested and checked by the use of other monomers and by quantitatively measuring the relationship between conversion and the polymerising droplet's glass–transition temperature, rather than relying on a linear model as was done here.

The mapping of the component of velocity not measured in this work, the radial velocity, would allow the calculation of extension rates, especially near the agitator tip, which was identified as the major locus for droplet break–up. This might enable a more detailed analysis of the droplet break–up processes to be incorporated into the models and may be an important parameter in understanding the distribution of product particle sizes in more detail.

References to Chapter Seven

[1] R. Stephenson, "The effect of agitation on stirred suspension drop size: A Model Study", Ints. Chem. Eng. Symp. Series, 38, C4, 1–22 (1974)

[2] K. Van't Riet, J. M. Smith, "The trailing vortex system produced by Ruston Turbine Agitator", Chem. Eng. Sci., 30, 1093–1105 (1975)

[3] M. Yianneskis, Z. Popiolek, J. H. Whitelaw, "An experimental study of the steady and unsteady flow characteristics of stirred reactors", J. Fluid Mech., 175, 537–555 (1987)

[4] F. D. Rumscheidt, S. G. Mason, "Particle Motion in Sheared Suspensions. 12. Deformation and Burst of Liquid Drops in Shear and Hyperbolic Flows", J. Colloid Int. Sci., 16, 238–261 (1961)

[5] M. A. Tehrani, "The role of agitation in suspension polymerisation processes", report to the Department of Chemical Engineering and Chemical Technology, Imperial College, London, (1987)

[6] F. Langner, H.–U. Moritz, K.–H. Reichert, "On particle size of suspension polymers. II. Polymerising two–phase system", Ger. Chem. Eng., 2, 329–336 (1979)

[7] R. Schröder, B. Piotrowski, "On particle formation during suspension polymerisation of styrene", Ger. Chem. Eng., 5, 139–146 (1982)

APPENDIX I

DERIVATION OF VIRTUAL POSITION OF CROSS-OVER FOR A SQUARE-SECTIONED GLASS CHANNEL

A ray of light going through several media will experience different degrees of refraction, according to the refractive index of the substances, and following the laws of geometrical optics.

The present case is shown in Figure I.1, where the cross-over is point A, the observer (or photomultiplier) is in air and the walls of the channel can be considered as a perfect parallel wall.

The observer will initially see (position o of the glass wall) the object A at point A′, due to multiple refraction at the air/glass and glass/water interfaces. If the glass plane parallel wall is moved by Δx away from the observer (or photomultiplier), then the same object A (unmoved in space) will have its virtual image at point A′′. The aim of this Appendix is to find out the relationship between the distance $\overline{A'A''}$ and Δx, i.e. the displacement required for the photomultiplier's position, in order to observe the new object position without refocusing.

$$\overline{A'A''} = \overline{AA'} - \overline{AA''}$$

where $\overline{AA'} = y - y'$ and $\overline{AA''} = (y - \Delta x) - y''$

$$\therefore \quad \overline{A'A''} = y' + \Delta x - y' \qquad (1)$$

Now $$y' = \frac{\overline{A'C'}}{\tan \alpha_3} - d$$

(α_3 is the beam–normal angle at the air/glass interface)

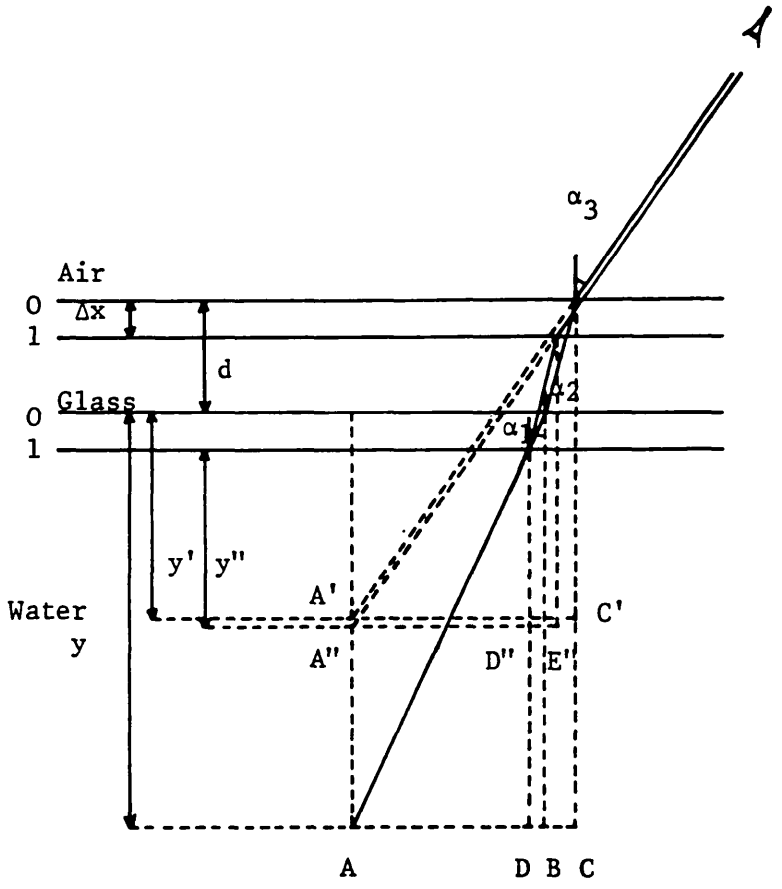


Figure I.1 Determination of virtual position of cross–over in a square–sectioned glass channel.

$$\overline{A'C'} = \overline{AC} = \overline{AB} + \overline{BC}$$

where $\overline{AB} = y \tan \alpha_1$ and $\overline{BC} = d \tan \alpha_2$

(α_2 and α_1 are the beam–normal angles at the glass/water interface)

$$\overline{A'C'} = y \tan \alpha_1 + d \tan \alpha_2$$

$$\therefore \quad y' = \frac{y \tan \alpha_1 + d(\tan \alpha_2 - \tan \alpha_3)}{\tan \alpha_3} \tag{2}$$

Now $$y'' = \frac{\overline{A''E''}}{\tan \alpha_3} - d$$

and similarly we obtain

$$\overline{A''E''} = \overline{A''D''} + \overline{D''E''}$$

where $\overline{A''D''} = \overline{AD} = (y - \Delta x)\tan \alpha_1$, and $\overline{D''E''} = d \tan \alpha_2$

$$\therefore \quad \overline{A''E''} = (y - \Delta x)\tan \alpha_1 + d \tan \alpha_2$$

and so $$y'' = \frac{(y-\Delta x)\tan \alpha_1 + d(\tan \alpha_2 - \tan \alpha_3)}{\tan \alpha_3} \tag{3}$$

Introducing expressions (2) and (3) in (1):

$$\overline{A'A''} = \Delta x \left[1 - \frac{\tan \alpha_1}{\tan \alpha_3}\right] \tag{4}$$

Now $$\frac{\tan \alpha_1}{\tan \alpha_3} = \frac{\sin \alpha_1}{\cos \alpha_1} \cdot \frac{\cos \alpha_3}{\sin \alpha_3}$$

and recalling that $\sin \alpha_3 / \sin \alpha_1 = m_{1,3}$, where $n_{1,3}$ is the refractive index of water relative to air, we can derive the following expression:

$$\frac{\tan \alpha_1}{\tan \alpha_3} = \frac{\cos \alpha_3}{\sqrt{n_{1,3}^2 - \sin^2 \alpha_3}} \tag{5}$$

This can be substituted in equation (4):

$$\overline{A'A''} = \Delta x \left[1 - \frac{\cos \alpha_3}{\sqrt{n_{1,3}^2 - \sin^2 \alpha_3}} \right] \tag{6}$$

For the present case in which $\alpha_3 = 0$ (cross-over and photomultiplier are on the same axis) expression (6) reduces to the final form of:

$$\overline{A'A''} = \Delta x \left[\frac{n_{1,3} - 1}{n_{1,3}} \right] \tag{7}$$

The photomultiplier displacement ($\overline{A'A''}$) is thus only a function of the glass wall movement (Δx) and the refractive index of water relative to air.

APPENDIX II

DERIVATION OF CROSS–OVER AND PHOTOMULTIPLIER POSITIONS FOR HORIZONTAL AND VERTICAL ANEMOMETER LASER BEAMS IN THE CASE OF THE GLASS REACTOR

The aim of this Appendix is to describe a method of determining the cross–over coordinates for the two anemometer laser beams (either in the horizontal or vertical plane) for a given starting position, knowing that they had to go through three different media: air, glass and water, and that the glass surface was curved. This will be dealt with in two separate parts, one for the laser beams in the horizontal plane, and the other one for the laser beams in the vertical plane. The last section deals with finding the appropiate position for the photomultiplier in order to view light scattered from the cross–over.

In all derivations the origin of coordinates was at the centre of the reactor, the laser position was known, as well as the half angle of intersection (β = 1.14576°) of the two laser beams in air, and the half distance (a = 1 cm) of the 2 laser beams, at source, and no assumptions were made, apart from the absence of imperfections in the shape and quality of the glass vessel walls.

Part I – Determination of cross–over position with laser beams in horizontal plane

Figure II.1 shows the refractions of the two laser beams when they are in the x–y plane. At the beginning the laser axis coordinates were known: (x_0, y_0), at the front of the converging lens, and we wanted to

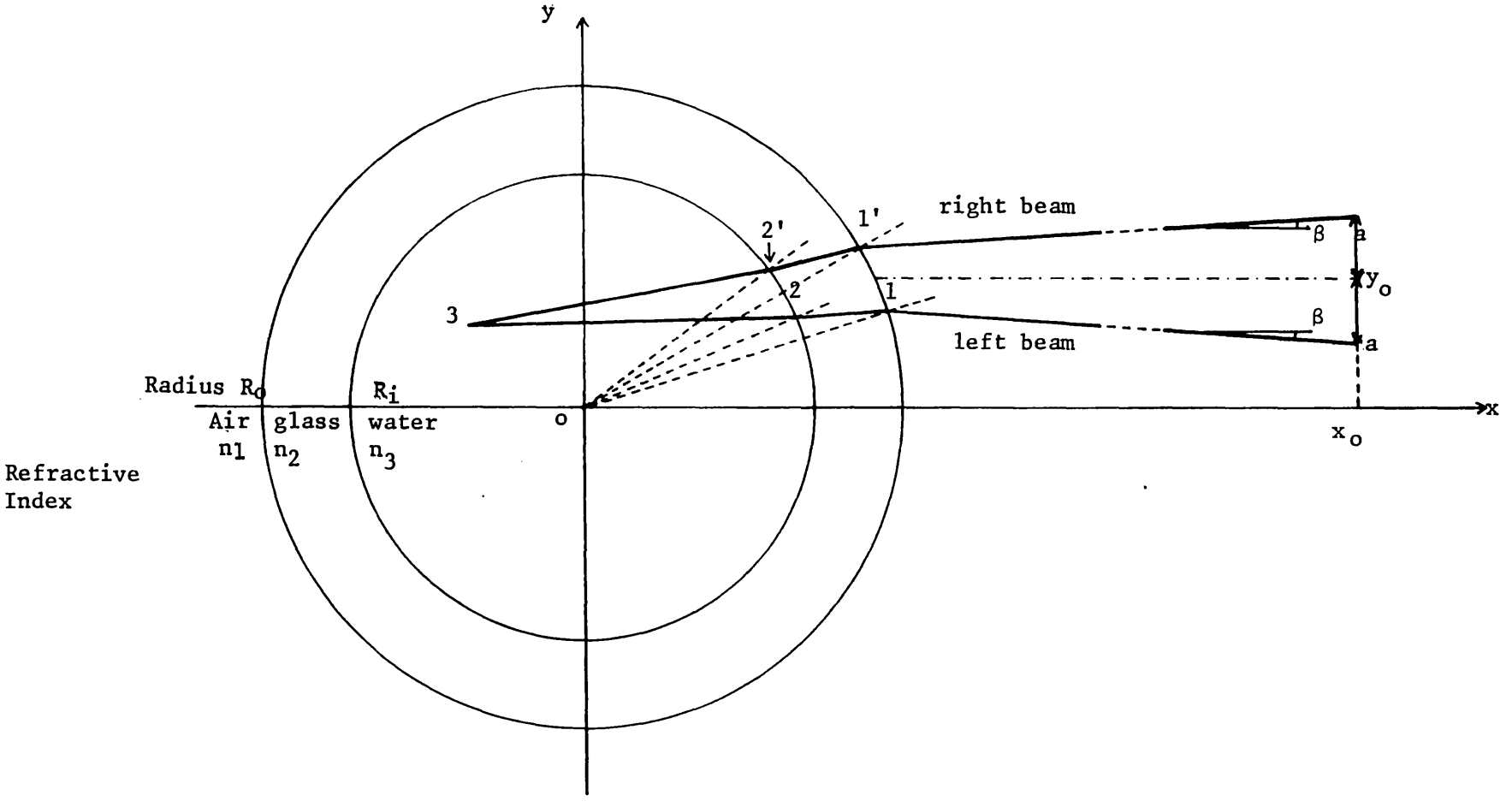


Figure II.1 Multiple refractions of laser beams, when in horizontal plane, and going through air, glass and water

obtain the cross–over coordinates: point 3.

The derivation will be done in two similar sections, one dealing with the closest beam (left beam) and the other one with the furthest beam (right beam).

(i) ***Left Beam*** (see Figure II.2)

The point of intersection of the left beam with the outer vessel wall, $l \equiv (x_1, y_1)$ can be first determined from the following relationships:

$$- \tan \beta = \frac{y_1 - (y_0 - a)}{x_1 - x_0} \tag{1}$$

$$x_1^2 + y_1^2 = R_0^2 \tag{2}$$

where R_0 is the radius of the outer glass vessel wall.

The beam–normal angle γ_1 is given by:

$$\gamma_1 = \alpha_1 + \beta \quad , \quad \text{where } \alpha_1 = \tan^{-1} \frac{y_1}{x_1}$$

Once γ_1 is obtained, the beam–normal angle γ_2, inside the glass, at the glass–air interface, is determined by the laws of refraction:

$$\gamma_2 = \sin^{-1} \left[\frac{n_1}{n_2} \sin \gamma_1 \right]$$

where n_1 and n_2 are the refractive indices of air and glass, respectively.

The auxiliary angle α_2 is:

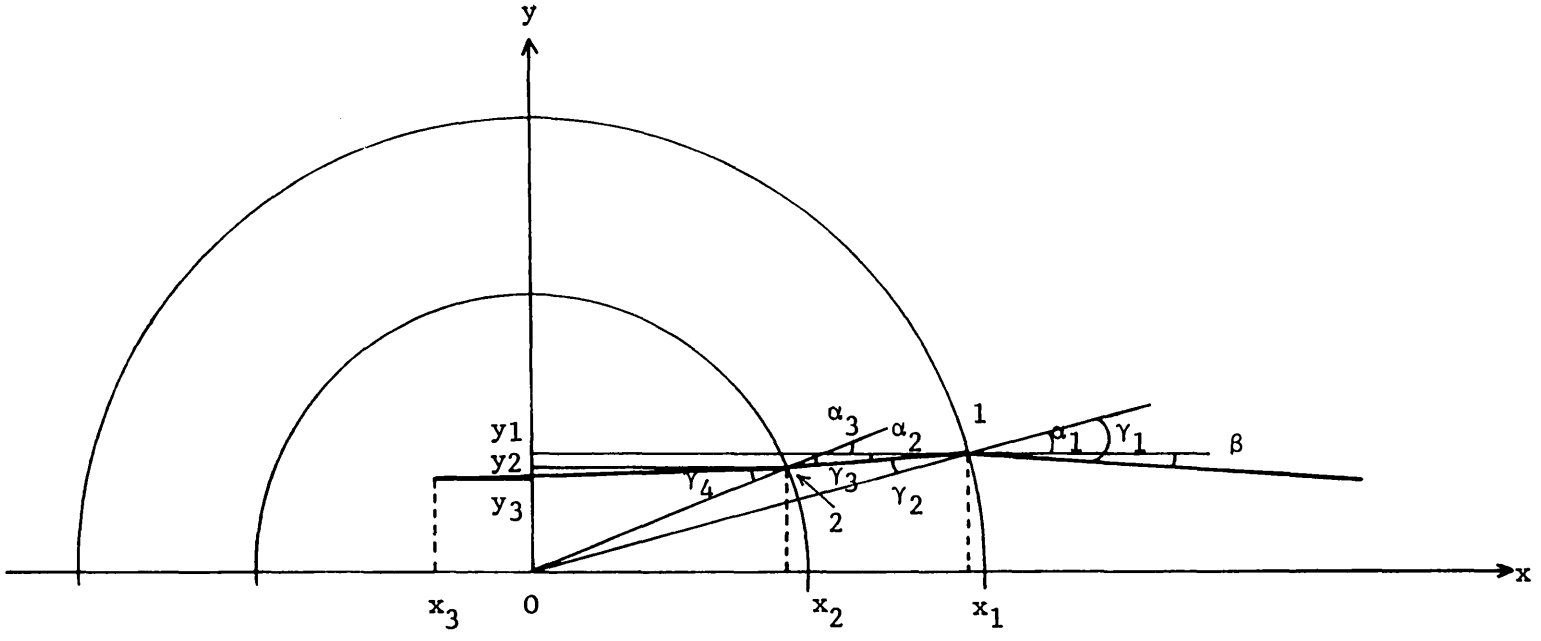


Figure II.2 Multiple refractions for left laser beam, horizontal plane, showing relevant points and angles

$$\alpha_2 = \alpha_1 - \gamma_2 \quad \text{and} \quad \tan \alpha_2 = \frac{y_2 - y_1}{x_2 - x_1} \tag{3}$$

Recalling that

$$x_2^2 + y_2^2 = R_i^2 \tag{4}$$

(where R_i is the inner radius of the vessel) equations (3) and (4) can be simultaneously solved to give (x_2, y_2).

Now

$$\alpha_3 = \tan^{-1} \frac{y_2}{x_2}$$

and

$$\alpha_3 = \alpha_2 + \gamma_3 \qquad \therefore \gamma_3 = \alpha_3 - \alpha_2$$

and therefore

$$\gamma_4 = \sin^{-1} \left[\frac{n_2}{n_3} \sin \gamma_3 \right]$$

If (x_3, y_3) are the coordinates of the cross–over, then:

$$\tan(\alpha_3 - \gamma_4) = \frac{y_3 - y_2}{x_3 - x_2} \tag{5}$$

At this point we have only one equation, (5), with two unknowns (x_3 and y_3), and in order to have another equation to enable x_3 and y_3 to be determined, similar calculations have to be done based on the right beam.

(ii) ***Right Beam*** (see Figure II.3)

The point of intersection of the right beam with the outer vessel wall, $1'(x'_1, y'_1)$ can be found by solving the two equations:

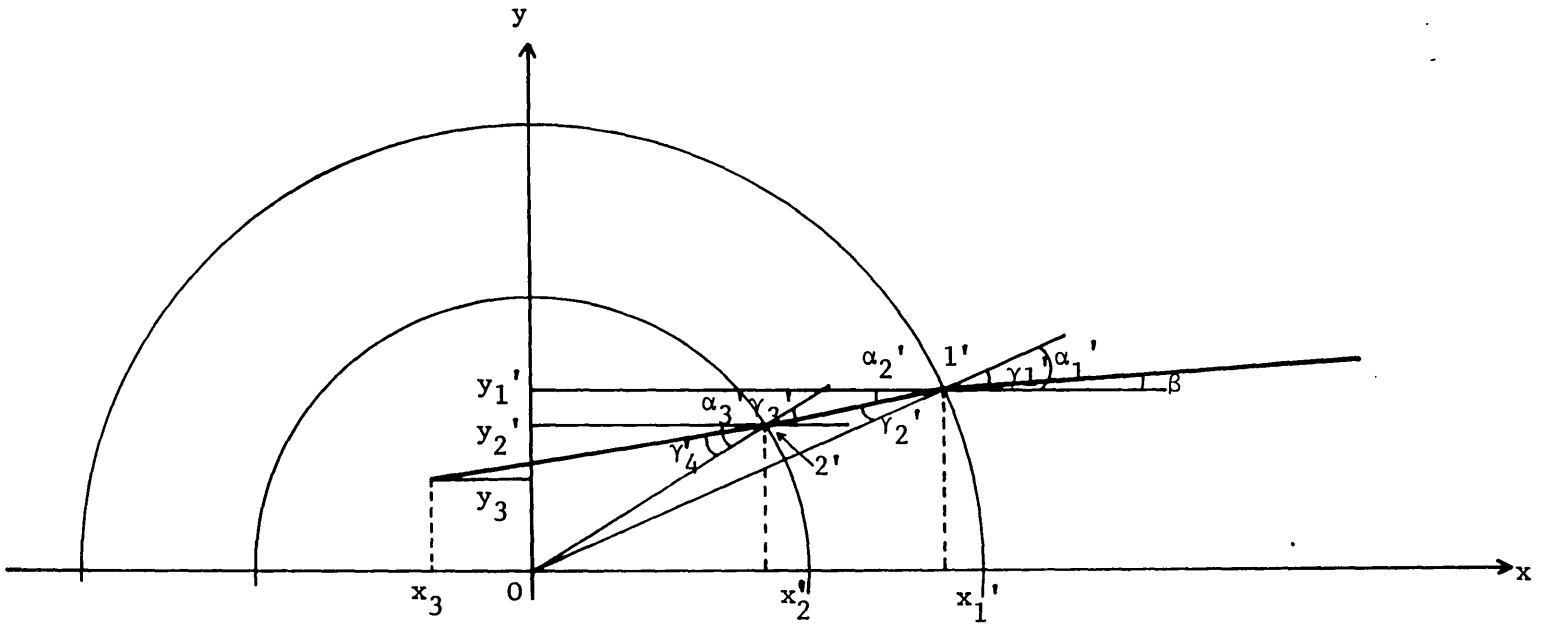


Figure II.3 Multiple refractions for right beam, horizontal plane, showing relevant points and angles

$$\tan \beta = \frac{y'_1 - (y_0+a)}{x'_1 - x_0} \tag{6}$$

$$x'^2_1 + y'^2_1 = R_0^2 \tag{7}$$

The beam–normal angle, γ'_1, is given by:

$$\gamma'_1 = \alpha'_1 - \beta \quad , \quad \text{where } \alpha'_1 = \tan^{-1}\left[\frac{y'_1}{x'_1}\right]$$

and hence the other beam–normal at the glass/air interface γ'_2 is:

$$\gamma'_2 = \sin^{-1}\left[\frac{n_1}{n_2} \sin \gamma'_1\right]$$

Now $\alpha'_2 = \alpha'_1 - \gamma'_2$ and $\tan \alpha'_2 = \frac{y'_2 - y'_1}{x'_2 - x'_1}$ (8)

Solving equation (8) simultaneously with equation (9):

$$x'^2_2 + y'^2_2 = R_i^2 \tag{9}$$

the coordinates of the intersection point of the right beam with the inner vessel wall, $2'(x'_2, y'_2)$ can be obtained.

The auxiliary angle α'_3 is:

$$\alpha'_3 = \tan^{-1}\left[\frac{y'_2}{x'_2}\right]$$

and

$$\gamma'_3 = \alpha'_3 - \alpha'_2$$

Hence, $$\gamma'_4 = \sin^{-1}\left[\frac{n_2}{n_3} \sin \gamma'_3\right]$$

The following relation can now be written:

$$\tan(\alpha'_3 - \gamma'_4) = \frac{y_3 - y'_2}{x_3 - x'_2} \qquad (10)$$

which, if solved with equation (5), will give the cross–over coordinates (x_3, y_3).

Part II – Determination of cross–over position with laser beams in vertical plane

The derivation will be done for the upper beam, since the cross–over point will be located on the laser axis, for whatever initial position; the lower beam going through a similar mirror image path through air/glass/water. The coordinates of the laser axis are (x, y, z) at the intersection point with the outer glass wall.

(i) *Incidence at outer glass surface (Finding γ_1)*

For this part it is necessary to pass through A′, a plane normal to line HH′, defining right–angled triangles AA′′B and AA′′A′ in the vertical and horizontal planes, respectively: Figure II.4.

$$\alpha_1 = \sin^{-1}(y/R_0)$$

From triangle OA′A, we have:

$$x_1 = \overline{AA'} = 2R_0 \sin(\alpha_1/2)$$

In triangle AA′′A′, we can write:

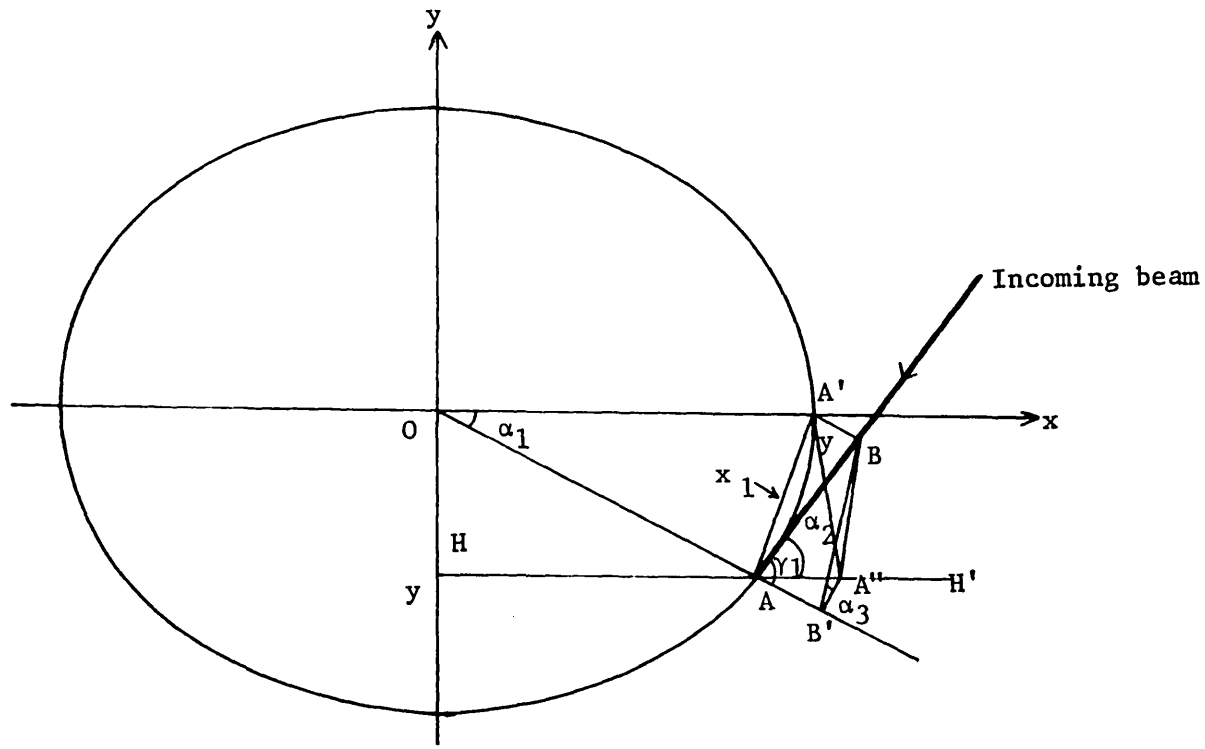


Figure II.4 Incidence of upper laser beam, vertical plane, on outer glass wall. (The angle of view is between 0° – 90°, i.e. between the horizontal and vertical planes)

$$x_2 = \overline{AA''} = \sqrt{x_1^2 - y^2}$$

and from triangle AA''B:

$$x_3 = \overline{A''B} = x_2 \tan \beta$$

Now we need to pass through line A''B a plane normal to line OA, defining right-angled triangles AB'B, BA''B' and AB'A'' in the beam-normal, vertical and horizontal planes, respectively. Hence, we have:

$$x_4 = \overline{A''B'} = x_2 \sin \alpha_1 \qquad \alpha_3 = \tan^{-1}\left[\frac{x_3}{x_4}\right] = \tan^{-1}\left[\frac{\tan \beta}{\sin \alpha_1}\right]$$

$$x_5 = \overline{BB'} = \sqrt{x_3^2 + x_4^2}$$

$$x_6 = \overline{AB'} = \sqrt{x_2^2 - x_4^2}$$

and so:

$$\gamma_1 = \tan^{-1}\left[\frac{x_5}{x_6}\right]$$

and

$$\gamma_2 = \sin^{-1}\left[\frac{n_1}{n_2} \sin \gamma_1\right]$$

where γ_1 is the angle of incidence (between laser beam and normal) at outer vessel wall,

γ_2 is the beam-normal angle inside the glass wall, at incidence point, and

α_3 is the angle between the beam-normal and horizontal planes.

Next, the beam goes down through the glass wall and we have to

find out the lowering in vertical component, when the beam reaches the inner surface of the wall (c) – Figure II.5(a) and (b).

(ii) *Lowering of beam (z–direction) inside glass wall (c)*

In Figure II.5(a) a slab is defined in which the upper and lower surfaces are the horizontal planes through A and E, respectively. $\overline{OA}$ and $\overline{O'E}$ are the normals at points A and E, respectively.

If we pass through EE′ a plane normal to normal $\overline{OA}$, intersecting it at point H, we can define the following right–angled triangles: EE′H, EHA and OHE in the vertical and beam–normal planes, respectively – Figure II.5(b).

Taking into consideration that the angle α_3 is still as defined above, and that triangle OEA is in the beam–normal plane, we can write:

$$\overline{EH} = h = a \sin \gamma_2$$

$$R_1 = \overline{AH} = a \cos \gamma_2 \text{ , and hence } R_2 = R_0 - R_1 = R_0 - a \cos \gamma_2$$

$$c = \overline{OO'} = \overline{EE'} = \overline{AE''} = h \sin \alpha_3 = a \sin \gamma_2 . \sin \alpha_3 \quad (1)$$

We have thus obtained the offset, c, but it is still a function of an unknown, a. Now:

$$b = \overline{OE} = \sqrt{h^2 + R_2^2} = \sqrt{a^2 \sin^2 \gamma_2 + (R_0 - a \cos \gamma_2)^2}$$

or

$$\overline{OE} = b = \sqrt{R_0^2 + a^2 - 2aR_0 \cos \gamma_2}$$

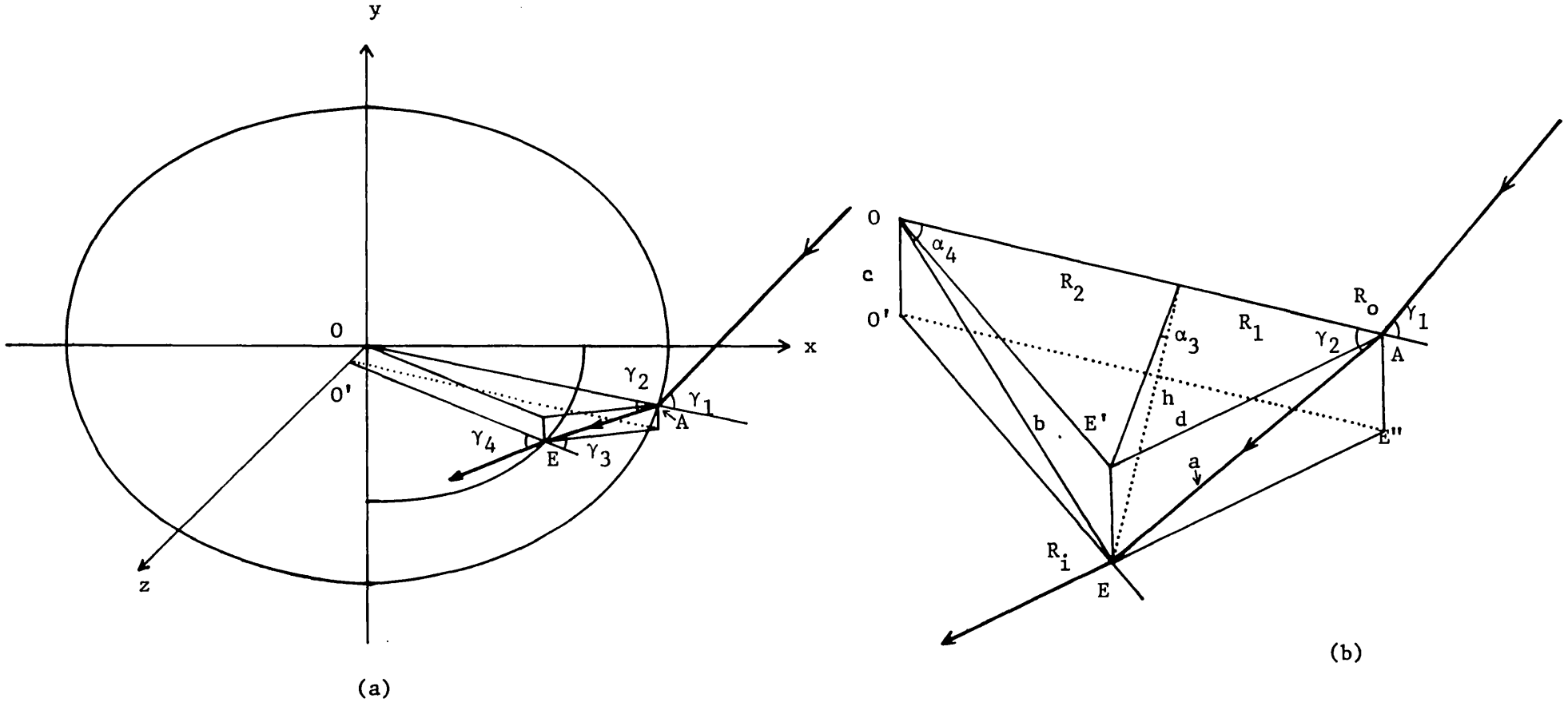


Figure II.5 Lowering of beam inside glass wall, in z–direction

(a) Positioning of slab in glass reactor

(b) Enlargement of slab showing relevant angles, positions and points

and

$$c^2 = b^2 - R_i^2 = R_0^2 + a^2 - 2aR_0 \cos \gamma_2 - R_i^2 \qquad (2)$$

From equations (1) and (2) we can write an expression for a:

$$a = \frac{(R_0^2 - R_i^2) + a^2(1 - \sin^2\gamma_2 \sin^2\alpha_3)}{2R_0 \cos \gamma_2}$$

that can be solved by trial and error. After the value for a is obtained, c and $d = \sqrt{a^2 - c^2}$ can be easily derived.

(iii) *Calculation of γ_3, the angle of incidence on the glass–water interface*

Consider again the same slab, but looking at the angles θ_1, θ_2, θ_3, ϵ_1, ϵ_2 and ϵ_3 – Figure II.6. In triangle AEO′ we can write the following relations [1]:

$$s = \tfrac{1}{2}(f + R_i + a), \quad \text{where} \quad f = \sqrt{c^2 + R_0^2}$$

and

$$r = \sqrt{\frac{(s-f)(s-R_i)(s-a)}{s}}$$

and hence

$$\tan \tfrac{1}{2}\epsilon_3 = \frac{r}{s-f} \quad \therefore \quad \epsilon_3 = 2 \tan^{-1}\left[\frac{r}{s-f}\right]$$

$$\tan \tfrac{1}{2}\epsilon_2 = \frac{r}{s-a} \quad \therefore \quad \epsilon_2 = 2 \tan^{-1}\left[\frac{r}{s-a}\right]$$

$$\tan \tfrac{1}{2}\epsilon_1 = \frac{r}{s-R_i} \quad \therefore \quad \epsilon_1 = 2 \tan^{-1}\left[\frac{r}{s-R_i}\right]$$

Then:

$$\gamma_3 = \epsilon_1 + \epsilon_2 = 2\left[\tan^{-1}\left[\frac{r}{s-a}\right] + \tan^{-1}\left[\frac{r}{s-R_i}\right]\right]$$

[1] "Perry's Chemical Engineers Handbook", R. H. Perry, D. Green (Editors), McGraw–Hill (New York), 1984.

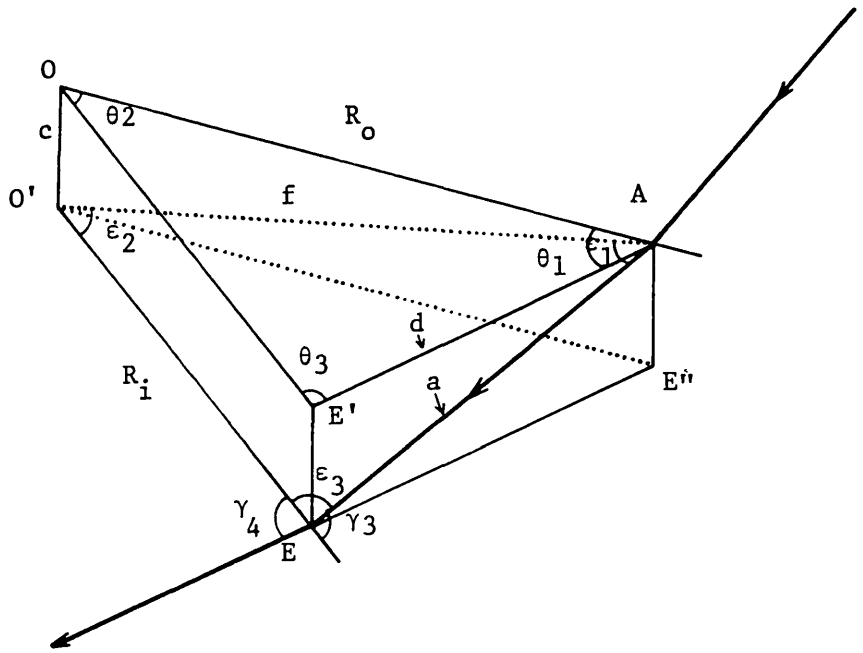


Figure II.6 Slab of reactor used for determination of angle of incidence of beam on glass/water interface

and

$$\gamma_4 = \sin^{-1}\left[\frac{n_2}{n_3}\sin\gamma_3\right]$$

In the upper horizontal plane, we find the triangle E′AO, and similarly we can write the following:

$$s' = \tfrac{1}{2}(R_0 + R_i + d)$$

$$r' = \sqrt{\frac{(s'-R_0)(s-R_i)(s-d)}{s}}$$

$$\tan\tfrac{1}{2}\theta_3 = \frac{r'}{s'-R_0} \quad \therefore \quad \theta_3 = 2\tan^{-1}\left[\frac{r'}{s'-R_0}\right]$$

$$\tan\tfrac{1}{2}\theta_2 = \frac{r'}{s'-d} \quad \therefore \quad \theta_2 = 2\tan^{-1}\left[\frac{r'}{s'-d}\right]$$

$$\tan\tfrac{1}{2}\theta_1 = \frac{r'}{s'-R_i} \quad \therefore \quad \theta_1 = 2\tan^{-1}\left[\frac{r'}{s'-R_i}\right]$$

(iv) *The beam in water*

Continuing on the same slab, let us consider the path when the beam goes into water Figure II.7.

Pass through AE′′ a plane perpendicular to OE′: triangle AE′′L is formed (right–angled), whose side c is known. Side ℓ can be known from triangle AO′L:

$$\ell = f\sin\epsilon_2$$

and

$$\alpha_5 = \sin^{-1}\left[\frac{c}{\ell}\right] = \sin^{-1}\left[\frac{a\sin\gamma_2\sin\alpha_3}{f\sin\epsilon_2}\right]$$

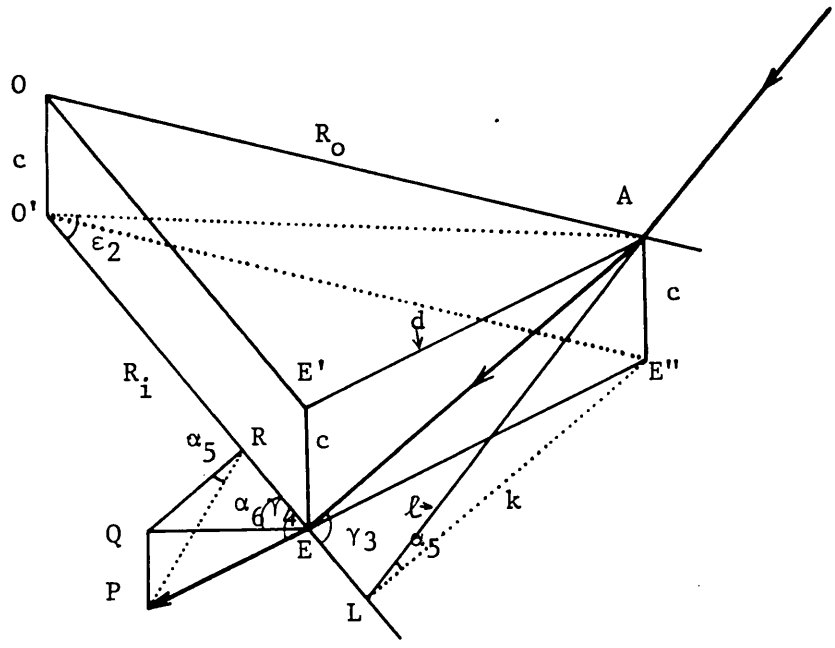


Figure II.7 Slab of reactor used for determination of cross–over point, in water

which is the angle between the beam–normal plane and the horizontal plane (in glass).

Now, let T be the beam separation at the entrance to glass (in glass–air interface), and let P be the crossing point of the two beams (it lies on the axis of symmetry of the two light beams). From P draw a line, normal to the bottom horizontal plane : $\overline{PQ}$, and pass through $\overline{PQ}$ a plane normal to line $\overline{O'E}$. This produces a right-angled triangle PQR, where the angle $\hat{PRQ}$ is equal to α_5.

$$\overline{PQ} + c = \frac{T}{2} \quad \therefore \quad \overline{PQ} = \frac{T}{2} - c$$

In triangle PQR: $\tan \alpha_5 = \dfrac{\overline{PQ}}{\overline{QR}}$ and $\overline{PR} = \dfrac{\overline{PQ}}{\sin \alpha_5}$

and in triangle ERP: $\overline{PR} = \overline{EP} \sin \gamma_4$

where $\overline{EP}$ is the actual length of beam from glass/water interface to cross–over.

In triangle PQE we have $u = \overline{EQ} = \sqrt{\overline{EP}^2 - \overline{PQ}^2}$, which is the image of $\overline{EP}$ on the horizontal plane.

In triangle ERQ: $\alpha_6 = \sin^{-1}\left[\dfrac{\overline{QR}}{\overline{QE}}\right]$

where α_6 is the angle between normal O'E and the image of $\overline{EP}$ on the bottom horizontal plane.

(v) ***Coordinates of cross–over***

In this final part we refer to the top view of the system Figure II.8.

The beam displacement, in glass, in the y–direction is:

$$w = d \sin(\alpha_1 - \theta_1)$$

$$\alpha_7 = \alpha_1 + \theta_2$$

$$\alpha_8 = \alpha_7 - \alpha_6$$

The beam displacement, in water, in the y–direction is now:

$$v = u \sin \alpha_8$$

The distance of cross–over from the entrance in the y–direction is:

$$v + w = u \sin \alpha_8 + d \sin(\alpha_1 - \theta_1)$$

and the distance of cross–over from the entrance in the x–direction is:

$$u \cos \alpha_3 + d \cos(\alpha_1 - \theta_1)$$

The cross–over coordinates are:

$$(x - [u \sin \alpha_8 + d \sin(\alpha_1 - \theta_1)],\ y - [u \cos \alpha_3 + d \cos(\alpha_1 - \theta_1)],\ z)$$

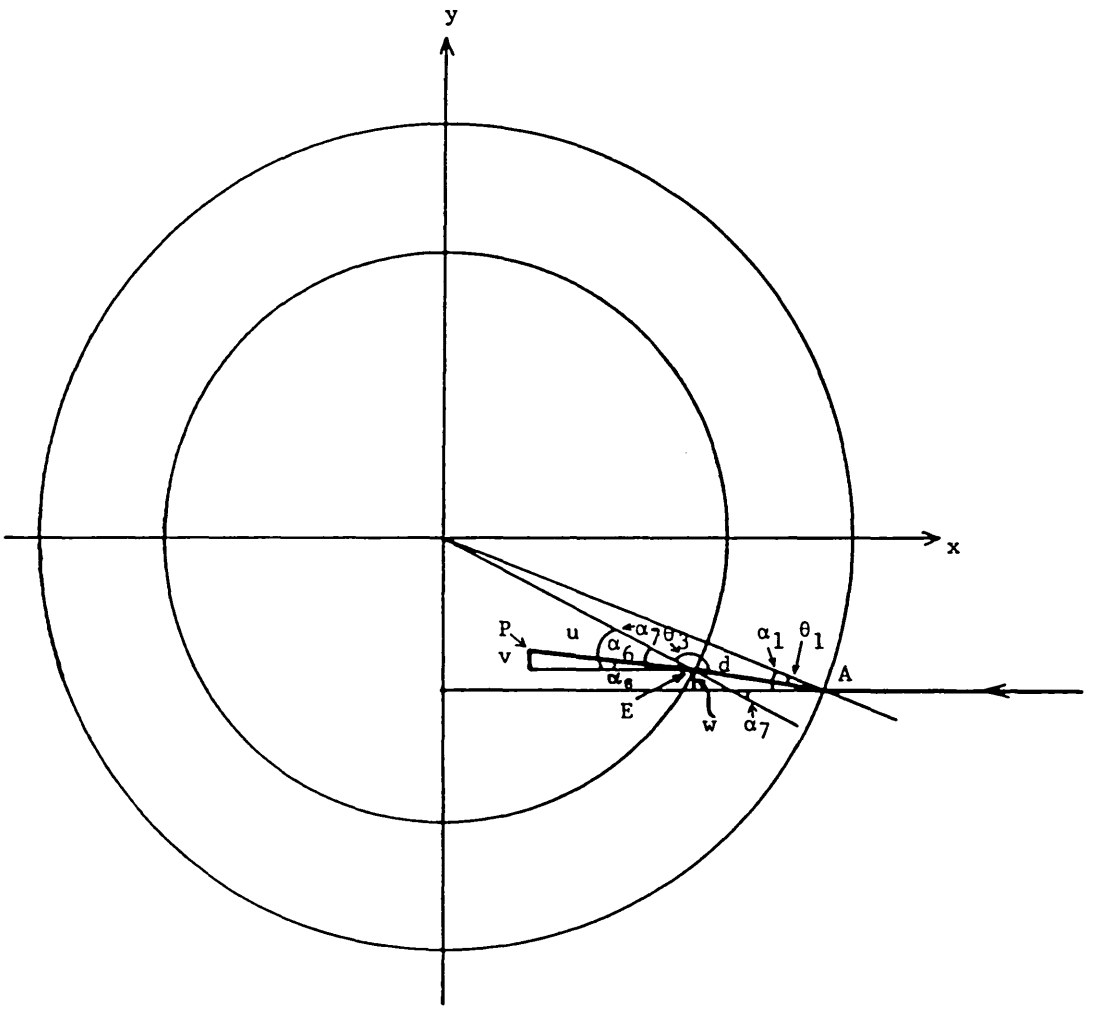


Figure II.8 Diagram of system showing movement of laser beam in the XY plane

Part III – Determination of photomultiplier position in order to see light scattered from the cross–over

The photomultiplier was placed parallel to the Y–axis (see Figure 3.23) and was physically focused at one position, chosen as the origin of coordinates. This section aims to find the coordinates $x_1 \equiv x_p$ and y_p which are the displacements in the x– and y–directions that the photomultiplier has to move from its original focusing position, to see light scattered from the cross–over (x_3, y_3).

In Figure II.9 the path of a ray of light coming from the cross–over and reaching the photomultiplier is drawn, with the relevant points and angles. We suppose the cross–over is in the 4th quadrant and we start the derivation by assuming a value for x_2 (at the intersection with the inner vessel wall).

Since (x_3, y_3) and x_2 are known, we have:

$$\tan \alpha_1 = \frac{x_2 - x_3}{y_2 - y_3} \tag{1}$$

and

$$x_2^2 + y_2^2 = R_i^2 \tag{2}$$

that upon solving we can find α_1 and y_2. Now:

$$\alpha_2 = \tan^{-1}\left[\frac{x_2}{y_2}\right]$$

and

$$\gamma_4 = \alpha_2 - \alpha_1$$

The beam normal angle at the glass/water interface, γ_3, is given by:

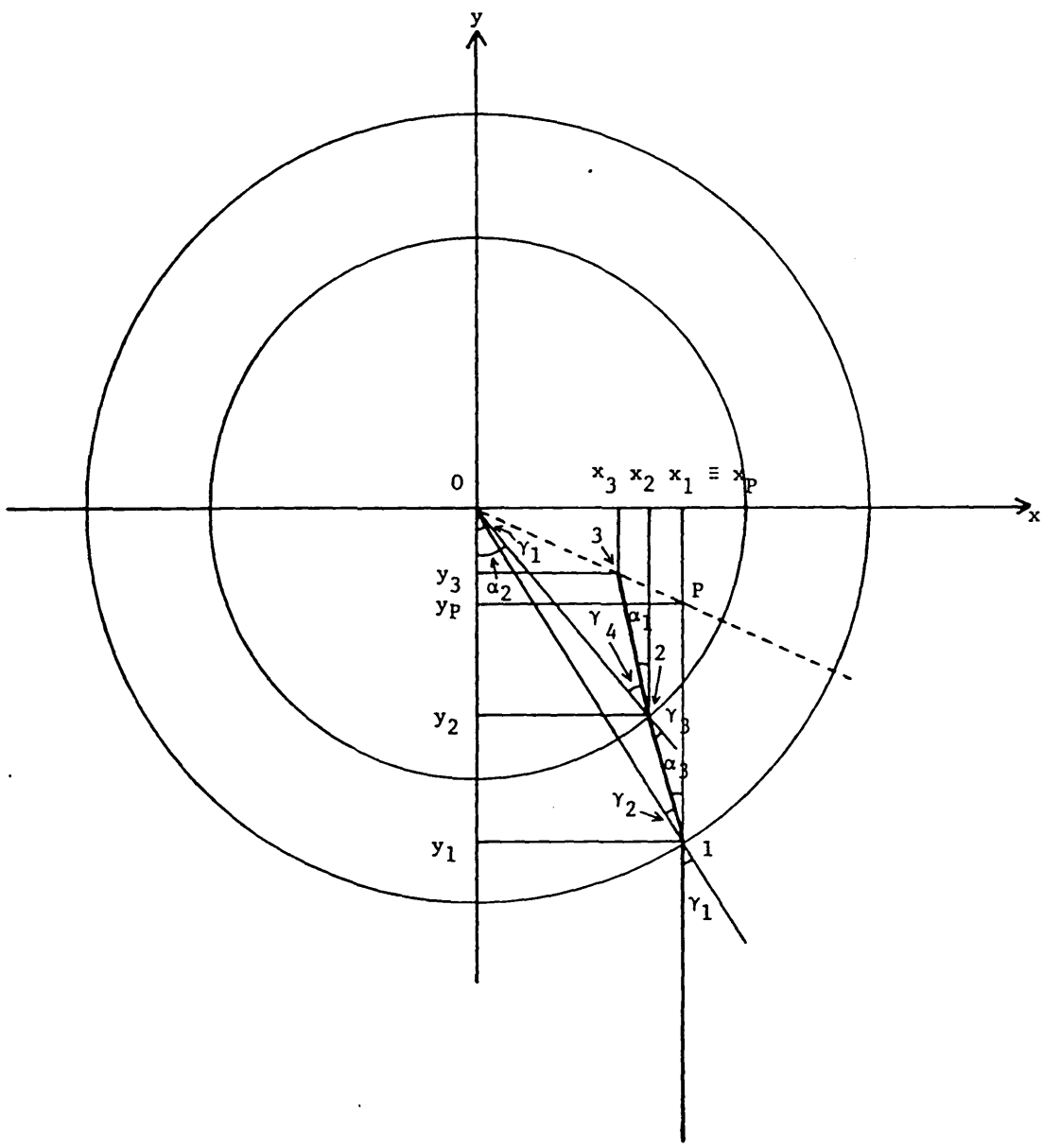


Figure II.9 Diagram of the path of a ray of light coming from the cross–over and reaching the photomultiplier

$$\gamma_3 = \sin^{-1}\left[\frac{n_3}{n_2}\sin\gamma_4\right]$$

The auxiliary angle α_3 is:

$$\alpha_3 = \alpha_2 - \gamma_3 \quad \text{and} \quad \tan\alpha_3 = \frac{x_1 - x_2}{y_1 - y_2} \tag{3}$$

Solving equations (3) and (4), the coordinates of the point of intersection at the glass/air interface can be determined:

$$x_1^2 + y_1^2 = R_0^2 \tag{4}$$

Now

$$\gamma_1 = \tan^{-1}\left[\frac{x_1}{y_1}\right]$$

and

$$\gamma_2 = \gamma_1 - \alpha_3$$

and therefore:

$$n_1 \sin\gamma_1 = n_2 \sin\gamma_2 \tag{5}$$

Using equation (5), the equality can be checked, with a tolerance of 1×10^{-5}, to see if the first choice of x_2 was correct. If not, the process must be repeated until x_2 is found. Then:

$$x_p \equiv x_1$$

and

$$y_p = \frac{x_p}{x_3} \cdot y_3$$

where x_p and y_p are the coordinates of the apparent cross–over, that is, the coordinates of the point where the photomultiplier sees the real cross–over (x_3, y_3).

NOMENCLATURE

γ	beam–normal angles
α, θ, ϵ	auxiliary angles
β	half–angle of intersection of laser beams in air ($\beta = 1.14576^0$)
a	half distance of laser beams at source (a = 1 cm)
R_0	radius of outer glass vessel wall
R_i	radius of inner glass vessel wall
n_1	refractive index of air
n_2	refractive index of glass
n_3	refractive index of water

APPENDIX III

DERIVATION OF AN EXPRESSION FOR MONOMER CONVERSION AS A FUNCTION OF TIME AND CALCULATION OF MONOMER CONVERSION AT VARIOUS TEMPERATURES. FOR ONSET OF AGGREGATION

In this appendix an expression for the variation of monomer concentration with time is derived, assuming a free–radical chain growth polymerisation mechanism, together with the calculation of monomer conversion at various temperatures and for specific times of aggregation.

The free–radical chain growth polymerisation of styrene can be described by the following mechanism:

$I \xrightarrow{k_i} 2R_1$		Initiation
$M + R_n \xrightarrow{k_p} R_{n+1}$		Propagation
$R_n + M \xrightarrow{k^M_{tr}} P_n + R_1$		Transfer to monomer
$R_n + P_j \xrightarrow{k^P_{tr}} P_n + R_j$		Transfer to polymer
$R_n + R_j \xrightarrow{k_{tc}} P_{n+j}$		Termination (combination)

where I is a initiator

R is a growing polymer radical

P is a dead polymer radical

M is the monomer and

k_i, k_p, k_{tc} and k_{tr} are the rate constants for initiation, propagation, termination and transfer, respectively.

Since chain transfer to polymer has only an effect in chain branching, it will not be considered in the following derivations. First, we will write the mass balances for the various species involved:

$$\frac{dI}{dt} = -k_i\, I \tag{1}$$

$$\frac{dR_1}{dt} = 2\, f\, k_i\, I - k_p\, M\, R_1 - k_{tc}\, R_1\, R + k^M_{tr}\, M\, (R - R_1) \tag{2}$$

$$\frac{dR_n}{dt} = k_p\, M\, R_{n-1} - k_p\, M\, R_n - k_{tc}\, R_n \sum_{n=1}^{\infty} R_n - k^M_{tr}\, M\, R_n \quad \text{for } n \geq 2 \tag{3}$$

$$\frac{dR}{dt} = 2\, f\, k_i\, I - k_{tc}\, R^2 \quad \text{where } R = \sum_{n=1}^{\infty} R_n \tag{4}$$

$$\frac{dM}{dt} = -k_p\, M \sum_{n=1}^{\infty} R_n - k^M_{tr}\, M \sum_{n=1}^{\infty} R_n \tag{5}$$

$$\frac{dP_n}{dt} = k^M_{tr}\, M\, R_n + \tfrac{1}{2} k_{tc} \sum_{j=1}^{n-1} R_n\, R_{n-j} \tag{6}$$

Assuming pseudo–steady state: $\frac{d}{dt}\left(\sum_{n=1}^{\infty} R_n\right) << \frac{dM}{dt}$, and $\frac{dR}{dt} = o$; $\frac{dR_1}{dt} = o$; and $\frac{dR_n}{dt} = o$

one can obtain (7) from (4):

$$R = \left(\frac{2\, f\, k_i\, I}{k_{tc}}\right)^{\frac{1}{2}} \tag{7}$$

and therefore:

$$M = M_o \exp\left[\frac{2}{k_i}(k_p + k_{t_r}^M)\left(\frac{2\ f\ k_i\ I_o}{k_{tc}}\right)^{\frac{1}{2}}(e^{-k_i/2^t} - 1)\right] \qquad (8)$$

or expression (9) if chain transfer to monomer is negligible:

$$M = M_o \exp\left[\frac{2\ k_p}{k_i}\left(\frac{2\ f\ k_i\ I_o}{k_{tc}}\right)^{\frac{1}{2}}(e^{-k_i/2^t} - 1)\right] \qquad (9)$$

where subscript o refers to initial conditions.

The values of the rate constants were taken from the literature [1], choosing only data points above 30 C (closer to the working temperature range in this work) and averaging all data for a given temperature , which was found to give the best correlation coefficient.

$$\ln k_i = 1.29 \times 10^{15} \exp\left[-127.6 \times 10^3/8.31\ (T + 273)\right] \qquad (T \text{ in C})$$

$$\ln k_p = 5250.634 \times \frac{1}{T} + 21.466 \qquad (T \text{ in K})$$

$$\ln k_t = 1912.783 \times \frac{1}{T} + 23.983 \qquad (T \text{ in K})$$

$$\ln C_M = 2770.02 \times \frac{1}{T} - 1.146 \qquad (T \text{ in K})$$

where k_i is expressed in sec^{-1}, and

k_p, k_t and k_t^M in $l.mole^{-1}.sec^{-1}$

$$C_M = \frac{k_{t\,r}^M}{k_p}$$

The polymerisation reaction provided experimental times of aggregation as a function of polymerisation temperature, which correspond to certain values of monomer

[1] "Polymer Handbook", J. Brandrup, E. H. Immergut (Editors), John Wiley and Sons, (London), 1975.

conversion. These values of conversion can be obtained from either expressions (8) or (9), depending whether chain transfer to monomer is important or not, respectively, and then they can be compared with the corresponding calculated conversion at each temperature, assuming the suggested mechanism, i.e. the conversion at which the $T_{g1,2}$ of the droplet equals the polymerisation temperature.

In Table III.1 are presented the values of conversion at aggregation time, based on the experimental values, as well as the calculated conversion from the proposed mechanism. All calculations were based on expression (9), without chain transfer to monomer, $I_0 = 0.0609$ M, $M_0 = 8.687$ M and initiator efficiency, $f = 0.6$.

Table III.1 Table of results for time and conversion at onset of aggregation, as a function of temperature.

T/C	$t_{agg-exp}$/h	$x_{agg-exp}$/%	$x_{agg-cal}$/%
71.0	4.95	74.4	77.7
75.5	3.63	77.2	81.2
78.0	3.15	79.1	83.1
80.0	2.81	80.6	84.8
86.0	1.95	81.1	89.5

Since the individual rate constants show a considerable dispersion in their values, the 95% confidence interval for both k_p and k_t were calculated. The results showed that the errors involved were always higher than 35%. Hence, it was decided to repeat the calculations for the experimental conversion at aggregation time, but introducing ± 20% errors in the values for k_i, k_p and k_t. Table II.2 presents the experimental time of aggregation as a function of temperature, when errors are considered in the individual rate

constants. The lower value corresponds to a –20% error in k_p and the higher value to a +20% error in k_p.

Table III.2 Table of results for variation of experimental conversion at onset of aggregation as a function of temperature, when errors are introduced.

T/C	$x_{agg-exp(-20\%\ k_t)}$/%	$x_{agg-exp(+20\%\ kp)}$/%
71.0	67.8	80.5
75.5	69.4	83.0
78.0	71.4	84.7
80.0	72.5	85.6
86.0	73.6	86.5

If chain transfer to monomer is introduced and monomer conversion is calculated from equation (8) there are only very small changes in monomer conversion, which do not justify its consideration.

A P P E N D I X I V

COMPUTER PROGRAMS FOR LDA

1 Bacscat 321

```
10 rem---program name is bacscat321
20 rem---this program finds the position of laser for various positions
21 rem---of cross-over [which have equal x coordinate].  laser is parallel
22 rem---to x-axis.    laser beams are horizontal.    origin is at the
23 rem---centre of the vessel.   program then calculates position of
25 rem---pm.   pm is parallel to y-axis.
26 clr:cl$=chr$(147):tp$=chr$(19):er$=chr$(20):bl$=chr$(7)
27 print cl$
28 dim d(1000):dim x(1000):dim u(1000):dim xa(1000)
30 input"enter inside radius of vessel [in cm]  ";ri
40 if ri>0 then 50
45 gosub 400:goto30
50 input"enter outside radius of vessel [in cm]  ";ro
60 if ro>ri then 80
65 gosub 400
70 print tp$:print:goto50
80 input"enter position of laser w.r.t. shaft [in cm]  ";x0
85 if x0>50-ro and x0<50+ro then 92
90 gosub 400
91 print tp$:print:print:goto80
92 input"enter beam spacing at source [in cm]  ";bs
93 if bs>0 and bs=<2 then 96
94 gosub 400
95 print tp$:print:print:print:goto 92
96 rem--input"enter starting position of laser axis w.r.t. X-axis [in cm]  ";yo
97 rem---if abs(yo)<ri then 110
98 rem---gosub 400
99 rem---print tp$:print:print:print:print:goto 96
110 input"enter refractive index of vessel wall  ";n21
111 if n21>0 then 115
112 gosub 400
113 print tp$:print:print:print:print:goto110
115 input"enter refractive index of liquid  ";n31
118 if n31>0 then 124
120 gosub 400
```

```
122 print tp$:print:print:print:print:print:goto115
124 input"enter x-coordinate of cross-over [in cm]  ";x3
126 if abs(x3)<ri then 132
128 gosub 400
130 print tp$:print:print:print:print:print:print:goto124
132 input"enter size of increment in Y-direction [in cm]  ";dy
134 if dy<>0 and abs(dy)<ri/2 then 140
136 gosub 400
138 print tp$:print:print:print:print:print:print:print
139 goto 132
140 print cl$:p=10:pp=0
141 input"do you require print out or screen display (p/s)";an$
142 if an$="p" then pl=1:lp=0:open4,4:cmd4:goto 145
143 if an$="s" then pl=0:goto 145
144 print bl$:goto 141
145 print cl$
146 rem---this section is for left-hand beam
150 rem---coordinates called x*,y* belong to lower beam
155 rem---angles called b* are beam-normal angles for lower beam
160 rem---angles called a* are auxiliary angles for lower beam
163 wc=fre(0)
165 yo=0:x0=50
166 j=0:dx=.02
167 j=j+1
170 xa(j)=x0
184 y0=yo-bs/2:tb=0.02:bt=atn(tb):rem---bt is beta, and tb is tan(beta)
186 if y0=<-(ro+x0*tb) then 365
188 q1=tb^2+1
190 q2=-2*(tb*y0+x0*(tb^2))
192 q3=y0^2+(tb^2)*(x0^2)+(2*tb)*(x0*y0)-ro^2
193 qs=q2^2-4*q1*q3:if qs<0 then 365
194 x1=(-q2+sqr(qs))/(2*q1)
196 y1=y0-tb*(x1-x0)
198 a1=atn(y1/x1):b1=a1+bt
200 js=sin(b1)/n21:jc=sqr(1-js^2):b2=atn(js/jc):a2=a1-b2:t2=tan(a2)
```

```
205 q4=1+t2^2:q5=2*(t2*y1-x1*(t2^2)):q6=(t2^2)*(x1^2)+y1^2-(2*y1)*(t2*x1)-ri^2
207 qs=q5^2-4*q4*q6:if qs<0 then 365
210 x2=(-q5+sqr(qs))/(2*q4)
215 y2=y1-t2*(x1-x2)
220 a3=atn(y2/x2):b3=a3-a2
225 js=sin(b3)*n21/n31:jc=sqr(1-js^2):b4=atn(js/jc)
230 t3=tan(a3-b4)
235 rem---
240 rem---this section is for right-hand beam
245 rem---coordinates called u*,v* belong to upper beam
250 rem---angles called d* are beam-normal angles for upper beam
255 rem---angles called c* are auxiliary angles for upper beam
260 v0=yo+bs/2:u0=x0
262 if v0=>(ro+x0*tb) then 365
265 s1=1+tb^2
270 s2=2*(v0*tb-u0*(tb^2))
275 s3=v0^2-ro^2+(tb*u0)^2-(2*v0)*(tb*u0)
277 qs=s2^2-4*s1*s3:if qs<0 then 365
280 u1=(-s2+sqr(qs))/(2*s1)
285 v1=v0+tb*(u1-u0)
290 c1=atn(v1/u1):d1=c1-bt
295 js=sin(d1)/n21:jc=sqr(1-js^2):d2=atn(js/jc):c2=c1-d2:t4=tan(c2)
300 s4=1+(t4^2)
302 s5=2*(v1*t4-(t4^2)*u1)
304 s6=v1^2-ri^2+(t4*u1)^2-(2*v1)*(t4*u1)
305 qs=s5^2-4*s4*s6:if qs<0 then 365
306 u2=(-s5+sqr(qs))/(2*s4)
308 v2=v1-t4*(u1-u2)
310 c3=atn(v2/u2):d3=c3-c2
312 js=sin(d3)*n21/n31:jc=sqr(1-js^2):d4=atn(js/jc)
314 t5=tan(c3-d4)
316 u3=(v2-y2-u2*t5+x2*t3)/(t3-t5):u(j)=u3
325 v3=y2-t3*(x2-u3):y3=v3
330 d(j)=u(j)-x3:if j=1 then 345
335 fi=u(j)-u(j-1):pf=fi/(abs(x3)+abs(u(j)))
```

```
337 if abs(pf)<.00001 then 360
340 sl=fi/(xa(j)-xa(j-1))
342 if sl<0 then dx=dx/2:goto 345
344 dx=-d(j)/sl
345 x0=x0+dx:goto167
360 gosub 2000
362 yo=yo+dy:goto 166
365 if pl=1 then printf4:close4
375 print:print"*************************  ";
380 print"press any key to repeat  *************************"
385 get q$:if q$="" then 385
390 run
400 for j=1 to 82:print er$;:next
405 print chr$(7):print"invalid entry";
410 for i=1 to 1000:next
420 for i=1 to 13:print chr$(20);:next
430 return
2000 rem---this section uses x3,y3 coordinates of cross-over to calculate
2005 rem---the position of photomultiplier.
2010 rem---x4 & x5=x2 & x1 and y4 & y5=y2 & y1 in pm direction
2011 rem---e1 to e4=a1 to a4 in pm direction
2015 m1=sqr(x3^2+y3^2)•
2020 if m1<ri then 2055
2030 if pp=0 then pp=1:m2=m1:print:return
2040 if m1<m2 then pp=0:print:return
2050 goto 365
2055 n=(ri-x3)*2.05644207
2060 m=.831990528+1.41616153*(4.01469697-x3)
2065 if abs((n-y3)/n)<.00001 then gosub 2250:goto 2267
2070 if abs((m-y3)/m)<.00001 then gosub 2255:goto 2267
2075 if m<y3 then print"no PM position":goto 375
2080 if n<y3 then kh=1
2085 if n>y3 then kh=-1
2145 if x3=0 then x3=.05:goto 2155
2150 if abs(x3)<.05 then x3=.05*abs(x3)/x3
```

```
2153 if kh=1 then 2600
2155 i=0:pm=.0002/(ri-abs(x3))
2160 x(1)=(abs(x3)+pm)*abs(x3)/x3:x(2)=(abs(x3)+2*pm)*abs(x3)/x3
2165 i=i+1:x4=x(i):qs=ri^2-x4^2:if qs<0 then print"no PM position":return
2170 y4=-sqr(qs):ga=atn((x4-x3)/(y4-y3)):te=atn(x4/y4)
2175 e4=te-ga:js=sin(e4)*n31/n21:jc=sqr(1-js^2):e3=atn(js/jc)
2180 be=te-e3:tt=tan(be):q1=1+tt^2:q2=-(2*y4)*(tt^2)+2*(tt*x4)
2185 q3=-(ro^2-x4^2+(2*tt)*(y4*x4)-(tt^2)*(y4^2))
2187 qs=q2^2-4*q1*q3:if qs<0 then print"no PM position":return
2190 y5=(-q2-sqr(qs))/(2*q1)
2195 x5=sqr(ro^2-y5^2)*abs(x3)/x3
2200 e1=atn(x5/y5):e2=e1-be
2205 d(i)=sin(e1)-n21*sin(e2)
2210 dd=d(i)*2/(sin(e1)+n21*sin(e2))
2215 if abs(dd)=<0.00001 then 2265
2220 if i=1 then 2165
2225 sl=(d(i)-d(i-1))/(x(i)-x(i-1))
2230 k=1
2235 x(i+1)=x(i)-d(i)/(k*sl)
2240 if abs(x(i+1))<ri then 2165
2245 k=k+1
2246 rem---if k>100 then print"no pm position here":kh=1:goto 362
2247 goto 2235
2250 x5=-(ro*(-5.02047586))/sqr(1+(-5.02047586)^2)
2251 yp=x5*y3/x3
2252 return
2255 x5=ro
2256 yp=x5*y3/x3
2257 return
2265 yp=x5*y3/x3
2267 x5=int(x5*1000)/1000:yp=int(yp*1000)/1000
2280 if p1=0 then gosub 2500:return:rem---this prints on screen
2285 gosub 4000:rem---this prints on printer
2310 return
2500 rem---this section prints on screen
```

```
2510 p=p+1:if p>10 then p=0
2515 if p=0 then gosub 3000
2517 x3=int(x3*1000)/1000:y3=int(y3*1000)/1000:yo=int(yo*1000)/1000
2518 x0=int(x0*1000)/1000
2520 printtab(3)x3tab(16)y3;
2530 print tab(31)yotab(45)x0;
2540 print tab(60)yptab(71)x5
2550 return
2600 rem---this section calculates cross-over for troublesome area
2605 i=0:pm=.1/(ri-abs(x3))
2610 gosub 2800
2615 pm=(ri-p3)/3
2617 x(1)=(abs(p3)+pm)*abs(p3)/p3:x(2)=(abs(p3)+2*pm)*abs(p3)/p3
2620 i=i+1
2625 x4=x(i):qs=ri^2-x4^2:if qs<0 then print"no PM position":return
2630 y4=+sqr(qs):ga=3.14158+atn((x4-x3)/(y4-y3)):te=atn(x4/y4)
2635 e4=ga-te:js=sin(e4)*n31/n21:jc=sqr(1-js^2):e3=atn(js/jc)
2640 be=3.14158-(te+e3):tt=tan(be):q1=1+tt^2:q2=-2*tt*(tt*y4+x4)
2645 q3=-(ro^2-x4^2-2*tt*(y4*x4)-(tt^2)*(y4^2))
2650 qs=q2^2-4*q1*q3:if qs<0 then print"no PM position":return
2660 y5=(-q2-sqr(qs))/(2*q1)
2665 x5=sqr(ro^2-y5^2)*abs(x3)/x3
2670 e1=atn(x5/y5):e2=e1-be
2675 dd=sin(e1)-n21*sin(e2)
2680 d(i)=dd*2/(sin(e1)+n21*sin(e2))
2685 if abs(d(i))=<0.00001 then 2265
2690 if i=1 then 2620
2695 if d(i)/d(i-1)<0 then pm=-pm/2:goto 2705
2700 if d(i)<0 and d(i)<d(i-1) then pm=-pm:goto 2705
2702 if d(i)>0 and d(i)>d(i-1) then pm=-pm
2705 x(i+1)=x(i)+pm
2710 goto 2620
2800 rem---this section calculates initial x4 for troublesome area
2805 tn=(2.28419-y3)/(2.98925-x3)
2810 q1=1+tn^2:q2=2*tn*y3-(2*x3)*(tn^2):q3=y3^2-ri^2+(tn*x3)^2-(2*tn)*(x3*y3)
```

```
2815 p3=(-q2+sqr(q2^2-4*q1*q3))/(2*q1)
2820 return
3000 print"90 deg backscatter.   laser beams in horizontal position."
3003 print"-------------------------------------------------------------------------";
3006 print"----------------"
3010 print" position of cross-over ";
3015 printtab(29)" distance of laser from ";
3020 print tab(58)" distance of PM from "
3025 print"     X             Y ";
3030 print "          X-axis          Y-axis ";
3035 print "      X-axis       Y-axis "
3040 print"-------------------------------------------------------------------------";
3045 print"----------------"
3050 return
3500 rem---this section prints heading for printer output
3505 print"90 deg backscatter.   laser beams in horizontal position."
3510 print"-------------------------------------------------------------------------";
3515 print"-----------------------------------------------------"
3520 print tab(5)" position of cross-over ";
3525 print tab(15)" distance of laser from ";
3530 print tab(15)" distance of PM from "
3540 print tab(10)" X          Y "tab(22)" X-axis      Y-axis ";
3541 print tab(18)" X-axis     Y-axis "
3560 print"-------------------------------------------------------------------------";
3570 print"-----------------------------------------------------"
3580 return
4000 rem---this section prints results on the printer
4015 if lp=0 then gosub 3500:lp=1
4016 x3=int(x3*1000)/1000:y3=int(y3*1000)/1000:yo=int(yo*1000)/1000
4017 x0=int(x0*1000)/1000
4020 printtab(8)x3tab(9)y3tab(22)yotab(6)x0tab(19)yptab(5)x5
4040 return
```

2 Bacscat 341

```
10 rem---program name is bacscat341
20 rem---this program finds the position of laser for various positions
21 rem---of cross-over [which have equal x coordinate].  laser is parallel
22 rem---to x-axis.    laser beams are verticle .    origin is at the
23 rem---centre of the vessel.   program then calculates position of
25 rem---pm.   pm is parallel to y-axis.
26 clr:cl$=chr$(147):tp$=chr$(19):er$=chr$(20):bl$=chr$(7)
27 print cl$
28 dim d(1000):dim x(1000):dim u(1000):dim xa(1000)
30 input"enter inside radius of vessel [in cm]  ";ri
40 if ri>0 then 50
45 gosub 400:goto30
50 input"enter outside radius of vessel [in cm]  ";ro
60 if ro>ri then 80
65 gosub 400
70 print tp$:print:goto50
80 input"enter position of laser w.r.t. shaft [in cm]  ";x0
85 if x0>50-ro and x0<50+ro then 92
90 gosub 400
91 print tp$:print:print:goto80
92 input"enter beam spacing at source [in cm]  ";sb:rem-beam spac @ source
93 if sb>0 and sb=<2 then 96
94 gosub 400
95 print tp$:print:print:print:goto 92
96 rem--input"enter starting position of laser axis w.r.t. X-axis [in cm]  ";yo
97 rem---if abs(yo)<ri then 110
98 rem---gosub 400
99 rem---print tp$:print:print:print:print:goto 96
110 input"enter refractive index of vessel wall  ";n21
111 if n21>0 then 115
112 gosub 400
113 print tp$:print:print:print:print:goto110
115 input"enter refractive index of liquid  ";n31
118 if n31>0 then 124
```

```
120 gosub 400
122 print tp$:print:print:print:print:print:goto115
124 input"enter x-coordinate of cross-over [in cm]  ";x3
126 if abs(x3)<ri then 132
128 gosub 400
130 print tp$:print:print:print:print:print:print:goto124
132 input"enter size of increment in Y-direction [in cm]  ";dy
134 if dy<>0 and abs(dy)<ri/2 then 140
136 gosub 400
138 print tp$:print:print:print:print:print:print:print
139 goto 132
140 print cl$:p=10:pp=0:qr=ro^2:ir=ri^2
141 input"do you require print out or screen display (p/s)";an$
142 if an$="p" then pl=1:lp=0:open4,4:cmd4:goto 145
143 if an$="s" then pl=0:goto 145
144 print bl$:goto 141
145 print cl$
146 rem---calculations are based on upper beam
150 rem---angles called b* are beam-normal angles
155 rem---angles called a* are auxiliary angles
160 rem---h* are lengths of auxiliary lines
165 wc=fre(0):y0=0:x0=50:tb=0.02
167 j=0:dx=.02
168 j=j+1
169 xa(j)=x0
170 if y0=0 then gosub 600:gosub 2000:y0=y0+dy:goto 167
172 hh=sqr(qr-y0^2):a1=atn(abs(y0/hh))
175 bs=2*((sb/2)-(x0-ro*cos(a1))*tb):x1=ro*cos(a1):y1=y0
177 h1=2*(ro*sin(a1/2)):h2=sqr(h1^2-y0^2):h3=h2*tb
180 h4=h2*sin(a1):sh=h4^2:h5=sqr(h3^2+sh):h6=sqr(h2^2-sh)
185 b1=atn(h5/h6):a3=atn(h3/h4)
190 ks=sin(b1)/n21:kc=sqr(1-ks^2):b2=atn(ks/kc)
195 q1=1-(sin(b2)^2)*(sin(a3)^2)
200 q2=-2*(ro*cos(b2))
205 q3=qr-ir
```

```
210 a=(-q2-sqr(q2^2-4*q1*q3))/(2*q1)
215 z1=abs(a*sin(b2)*sin(a3)):sz=z1^2:d=sqr(a^2-sz)
220 f=sqr(sz+qr)
225 s1=(f+ri+a)/2:r1=sqr((s1-f)*(s1-ri)*(s1-a)/s1)
230 e1=2*atn(r1/(s1-ri)):e2=2*atn(r1/(s1-a))
235 b3=e1+e2:b4=atn((sin(b3)*n21/n31)/sqr(1-(sin(b3)*n21/n31)^2))
240 s2=(ro+ri+d)/2:r2=sqr((s2-ro)*(s2-ri)*(s2-d)/s2)
245 i1=2*atn(r2/(s2-ri)):i2=2*atn(r2/(s2-d))
250 l=f*sin(e2):js=a*sin(b2)*sin(a3)/(f*sin(e2)):jc=sqr(1-js^2)
255 a4=atn(js/jc)
260 z2=(bs/2)-z1
265 qt=z2/tan(a4):pr=z2/sin(a4):ep=pr/sin(b4):rem---qt is in fact qr
270 uu=sqr(ep^2-z2^2)
275 js=qt/uu:jc=sqr(1-js^2):a5=atn(js/jc)
280 a6=a1+i2:y2=y1-d*sin(a1-i1)*abs(y1)/y1
285 a7=a6-a5
290 y3=y2-uu*sin(a7)*abs(y1)/y1
295 x2=x1-d*cos(a1-i1):u(j)=x2-uu*cos(a7)
348 d(j)=u(j)-x3:if j=1 then 360
350 fi=u(j)-u(j-1):pf=fi/(abs(x3)+abs(u(j)))
352 if abs(pf)<.00001 then 365
355 sl=fi/(xa(j)-xa(j-1))
356 if sl<0 then dx=dx/2:goto 360
357 dx=-d(j)/sl
360 x0=x0+dx:goto 168
365 gosub 2000
372 y0=y0+dy:goto 167
375 if pl=1 then print£4:close4
382 print:print"**************************  ";
384 print"press any key to repeat  **************************"
385 get q$:if q$="" then 385
390 run
400 for j=1 to 82:print er$;:next
405 print chr$(7):print"invalid entry";
410 for i=1 to 1000:next
```

```
420 for i=1 to 13:print chr$(20);:next
430 return
600 rem---this subroutine calculates cross-over when y0=0
610 b1=atn(tb):gs=sin(b1)/n21:gc=sqr(1-gs^2):b2=atn(gs/gc):b3=b2
620 z1=(ro-ri)*tan(b2):bs=2*(sb/2-(x0-ro)*tb):z2=bs/2-z1
630 ms=sin(b3)*n21/n31:mc=sqr(1-ms^2):b4=atn(ms/mc)
640 u(j)=ri-z2/tan(b4):y3=y0
642 d(j)=u(j)-x3:if j=1 then 660
645 fi=u(j)-u(j-1):pf=fi/(abs(x3)+abs(u(j)))
647 if abs(pf)<0.00001 then return
650 sl=fi/(xa(j)-xa(j-1))
655 if sl<0 then dx=dx/2:goto 660
657 dx=-d(j)/sl
660 x0=x0+dx:goto 168
2000 rem---this section uses x3,y3 coordinates of cross-over to calculate
2005 rem---the position of photomultiplier.
2010 rem---x4 & x5=x2 & x1 and y4 & y5=y2 & y1 in pm direction
2011 rem---c1 to c4=a1 to a4 in pm direction
2015 m1=sqr(x3^2+y3^2)
2020 if m1<ri then 2055
2030 if pp=0 then pp=1:m2=m1:print:return
2040 if m1<m2 then pp=0:print:return
2050 goto 365
2055 n=(ri-x3)*2.05644207
2060 m=.831990528+1.41616153*(4.01469697-x3)
2065 if abs((n-y3)/n)<.00001 then gosub 2250:goto 2267
2070 if abs((m-y3)/m)<.00001 then gosub 2255:goto 2267
2075 if m<y3 then print"no PM position":goto 382
2080 if n<y3 then kh=1
2085 if n>y3 then kh=-1
2145 if x3=0 then x3=.05:goto 2155
2150 if abs(x3)<.05 then x3=.05*abs(x3)/x3
2153 if kh=1 then 2600
2155 i=0:pm=.0002/(ri-abs(x3))
2160 x(1)=(abs(x3)+pm)*abs(x3)/x3:x(2)=(abs(x3)+2*pm)*abs(x3)/x3
```

```
2165 i=i+1:x4=x(i):qs=ri^2-x4^2:if qs<0 then print"no PM position":return
2170 y4=-sqr(qs):ga=atn((x4-x3)/(y4-y3)):te=atn(x4/y4)
2175 c4=te-ga:js=sin(c4)*n31/n21:jc=sqr(1-js^2):c3=atn(js/jc)
2180 be=te-c3:tt=tan(be):q1=1+tt^2:q2=-(2*y4)*(tt^2)+2*(tt*x4)
2185 q3=-(ro^2-x4^2+(2*tt)*(y4*x4)-(tt^2)*(y4^2))
2187 qs=q2^2-4*q1*q3:if qs<0 then print"no PM position":return
2190 y5=(-q2-sqr(qs))/(2*q1)
2195 x5=sqr(ro^2-y5^2)*abs(x3)/x3
2200 c1=atn(x5/y5):c2=c1-be
2205 d(i)=sin(c1)-n21*sin(c2)
2210 dd=d(i)*2/(sin(c1)+n21*sin(c2))
2215 if abs(dd)=<0.00001 then 2265
2220 if i=1 then 2165
2225 s1=(d(i)-d(i-1))/(x(i)-x(i-1))
2230 k=1
2235 x(i+1)=x(i)-d(i)/(k*s1)
2240 if abs(x(i+1))<ri then 2165
2245 k=k+1
2246 rem---if k>100 then print"no pm position here":kh=1:goto 362
2247 goto 2235
2250 x5=-(ro*(-5.02047586))/sqr(1+(-5.02047586)^2)
2251 yp=x5*y3/x3
2252 return
2255 x5=ro
2256 yp=x5*y3/x3
2257 return
2265 yp=x5*y3/x3
2267 x5=int(x5*1000)/1000:yp=int(yp*1000)/1000
2280 if p1=0 then gosub 2500:return:rem---this prints on screen
2285 gosub 4000:rem---this prints on printer
2310 return
2500 rem---this section prints on screen
2510 p=p+1:if p>10 then p=0
2515 if p=0 then gosub 3000
```

```
2517 x3=int(x3*1000)/1000:y3=int(y3*1000)/1000:y0=int(y0*1000)/1000
2518 x0=int(x0*1000)/1000
2520 printtab(3)x3tab(16)y3;
2530 print tab(31)y0tab(45)x0;
2540 print tab(60)yptab(71)x5
2550 return
2600 rem---this section calculates cross-over for troublesome area
2605 i=0:pm=.1/(ri-abs(x3))
2610 gosub 2800
2615 pm=(ri-p3)/3
2617 x(1)=(abs(p3)+pm)*abs(p3)/p3:x(2)=(abs(p3)+2*pm)*abs(p3)/p3
2620 i=i+1
2625 x4=x(i):qs=ri^2-x4^2:if qs<0 then print"no PM position":return
2630 y4=+sqr(qs):ga=3.14158+atn((x4-x3)/(y4-y3)):te=atn(x4/y4)
2635 c4=ga-te:js=sin(c4)*n31/n21:jc=sqr(1-js^2):c3=atn(js/jc)
2640 be=3.14158-(te-c3):tt=tan(be):q1=1+tt^2:q2=-2*tt*(tt*y4+x4)
2645 q3=-(ro^2-x4^2-2*tt*(y4*x4)-(tt^2)*(y4^2))
2650 qs=q2^2-4*q1*q3:if qs<0 then print"no PM position":return
2660 y5=(-q2-sqr(qs))/(2*q1)
2665 x5=sqr(ro^2-y5^2)*abs(x3)/x3
2670 c1=atn(x5/y5):c2=e1-be
2675 dd=sin(c1)-n21*sin(c2)
2680 d(i)=dd*2/(sin(c1)+n21*sin(c2))
2685 if abs(d(i))=<0.00001 then 2265
2690 if i=1 then 2620
2695 if d(i)/d(i-1)<0 then pm=-pm/2:goto 2705
2700 if d(i)<0 and d(i)<d(i-1) then pm=-pm:goto 2705
2702 if d(i)>0 and d(i)>d(i-1) then pm=-pm
2705 x(i+1)=x(i)+pm
2710 goto 2620
2800 rem---this section calculates initial x4 for troublesome area
2805 tn=(2.28419-y3)/(2.98925-x3)
2810 q1=1+tn^2:q2=2*tn*y3-(2*x3)*(tn^2):q3=y3^2-ri^2+(tn*x3)^2-(2*tn)*(x3*y3)
2815 p3=(-q2+sqr(q2^2-4*q1*q3))/(2*q1)
2820 return
```

```
3000 print"90 deg backscatter.   laser beams in vertical position."
3003 print"-------------------------------------------------------------------";
3006 print"----------------"
3010 print" position of cross-over ";
3015 printtab(29)" distance of laser from ";
3020 print tab(58)" distance of PM from "
3025 print"     X             Y ";
3030 print "          X-axis          Y-axis ";
3035 print "      X-axis       Y-axis "
3040 print"-------------------------------------------------------------------";
3045 print"----------------"
3050 return
3500 rem---this section prints heading for printer output
3505 print"90 deg backscatter.   laser beams in vertical position."
3510 print"-------------------------------------------------------------------";
3515 print"-----------------------------------------------------"
3520 print tab(5)" position of cross-over ";
3525 print tab(15)" distance of laser from ";
3530 print tab(15)" distance of PM from "
3540 print tab(10)" X          Y "tab(22)" X-axis      Y-axis ";
3541 print tab(18)" X-axis     Y-axis "
3560 print"-------------------------------------------------------------------";
3570 print"-----------------------------------------------------"
3580 return
4000 rem---this section prints results on the printer
4015 if lp=0 then gosub 3500:lp=1
4016 x3=int(x3*1000)/1000:y3=int(y3*1000)/1000:y0=int(y0*1000)/1000
4017 x0=int(x0*1000)/1000
4020 printtab(8)x3tab(9)y3tab(22)y0tab(6)x0tab(19)yptab(5)x5
4040 return
```

NOMENCLATURE

a, b	Constants
c, c_1 to c_6	Constants
D	Agitator diameter [m]
d_{50}	50% Undersize particle diameter of volume distribution [μm]
d_{32}	Sauter Mean Diameter = $\Sigma_i Nidi^3/\Sigma_i Nid_i^2$ [μm]
g	Acceleration of gravity = 9.8 $m.s^{-2}$
G(sT)	Autocorrelation function (for LDA)
$G(\tau)_T$	Autocorrelation function in turbulent flow
H	Phase hold up = Volume dispersed phase/volume continuous phase
I	Initiator
I_R	Relative turbulence intensity = $\frac{u}{U}$
K	Constant in equation (7, 4) [μm.sec]
k_i	Rate constant for initiation [sec^{-1}]
k_p, k_t k^M_{tr}	Rate constants for propogation, termination and transfer to monomer [l. $mole^{-1}.sec^{-1}$]
m	Molecular weight of monomer
M	Monomer
M_n, M_w	Number and weight average molecular weight
N_F	Number of fringes in beam waist diameter
N(t)	Number of photons detected in time interval T
N_b	Number of blades (of agitator)
N_s	Stirrer speed [$rev.sec^{-1}$ or $rev.\ min^{-1}$]
P_o	Power Number = $P/N_s^3 D^4 \rho$
P	Power applied to agitator [W]
P_{rev}	Probability of flow reversal
P_n	Concentration of a polymer of chain length n, per unit volume
$P_f(U)$	Fluid velocity probability density function
r	Radius of particle [m]
R_n	Concentration of a growing polymer of chain length n, per unit volume

t_c	Circulation time [sec]
t_{eff}	Effective circulation time = t_{cmax} (1 – Prev) [sec]
T	Time interval [ns]
T_g	Glass transition temperature [K]
U	Mean velocity [$m.s^{-1}$]
u	Root mean square velocity fluctuation [$m.s^{-1}$]
V	Volume of liquid in reactor [m^3]
V_{tip}	Tip speed of agitator [$m.s^{-1}$]
v_z, v_t	Vertical and tangential velocity [$m.s^{-1}$]
We	Weber number – $N_s^2 D^3 \rho/\sigma$
W_n	Weight of a polymer of chain length n
W	Width of peak of particle size distribution [μm]
x	Conversion
Z_p	Polydispersity
$\dot{\gamma}$	Shear rate [sec^{-1}]
μ_c, μ_d	Viscosity of continuous and dispersed phase [Nsm^{-2}]
μ_n, μ_w	Number and weight average chain length
ρ, ρ_p	Density of fluid and particle [Kgm^{-3}]
σ	Interfacial tension [Nm^{-1}]
τ	Period of autocorrelation function
λ	Laser wavelength [Å]
ϕ	Half angle of intersection of 2 laser beams